



Division of Molecular Therapeutics and Formulation

School of Pharmacy

Investigation of Polymer Drug Conjugates for Pancreatic Cancer

Akosua Bema Anane-Adjei,

MPharm (Hons)

Thesis submitted to the University of Nottingham for the degree of

Doctor of Philosophy

September 2019

“The definition of insanity is doing the same thing over and over again and expecting different results”

-Unknown

Abstract

Pancreatic ductal adenocarcinoma (PDAC) is one of the most fatal forms of cancer with a 10-year survival rate of <1 %. Although considerable advancement has been made in understanding the biology of the disease, most patients presenting with locally advanced or metastatic disease have an extremely poor prognosis. Gemcitabine (GEM), a nucleoside analogue of cytidine is the first-line treatment for patients diagnosed with locally advanced or metastatic disease. However, approx. 90 % of the intravenously administered dose of GEM undergoes rapid deamination in the bloodstream by cytidine deaminase (CDA), affecting the drug's therapeutic efficiency. Due to this, large doses are needed to achieve significant therapeutic efficacy leading to increased adverse effects.

In the work presented here, we report on the synthesis of hyperbranched *N*-(2-hydroxypropyl)methacrylamide) (HPMA) polymer-drug conjugates for improved biodistribution and pharmacokinetic profiles of the administered drug(s). The polymers were evaluated in two-dimensional (2D) and three-dimensional (3D) cell culture models of MIA PaCa-2 pancreatic cancer cell line.

In chapter 3, we showed the development and characterisation of the 3D pancreatic cancer models used in this work for assessing the efficacy of the drug delivery system. The MIA PaCa-2 cells were mono and cocultured with mesenchymal stem cells (MSCs) and characterised for growth, the viability of the cells in the spheroid and MSCs retention in order to select the optimum conditions for all subsequent spheroid experiments. From this experiment, we determined that 1000 cell/well and 1:1 (1000 cells each) ratio were the ideal seeding densities for the mono and coculture models of the pancreatic cancer line respectively.

In chapter 4, we synthesised three hyperbranched HPMA polymers with different hydrodynamic diameters (7 nm, 20 nm and 40 nm) to determine the ideal size for our system. All three polymers were found to be biocompatible with macrophage and the MIA PaCa-2 pancreatic cancer cell line. They were also found to exhibit 'stealth-like' properties with low uptake into RAW 264.7 macrophage cells. The biodistribution studies show differences between the fluorescent and PET-CT assays. The small-sized polymer (7 nm) was found to accumulate more in the kidneys than the 20 nm and 40 nm diameter polymers in the fluorescent studies, which is thought to be due to the small diameter of the glomerular capillary. However, in the PET-CT assay, all three polymers had enhanced liver and spleen uptake with the smallest polymer having the highest accumulation in these tissues. This is thought to be due to potential conformational changes to the polymers as a result of the conjugation of the deferoxamine (DFO) chelator. The 20 nm hydrodynamic diameter was chosen for the development of our polymer-drug conjugate systems as it exhibited the most desirable characteristics.

Chapters 5 and 6 focus on the development of our polymer-drug conjugates. Three polymer conjugates were synthesised (**HPMA-GEM**, **HPMA-DOX** and **HPMA-DOX-GEM**) for mono and combination therapy and evaluated in 2D and 3D cell culture models. The results show that the IC_{50} of the free drugs (gemcitabine and doxorubicin) was significantly lower than the IC_{50} of their respective polymer conjugates in the 2D cell culture model. Observed toxicities in the cells showed the polymer conjugates could deliver the chemotherapeutic agents effectively. In 3D cell culture, we saw less pronounced differences in efficacy between the free drugs and conjugated drugs. This may be due to improved polymer penetration through the spheroids over the small molecule free drugs. The efficacy of the polymer-drug conjugates especially in the 3D cell culture makes our hyperbranched HPMA polymer a promising delivery system for pancreatic cancer. In combination therapy,

the two drugs were found to have a synergistic effect on the pancreatic cancer cells in the 2D cell culture model. However, in the 3D cell culture assay, the drugs were shown to display antagonistic effect potentially due to the reduced effectiveness of doxorubicin in the combination. This observed difference could be attributed to the inability of the 2D cell culture model to accurately predict the *in vivo* behaviour as a result of the lack of complexity of the model; demonstrating the need to adopt 3D cell culture models for the screening of cancer therapeutics.

List of Publications

PAPERS

- A.K. Pearce, C.E. Vasey, A.B. Anane-Adjei, F. Sodano, D.J. Irvine, S.M. Howdle, C. Alexander, V. Taresco. Versatile, Highly Controlled Synthesis of Hybrid (Meth)acrylate-Polyester-Carbonates and their Exploitation in Tandem Post-Polymerization-Functionalization. Macromol. Chem. Phys. 2019, 220, 1900270.
- C.E. Vasey, A.K. Pearce, F. Sodano, R. Cavanagh, T. Abelha, V. Cuzzucoli Crucitti, A.B. Anane-Adjei, M. Ashford, P. Gellert, V. Taresco, C. Alexander. Amphiphilic tri- and tetra-block co-polymers combining versatile functionality with facile assembly into cytocompatible nanoparticles. Biomaterials Science 2019, 7 (9), 3832-3845.

CONFERENCE PRESENTATIONS

Oral Presentations

- 37th Australasian Polymer Symposium, Sunshine Coast, Queensland, Australia, November 2019;
- School of Pharmacy, Final Year School Seminar, University of Nottingham, UK, 2019;
- CDT Colloquia: AstraZeneca, Macclesfield, October 2018/ UCL, London, January 2018/ University of Nottingham, January 2017.

Poster presentations

- ULLA Summer School, Helsinki, 2019;
- AstraZeneca Pharmaceutical Development PhD Day, AstraZeneca, Macclesfield, UK, 2019;
- Postgraduate poster presentation, University of Nottingham, Nottingham, UK, 2018.

Acknowledgements

I would like to extend my greatest gratitude to my supervisors Cameron Alexander, Barrie Kellam and Kristofer Thurecht for all the guidance, support and encouragement they provided me throughout the project. They have been outstanding mentors, and their constant advice and optimism guided me in my growth as a researcher. I particularly would like to thank Cameron for always being available when needed and for his willingness and enthusiasm to discuss data and provide advice and support. I would also like to thank Kris for giving me the opportunity to visit his research lab, allowing me to spend time with and learn from his group.

I am also thankful to my supervisors at AstraZeneca, namely Marianne Ashford and Paul Gellert for their advice, ideas and support. My internal assessor, Mike Stocks, who's useful discussions, constructive criticism and technical suggestions aided in the progression of this project.

A special thank you to Amanda Pearce whose careful guidance and expertise in polymer chemistry have been vital to me since the start of my PhD. I am so grateful for the support and help you've provided and continue to provide me despite moving to a new group.

I would like to thank all the PhD students and Postdocs, past and present, in Cameron's group especially Vincenzo, Giovanna, Ruggero, Patricia, Alessandra, Lucy, Rob, Shelly and Pratik for their advice and support throughout the project. Thank you to Catherine Vasey, Addie, Paula, Ami and everyone in the office for your friendship and keeping me sane over the years. I would also like to thank the group in Kris' lab, especially Nick and Zach for their help and support and making me feel welcome during my stay.

I'd like to acknowledge EPSRC, grant number EP/L01646X, for funding this project. Thank you to the CDT family, mainly, Claudia Matz for always being there to listen and for making my life considerably easier over the four years. I would also like to thank all the technicians at Boots Science Building and Cancer Biology, particularly, Carol, Amy, Julia, Pam and Catherine for their technical assistance and support.

Finally, I would like to extend my deepest gratitude to the special people in my life whose love, support and believe in me have been invaluable. To my incredible partner Jamie, I am so grateful for your love and support during these past years - from having to endure the constant groan and the incessant stress to taking interest in my work although you may not always understand what I'm talking about. Also, thank you for all the hours spent on Photoshop helping me create diagrams and figures to help bring life to my work. Finally, to my amazing family, Mum, Dad, Nanama, Adjoa and Awuradjoa, I cannot thank you enough for your endless love and support throughout this journey. The unconditional love you provide me will carry me forever and I am immensely grateful. Mum and Dad, thank you for always being there to listen through the tough times and the best and always being incredibly supportive and encouraging – none of this would be possible without you.

Table of Contents

Chapter 1 Introduction 1

1.1 Pancreatic Ductal Adenocarcinoma (PDAC) 5

1.1.1 Pathophysiology of PDAC 7

1.1.2 Epidemiology and aetiology 9

1.1.3 Diagnosis of PDAC 10

1.1.3.1 Clinical presentation 10

1.1.3.2 Imaging 10

1.1.3.3 Cytology 11

1.1.4 PDAC staging 12

1.1.5 Management of PDAC 13

1.1.5.1 Surgery 13

1.1.5.2 Adjuvant therapy 13

1.1.5.3 Neoadjuvant treatment 15

1.1.5.4 Palliative care 16

1.2 Gemcitabine 18

1.2.1 Clinical pharmacology 18

1.2.2 Pharmacokinetics of Gemcitabine 18

1.2.3 Uptake and metabolism 19

1.2.4 Mechanism of action 20

1.2.5 Inactivation 22

1.3 Polymers as drug delivery systems 22

1.3.1 Polymer-drug conjugates 24

1.3.2 Stimuli-responsive prodrugs for drug delivery 26

1.3.2.1 pH-responsive systems 26

1.3.2.2 Redox-responsive systems 27

1.3.2.3 Self-immolative stimuli-responsive systems 28

1.3.3 Difficulties in clinical translation 30

1.4 *N*-(2-hydroxypropyl)methacrylamide (HPMA) polymers 31

1.4.1 HPMA polymer-drug conjugates 32

1.5 Hyperbranched polymers 35

1.6 RAFT polymerisation 37

1.7 *In vitro* cancer models 40

1.7.1 3D cancer models 41

1.8 Mouse models for pancreatic cancer 44

1.9 Aims and Objectives 46

Chapter 2 Materials and Instrumentation 49

2.1 Materials 49

2.1.1 Synthesis....49

2.1.2 Cell Biology....50

2.2 Instrumentation....50

2.3 Supplementary Information....57

Chapter 3 Development and characterisation of a 3D Spheroid Model of Pancreatic Cancer....58

3.1 Introduction....58

3.2 Experimental....59

3.2.1 Tissue Culture of the cell monolayer....59

3.2.1.1 Culturing of the cell monolayer....59

3.2.1.2 Freezing cell stocks....59

3.2.1.3 Thawing cell stocks....60

3.2.2 3D Spheroid generation....60

3.2.3 3D Spheroid characterisation....60

3.2.3.1 Spheroid imaging....60

3.2.3.2 Growth analysis....61

3.2.3.3 Monitoring Cell Viability in the 3D Spheroid....61

3.2.3.4 Statistical Analysis....61

3.3 Results and Discussion....62

3.3.1 Monitoring MIA PaCa-2 mono-culture spheroid growth.....62

3.3.2 Monitoring Cell Viability in the 3D Spheroid 65

3.3.3 Retention of GFP labelled MSCs in MIA PaCa-2 spheroid co-culture model 68

3.4 Conclusions.....71

3.5 Chapter acknowledgements 72

Chapter 4 Size effect on cellular uptake and *in vivo* distribution of non-degradable hyperbranched HPMA polymer.....73

4.1 Introduction.....73

4.2 Experimental 73

4.2.1 Synthesis of hyperbranched HPMA polymer.....73

4.2.2 Cyanine 5 (Cy5) conjugation to HB-HPMA polymers 77

4.2.3 Conjugation of deferoxamine chelator to Cy5 labelled HB-HPMA polymer 78

4.2.4 Cell culture 79

4.2.5 *In vitro* 2D cell viability assay of MIA PaCa-2 cell line 79

4.2.6 *In vitro* 2D cellular uptake assay in MIA PaCa-2 cell line 80

4.2.7 *In vitro* 3D cell viability assay of MIA PaCa-2 cell line 80

4.2.8 CellTiter-Glo® 3D cell viability assay in MIA PaCa-2 cell line.....81

4.2.9 *In vitro* 3D cell uptake assay in MIA PaCa-2 cell line 81

4.2.10 Spheroid dissociation....81

4.2.11 Cytocompatibility evaluation in macrophages....82

4.2.12 Macrophage uptake of particles assessed by spectrophotometry....83

4.2.13 Statistical Analysis....83

4.2.14 *In vivo* biodistribution studies....83

4.2.14.1 Fluorescent biodistribution study....83

4.2.14.2 PET-CT biodistribution study in tumour naïve and tumour bearing mice 85

4.3 Results and discussion....87

4.3.1 Synthesis and physical characterisation of HB-HPMA polymers....87

4.3.2 *In vitro* toxicity and cellular uptake of synthesised polymers....92

4.3.3 *In vitro* macrophage cytotoxicity and uptake....97

4.3.4 *In vivo* analysis of organ distribution....100

4.3.4.1 Fluorescent biodistribution study....100

4.3.4.2 PET-CT biodistribution study in tumour naïve and tumour bearing mice 103

4.4 Conclusions....114

4.5 Chapter acknowledgements....115

4.6 Supplementary Information....115

Chapter 5 Development, *in vitro* and *in vivo* evaluation of synthesised HPMA-GEM polymer 122

5.1 Introduction 122

5.1.1 GEM prodrugs 122

5.2 Aims 125

5.3 Experimental 126

5.3.1 Synthesis of 4-((1-methacrylamidopropan-2-yl)oxy)-4-oxobutanoic acid (HPMA Acid) 126

5.3.2 Synthesis of HPMA-GEM monomer 127

5.3.3 Synthesis and purification of HPMA-GEM hyperbranched polymer conjugate 127

5.3.4 *In vitro* 2D cell viability assay 128

5.3.5 *In vitro* 3D cell viability assay 128

5.3.6 CellTiter-Glo® 3D cell viability assay 129

5.4 Results and discussion 129

5.4.1 Synthesis of HPMA-GEM polymer conjugate 129

5.4.2 *In vitro* cytotoxicity assay 135

5.5 Conclusions 142

5.6 Supplementary Information 143

Chapter 6 Combination therapy 145

6.1 Introduction....145

6.2 Experimental....146

6.2.1 Synthesis of HPMA-aminoethyl-2' -Hydroxyethyl disulfide (HPMA-Disulfide)....146

6.2.2 Synthesis of HPMA-DOX monomer....147

6.2.3 Synthesis, characterisation and purification of HPMA-DOX....150

6.2.4 Synthesis and purification of HPMA-DOX-GEM polymer....150

6.2.5 *In vitro* 2D cell viability assay....151

6.2.6 *In vitro* 3D cell viability assay....151

6.3 Results and discussion....151

6.3.1 Synthesis of the prodrug HPMA polymers....151

6.3.2 *In vitro* 2D cytotoxicity assay....154

6.3.3 *In vitro* 3D cytotoxicity assay....159

6.3.3.1 HPMA-DOX 3D assay....159

6.3.3.2 Combinational therapy 3D assay....164

6.4 Conclusions....169

6.5 Supplementary Information....170

Chapter 7 Summary and outlook....172

7.1 Summary....172

7.2 Future work 176

7.2.1 Short term.....176

7.2.2 Long term 177

Chapter 8 References 179

Chapter 9 Appendix 218

Table of Figures

Figure 1-1 Crystal structures of Pembrolizumab and Atezolizumab. Ref [21-22] 3

Figure 1-2 Examples of kinase inhibitors used to molecularly target proteins involved in cell proliferation..... 4

Figure 1-3 Chemical structures of gemcitabine and doxorubicin, an example of traditional chemotherapeutic agents used in clinics. 5

Figure 1-4 Anatomy of the Pancreas. Reproduced (adapted) with permission from Blausen Medical 2014 6

Figure 1-5 Genetic and morphological progression of pancreatic carcinogenesis. Reproduced with permission from BMJ Publishing Group Ltd. License number 4630150369693..... 8

Figure 1-6 Cystic precursors of pancreatic cancer. A) Low power view of an intraductal papillary mucinous neoplasm. B) Low power view of a mucinous cystadenoma. C) High power view of (B), illustrating the presence of ovarian-like stroma underlying the mucinous epithelium. Reproduced with permission from BMJ Publishing Group Ltd. License number 4630150369693..... 8

Figure 1-7 Chemical structure of 5-fluorouracil (5-FU) 16

Figure 1-8 Chemical structure of Gemcitabine [2′-Deoxy-2′,2′-difluorocytidine] 18

Figure 1-9 Cellular metabolism of Gemcitabine. Reproduced (adapted) with permission from Elsevier. License number 4631920244015 19

Figure 1-10 The main mechanism of actions of Gemcitabine. (A) Represents the masked chain termination. (B) Gemcitabine self-potentiation. Reproduced with permission from Elsevier. License number 4631920244015. 21

Figure 1-11 Schematic representation of polymer therapeutics. Mw = molecular weight. Reproduced with permission from Springer Nature. License number 4631940222031.....23

Figure 1-12 The Ringsdorf model which rationalises drug delivery via polymer-drug conjugates. Reproduced with permission from ref [144] Copyright © (2012) American Chemical Society. 24

Figure 1-13 Examples of covalent linkers used in pH responsive drug release 27

Figure 1-14 Schematic representation of A) Diselenide linked polymer-drug conjugate, B) Disulfide linked polymer-drug conjugate and C) Chemical reduction of redox-sensitive polymer based on TMBQ. 28

Figure 1-15 Self-immolative stimuli responsive system. SIE = self-immolative elimination. Reproduced (adapted) with permission from Royal Society of Chemistry. License ID 4630811104161. 29

Figure 1-16 Graphical representation of I) First generation (G1) SID with a trigger and two reporter molecules. II) Second generation (G2) SID with a trigger and four reporter molecules. Reproduced (adapted) with permission from John Wiley and Sons. Licence number 4666530959531.....30

Figure 1-17 Summary of the different nanostructures based on pHPMA with abundant functionalities for drugs, imaging probes and ligand attachments. Reproduced with permission from Royal Society of Chemistry. License number 4651820176076.....32

Figure 1-18 Structures of HPMA polymer-anticancer drug conjugates used in clinical trials. Reproduced with permission from ref [187] Copyright © (2017) Current Opinion in Colloid & Interface Science. 34

Figure 1-19 Schematic presentation of dendritic polymers. Reproduced with permission from ref. [197]. Copyright (2016), Theranostics. 36

Figure 1-20 Comparison between polymers made with traditional radical polymerisation and RAFT polymerisation. Reproduced (adapted) with permission from ref [202]. Copyright (2008), American Chemical Society. 37

Figure 1-21 General structure of a RAFT agent. Type of agent and stability of adduct is crucial to obtaining control over the polymerisation with low polydispersity index and controlled architecture. 37

Figure 1-23 3D cell culture models for cancer. Reproduced (adapted) with permission from Elsevier. License number 4675280095831. 42

Figure 1-24 Liquid overlay method for the generation of 3D spheroids using Ultra-low attachment (ULA) 96-well round bottom plates. The cell suspension is seeded into wells and the plate centrifuged for 5 min at 300 xg and incubated for approx. 3-4 days to enable spheroid formation. 44

Figure 1-25 Representation of size effect of polymeric nanoparticles. Reproduced (adapted) with permission from ref [244]. Copyright (2014), Molecular and Cellular Therapies 46

Figure 2-1 Refractive index as a function of HB-HPMA polymer concentration for dn/dc determination. 57

Figure 3-1 Representative brightfield microscope images (x4 objective) of MIA PaCa-2 spheroid formation and growth at different seeding densities (1K, 2K and 4K) over 7 days, (N = 4). Scale bar = 500 µm. 63

Figure 3-2 Analysis of spheroid growth. A) Growth curve of Mia-PaCa2 spheroids of varying seeding densities (1K, 2K, and 4K) monitored from day 3 to 7; B)

Percentage volume increase of spheroids between day 3 and 7. The volume of the spheroids was calculated using the formula $4/3*\pi*r^3$, where the radius 'r' was derived from the analysis of spheroid area in ImageJ. Percentage volume increase was calculated using the equation: (Day7-Day3)/Day3 x 100. P value of <0.05 was considered statistically significant (n=4). (*p < 0.05, two-way ANOVA with Tukey's multiple comparison test).....64

Figure 3-3 Cell viability analysis of MIA PaCa-2 spheroids of varying seeding densities. Representative widefield fluorescence microscope images (x10 objective) of spheroids stained with calcein AM (green), PI (red) and Hoechst (blue) on days 3, 5, 6 and 7 in culture, (n = 4). From the enlarged images, it is clear that the necrotic core is only present in 4K seeding density on day 7 of incubation. Scale bar = 250 µm for original images and 100 µm for enlarged images.....66

Figure 3-4 Green/red (g/r) ratio of the MIA PaCa-2 spheroids for the different seeding densities on day 3-7. Green represents calcein AM stain for live cells and red represents PI stain for dead cells.....67

Figure 3-5 Representative widefield fluorescence microscope images (x10 objective) of MIA PaCa-2 cells (1K/well) co-cultured with different ratio of MSCs; A) 1:1, B) 1:2 and C) 2:1 MIA PaCa-2 to MSCs from day 3-6, (N = 4). Scale bar = 250 µm for original images and 100 µm for enlarged images. As depicted, the formation of intact spheroids over the assay period is only present in 1:1 ratio.....69

Figure 3-6 Representative widefield fluorescence microscope images (x10 objective) of MIA PaCa-2 cells co-cultured with MSCs at 1:1, 1:2 and 2:1 ratio, (N = 4). The total number of cells/well was kept constant (2K) to study the effect of total cell number on the formation of the co-cultured spheroids. Scale bar =250 µm.....70

Figure 4-1 Schematic presentation of hyperbranched HPMA polymer synthesis using RAFT polymerisation technique.....76

Figure 4-2 Schematic representation of the attachment of the ^{89}Zr chelator, deferoxamine (DFO) to a Cy5-labelled HB-HPMA polymer to enable ^{89}Zr PET imaging.....78

Figure 4-3 ^{1}H NMR spectrum of HPMA monomer in $CDCl_3$.....88

Figure 4-4. Representative ^{1}H NMR spectrum of hyperbranced HPMA polymer (HB-HPMA) in DMSO-d6. 88

Figure 4-5 A) Dynamic light scattering measurements of the different size polymers. B) Representative transmission electron microscopy images (scale bar = 200 nm) of (1) **HB-HPMA-7**, (2) **HB-HPMA-20** and (3) **HB-HPMA-40.** 90

Figure 4-6 Schematic depiction of size differences observed by DLS and TEM. 91

Figure 4-7 In vitro 2D cell viability assay at 72h post treatment with different concentrations of the three **HB-HPMA** polymers on MIA PaCa-2 pancreatic cancer cell line using trypan blue dye exclusion test of cell viability. Error bars show standard deviation (N = 4). (**p <0.01, two-way ANOVA with Tukey's multiple comparison test). 92

Figure 4-8 3D cell cytocompatibility assay with the three polymers at different concentrations (A) Percentage volume change between day 3 (pre-treatment) and day 6 (72 hours post treatment). (B) Representative brightfield images of control and treated spheroids (1000 µg/mL), demonstrating volume increase over the assay period, (N = 4).....93

Figure 4-9 In vitro CellTiter-Glo® 3D cell viability assay for the three HB-HPMA polymers in MIA PaCa-2 pancreatic cancer cell line Error bars show standard

deviation (N = 4). (*p <0.05, two-way ANOVA with Tukey's multiple comparison test). 94

Figure 4-10 2D cellular uptake of Cy5-labelled HB-HPMA polymers by MIA PaCa-2 pancreatic cancer cells after 1-hour incubation. A) Representative fluorescence microscopy images confirming intracellular localisation of **HB-HPMA-7** polymers during uptake studies (scale bar = 250 µm and 20 µm). B) FACS uptake histograms for all three polymers compared to control. Percentage of Cy5 positive cells of HB-HPMA polymers in C) mono and D) co-cultured spheroids after 2 hours incubation. Data are representative of three experiments (N = 3) (****p ≤ 0.0001 two-way ANOVA with Tukey's multiple comparisons test).....95

Figure 4-11 . In vitro cellular uptake of HB-HPMA polymers in 3D MIA PaCa-2 mono and coculture cell models. (A) Representative microscope images of cellular uptake of **HB-HPMA-7** in 3D MIA PaCa-2 monoculture system. (B) Representative microscope images of cellular uptake of **HB-HPMA-7** in co-culture spheroids (cell nuclei stained with Hoechst 33342: blue; MSC: green; Cy5 polymer: red). Percentage of Cy5 positive cells in FACS analyses of **HB-HPMA** polymers in (C) mono and (D) co-cultured spheroids after 2 hours incubation. The scale bar represents 250 µM. Data are represented as a mean (N = 3, n = 10) (**p ≤ 0.01, ****p ≤ 0.0001 two-way ANOVA with Tukey's multiple comparisons test).....96

Figure 4-12 In vitro macrophage studies. (A) Evaluation of HB-HPMA polymers biocompatibility in RAW 264.7 macrophages polymers applied in 10 % FBS/DMEM for 24 hours, (1) PrestoBlue™ cell metabolic assay (2) LDH release assay. Data are presented as mean ± S.D (N = 3, n = 3). (B) Time-dependent NP uptake in RAW 264.7 macrophages polymers applied at 50 µg/mL in 10 % FBS/DMEM. Data generated and analysed by Dr Robert Cavanagh. 98

Figure 4-13. A) Representative in vivo images (4 hr post injection), B) Ex vivo images at 1 hr, 4 hr and 24 hr post injection (Br = brain, H = heart, Lu = lungs, Li = liver, P = pancreas, Sp = spleen, K = kidney, U = urine, Bl = bladder). C) Quantitative data to highlight fluorescence signal in nanoparticle clearance organs as a percentage of total organ signal (n = 2) and D) Ratio between signal in MPS organs (spleen, lungs and liver) and renal organs (kidney) over time. Data generated by Alison Ritchie and Dr Phillip Clarke. 101

Figure 4-14 Representative in vivo PET-CT images of the ^{89}Zr-labelled HB-HPMA polymers at 3H, 27H and 72H post-injection in MIA PaCa-2 xenograft mice models. (A-C) Distribution behaviour of **HB-HPMA-7**, **HB-HPMA-20** and **HB-HPMA-40** at the indicated time points post-injection. White circles highlight the tumour location in each image. The intensity bar of the PET images represents the %ID/g whereby black = 0 %, blue = approx. 4 % and red = approx. 16 %. Data generated and analysed by Dr Nicholas Fletcher, Dr Zachary Houston and Theo Crawford. 107

Figure 4-15 PET-CT imaging of ^{89}Zr-labelled **HB-HPMA** polymers in MIA PaCa-2 xenograft model. Representative two orientation maximum intensity projection (MIP) images of all three polymers showing majority of the particles in circulation at 3 H post injection. This is followed by retention of the particles mostly in the liver in the later timepoints. The intensity bar represents the %ID/g whereby black = 0 %, white = 15 %ID/g, dark blue = 1 %ID/g and red = approx. 10 %ID/g. Data generated and analysed by Dr Nicholas Fletcher, Dr Zachary Houston and Theo Crawford.....108

Figure 4-16 PET ROI analysis of in vivo tissues accumulation of HB-HPMA polymers in MIA PaCa-2 xenograft model. A-E) Graphs of hyperbranched HPMA polymer distribution over time in heart, kidneys, liver, spleen and tumour respectively. Data generated by Dr Nicholas Fletcher and Dr Zachary Houston. .109

Figure 4-17 Comparison between the in vitro time-dependent uptake of **HB-HPMA** and **HB-HPMA-DFO** polymers in RAW264.7 macrophage cells at a concentration of 50 µg/m. Cells were cultured for 24h prior to assaying. Hyperbranched polymers were applied in DMEM containing 10 % (v/v) FBS. Data are presented as mean ± S.D (N = 3, n=3). Data generated and analysed by Dr Robert Cavanagh 111

Figure 4-18 Ex vivo λ-scintillation biodistribution data across all tissues 8 days post injection. Data generated by Dr Nicholas Fletcher and Dr Zachary Houston. 112

Figure 4-19 PET ROI analysis of in vivo tissues accumulation of HB-HPMA polymers in tumour naïve mice. A-D) Graphs of hyperbranched HPMA polymer distribution over time in heart, kidneys, liver and spleen respectively. E) Ex vivo λ-scintillation biodistribution data across all tissues 5 days post injection. Data generated by Dr Nicholas Fletcher and Dr Zachary Houston. 113

Figure 4-20 Standard calibration curve of Cy5 stock solutions. Absorbance was measure at 670 nm. 115

Figure 4-21 ^{13}C NMR spectrum of HPMA monomer in $CDCl_3$. 116

Figure 4-22 ^{1}H NMR spectrum of EDMA in $CDCl_3$. 116

Figure 4-23 ^{13}C NMR spectrum of EDMA in $CDCl_3$. 116

Figure 4-24. ^{1}H NMR spectrum of Alkyne-CTA in $CDCl_3$. 117

Figure 4-25 ^{13}C NMR spectrum of Alkyne-CTA in $CDCl_3$. 117

Figure 4-26. Graphs showing changes in spheroid volume over the 72 hours incubation with the three **HB-HPMA** polymers, (N = 4). 118

Figure 4-27 FACS histograms showing control MIA PaCa-2 only, mixed MIA PaCa-2/GFP_MSC and GFP_MSC only cell populations.....118

Figure 4-28 Representative FACS quadrants of cellular uptakes of Cy5-labelled HB-HPMA polymers in A) 2D MIA PaCa-2 cells, B) 2D MIA PaCa-2/MSC cocultured cells C) 3D MIA PaCa-2 cells and D) 3D MIA PaCa-2/MSC cocultured cells. 119

Figure 4-29 Representative ^{1}H NMR spectra for HPMA-DFO conjugation. Top) HPMA-DFO polymer. Middle) HPMA polymer and Bottom) DFO. The comparison between the different spectrum shows succesful conjugation of DFO to the backbone of the polymer.....120

Figure 4-30 Radiographic TLC of all three polymers post ^{89}Zr labelling +/-DTPA. The signals at the bottom of the TLC represent polymer bound radioisotope and any movement up the plate represents unbound ^{89}Zr (+DTPA plate) or free DFO in the sample bound to ^{89}Zr (-DTPA plate). From the TLC plates, it is clear that the polymer solutions injected for the biodistribution assay were free from unconjugated DFO. 120

Figure 4-31 PET-CT imaging of ^{89}Zr-labelled HB-HPMA polymers in MIA PaCa-2 xenograft model. A) 3 orientations of 3D rendering of the distribution of all three polymers at 27 H post injection. B) The corresponding biodistribution profile as determined by ROI analysis of PET-CT images (n=4).....121

Figure 5-1 Circled groups in the structure of gemcitabine illustrates site for chemical modification 123

Figure 5-2 Examples of gemcitabine (GEM) prodrugs and polymer conjugates 124

Figure 5-3 Schematic representation of the HPMA-GEM hyperbranched system. 125

Figure 5-4 Experimental procedure for the synthesis of HPMA-GEM polymer 126

Figure 5-5 ^{1}H NMR of **HPMA-GEM** monomer in DMSO-d_6 130

Figure 5-6 NMR spectra of HPMA-GEM polymer conjugate in DMSO-d_6. A) ^{19}F NMR showing the broadening of the fluorine peaks post polymerisation. B) ^{1}H NMR exhibiting successful polymerisation of PMA-GEM conjugate. 131

Figure 5-7 Representative microscope images of free and conjugate GEM. (A) TEM images showing the morphology of the **HPMA-GEM** polymer. Scale = 500 nm (B) Polarised optical microscopy images of: (B) Free GEM with filter, (C) Free GEM without filter, (D) HPMA-GEM polymer with filter, (E) HPMA-GEM polymer without filter. Images were acquired at room temperature. The optical images show free GEM as crystals, however when conjugated to the polymeric backbone, the drug changes physical traits to amorphous due to the lack of birefringence (E) 133

Figure 5-8 FT-IR spectra of (A) GEM, (B) control HPMA polymer and (C) **HPMA-GEM** prodrug polymer.....134

Figure 5-9 2D MIA PaCa-2 cytotoxicity assay of (A) Free and HPMA-GEM polymer conjugate incubated for 72 hours at different concentrations (the concentration of GEM was kept constant between the free drug and HPMA-GEM to allow for direct comparison between the two treatment groups). (B) Time dependent assay of HPMA-GEM - the MIA PaCa-2 cells were treated varying concentrations of HPMA-GEM and incubated for 72 or 96 hours to study the effect of incubation time on the toxicity of the polymer conjugate.....135

Figure 5-10 3D MIA PaCa-2 spheroids cytotoxicity assay. A). Representative microscope images of different drug concentrations to show differences in volume on day 4 and day 7 of the co-cultured population, (N = 4). B) Graph showing changes in the spheroid volume between days 4 and 7 expressed as a percentage; 1) Free GEM and 2) HPMA-GEM. The scale bar represents 500 µM.....138

Figure 5-11 CellTiter-Glo® 3D Cell viability assay of MIA PaCa-2 cells in mono and cocultured systems with (A) Free GEM and (B) Conjugated **HPMA-GEM** polymer. (C) MSC effect on free and conjugated **HPMA-GEM** polymer; and (D) 3D spheroid cytotoxicity. Error bars show standard deviation (N = 4). (*p ≤ 0.05, **p ≤0.01, ***p ≤ 0.001, two-way ANOVA with Sidak's multiple comparison test). 139

Figure 5-12 Optical images of mice, organs and tumour. A) In vivo images acquired at 72 hours post administration of the first dose of HPMA-GEM (1-2) and free GEM group (3). B) In vivo images acquired at 72 hours post injection of HPMA-GEM second dose C) Following excision from representative mouse 72 hours post administration of the second dose of HPMA-GEM. H heart, Lu lungs, S spleen, T tumour, Li liver, G gut, K kidneys, B blood. 142

Figure 5-13 ^{13}C NMR of HPMA-GEM monomer in DMSO-d_6 143

Figure 5-14 Microscopy images of 2D MIA PaCa-2 cells post 72-hour incubation with HPMA-GEM polymer (1 µM concentration). Hoechst = nuclei stain, PI = apoptotic cells and Calcein AM = viable cells. The stains were applied for approx. 20 min before imaging. 144

Figure 5-15 Graphs showing changes in spheroid volume over the 72 hours incubation period with free GEM and conjugated HPMA-GEM polymer, (N = 4). ..144

Figure 6-1 Schematic representation of the synthesis of **HPMA-DOX** monomer...146

Figure 6-2 Schematic representation of **HPMA-DOX** and **HPMA-DOX-GEM** polymers.....149

Figure 6-3 ^{1}H NMR spectrum of **HPMA-DOX** monomer in DMSO-d_6 151

Figure 6-4 ^{1}H NMR spectrum of **HPMA-DOX** polymer in DMSO-d_6.....152

Figure 6-5 ^{1}H NMR spectrum of HPMS-DOX-GEM polymer in DMSO-d_6.....153

Figure 6-6 Physical characteristics of **HPMA-DOX** and **HPMA-DOX-GEM** hyperbranched polymers. A) Representative transmission electron microscopy images of a) **HPMA-DOX** and b) **HPMA-DOX-GEM**. B) Dynamic Light scattering measurements. Scale bar= 200 nm for TEM images 154

Figure 6-7 2D cell viability acitvities of MIA PaCa-2 cells incubated with free and conjugarted DOX. Error bars show standard deviation (n = 4). (* p ≤ 0.05, ****p <0.0001, two-way ANOVA with Sidak's multiple comparison test). 155

Figure 6-8 Proposed mechanism for the self-immolative DOX release from the backbone of the HPMA polymer 156

Figure 6-9 3D MIA PaCa-2 spheroids cytotoxicity assay. A&B). Representative microscope images of different drug concentrations to show differences in volume on day 4 and day 7 of the mono and co-cultured systems respectively. C&D) Graphs showing changes in the spheroid volume between days 4 and 7 expressed as a percentage (C) Free GEM and (D) HPMA-GEM. The scale bar represents 500 µm. Error bars show standard deviation (n = 4). (*p ≤ 0.05, **p <0.01, p*** ≤0.001, two-way ANOVA with Sidak's multiple comparison test).....161

Figure 6-10 CellTiter-Glo® 3D Cell viability assay (A) Free DOX, (B) Conjugated **HPMA-DOX** polymer, (C) Comparison between free and conjugated DOX in monocultured spheroid and D) Comparison between free and conjugated DOX in cocultured system. Error bars show standard deviation (n = 4). (**p ≤0.01, ***p ≤ 0.001, ****p ≤0.0001, two-way ANOVA with Sidak's multiple comparison test). 162

Figure 6-11 3D MIA PaCa-2 spheroid cytotoxicity od combination therapy. A) Microscope images of the spheroids on days 4 and 7 in culture. B) Percentage volume changes between days 4 and 7 of mixed **HPMA-GEM** and **HPMA-DOX**

treatment. C) Percentage volume changes between days 4 and 7 of conjugated **HPMA-DOX-GEM**. D) Table depicting statistically significant resutls of the percentage volume change analysis. Error bars show standard deviation (n = 4). (*p ≤0.05, ***p ≤0.001, ****p ≤ 0.0001, two-way ANOVA with Dunnett's multiple comparisons test.....165

Figure 6-12 Combination index of DOX and GEM against MIA PaCa-2 cell line in 3D cell culture assay. 167

Figure 6-13 CellTiter-Glo® 3D Cell viability assay 72 hours post treatment with (A) **HPMA-DOX-GEM-m**, (B) **HPMA-DOX-GEM-c**. C) Comparison between mixed and conjugated **HPMA-DOX-GEM** in monoculture spheroid D) Comparison between mixed and conjugated **HPMA-DOX-GEM** in coculture system. Error bars show standard deviation (n = 4). (*p ≤0.05, two-way ANOVA with Sidak's multiple comparisons test) 168

Figure 6-14 ^{1}H NMR of HPMA-Disulfide in DMSO-d_6.....170

Figure 6-15 ^{13}C NMR of HPMA-Disulfide in DMSO-d_6.....171

Figure 6-16 ^{13}C NMR of **HPMA-DOX** monomer in DMSO-d_6 171

Figure 7-1 Proposed mechanism for attachment of Paclitaxel to HPMA backbone using cystamine as the linker.....177

Table of Tables

Table 1 TNM staging system of pancreatic cancer[86] 12

Table 2 HPMA based polymer-drug conjugates in clinical trials as anticancer agents. ..... **Error! Bookmark not defined.**

Table 3 Key features of tumour cells in 2D cell culture, 3D spheroids and in vivo tumour. Adapted from[235] 40

Table 4 Advantages and disadvantages of commonly used 3D spheroid methods. Adapted from[248] 42

Table 5 Reaction conditions used for the synthesis of the three hyperbranched HPMA polymers.....77

Table 6 Physical characterisation of varying size HB-HPMA polymers. 89

Table 7 Percentage of DFO units HB-HPMA polymer.....103

Table 8 Characteristics of **HPMA-GEM** polymer 132

Table 9 IC_{50} of free and **HPMA-GEM** polymer conjugate in 2D cell culture assay.136

Table 10 Reaction conditions used in the synthesis of **HPMA-DOX** and **HPMA-DOX-GEM** polymers.....150

Table 11 Physical characteristics of the synthesised **HPMA-DOX** and **HPMA-DOX-GEM** polymers.....152

Table 12 IC_{50} values for the 2D cell viability assays of free DOX, **HPMA-DOX** conjugate and conjugated and mixed **HPMA-DOX-GEM**. 156

Table 13 Dosing regimen for 2D cell viability assay of the combination therapy....157

Table 14 Dose-effect parameters and mean combination index (CI) values as a function of cell viability of GEM and DOX individually and as a combination of MIA PaCa-2 pancreatic cancer cell line.....158

Table 15 Comparison between the IC_{50} of the 2D and 3D cytotoxicity assay of free and conjugated DOX in the pancreatic cancer cell line. 163

Table 16 IC_{50} values for the 3D cell culture assessment of DOX and GEM combinational therapy.....166

Abbreviations

^{13}C NMR	carbon nuclear magnetic resonance spectroscopy
^{19}F NMR	fluorine nuclear magnetic resonance spectroscopy
^{1}H NMR	proton nuclear magnetic resonance spectroscopy
2D	two-dimensional
3D	three-dimensional
^{89}Zr	zirconium-89
ADM	acinar-to-ductal metaplasia
AIBN	azobisisobutyronitrile
ATP	adenosine triphosphate
BME	basement membrane extract
BM-MSCS	bone marrow-derived mesenchymal stem cells
CAFs	cancer-associated fibroblasts
CDCl3	deuterated chloroform
CEPA	4-cyano-4-(ethylsulfanylthiocarbonyl) sulfanyl pentanoic acid
CI	combination index
CT	x-ray computed tomography
Cy5	cyanine 5
DCM	dichloromethane
Dh	hydrodynamic diameter
DLS	dynamic light scattering
DMAP	4-dimethylaminopyridine
DMEM	Dulbecco's modified Eagle's medium
DMF	dimethylformamide
DMSO	dimethyl sulfoxide
DMSO-d6	deuterated dimethyl sulfoxide
DNA	deoxyribonucleic acid
DOX	doxorubicin
ECM	extracellular matrix
EDC	1-ethyl-3-(3-dimethylaminopropyl)carbodiimide
EDMA	ethylene dimethacrylamide
EDTA	ethylenediaminetetraacetic acid
eGFP	enhanced green fluorescent protein

EPR	enhanced permeability and retention
FACS	fluorescence-activated cell sorting
FBS	foetal bovine serum
GEM	gemcitabine
GFP	green fluorescent protein
GPC	gel permeation chromatography
HB	hyperbranched
HPMA	N-(2-hydroxypropyl)methacrylamide
ID	injected dose
kDa	kilodalton
MCTS	multicellular tumour spheroids
MeOH	methanol
MgSO4	magnesium sulphate
MIPs	maximum intensity projections
Mn	number average molecular weight
MPS	mononuclear phagocyte system
MS	mass spectroscopy
MSCGS	mesenchymal stem cell growth supplement
MSCM	mesenchymal stem cell medium
MSCs	mesenchymal stem cells
MWCO	molecular weight cut-off
ns	not significant
PaCa	pancreatic cancer
PBS	phosphate-buffered saline
pCAF	pancreatic cancer-associated fibroblasts
PDAC	Pancreatic ductal adenocarcinoma
PEG	poly(ethylene glycol)
PET	positron emission tomography
PI	propidium iodide
PSCs	pancreatic stellate cells
RAFT	reversible addition-fragmentation chain-transfer
RCF	relative centrifugal force
ref	reference
Rf	retention factor

RI	refractive index
ROI	region of interest
SI	supporting information
TEA	triethylamine
TEM	transmission electron microscopy
TFA	trifluoroacetic acid
TME	tumour microenvironment
ULA	ultra-low attachment
UV	ultraviolet

Chapter 1 Introduction

Cancer occurs due to an abnormality in cell growth causing a disruption in the process of cell division. This disruption results in an imbalance in cell growth and apoptosis mechanisms leading to the formation of a mass of tissue commonly referred to as a solid tumour. The global burden of cancer is vast and continues to increase, particularly in economically developed countries as a result of an ageing population and espousal of cancer-related lifestyles such as smoking and reduced physical activity.[1] However significant improvements in the survival rate of cancer have been made through early diagnosis, accessibility to healthcare and development of therapies such as radiotherapy, cytotoxic chemotherapy and molecularly targeted therapy.[2]

For many years, cytotoxic chemotherapeutics such as DNA-damaging drugs that work by killing or inhibiting rapidly dividing cells, have dominated systemic cancer therapy.[2] Although these therapeutics are effective, their unspecific mechanism of action means all rapidly dividing cells in the body including non-cancerous cells are targeted thereby inducing adverse side effects such as hair loss, neutropenia, nausea and vomiting, thrombocytopenia and bone marrow depression in the patients. In addition to this, a high incidence rate of tumour relapse arising from the development of drug resistance mechanisms has been reported with conventional chemotherapeutic and radiation therapies.[3]

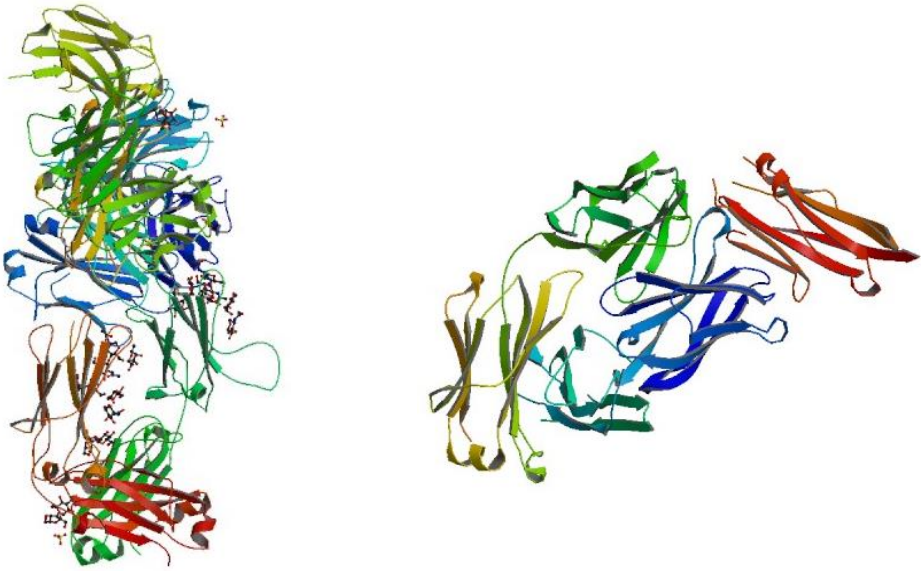
This has consequently shifted the focus of cancer therapeutics from traditional cytotoxic chemotherapy to alternative treatment approaches such as cancer immunotherapy and molecularly targeted cancer therapy to eliminate resistant tumour cells and improve outcome.[4-6]

Cancer immunotherapy has become an appealing and attractive strategy in the treatment of a wide range of haematological and solid tumours due to perceived

improved prognosis.[3, 6, 7] Immunotherapy uses the body's own immune system to induce an anti-tumour response to fight the cancer cells.[3, 8, 9]

Several immune cells affect the growth of tumour in humans. The fundamental role of the immune system is to protect against diseases such as infections caused by foreign pathogens.[6] The immune system consists of innate cells [mediates fast and short-lived response using immune cells such as monocytes, macrophages, dendritic and natural killer (NK) cells], and adaptive cells (which develop long-lived responses and memory and comprise T cells and B cells).[3] Both innate and adaptive immune systems play a vital role in anticancer immune response.[10, 11] The innate system provides the earliest response to abnormal cell growth by releasing cytokines to lyse the cells (NK cells) or engulfing and presenting (monocytes, macrophages, and dendritic cells) peptide fragments of specific foreign antigens from debris of dead cells to T cells.[3] T cells and B cells from the adaptive immune system generate delayed antigen-specific response as a result of proliferation and differentiation of the minor subpopulations expressing antigen-specific receptors.[3] This proliferation and differentiation events are promoted by inflammatory cytokines [interferon (IFN)-γ, interleukin (IL)-12)] produced by activated innate immune cells or T cells, leading to the production of an array of competent and activated effector cells.[3] The role of T cells is to either directly induce cell lysis [$CD8^+$ cytolytic (CTL)] or release immunomodulatory cytokines [CD4+ helper (Th)] to the same effect. However, B cells elicit a humoral response by secreting antigen-specific immunoglobulin (Ig).[3] There has been a rise in the reported rate of positive response with cancer immunotherapy – at times, with complete or long-lasting responses or cure in patients with aggressive malignancies.[12-15] Checkpoint inhibitors (CPIs) and chimeric antigen receptor (CAR) T cells are the main driving forces behind this success.[7] Current studies of CPIs for cancer therapy focus on combinational approaches, new tumour entities, perioperative use, toxicity management, response

prediction, and use in special patient populations.[7] Malignant tumours are able to evade immune recognition by *inhibiting programmed cell death protein 1/programmed cell death protein ligand 1* (PD-1 / PD-L1) or *cytotoxic T-lymphocyte-associated protein* (CTLA-4) pathways.[7, 16] There have been several successful phase III clinical trials for the combinational use of PD-1 / PD-L1-blockades, such as pembrolizumab and atezolizumab (Figure 1-1) with chemotherapeutic agents in non-small cell and small cell lung cancer (NSCLC and SCLC respectively), breast, and head and neck squamous cell carcinoma (HNSCC).[17-22]



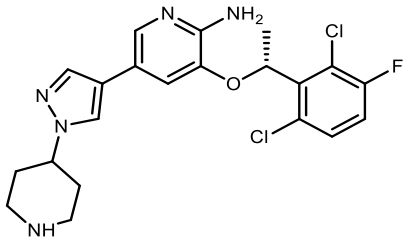
Pembrolizumab **Atezolizumab**

Figure 1-1 Crystal structures of Pembrolizumab and Atezolizumab. Ref [21-22]

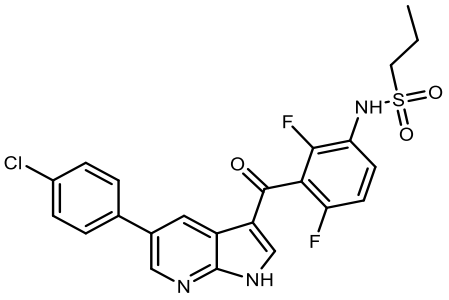
Axicabtagene-ciloleucel and *Tisagenlecleucel* were the first CAR T cell cancer immunotherapies approved by the FDA and EMA for the treatment of acute lymphoblastic leukaemia (ALL, *tisagenlecleucel*) and diffuse large B-cell lymphoma *(*DLBCL*, tisagenlecleucel* and *axicabtagene-ciloleucel*). In the ELIANA trial, *tisagenlecleucel* was found to exhibit a remarkable response rate in paediatric and young adult patients presenting with relapsed or refractory ALL.[23] The JULIETH trial also found high rates of lasting response in adult patients with relapsed or refractory

DLBCL treated with *tisagenlecleucel*.[24] Finally, patients with refractory large B cell lymphoma who were treated with *axicabtagene-ciloleucel* achieved high levels of durable response with a 52 % overall survival rate at 18 months.[25] Due to the clinical successes of these agents, many trials are investigating the use of CPIs and CAR T cell therapies in a range of other haematological and solid cancer types.[26] However, due to their mode of action, immunotherapies can induce toxicities such as cytokine release syndrome, colitis, autoimmune hepatitis, endocrine or neurological side effects and myelosuppression.[7, 25] In addition to this, clinical success rate with the adoptive T cell therapy has mostly been seen in haematological malignancies with poor translation to solid tumours and thus are not a treatment option for many solid tumours such as pancreatic cancer.[7] Therefore, a more advanced protocol for the use of tumour reactive (TCR-native) T cells and advancement in the genetic engineering of CAR T cell are needed to enable this transition.

Molecularly targeted therapy is another example of a new treatment approach for cancer therapy. They focus on the specific modulation of the functions of proteins and other cellular components directly linked to the disease, such as the inhibition of protein kinases involved in cell proliferation. This approach has led to increasing numbers of successful therapies for the treatment of diseases including breast and prostate cancers.



Crizotinib



Vemurafenib

Figure 1-2 Examples of kinase inhibitors used to molecularly target proteins involved in cell proliferation.

However there are some drawbacks to the use of molecularly targeted therapy such as rapid development of resistance (e.g. crizotinib and vemurafenib, Figure 1-2) due to mutation of the target itself prompting activation of adaptive feedback loop or exploitation of alternative oncogenic pathways.[4, 27-31] Additionally, for many patients, this therapeutic option is very limited due to high failure rates in target identification and even when available, must be used in combination with other treatments such as chemotherapy, radiation and/or surgery.[32] Therefore it is of benefit to improve the delivery of traditional chemotherapeutic agents such as gemcitabine and doxorubicin (Figure 1-3), especially for patients, including pancreatic cancer patients, whom single-agent molecularly targeted therapy is not an option.

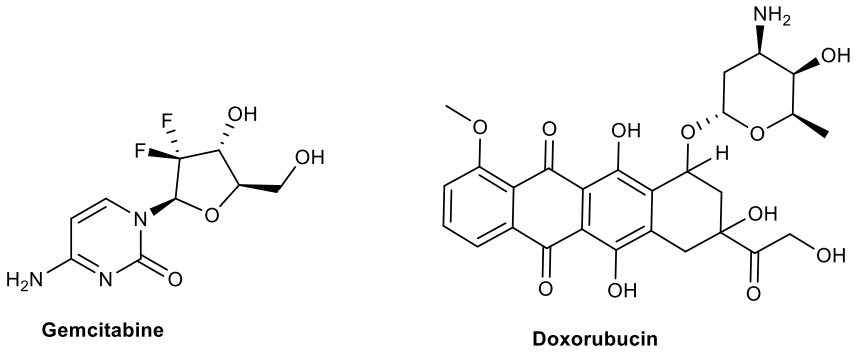


Figure 1-3 Chemical structures of gemcitabine and doxorubicin, an example of traditional chemotherapeutic agents used in clinics.

1.1 Pancreatic Ductal Adenocarcinoma (PDAC)

The pancreas (Figure 1-4) is an organ situated posterior to the peritoneum and weighs approx. 75-100 grams with an estimated length of 15-20 cm.[33] The pancreas is primarily an exocrine organ, constituting to approx. 95 % of pancreatic mass. The exocrine pancreas is responsible for the secretion of several digestive enzymes, including pancreatic lipase, proteases and amylase from acinar cells for the digestion of fats, proteins and carbohydrates respectively.[34] It also controls the secretion of an aqueous solution containing bicarbonate from the ductal epithelial cells to neutralise the pH of the chyme from the stomach.[35]

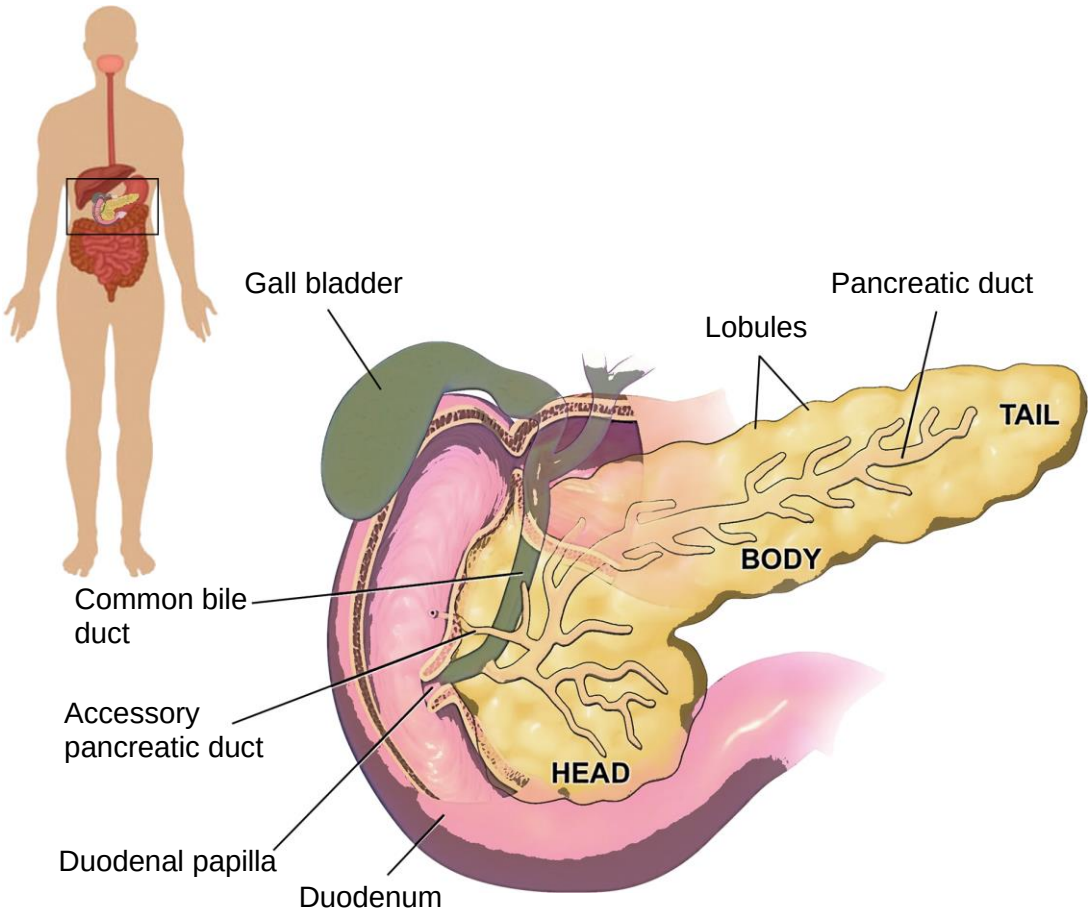


Figure 1-4 Anatomy of the Pancreas. Reproduced (adapted) with permission from Blausen Medical 2014.

The pancreas also functions as an endocrine organ, regulating the blood glucose levels through the secretion of hormones such as glucagon and insulin.[34] The islet of Langerhans, from which these hormones are produced is a cluster of cells within the pancreas responsible for the production and secretion of hormones for regulation of glucose levels.[36]

Histological analysis of the pancreas provides an understanding of the normal structural features of the organ and hence is useful for studies into the diseases such as pancreatic ductal adenocarcinoma (PDAC).[37]

PDAC, commonly referred to as pancreatic cancer, is a cancer of the exocrine pancreas and accounts for over 85 % of pancreatic malignancies.[38] The defining characteristic of PDAC is the differentiation of columnar and cuboidal cells to ductal

cells in a process known as acinar-to-ductal metaplasia (ADM).[39] The overproduction of extracellular matrix (ECM)-rich connective tissues, fibroblasts, immune cells and pancreatic stellate cells surrounding these ductal cells give rise to the characteristic desmoplasia feature commonly seen in PDAC tumours.[40] PDAC originates from the ductal epithelium, with approx. 70 % arising from the head of the pancreas and the rest from the body and tail (Figure 1-4).[41-43] Cancer lesions of the body and tail are known to have poorer clinical outcomes compared with head lesions.[44] Surgical intervention remains the only chance for cure of PDAC, however approx. 90 % of cases are surgically incurable at the time of diagnosis.[45]

1.1.1 Pathophysiology of PDAC

The ductal and ductular epithelium is normally seen as a cuboidal to low-columnar epithelium with amphophilic cytoplasm without atypia, mucinous cytoplasm or nuclear crowding.[46] However, these features diminish in pancreatic cancer. Three main precursor lesions have been identified to play a vital role in the development of pancreatic cancer. These are pancreatic intraepithelial neoplasia (PanIN); intraductal papillary mucinous neoplasm (IPMN) and mucinous cystic neoplasm (MCN) with PanIN being the most common precursor lesion.[47-49] PanINs are microscopic lesions that arise in the small pancreatic ducts (<5 mm) and lead to the development of conventional ductal adenocarcinoma (Figure 1-5).[47, 50] PanIN-1s are classed as low-grade lesions and sub-divided into 1A and 1B.[46, 51, 52] PanIN-1As appear as flat epithelial lesions comprising of tall columnar cells with abundant supranuclear mucin and basally located nuclei.[46] PanIN-1Bs are structurally identical to PanIN-1A. However, the architectural nature of the epithelial lesions is papillary, micropapillary or basally pseudostratified.[46] PanIN-2 are characterised as intermediate lesions as they are architecturally more complex than PanIN-1.[46, 52] PanIN-2 lesions have nuclear abnormalities such as enlargement of the nuclei, loss

of polarity and nuclear crowding. Mitosis rarely occurs but when present is atypical.[46, 51, 52]

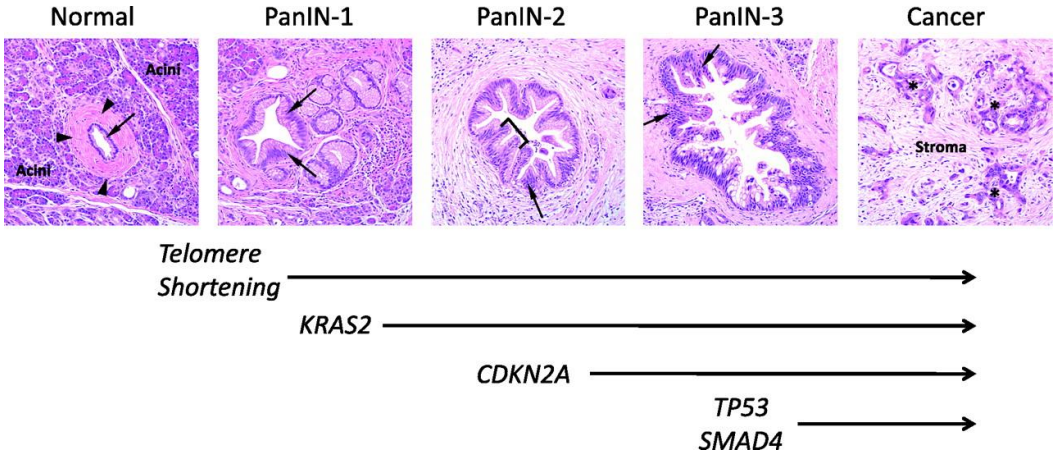


Figure 1-5 Genetic and morphological progression of pancreatic carcinogenesis. Reproduced with permission from BMJ Publishing Group Ltd. License number 4630150369693.

PanIN-3 displays the highest-grade lesions and hence dysplasia. The lesions are architecturally more complex with the presence of cytologic abnormalities such as the formation of cribriform and papillae structures.[46, 52] The 'budding off' of small clusters of epithelial cells into the lumen and necrosis of the lumen leads to the diagnosis of PanIN-3 lesions.[46] The nucleus in PanIN-3 is enlarged with loss of polarity and is poorly oriented with occasional abnormal mitoses.[46, 52]

As mentioned above, pancreatic cancer can also develop from IPMN and MCN (Figure 1-6).[47] However, the incidence of these lesions is 13-100-fold less common than PanIN lesions.[47, 53]

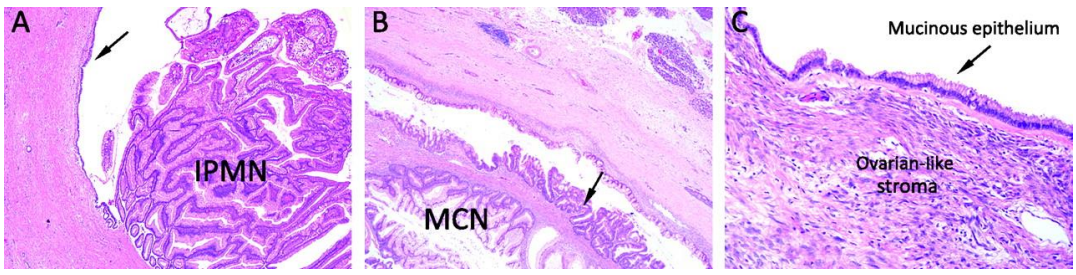


Figure 1-6 Cystic precursors of pancreatic cancer. A) Low power view of an intraductal papillary mucinous neoplasm. B) Low power view of a mucinous cystadenoma. C) High power view of (B), illustrating the presence of ovarian-like stroma underlying the mucinous epithelium. Reproduced with permission from BMJ Publishing Group Ltd. License number 4630150369693.

IPMNs and MCNs are both macroscopically visible cystic neoplasms. IPMNs lesions are larger than 1 cm in maximum diameter and arise mainly in the mucin-producing part of the pancreatic duct (Figure 1-6A).[47, 51, 54] The secretion of mucin out of a patulous ampulla of Vater (air in the pancreatic duct), as observed on an endoscope leads to the diagnosis of IPMN. MCN lesions are the least common of the three precursor lesions. Their epithelial lining is mucinous and seen to be associated with an ovarian-like stroma (Figure 1-6B-C).[47, 55]

1.1.2 Epidemiology and aetiology

Pancreatic cancer is the 11th most common cancer in the UK with an overall 5-year survival rate of 5-6 %, further depleting to <1 % after 10 years.[56, 57] It accounts for 3 % of all new cancer cases in the UK, where there were approximately 10,000 new pancreatic cancer cases between 2014-2016, with 52 % of these cases in men. There has been a 16 % increase in the incidence rate of the disease since 1990.[58] The causes of pancreatic cancer are complex and multifactorial.[59] Several risk factors such as smoking, family history of chronic pancreatitis, advancing age, male sex, African-American ethnic origin, diabetes mellitus, obesity and non-O blood group, have been linked to the development of the disease.[59-62] However, cigarette smoking and family history have been described as the leading causes of pancreatic cancer, with approx. 20 % of all cases being attributed to cigarette smoking.[63] Familial pancreatic cancer, which is described as a pair of first-degree relatives having been diagnosed with the disease, accounts for approx. 7-10 % of all pancreatic cancer cases.[64]

Additionally, cystic fibrosis, a genetic disorder which leads to the build-up of mucus in the lungs and digestive system, can cause blockage of the pancreatic duct and hence increase a person's risk of developing pancreatic cancer.[65]

Finally, an inflammatory disease of the pancreas known as chronic pancreatitis can give rise to ADM.[66] ADM is known to be the main origin for the formation of pre-neoplastic lesions which eventually develop into PDAC.[66, 67]

1.1.3 Diagnosis of PDAC

Diagnosis of PDAC can be challenging especially in the early stages due to lack of noticeable signs and symptoms - symptoms, when presented, are often mistaken for conditions such as pancreatitis or an ulcer.[68] In addition, due to the positioning of the pancreas, the ability to visualise it on imaging tests can be obscured by other organs. As a result, a combination of techniques such as imaging, clinical findings and cytology is used in the diagnosis of the disease.[69]

1.1.3.1 Clinical presentation

The clinical presentation of pancreatic cancer is often late on the onset and the presenting symptoms such as anorexia, fatigue, and back or mid epigastric pain are mostly subtle and nonspecific.[68]

The location of the tumour and disease stage affects the clinical presentation reported by the patient.[44] Tumours originating from the head of the pancreas often lead to symptoms such as obstructive jaundice because of pressure on the common bile duct.[70] Patients with this tumour will mostly present with yellowing of the skin and eyes, pale coloured stool and darkening of the urine.[70] These patients may also suffer from unexplained weight loss. The presentation of abdominal pain radiating to the back is often indicative of nerve infiltration by the tumour. Patients describe this pain as dull, deep and achy in nature.[71]

1.1.3.2 Imaging

Several invasive and non-invasive imaging tools are used to facilitate the diagnosis of PDAC.[72]

Computed tomography (CT) scans, ultrasounds and magnetic resonance imaging (MRI) are all examples of the non-invasive imaging modalities used in PDAC diagnosis. CT scan, which is the most validated initial diagnostic tool, allows for the clear visualisation of the primary tumour and assessment of the involvement of surrounding organs and vasculature.[72-74] MRI is also utilised as an imaging modality in conjunction with CT scan, especially in cases where CT scans fail to provide conclusive results.[72] Abdominal ultrasound is employed in patients presenting with jaundice and abdominal pain as a differential diagnosis tool to rule out choledocholithiasis and confirm the presence of biliary dilation.[72] The accuracy of conventional abdominal ultrasound in diagnosing pancreatic tumour is 50 to 70 %.[75] Invasive imaging modalities such as endoscopic ultrasound (EUS), endoscopic ultrasound-guided fine-needle aspiration (EUS-FNA) and endoscopic retrograde cholangiopancreatography (ERCP) are used to provide a definitive diagnosis of pancreatic cancer, particularly in patients with suspected cancer not diagnosed by conventional imaging.[72] The fine needle aspiration is used to obtain samples for cytology assessment.[72] The absence of an identifiable mass lesion during a EUS examination rules out the presence of pancreatic cancer with approx. 100 % certainty when performed by an experienced endosonographer.[76] ERCP has a sensitivity of approx. 77 % for pancreatic cancer diagnosis whereas the sensitivity of EUS-FNA has been reported to range from 80-95 %.[77-80]

1.1.3.3 Cytology

Biopsies taken during EUS-FNA and/or ERCP assessments are further analysed for cytological changes in the tissue for a definitive diagnosis before surgery.[81, 82] Cytology analysis can help in detecting and staging pancreatic malignancies because it is easier to visualise and detect pancreatic lesions on a smaller sample size.[81-85]

1.1.4 PDAC staging

The clinical staging of PDAC is done according to the tumour, node and metastasis (TNM) classification (Table 1).[86, 87]

Table 1 TNM staging system of pancreatic cancer[86]

		Stage	T	N	M
T1	Maximum tumour diameter ≤2 cm	**IA**	T1	N0	M0
T2	Maximum tumour diameter >2, ≤4 cm	**IB**	T2	N0	M0
T3	Maximum tumour diameter >4 cm	**IIA**	T3	N0	M0
T4	Tumour involves the celiac axis, common hepatic artery or the superior mesenteric artery	**IIB**	T1-T3	N1	M0
N0	No regional lymph node metastasis	**III**	T4 (any T)	any N (N2)	M0
N1	Metastasis in 1–3 regional lymph nodes	**IV**	any T	any N	M1
N2	Metastasis in ≥ 4 regional lymph nodes				
M0	No distant metastasis				
M1	Distant metastasis				

This staging classification is based on results from imaging tests, physical examination and biopsy and helps to guide treatment and predict the prognosis of the disease.[87] The stages of the TNM classification are organised into three different classes based on the tumour's resectability.[86]

Stages ***IA*** and ***IIB*** are classed as a local or resectable tumour with approx. 10 % median survival of 17-23 months.[59] Locally advanced or unresectable comprises patients with stage **III** pancreatic cancer. These patients have approx. 30 % median

survival of 8-14 months.[59] Finally, stage **IV** pancreatic cancer is classed as metastatic and patients normally have about 60 % median survival of 4-6 month.[59]

1.1.5 Management of PDAC

Management of pancreatic cancer patients is achieved with a multidisciplinary team consisting of oncologists, gastroenterologists, surgeons, radiologists, radiation oncologists, pathologists, clinical pharmacists, pain management experts, social workers and where appropriate, palliative care experts.[59, 88]

The heterogeneous nature of pancreatic cancer at the clinical, molecular and pathological level means a patient's response to treatment is dependent on several factors including the pattern of their disease progression and the biology of the cancer.[59]

1.1.5.1 Surgery

Surgery remains the treatment of choice for patients with resectable tumours.[86] The location of the tumour determines whether the surgery involves distal pancreatectomy (tumour lesions in the body and tail of the pancreas), pancreatoduodenectomy (lesions confined to the head of the pancreas) or total pancreatectomy.[86] Due to the high rate of postoperative comorbidities such as diabetes mellitus, total pancreatectomy is only reserved for patients with large or multilocular tumours of the pancreas.[89, 90]

1.1.5.2 Adjuvant therapy

Adjuvant therapy such as chemotherapy is often given after curative tumour resection as a standard of care for early-stage pancreatic cancer patients with improved median survival.[91-93] The addition of chemotherapy, such as gemcitabine post-surgery has been shown to improve survival rates and decrease the risk of tumour reoccurrence.[92, 94] The randomised CONKO-001 study demonstrated a significantly improved median disease-free survival of 13.4 months vs 6.7 months

for adjuvant gemcitabine after surgical resection over surgery alone.[91, 94] The study also found patients in the gemcitabine adjuvant arm to have an overall five-year survival of 20.7 % compared with 10.4 % in the surgery only arm. This benefit of the adjuvant therapy was also observed with the ten-year survival rate of 12.2 % and 7.7 % in the gemcitabine adjuvant and surgery only arms respectively.[91]

Other studies such as ESPAC-3 trial have also sought to identify the best chemotherapy for the adjuvant therapy.[93] It was found that gemcitabine and 5-fluorouracil provided comparable survival outcomes. However, gemcitabine was better tolerated by patients and hence found to be the agent of choice in adjuvant monotherapy.[93] The ESPAC-4 trial studied the effects of dual therapy of gemcitabine and capecitabine as adjuvant therapy in patients with resected tumour due to its successful use in patients with advanced and metastatic tumour.[95] An improved overall median survival of 28 months in dual therapy compared with gemcitabine alone (25.5 months) was reported.[95]

The PRODIGE24/CCTG PA.6 randomised trial investigated the difference in outcome for patients on either gemcitabine or mFOLFIRINOX (modified 5-FU, oxaliplatin, leucovorin and irinotecan) post-surgical resection.[96] At the median follow-up time of 33.6 months, patients in the mFOLFIRINOX arm had a median disease-free survival of 21.6 months compared to 12.8 months in the gemcitabine arm. The 3-year disease-free survival rate was found to be 39.7 % in the mFOLFIRINOX arm and 21.4 % in gemcitabine arm.[96] However the administration of mFOLFIRINOX was associated with significantly more toxic effect than gemcitabine alone.[96] Based on these findings, the standard of care for selected and fit patients post pancreatic cancer resection is mFOLFIRINOX.[97] For more frail patients such as those over the age of 70 or who are contraindicated to any of the drugs used in mFOLFIRINOX, combined gemcitabine and capecitabine may be used.[97] Gemcitabine alone may be

reserved for use in frail patients who cannot tolerate gemcitabine and capecitabine dual therapy.[97]

1.1.5.3 Neoadjuvant treatment

Approx. 80 % of pancreatic cancers are not resectable due to the advancement of the disease at the time of diagnosis.[94] Neoadjuvant therapy is used in patients with locally advanced disease with the purpose of downstaging the tumour to achieve R0 resection (pathologically negative margin) and as a result, decrease surgical complexity.[98] Several trials and large scale meta-analyses have been shown to support the use of neoadjuvant therapy and underline its impact on survival rate in pancreatic cancer.[99-103] Gillen *et al.* conducted a meta-analysis, pooling together data from 111 neoadjuvant trials of 4,394 patients with diagnosed pancreatic cancer between 1966 and 2009.[99] The patients were grouped into either resectable or nonresectable disease cohorts. Of the patients who were initially diagnosed with nonresectable tumours, 46.9 % underwent surgical exploration after neoadjuvant therapy and approx. 70 % underwent successful tumour resection with a 79.2 % R0 resection rate.[99] The median survival rate of 20.5 months for these patients was comparable to that of patients with resectable tumours at diagnosis.[99] The Preopanc-1 trial involving 246 patients with the pathologically confirmed resectable or borderline resectable disease were randomised between neoadjuvant or immediate surgery arms.[104] They found an improved median survival rate of 17.1 months in the neoadjuvant arm and 13.7 months in the immediate surgery arm in the intention to treat analysis. However, the difference was not statistically significant ($P = 0.07$). There was a significantly improved overall median survival in the neoadjuvant arm over the immediate surgery arm (42.2 months vs. 16.8 months; $p < 0.001$) in patients who underwent an R0 or R1 resection with significantly increased time until distant metastases and locoregional recurrence.[104]

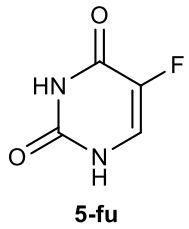


Figure 1-7 Chemical structure of 5-fluorouracil (5-FU).

Until the late 90s, 5-FU (Figure 1-7) was the only chemotherapeutic of choice for patients in the advanced setting of the disease.[105] However the randomised trial conducted by Burris *et. al.* exhibited an improvement in the median survival rate from 4.41 months to 5.65 months for patients treated with 5-FU and gemcitabine respectively.[106] In addition to this, patients in the gemcitabine arm presented with improved quality of life as shown by reduced pain, increased weight gain and low toxicity profile.[106] As a result, the Food and Drug Administration (FDA) approved gemcitabine as the standard of care therapy for advanced PDAC treatment.[106]

1.1.5.4 Palliative care

The majority of patients with pancreatic cancer present with locally advanced or metastatic disease.[107-109] In most of the cases, patients presenting with the localised disease will relapse despite multiple therapeutic interventions, including surgical resection with neoadjuvant or adjuvant chemotherapy.[110] As a result, palliative care is a common endpoint for pancreatic cancer patients.[110]

The World Health Organisation (WHO) describes palliative care as “An approach to improve the quality of life of patients and their families facing the problem associated with life-threatening illness, through the prevention and relief of suffering by means of early identification and impeccable assessment and treatment of pain and other problems, physical, psychosocial and spiritual.”[111]

The aim of palliative care is not to hasten nor postpone death but rather to relieve the patient of any pain or distressing symptoms, offer a support system to help

patients live as actively as possible until death and in doing so, support the family in coping during the patient's illness and in their own bereavement.[111]

In advanced-stage pancreatic cancer, palliative care is focused on relieving symptoms such as delayed gastric emptying and jaundice caused by an obstruction in the duodenal and biliary tract. Patients presenting with these symptoms undergo an endoscopic procedure whereby a stent is placed in the biliary duct and duodenum during an ERCP procedure with a 90 % success rate.[110]

Another common presenting problem among patients in advanced stages of the disease is abdominal and/or lower back pain.[110] Eighty per cent of these patients will experience severe pain commonly associated with malignant invasion of the coeliac plexus prior to death.[107, 112, 113] Most patients undergo treatment with oral and transdermal analgesics, however, there is evidence to show that patients have a better quality of life with early regional neurolysis of the coeliac plexus.[108, 113]

Due to pancreatic exocrine insufficiency resulting from pancreatic duct obstructions, around 65 % and 50 % of pancreatic cancer patients will experience symptoms associated with fat and protein malabsorption respectively. Pancreatic enzyme replacement therapy has been found to improve malabsorption and bloating, as well as preventing weight loss.[107, 114]

It is important for the patient, their family, physicians and advocacy groups to be involved in the care process from the time of diagnosis to provide the patient with the right treatment option and focus on ways to empower them to create new achievable goals.[110] This will help patients and their families to reframe how they perceive hope – which is central to all dealing with cancer.[110]

1.2 Gemcitabine

1.2.1 Clinical pharmacology

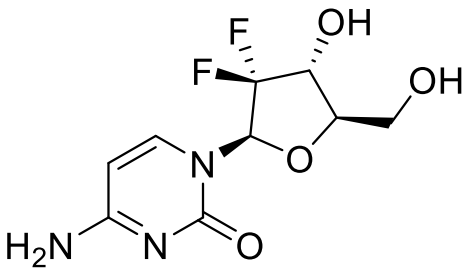


Figure 1-8 Chemical structure of Gemcitabine [2'-Deoxy-2',2'-difluorocytidine].

As mentioned above, Gemcitabine [2′-Deoxy-2′,2′-difluorocytidine] a nucleoside analogue of cytidine, is the first-line treatment for patients with advanced or metastatic pancreatic cancer.[106, 115, 116] It is administered intravenously at a dose of 1000 mg/m^2 once a week for 3 weeks of each 28-day cycle as an infusion over 30 minutes.[117]

1.2.2 Pharmacokinetics of Gemcitabine

The peak plasma concentration of gemcitabine reaches a plateau of 10 to 40 mg/L, at around 15 – 30 minutes during a 30 minutes infusion.[118, 119] In one study of patients with a range of malignancies, there was an observable linear relationship between the steady-state gemcitabine concentration and dose over the range of 53 to 1000 mg/m^2.[118, 119] There is minimal binding of gemcitabine to plasma proteins in the bloodstream and short infusion times does not lead to extensive tissue distribution of the drug.[118] The median elimination half-life was found to be approx. 8 minutes in a study of patients with cancer due to the rapid metabolism of gemcitabine in the liver and bloodstream.[118-120] In this study, they observed that only the deamination product, 2'-deoxy-2',2'-difluorouridine (dFdU) was detected in the plasma consequently significant levels were found in the urine.[118, 119]

1.2.3 Uptake and metabolism

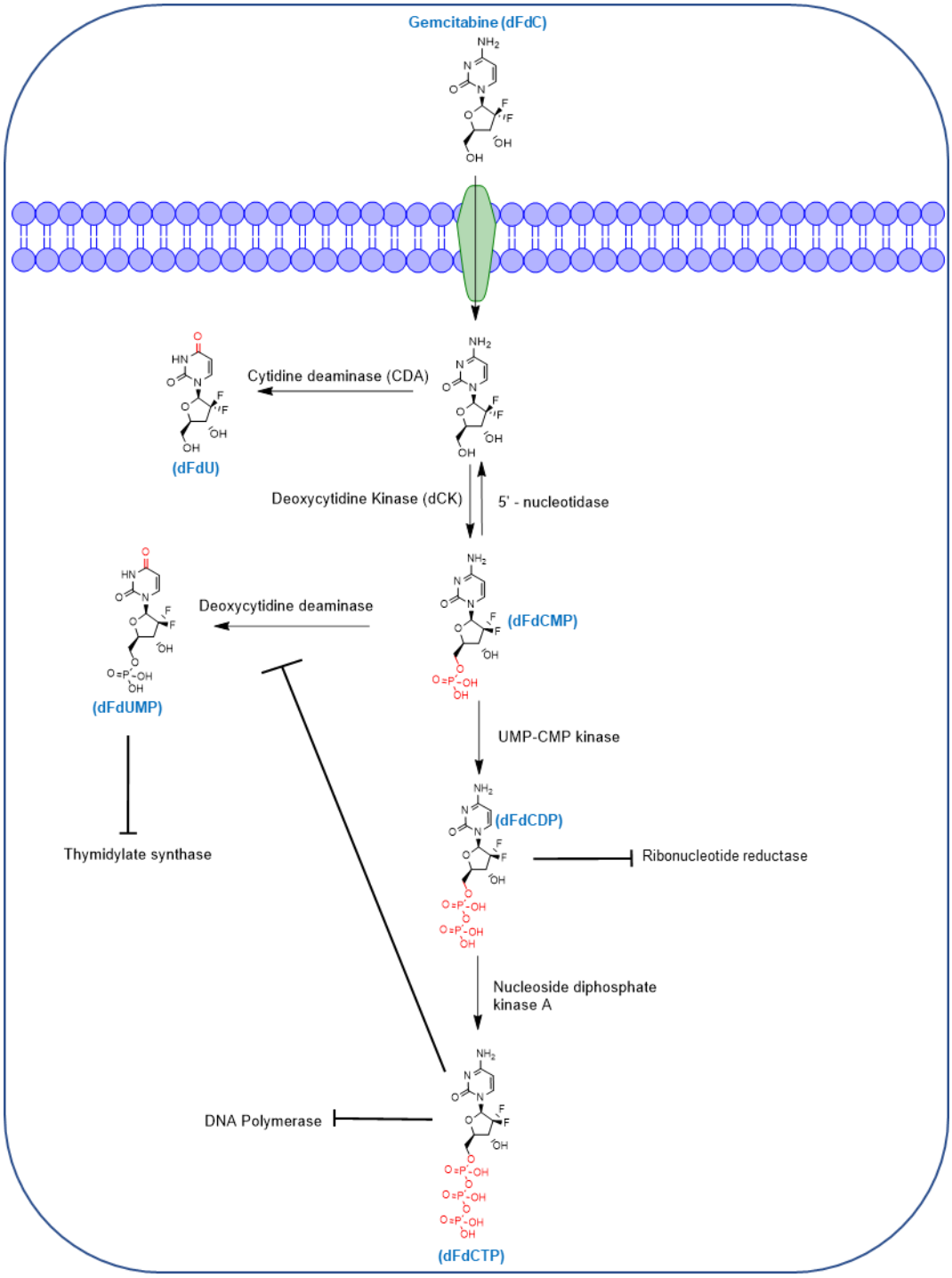


Figure 1-9 Cellular metabolism of Gemcitabine. Reproduced (adapted) with permission from Elsevier. License number 4631920244015.

Gemcitabine is a highly hydrophilic compound (logP = -1.4), therefore, it requires uptake by human nucleoside transporters (hNTs) which are a family of integral membrane proteins.[121] There are two types of hNTs, equilibrative (hENT) and

concentrative (hCNT), that differ according to their mechanism of transport.[122] Four subsets of hENTs (hENT1, hENT2, hENT3 and hENT4) and three of hCNTs (hCNT1, hCNT2 and hCNT3) have been identified, and it has been shown that gemcitabine uptake is mediated mostly by hENT1 and to a lesser extent, also by hENT2, hCNT1 and hCNT3.[116, 121, 123]

Gemcitabine is activated through phosphorylation processes to its active metabolite, dFdCTP, in the cytoplasm of the cells by kinases (Figure 1-9).[116] The first step is the phosphorylation by deoxycytidine kinase (dCK) to the monophosphate dFdCMP, which is considered to be the rate-limiting step.[124, 125] This is then followed by a second phosphorylation step by pyrimidine nucleoside monophosphate kinase to give gemcitabine diphosphate (dFdCDP).[126-129] Although the enzyme responsible for the final phosphorylation step from dFdCDP to the active dFdCTP is unclear, Wong *et. al.* reported nucleoside diphosphate kinase may play a role.[130]

1.2.4 Mechanism of action

Gemcitabine exerts its toxicity through several mechanisms (Figure 1-10).[116] However, the main mechanism of action is through the inhibition of DNA synthesis.[131] The incorporation of dFdCTP into DNA at the non-terminal position inhibits the action of DNA polymerases, haltering the chain elongation process.[132] This action also prevents removal of the incorporated gemcitabine due to the effect of insertion of the single deoxynucleotide. This process is described as ‘masked chain termination’ (Figure 1-10A).[116, 131]

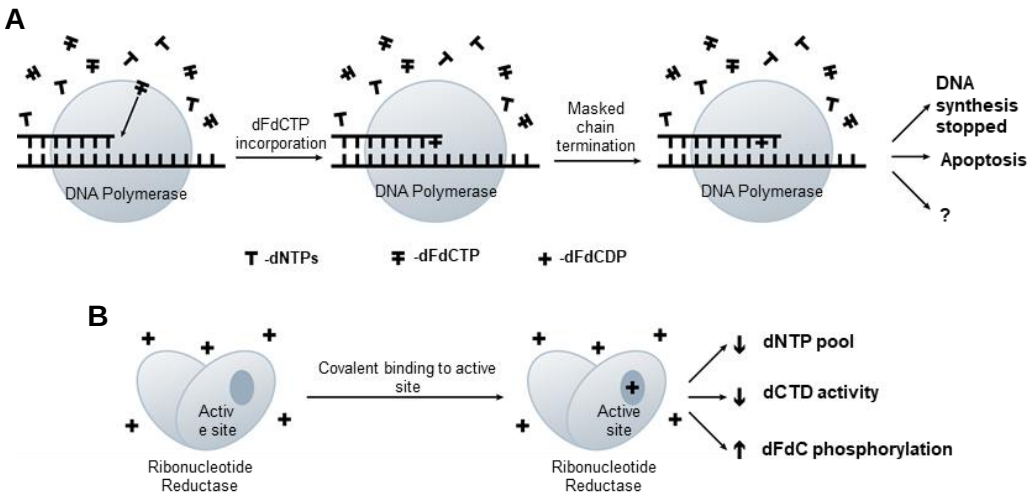


Figure 1-10 The main mechanism of actions of Gemcitabine. (A) Represents the masked chain termination. (B) Gemcitabine self-potentiation. Reproduced (adapted) with permission from Elsevier. License number 4631920244015.

Another mechanism of action of gemcitabine is self-potentiation whereby it inhibits the enzymes related to deoxynucleotide metabolism such as deoxycytidylate deaminase (dCTD). dCTD is directly and indirectly inhibited by dFdCTP and dFdCDP respectively.[133] The indirect inhibition by dFdCDP is as a result of the inhibition of ribonucleotide reductase, an enzyme which catalyses the reduction of ribonucleotides to deoxyribonucleotides, by dFdCDP through covalent binding to the active site.[134, 135] This leads to a reduction in the intracellular deoxyribonucleotide triphosphate (dNTP) pool and consequently reduction of dCTD activity.[133] The activity of dCK is regulated by deoxycytidine triphosphate (dCTP), therefore the lowering of the dNTP pool leads to phosphorylation of dFdC which in turn increases the levels of dFdCTP and therefore its incorporation into DNA (Figure 1-10B).[116, 136]

Another important mechanism of action of gemcitabine is the induction of apoptosis through caspase and p38 signalling.[137-139] It does this by activating p38 mitogen-activated protein kinase (MAPK) which triggers apoptosis in response to cellular stress in tumour cells only.[138, 140]

1.2.5 Inactivation

The inactivation of gemcitabine can occur in several ways including deamination by cytidine deaminase (CDA) and dCTD when in the monophosphate form.[133, 141] CDA deamination of gemcitabine produces 2′,2′-difluoro-2′-deoxyuridine (dFdU), a less potent metabolite which has a number of intracellular significances including cytotoxicity, and transport and accumulation of gemcitabine.[142-144] In addition, the monophosphate form of the metabolite, dFdUMP can inhibit the activity of thymidylate synthase which directly affects the dNTP pool.[145]

Gemcitabine can also be inactivated by conversion of the nucleotide to nucleoside through a dephosphorylation reaction of dFdCMP by 5' -nucleosidases (5' -NTs).[146-148] These enzymes are vital in balancing the dNTP pools and hence gemcitabine metabolism. This process, therefore, affects the rate-limiting step of gemcitabine phosphorylation by dCK and as a result, gemcitabine cytotoxicity.[116]

Although in isolation gemcitabine is very active against pancreatic cancer, mechanisms related to inactivation such as deamination by CDA and rapid clearance from the bloodstream affects its overall therapeutic efficacy. Therefore, various strategies, including modifications of its chemical structure through the formation of polymeric prodrugs at the 5'-OH or the amino position, are being studied to enhance its sensitivity. These modifications have been shown to offer enzymatic stability and improved blood circulation time compared to the parent drug.[149-151]

1.3 Polymers as drug delivery systems

The use of polymers in the pharmaceutical field has now extended beyond excipients in extended drug release formulations.[152] Polymer therapeutics (Figure 1-11) such as polymeric drugs, polymer-drug conjugates, polymeric micelles and multi-component polyplexes are being employed for drug delivery in clinical trials

and humans due to the improved pharmacokinetic and pharmacodynamic properties over small molecules. The aim in all cases is to maximise therapeutic activity and minimise side effects.[153, 154] It should be noted that, although most cancer therapeutics are dosed via injection, some such as capecitabine and many kinase inhibitors are taken orally.[155] Polymers as delivery agents have the potential to target specific tissues, increase plasma half-life of the therapeutic agent, protect against degradation by proteolytic enzymes, enhance solubility and reduce immunogenicity.[156, 157]

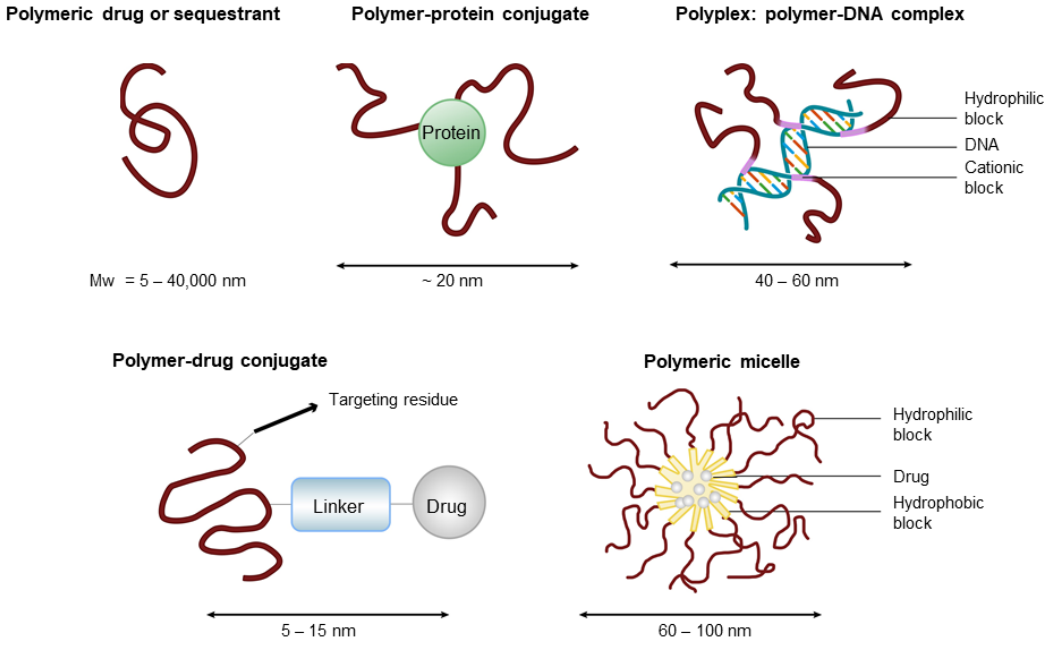


Figure 1-11 Schematic representation of polymer therapeutics. Mw = molecular weight. Reproduced (adapted) with permission from Springer Nature. License number 4631940222031.

In order to sustain an adequate supply of nutrients and oxygen for rapid growth, tumour tissues are densely vascularised.[158] However, these blood vessels present with several abnormalities compared with normal vasculature such as leaky endothelia which leads to increased permeability of the blood vessels over normal vasculature.[159] This enhanced permeability of the tumour vasculature governs the passive extravasation of delivery systems such as polymeric nanoparticles into the tumour microenvironment (TME).

In addition to this, tumours lack an effective lymphatic drainage system which leads to selective accumulation of macromolecules.[160] These hyperpermeability and reduced clearance traits of tumours are termed the enhanced permeability and retention (EPR) effect.[161-163] The existence of the EPR effect has been shown in gastric tumours in humans.[164] However, this is subject of some controversy as the effect has mainly been demonstrated in large solid tumours in mice rather than in humans.[165]

1.3.1 Polymer-drug conjugates

The initial hypothesis by Helmut Ringsdorf for pharmacologically active polymer conjugates whereby drugs are covalently bonded to polymers still forms the basis for the work into these systems to date.[166, 167]

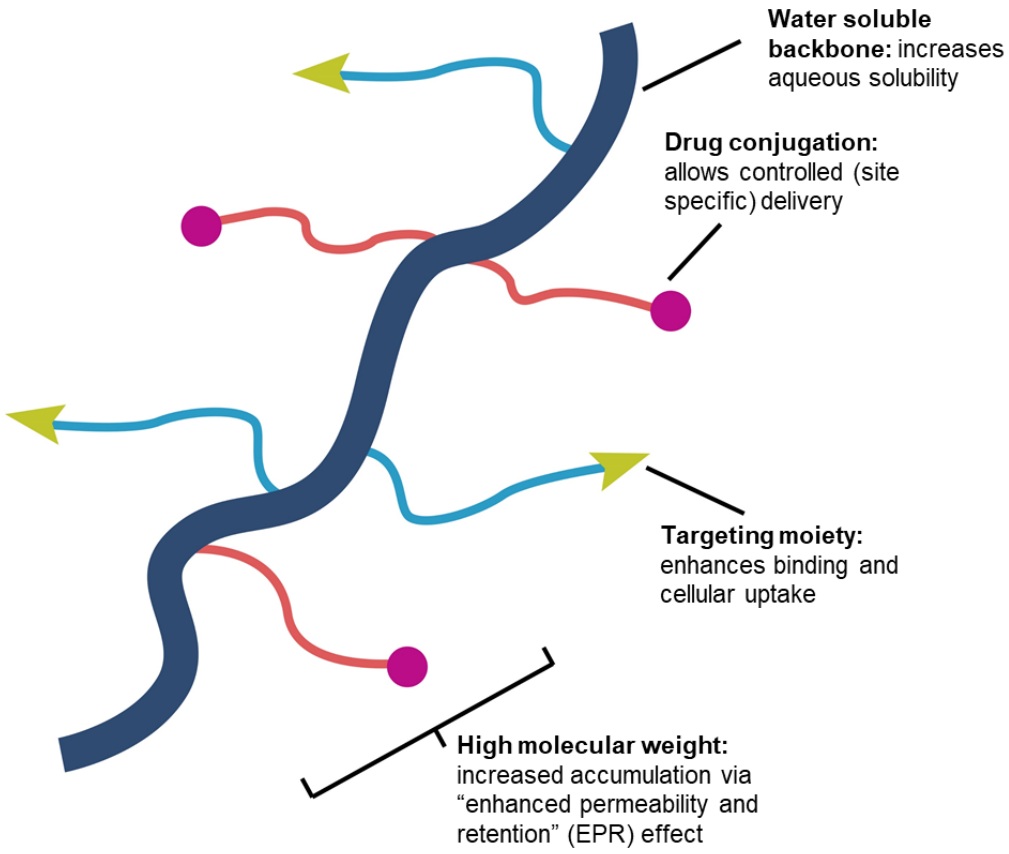


Figure 1-12 The Ringsdorf model which rationalises drug delivery via polymer-drug conjugates. Reproduced (adapted) with permission from ref [144] Copyright © (2012) American Chemical Society.

Polymer-drug conjugates aim to improve bioavailability and cell specificity of low-molecular-weight drugs.[153] The linkages between the polymer backbone and the drug molecules are usually chosen to be sensitive to the different physiological environments of the cancer tissues. The Ringsdorf model (Figure 1-12) consists of four main components; a water-soluble polymer backbone such as poly(*N*-(2-hydroxypropyl)methacrylamide poly(HPMA), to increase hydrophilicity and ensure water solubility; a drug bonded to the polymer backbone *via* stimuli-responsive linker to allow for site-specific release of the drug at an optimum rate; a targeting moiety to enhance specific cellular uptake of the conjugate and/or a high molecular weight to utilise passive targeting through EPR effect.[153, 167]

Many anticancer agents present with low therapeutic index due to the nonspecific distribution of drugs in the body. In addition, most small-molecule cancer therapeutics are rapidly cleared from the body, reducing their accumulation into tumour tissues. This has led to the desire for polymer-drug conjugates which might enhance tumour targeting and improve bioavailability due to the different pharmacokinetic properties of high molecular weight polymers.[153, 163] It was initially believed that active targeting of polymer-drug conjugates was an essential prerequisite for the development of these systems.[153] However, prolonged plasma circulation has been linked to significant passive tumour targeting *via* the EPR effect leading to continual clinical development of simpler polymer-drug conjugates with no targeting ligands.[153, 163, 168, 169] A controlled rate of drug release can also be achieved with polymer-drug conjugates through careful design of the linker to attain the desired effective therapeutic concentration.[153, 167] This can lead to a reduction in the fluctuation of anticancer doses typically associated with intermittent administration.[167]

Lastly, conjugating small molecules to the water-soluble polymer can dramatically improve the aqueous solubility of these molecules leading to the enhanced

distribution when injected.[170, 171] This is particularly important as it has been predicted that approx. 40-60 % of drugs in development exhibit low aqueous solubility, affecting their bioavailability.[167, 172] An example of water-soluble polymer which can be employed to achieve this effect is poly(HPMA).[153, 169]

1.3.2 Stimuli-responsive prodrugs for drug delivery

Stimuli-responsive prodrugs are designed to release therapeutic agents in response to the application of chemical, physical or biological stimuli at the targeted site of delivery.[173-175] Polymeric prodrugs offer an ideal approach to achieve this strategy compared to physical entrapment of therapeutic agents in delivery carriers such as micelles.[173] As mentioned above, TME exhibits abnormalities such as low pH, hypoxia, overexpression of enzymes and proteins, elevated levels of metabolites and reactive oxygen species (ROS) compared with normal tissues.[173, 176, 177] These characteristics can be used to trigger specific physicochemical transformations of the polymeric prodrug such as disassembly, dissociation, and molecular structural rearrangement resulting in the release of the drug.[178, 179]

1.3.2.1 pH-responsive systems

The pH of the extracellular environment of tumours has been reported to be lower than physiological pH, approx. 6.5 and 7.4 respectively mainly due to lactic acid build-up as a result of anaerobic glycolysis in hypoxia.[180, 181] This pH further reduces to approx. 5.5 within endosomal and lysosomal vesicles within the cell.[180]

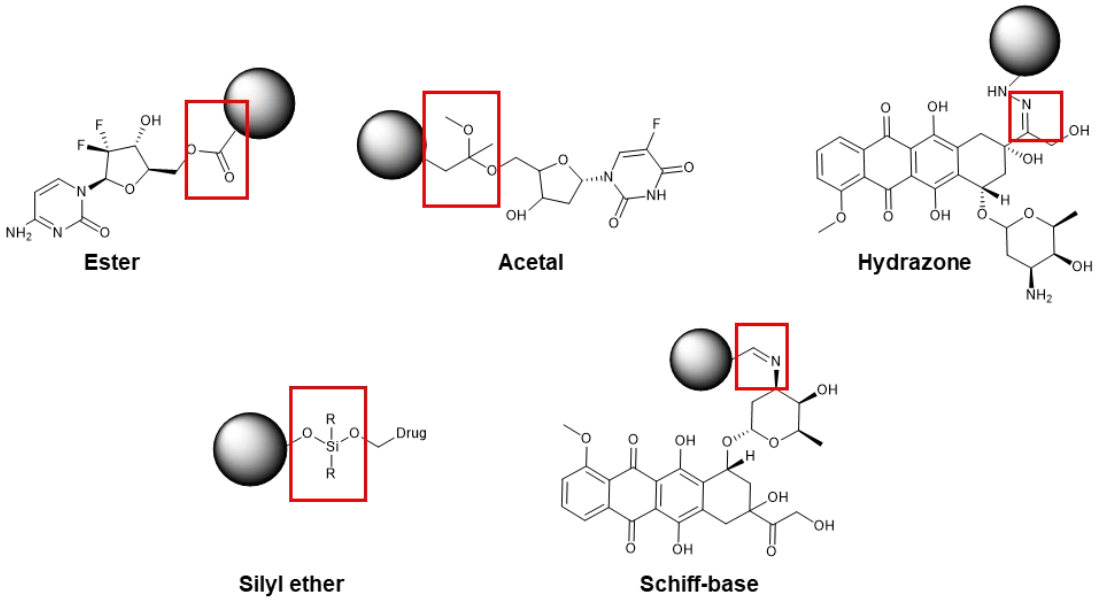


Figure 1-13 Examples of covalent linkers used in pH responsive drug release.

Upon entry into the cell *via* receptor-mediated endocytosis, the transferring vesicle will acidify lowering the local pH to approx. 5 to 6.[173] This vesicle can then undergo lysosomal fusion which further lowers the pH to approx. 4 to 5, triggering hydrolysis of suitable acid-labile polymer-drug conjugates.[173] Examples of covalent linkers which have been studied for potential use in pH-responsive drug release are esters, acetal, hydrazone, Schiff-base and silyl ether (Figure 1-13).[182-186]

1.3.2.2 Redox-responsive systems

Reduction-sensitive polymeric nanocarriers (RSPNs) are reported to demonstrate high hydrolytic stability in circulation and produce a fast response to reductive conditions intracellularly.[187] This reducing ability of cancer cells is attributed to the abnormal levels of glutathione (GSH), a biological reducing agent.[188] GSH is present intracellularly in organelles such as mitochondria and cell nuclei at concentrations of approx. 2-10 mM in cancer cells.[188-190] However, the levels in the normal body fluids such as the blood and extracellular matrix are a thousand-fold less (approx. 2-20 µM).[189, 190] In addition to this, the GSH concentration in tumour tissues has been reported to be four times higher than in normal tissues, 4 µM g^{-1} and 1 µM g^{-1}

respectively.[191] This is because cancer cells exhibit greater levels of reactive oxygen species (ROS) compared to normal cells, in order to meet the enhanced metabolism and proliferation activities. GSH is therefore produced as an antioxidant defence system to cope with the high oxidant state.[192] The high concentration of GSH, therefore, provides RSPNs with a unique advantage for use as stimuli-responsive drug delivery system for cancer therapy.[187] RSPNs are generally synthesised from a reducible polymer or comprise a reduction cleavable linkage such as diselenide linkers (Figure 1-14A), disulfide linkers (Figure 1-14B) and trimethyl-locked benzoquinone (TMBQ) (Figure 1-14C).[193-195]

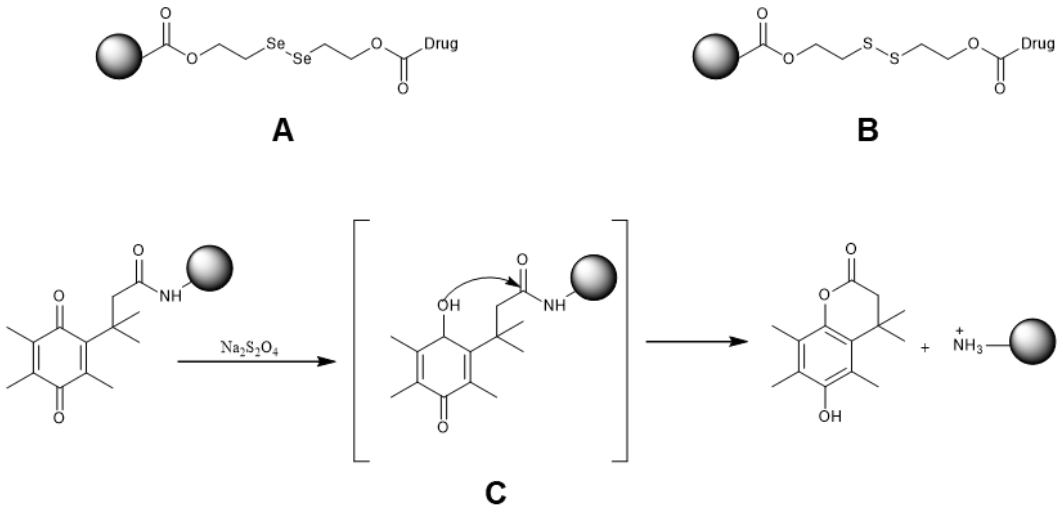


Figure 1-14 Schematic representation of A) Diselenide linked polymer-drug conjugate, B) Disulfide linked polymer-drug conjugate and C) Chemical reduction of redox-sensitive polymer based on TMBQ.

1.3.2.3 Self-immolative stimuli-responsive systems

Self-immolative delivery systems involve the controlled disassembly of macromolecules through a stimulus triggered catalysis.[196] Self-immolative materials respond to external stimuli such as pH and GSH prompting the cleavage of a trigger leading to a cascade of intramolecular chemical reactions resulting in the release of a pharmacologically active compound.[173]

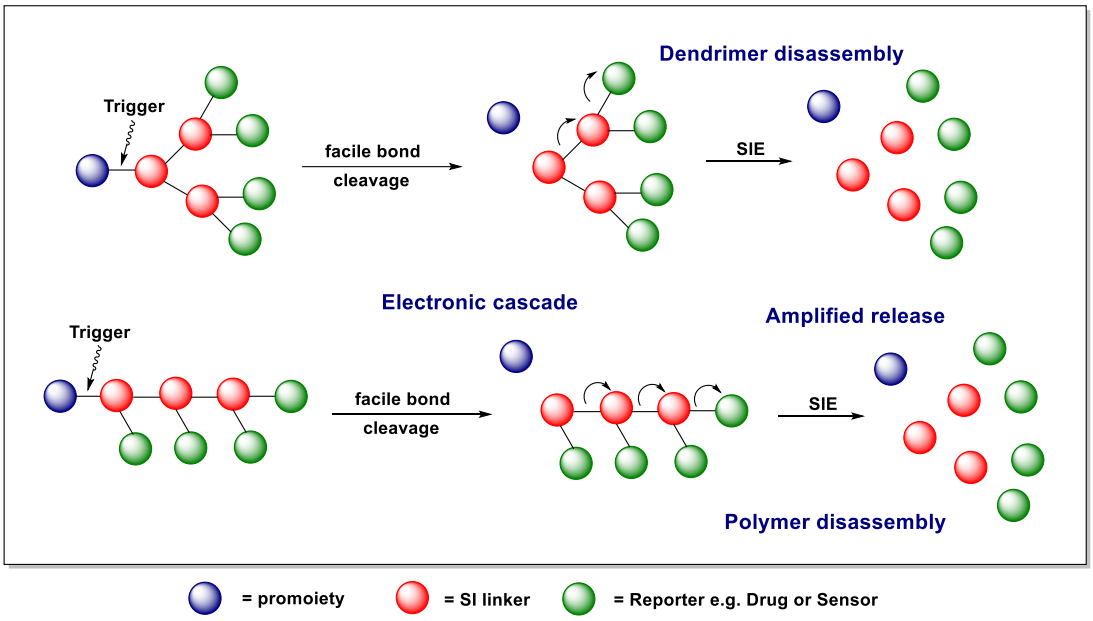


Figure 1-15 Self-immolative stimuli responsive system. SIE = self-immolative elimination. Reproduced (adapted) with permission from Royal Society of Chemistry. License ID 4630811104161.

This approach to responsive drug release is beneficial in bulky macromolecules, such as dendrimers, whereby drug release can be impaired by spatial proximity. This linker technology has increased in popularity with several proof of concept studies highlighting its potential use as a conjugated system for drug delivery.[197-200] Self-immolative dendron (SID) is an example of a macromolecule developed to utilise this stimulus-responsive system. The dendrimer is structurally designed to release all the payload with a single cleavage event at its core.[201] The first-generation SID was designed to have two identical functionalities linked to reporter molecules and a third attached to the trigger (Figure 1-16).[201] Cleaving of the trigger prompted a sequence of self-immolative reactions that led to spontaneous release of the two reporter molecules.

The adaptor unit could also be extended to incorporate two additional identical units, increasing the number of attached reporter molecules to four (Figure 1-16**A**). Hence cleaving of the trigger initiated a cascade of self-immolative reactions, releasing the

four reporter molecules.

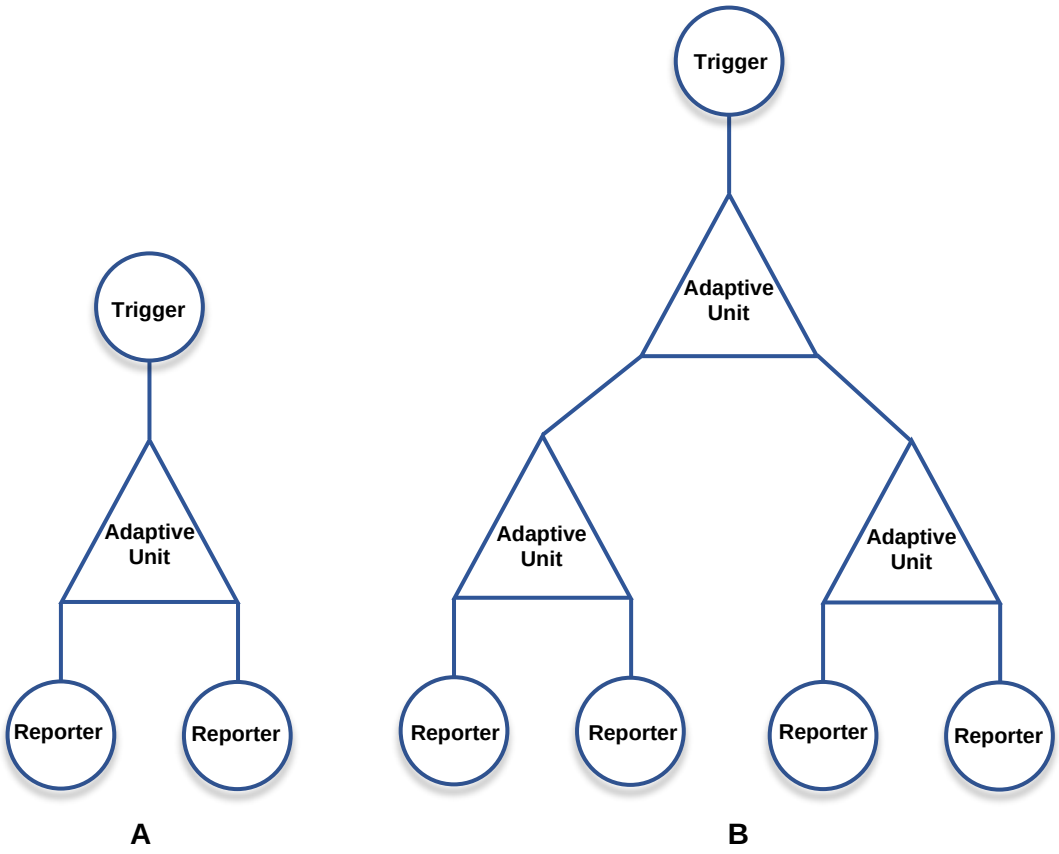


Figure 1-16 Graphical representation of I) First generation (G1) SID with a trigger and two reporter molecules. II) Second generation (G2) SID with a trigger and four reporter molecules. Reproduced (adapted) with permission from John Wiley and Sons. Licence number 4666530959531.

1.3.3 Difficulties in clinical translation

Although there has been extensive research into the use of polymeric nanoparticles such as polymer-drug conjugates in the delivery of cancer chemotherapeutic agents, the clinical prospect of most of these particles are low and hence may never enter the clinics.[202]

Nanocarriers are designed to increase the plasma half-life of administered drugs. However, they face a series of complex biological barriers (such as opsonisation by the organs of the mononuclear phagocyte system (MPS), high intratumoral pressure, cellular internalisation, and endosomal and lysosomal escape) which can greatly affect the accumulation of the particles at the target site, thus affecting the

efficacy of the drug.[202, 203] In addition to this, factors such as route of administration, disease progression and disease types should be considered in their design in ordered to improve their clinical translation.[202]

Secondly, the safety concerns over these drug delivery systems are one of the reasons for their poor translation into clinical use. The pharmacokinetic properties such as metabolism and excretion need to be studied thoroughly in order to understand and eliminate any potential problem with toxicity, immunogenicity, carcinogenicity by both the nanomaterial and their metabolites.[202] Furthermore, a major issue with clinical translation of nanoparticle delivery systems include industrial scale-up validation, controllability of nanomaterials' physicochemical properties and batch-to-batch reproducibility. Processes for the manufacturing and testing of the particles should be validated and good manufacturing practice (GMP) should be adhered to in order to ensure that any observed small-scale laboratory efficacy can be translated to the clinics.[202]

1.4 *N*-(2-hydroxypropyl)methacrylamide (HPMA) polymers

The development of poly(*N*-(2-hydroxypropyl) methacrylamide) (pHPMA) materials by Kopeček and co-workers have provided alternatives to the use of poly(ethylene glycol) (PEG), which is the most commonly used water-soluble polymer employed in the drug delivery field. [204] However, the use of PEG as a drug delivery system is hindered by the inability to functionalise the backbone of the polymer affecting the amount of drug that can be loaded onto the polymer. In addition, some recent studies have shown PEG-containing products to activate the complement system and be rapidly cleared after repeated injections.[205] As a result, pHPMA is emerging as an attractive alternative to PEG as a water-soluble polymer for drug delivery applications.[204] The potential biological application of pHPMA was first highlighted by Kopeček *et al.* in the 1970s.[206] Unlike PEG, pHPMA has a secondary hydroxyl

group for post polymerisation modifications such as the attachment of drugs through a linker for drug delivery (Figure 1-17).

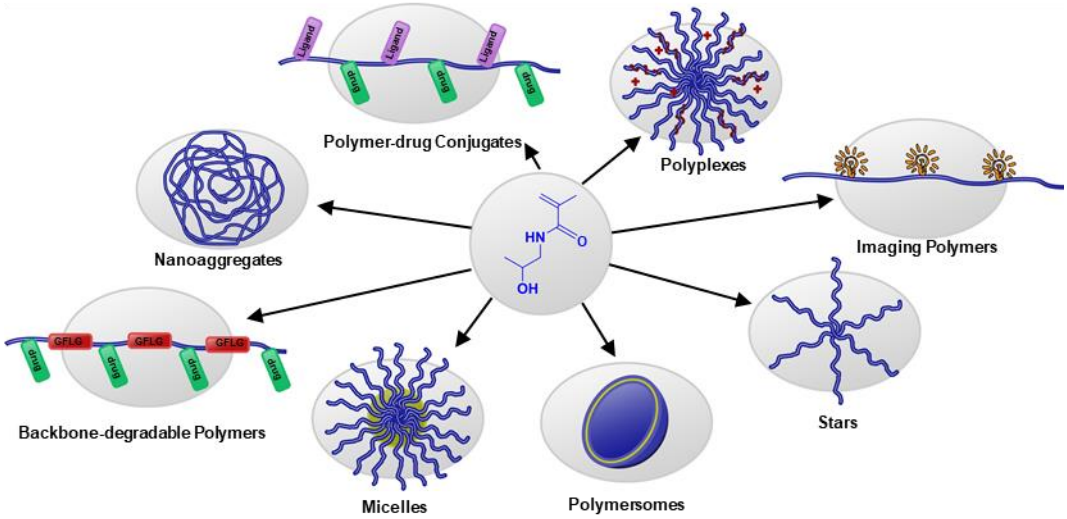


Figure 1-17 Summary of the different nanostructures based on pHPMA with abundant functionalities for drugs, imaging probes and ligand attachments. Reproduced (adapted) with permission from Royal Society of Chemistry. License number 4651820176076.

Like many other *N*-substituted methacrylamides polymers, pHPMA is known to have desirable *in vivo* properties owning to its hydrolytic stability.[204] Several polymerisation techniques such as reversible addition-fragmentation chain transfer (RAFT) and atom transfer radical polymerisation (ATRP) have been employed for the synthesis of HPMA polymers affording exceptional control over molecular weight and molecular weight distribution of the polymerisation.[206-208]

1.4.1 HPMA polymer-drug conjugates

There have been extensive studies concerning the biological applicability of HPMA conjugates in cancer therapeutics.[209-211] These studies look to take advantage of the water solubility, stability, improved half-life in circulating blood and good renal clearance properties of HPMA to improve the efficacy of low molecular weight drugs.[212] Enzyme degradable amino acid linkers have been utilised in the conjugation of anticancer agents to HPMA. One example of this was the HPMA copolymer-cyclopamine conjugate that was designed to target prostate cancer stem

cells (CSC).[210] Similar to free cyclopamine, the copolymer conjugate showed selective inhibitory effects against the prostate CSC in an *in vitro* prostate cancer models.

Table 2 HPMA based polymer-drug conjugates in clinical trials as anticancer agents

Code	Composition	Status	References
FCE 28068	HPMA copolymer–GFLG–doxorubicin	Phase I/II	[211]
FCE 28069	HPMA copolymer–GFLG–doxorubicin–galactosamine	Phase I/II	[213]
PNU166945	HPMA copolymer–paclitaxel	Phase I - stopped	[214]
MAG-CPT, PCNU166148	HPMA copolymer–camptothecin	Phase I - stopped	[215]
AP5280	HPMA copolymer–carboplatinate analogue	Phase I/II	[216]
AP5346	HPMA copolymer–DACH platinate analogue	Phase II	[217]

In addition to this, pH-sensitive linkers have been employed for the attachment of chemotherapeutics to the backbone of HPMA polymers. Etrych *et al.* developed pH-sensitive conjugates of paclitaxel and docetaxel with HPMA *via* an acid-cleavable hydrazone linker.[218] The polymer conjugates were tested in mice bearing 4TI mammary carcinoma and EL4 T-cell lymphoma and were able to achieve complete regression of established tumours in a significant proportion of the animals. Furthermore, the HPMA copolymer conjugates were free of side toxicity in both tumour models compared with the free drugs. Along with the laboratory successes, HPMA conjugates have also progressed to clinical trials (Figure 1-18 and Table 2).[212] HPMA copolymer-Gly-Phe-Leu-Gly-doxorubicin (PK1, FCE28068) was the first

synthetic polymer-anticancer conjugate to enter clinical trials in 1994.[211] In phase I, the polymer conjugate was injected as a short infusion every 3 weeks with a maximum tolerated dose of 320mg/m^2 (doxorubicin equivalent), approx. four-fold higher than the normal safe clinical dose of doxorubicin and cumulative dose up to 1680 mg/m^2.[219] However, no cardiotoxicity was observed and in the phase II trial,

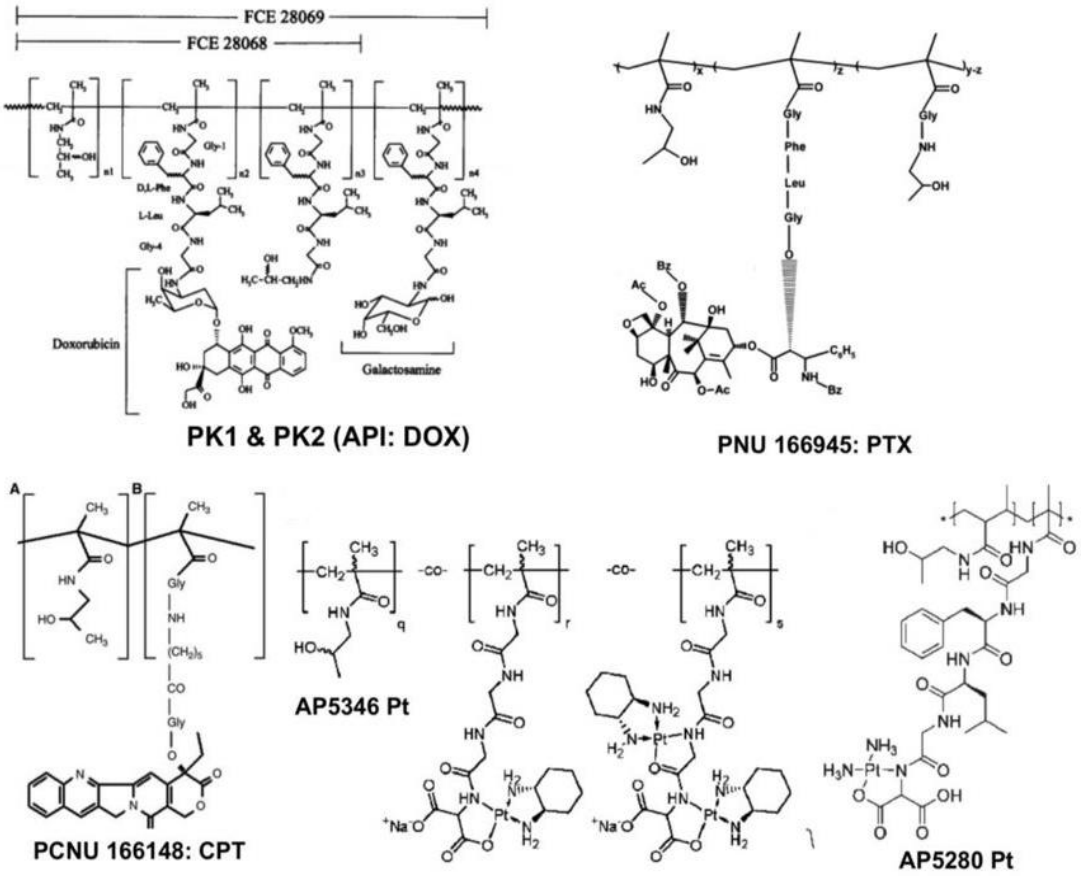


Figure 1-18 Structures of HPMA polymer-anticancer drug conjugates used in clinical trials. Reproduced with permission from ref [187] Copyright © (2017) Current Opinion in Colloid & Interface Science.

antitumor activity was seen in patients who were otherwise considered to be chemotherapy-resistant even at low concentrations (80 – 180 mg/m^2).[220]

PK2, a follow-up study of PK1 was the first ligand-targeted polymer conjugate to progress to clinical trials.[213] It was designed as a treatment modality for hepatocellular carcinoma by targeting the hepatocyte asialoglycoprotein receptor. The maximum tolerated dose in phase I/II trials was found to be 160 mg/m^2 (doxorubicin equivalent) and the conjugate was found to localise mainly to the liver.

Although the majority of the injected polymer was found in the normal hepatocytes (16.9 % of the dose, after 24 h) compared to hepatic tumours (3.2 % of the dose), the accumulation in the hepatic tumour was reported to be 12-50-fold higher than levels achieved with free doxorubicin. Administration of the polymer led to observable antitumour activity in patients with primary hepatocellular carcinoma.

The studies highlighted above show the potential benefit in the use of HPMA homo- and copolymers in the treatment of cancer. Although significant advantages for these polymers have been demonstrated, none of them has made it past phase I/II trials mainly due to modest outcome of the clinical trials and by no means an inherent limitation of the HPMA polymer-conjugate platform itself. These outcomes were as a result of the low drug loading on the polymers. All the early pHPMA polymers were linear, hence the addition of large amounts of drugs to the side chains caused the polymers to adopt a unimolecular micelles morphology leading to unpredictable transportation in the body. Therefore, further studies are needed with different polymeric architectures, such as hyperbranched polymers, so that drugs can be loaded at high levels in the core without changing their solubility and transport properties.

1.5 Hyperbranched polymers

Hyperbranched polymers are highly branched three-dimensional structures with irregular topology and abundant functional groups for high drug loading and post polymerisation modification.[221] They are an example of dendritic architectures, which also comprise others such as multi-arm star polymers and dendronised polymers (Figure 1-19).[222]

The degree of branching of dendrimers, linear-dendritic hybrids and dendronised polymers are controlled whereas that of hyperbranched, multi-arm star and hypergrafted polymers are random, increasing their polydispersity index (Đ).

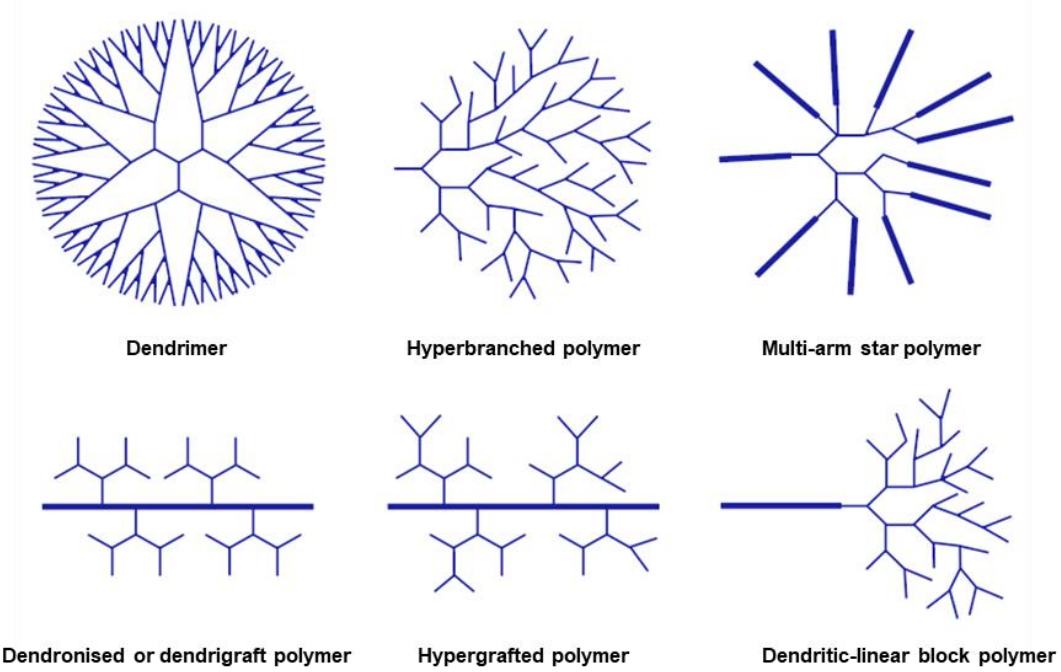


Figure 1-19 Schematic presentation of dendritic polymers. Reproduced with permission from ref. [197]. *Copyright (2016), Theranostics.*

Although the branching events in hyperbranched systems are largely random, they can be synthesised by a one-pot polymerisation whilst dendrimers and dendrons require a step by step convergent and divergent synthesis approach making them labour-intensive and time-consuming.[221] Since their evolution by Kim and Webster in 1988, hyperbranched polymers have attracted increasing attention as a result of their unique properties (such as enhanced solubility, low viscosity, ease of synthesis and a high degree of pendant groups available for post polymerisation modification) and greater availability as compared with dendrimers.[223-225] The synthesis of the hyperbranched polymers for this work was *via* RAFT (reversible addition-fragmentation chain-transfer) polymerisation.

1.6 RAFT polymerisation

RAFT polymerisation is an example of a class of reversible deactivation radical polymerisation (RDRPs) that provides a versatile method for radical polymerisation.[226]

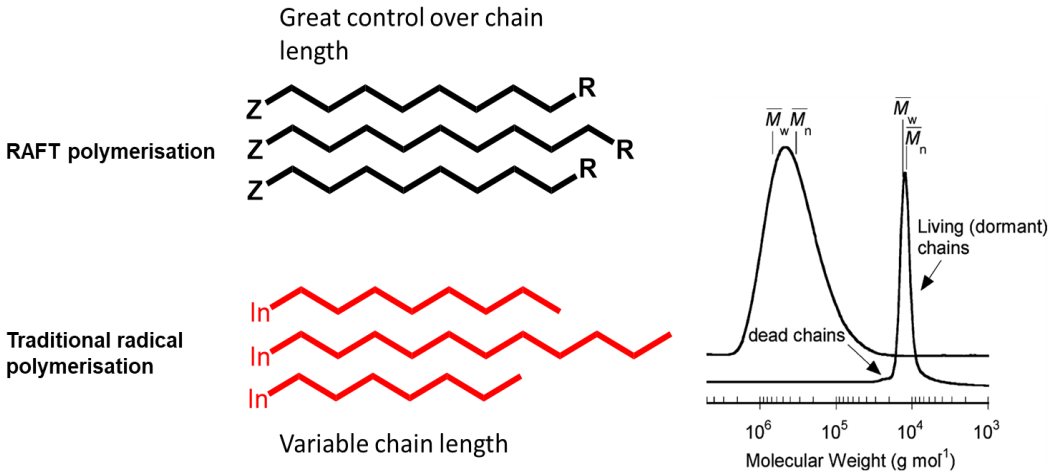


Figure 1-21 Comparison between polymers made with traditional radical polymerisation and RAFT polymerisation. Reproduced (adapted) with permission from ref [202]. Copyright (2008), American Chemical Society.

This polymerisation method allows for the synthesis of macromolecules with or without complex architecture, such as linear, star, comb, graft polymers, with predetermined molecular weights and hence low polydispersity. In an ideal polymer

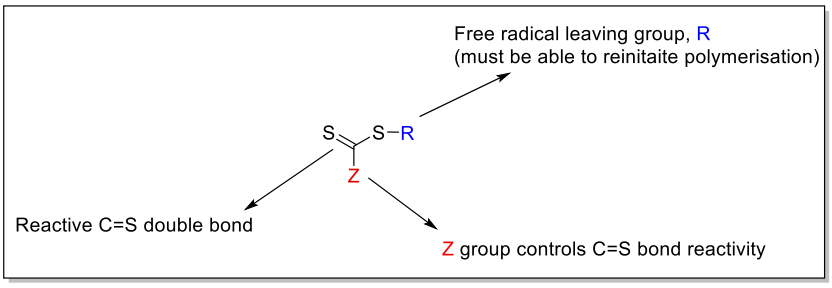


Figure 1-20 General structure of a RAFT agent. Type of agent and stability of adduct is crucial to obtaining control over the polymerisation with low polydispersity index and controlled architecture.

synthesis, the chains will be initiated at the beginning of the polymerisation and extend at a similar and controlled rate with no premature termination or irreversible chain transfer.[226] However, this phenomenon is difficult to achieve with traditional

radical polymerisation (Figure 1-21) as all the chains cannot be active simultaneously leading to inconsistency in chain lengths.[227]

RDRPs such as RAFT afford control over the polymerisation through the equilibrium formed between active and dormant species of the growing polymer radical chains. The equilibrium is shifted towards the dormant species ensuring a low concentration

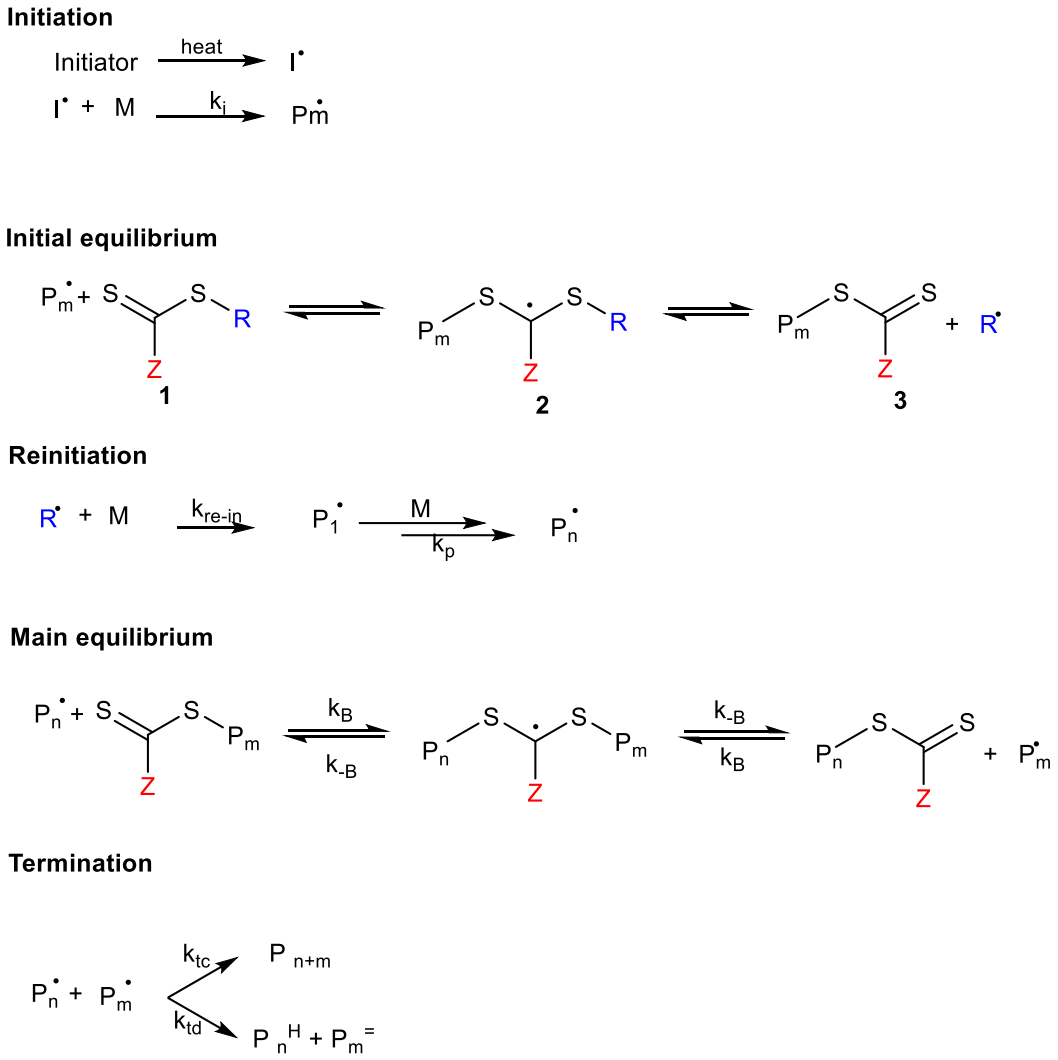


Figure 1-22 Mechanism for RAFT polymerisation.

of active growing radical and reduction in the amount of irreversible termination of growing chains which would otherwise broaden the molar mass distribution of the synthesised polymer.[226, 228]

For the equilibrium to be established, a chain transfer agent (CTA or RAFT agent) is employed. The RAFT agent, usually a thiocarbonylthio group, (Figure 1-20), mediates the polymerisation through a reversible chain-transfer process.

RAFT polymerisation (**Error! Reference source not found.**) is initiated when an azo initiator, such as Azobisisobutyronitrile (AIBN), is heated to form radicals (I$^{\cdot}$). These radicals propagate with monomers (M) in the reaction mixture to generate a polymeric radical ($P_n^{\cdot}$), which then reacts with the RAFT agent forming the intermediate (**2**). This intermediate fragment to give the macro-RAFT agent (**3**) and the radical R$^{\cdot}$, re-initiating the polymerisation with the RAFT agent and constantly exchanging with the propagating chains to form the main equilibrium. Once termination has occurred, the resultant polymer will feature the thiocarbonylthio moiety on one end and the R group on the other end.[229] These RAFT end groups can be engineered to conjugate to a number of molecules such as proteins, peptides and fluorophores for targeting, imaging and other biological applications.[230] In this work, cyanine 5 (Cy5) dye was conjugated to the RAFT agent end group to introduce imaging capabilities to the polymers for *in vitro* uptake and *in vivo* biodistribution assays.

The hyperbranched HPMA (**HB-HPMA**) polymer conjugates developed in this work will then be screened for their biological efficacy in two-dimensional (2D) and three-dimensional (3D) cell culture models.

1.7 *In vitro* cancer models

For many years, the biological activity of chemotherapeutics has been evaluated using two-dimensional (2D) *in vitro* cell culture models during preclinical screening studies.[231, 232]

Table 3 Key features of tumour cells in 2D cell culture, 3D spheroids and in vivo tumour. Adapted from[233]

Features	2D Cell culture	3D Spheroids	*In vivo* tumour
Spatial restriction of cells	✓	✗	✗
A concentration gradient of O_2, nutrients, and metabolic wastes	✗	✓	✓
Heterogenous clonal subpopulation	✓	✓	✓
Biological zones – proliferative, quiescent and necrotic zones	✗	✓	✓
Hypoxic core	✗	✓	✓
Cancer stem cell niche	✗	✓	✓
Gene expression profile	Different	Similar	Similar
Glucose flux rate	Low	High	High

The lack of complexity in the 2D cell culture models could account for the high attrition of anticancer drugs in clinical trials. This is because approx. 95 % of anticancer drugs fail during clinical trials owing to poor efficacy and toxicity despite

promising results in preclinical screening.[234] Although these models are of low cost and good reproducibility, due to the oversimplification of their structure, they are unable to accurately predict *in vivo* efficacy (Table 3). 2D cell culture models have been shown to lack extracellular matrix (ECM) proteins such as collagen and fibronectin observed *in vivo*, and hence have poor ECM-cell interactions; they also fail to mimic the three-dimensional (3D) organisation of tumours *in vivo*, and it is not possible to study the effect of different barriers such as stroma on drug penetration.[231, 232, 235] As a result, 3D cell culture models are emerging as more realistic *in vitro* drug screening methods.[236, 237]

1.7.1 3D cancer models

3D cell culture better describes the *in vivo* architecture of tumours and tissue, exhibiting similar gene expression as tumours *in vivo*.[238] Furthermore, the presence of cell-cell interaction and the highly-dense ECM network provides an ideal environment for evaluating impaired drug penetration, establishing them as superior preclinical models in drug development.[231, 232, 235, 239]

There are three main types of 3D culture models of cancer, namely, tumour tissue explant, tumour on chip and multicellular tumour spheroids (MCTS) (Figure 1-23).[233]

Tumour tissue explant is the culturing of excised human tissues from a biopsy on a collagen-coated surface to either adhere to or get embedded in the collagen.[240] This process offers several advantages such as the ability to preserve the original tumour architecture and microenvironment. However, due to the natural heterogenicity of donor tissues, there is a lack of reproducibility with this model.[233] In addition, the incompatibility of this model with investigational techniques such as flow cytometry and imaging limits its application in *in vitro* drug screening.[233]

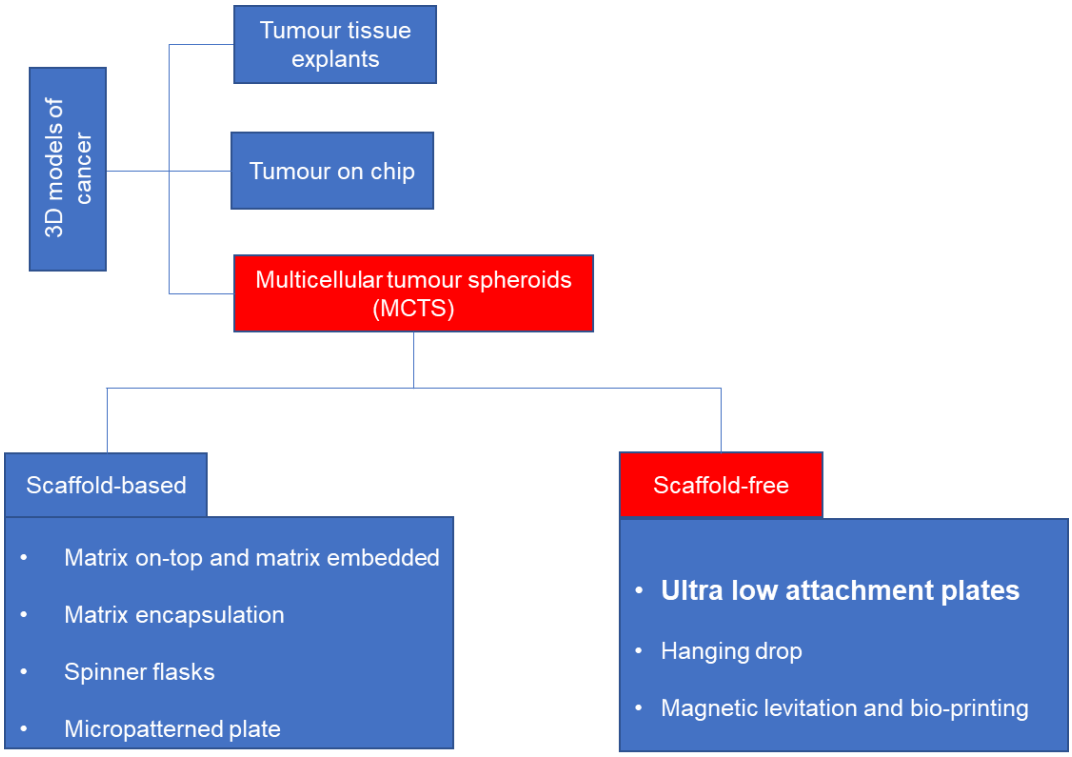


Figure 1-23 3D cell culture models for cancer. Reproduced (adapted) with permission from Elsevier. License number 4675280095831.

Table 4 Advantages and disadvantages of commonly used 3D spheroid methods. Adapted from[241]

Cell Cultures	Advantages	Disadvantages
Hydrogel Matrix	Cell-ECM interactions, easy to incorporate growth factors, *in vivo*-like microenvironments, long-term culture, uniform spheroids	Cumbersome to dispense cells, change growth media, hence low throughput, difficult to retrieve cells after the 3D formation
Hanging Droplet	Simple spheroid formation by gravity, homogenous spheroids	Labour intensive, no cell-ECM interaction, difficult to change media, sensitive to mechanical shocks
Liquid overlay	Simple to use, inexpensive, long-term culture	Labour intensive, heterogeneous, difficult to mass-produce

The “Tumour on a chip” is a biomimetic 3D model that allows co-culturing of different tumour cells on a microfluidic device thereby replicating the tumour microenvironment.[242, 243] The different microfluidic channels mimics the vasculature whilst the tumour cells grow in the microwells (250 µm – 450 µm). This model benefits from the ability to generate complex 3D co-culture models of different cells in addition to custom microfabrication of the chip and real-time data recording. However, issues with tissue size control and spheroid collection for post-analysis limits its use.[233, 244, 245]

MCTSs are the most common 3D tumour models currently under investigation.[246] The spheroids are constructed from tumour cells with or without scaffolds, alone or in combination with other cell types.[247] There are several literature reports that demonstrate the importance of MCTSs in drug delivery screening: it is well established that MCTSs form a realistic organisational environment with 3D spatial arrangements, cell-cell and cell-matrix interaction, hypoxic core and relevant pH.[236, 237] These characteristics displayed by MCTSs are important in *in vitro* drug screening as they are believed to affect drug resistance.[248]

Spheroids can be generated with or without a scaffold. The scaffold method promotes cell-cell and cell-matrix interaction, in addition to support for the 3D arrangement.

ECM-based natural hydrogels, synthetic hydrogels and engineered synthetic hydrogels are all examples of scaffolds that are employed with this method.[249] In contrast, scaffold-free methods focus on promoting cell-cell contact through suppression of cell-surface interactions. Typical scaffold-free methods include hanging drop, liquid overlay and magnetic levitation and bio-printing.[250, 251]

Summarised in Table 4 are the advantages and disadvantages of the different methods of generating spheroids.

In this work, the liquid overlay method was employed to generate spheroids for the screening of our developed systems (Figure 1-24). This method enables spheroid formation through cell-cell interactions.

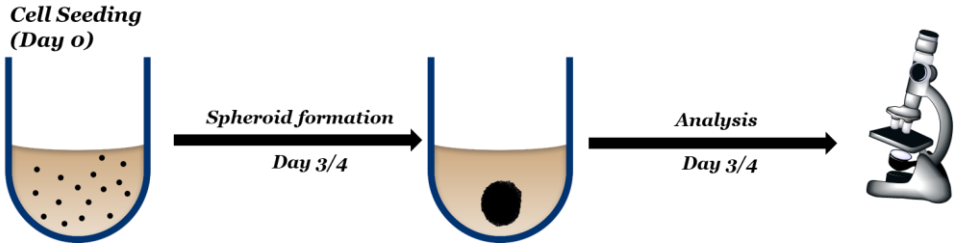


Figure 1-24 Liquid overlay method for the generation of 3D spheroids using Ultra-low attachment (ULA) 96-well round bottom plates. The cell suspension is seeded into wells and the plate centrifuged for 5 min at 300 xg and incubated for approx. 3-4 days to enable spheroid formation.

Ultra-low attachment plates, pre-coated with a hydrophilic polymer to prevent cell-cell adhesion, were used to produce the spheroids. Upon seeding the cells, the plate was put through a centrifugation step to facilitate cell aggregation in addition to suppression of cell apoptosis through activation of paracrine signalling.[251, 252] This method has been successfully employed in-house for the production of neurospheres and to study the penetration and uptake of nanoparticles.[253, 254]

The employment of 3D spheroids in this work was designed specifically to help provide a more realistic pancreatic cancer *in vitro* model for the screening of the investigational prodrug polymer conjugates.

1.8 Mouse models for pancreatic cancer

To advance in the treatment of pancreatic cancer, there is a need for robust experimental models for the effective evaluation of new therapeutic strategies that will correctly predict clinical outcome. Tumour xenografts in immunodeficient mice and transgenic mouse models are the most commonly used preclinical animal models for pancreatic cancer research.[255-259]

Transgenic mouse models are the development of tumours in genetically modified mice that express mutated tumour suppressor and oncogenes.[260, 261] Due to the complexity of pancreatic cancer, traditional approaches to produce transgenic mice with pancreatic cancer failed potentially due to the non-physiological control of gene expression.[262] However, recent progress in gene targeting and improved understanding of the cellular and molecular events of pancreatic cancer has led to increased interest in this model for *in vivo* screening of pancreatic cancer therapy.[262]

Xenograft mouse models are created by the implantation of human tumour cells *via* injection either subcutaneously under the dermis and underlying muscle (subcutaneous model) or directly into the pancreas (orthotopic model).[259] Xenograft models are able to mimic the existing abnormal genetic and epigenetic factors in tumours.[263] The use of xenograft models for the evaluation of drug's effectiveness is considered acceptable by the FDA for clinical trial approval and the subcutaneous xenograft model remains the model of choice for pharmaceutical drug screening.[264] Although there are concerns over the elimination of the unique desmoplasia of the pancreatic cancer tumour when using the subcutaneous model, it has been reported that the human pancreatic cancer cells can produce their own desmoplastic microenvironment.[265-267] In this project, the MIA PaCa-2 xenograft model was employed for the biological evaluation of the developed systems *in vivo*.

1.9 Aims and Objectives

The aim of this research was to synthesis polymeric prodrug materials to enhance the delivery of chemotherapeutics for the treatment of pancreatic cancer. The first approach was to understand the effect polymeric size will have on the delivery properties of the HPMA polymers as differences have been described in literature whereby lager particles have enhanced circulation in the bloodstream but smaller particles are better at penetration through tumour tissues (Figure 1-25).[268, 269]

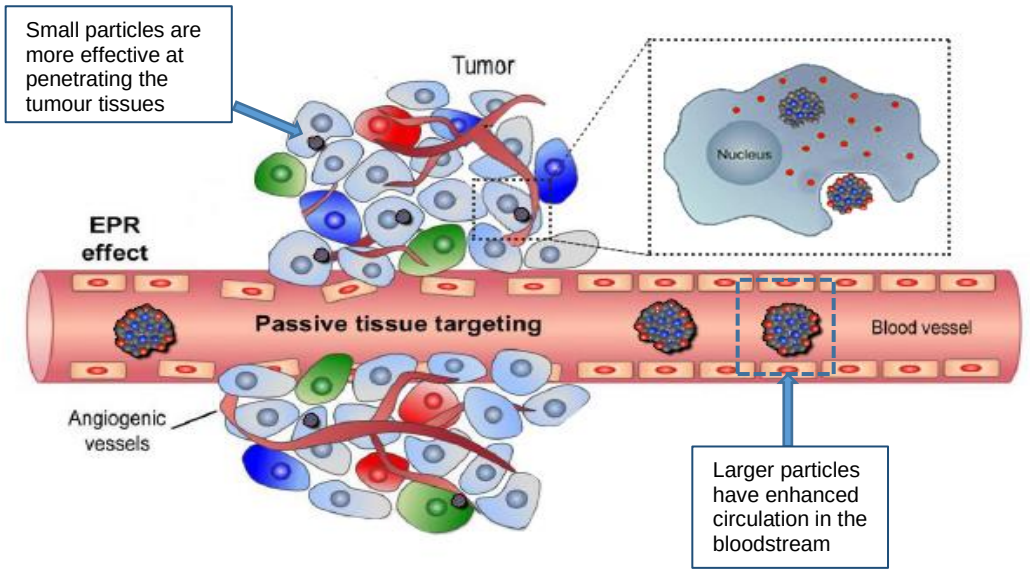


Figure 1-25 Representation of size effect of polymeric nanoparticles. Reproduced (adapted) with permission from ref [244]. Copyright (2014), Molecular and Cellular Therapies.

Three polymers with differing physical size and molecular weight were synthesised and tested *in vitro* and *in vivo*.

The second approach was the development of gemcitabine polymer conjugate through an amide linker for stimuli-responsive drug release in the tumour microenvironment. Amides have been shown to be very stable in the bloodstream with the release of drug occurring only in the presence of amide-specific enzymes.[270] There is some evidence to support the upregulation of specific deubiquitinase enzymes (a large group of proteases) in pancreatic cancer.[271] Hence there is a rationale for the use of amide linker in this work.

Efficacy studies of these particles were conducted in pancreatic cancer cell lines in monolayer and 3D tumour spheroids. A combinational therapy approach to the treatment of pancreatic cancer using the HPMA polymer conjugate was also investigated. This involved the conjugation of the GEM and doxorubicin to the polymeric backbone. These particles were also tested for the efficacy properties in monolayer and 3D tumour spheroids.

The rationale behind this project was the need to improve the delivery of chemotherapeutic agents such as GEM for the treatment of non-resectable pancreatic cancer. Although chemotherapy is the only approved option for patients with non-resectable tumours, it rarely leads to a cure. This is due to enhanced inactivation of chemotherapeutics such as GEM upon systemic delivery and the abundance of dysplastic stroma surrounding pancreatic tumour interfering with drug delivery. The use of nanoparticles such as the polymer-drug conjugates developed in this project was hypothesised to enhance efficacy *via* the following mechanism:

1. Improved pharmacokinetic properties of the anticancer agents when linked to the polymer thus increasing its bioavailability;
2. Better transport through multicellular layers due to altered endocytic pathways of polymer conjugates compared to free drugs;[272]
3. Higher drug loading while retaining solubility of hyperbranched pHPMA compared to previous linear analogues.[211]

Additional objectives of the project:

- Synthesis of functional monomers including **HPMA**, **HPMA-GEM** and **HPMA-DOX** monomers.
- Synthesis of **HPMA**, **HPMA-GEM**, **HPMA-DOX** and **HPMA-DOX-GEM** polymers with the relevant bio-responsive linkers

- Development of mono- and co-cultured 3D tumour spheroids for MIA PaCa-2 pancreatic cancer cell line.
- *In vitro* cellular uptake and cytotoxicity studies in 2D and 3D cell culture models
- Biodistribution studies of the **HPMA** polymers in tumour bearing and tumour naïve mouse models.

Chapter 2 Materials and Instrumentation

2.1 Materials

2.1.1 Synthesis

Methacryloyl chloride (Sigma-Aldrich, 97 %), 1-amino-2-propanol (Sigma-Aldrich,>99 %), Methacrylic anhydride (Sigma-Aldrich, 94 %), Ethylenediamine (Alfa Aesar, 99 %), Anhydrous pyridine (Sigma-Aldrich, 99.8 %), Ethanethiol (Sigma-Aldrich, 97 %), Sodium hydride (Sigma-Aldrich, 60 % dispersion in mineral oil), Carbon disulfide (anhydrous, Sigma-Aldrich, 99 %), Iodine (Sigma-Aldrich, >99 %), Sodium thiosulfate (Sigma-Aldrich, ReagentPlus®, 99 %), 4'4'-Azobis(4-cyanovaleric acid) (ACVA, Sigma-Aldrich, 75 %), Propargyl alcohol (Sigma-Aldrich, 99 %), 4-Dimethylaminopyridine (DMAP, Alfa Aesar, 99 %), 1-Ethyl-3-(3-dimethylaminopropyl)carbodiimide (EDC, Sigma-Aldrich, > 98 %), 2,2′-Azobis(2-methylpropionitrile) (AIBN, Sigma-Aldrich, 98 % - recrystallised before use), Anhydrous *N,N*-Dimethylacetamide (DMAc, Sigma-Aldrich, 99.8 %), Gemcitabine Hydrochloride (Carbosynth Ltd, > 98 %), Cyanine5 (Cy5) azide fluorescent dye was purchased from Lumiprobe, Copper (II) sulfate (Sigma-Aldrich, 99.9 %), Ascorbic acid sodium salt (Sigma-Aldrich, ≥98 %), Succinic anhydride (Sigma-Aldrich, ≥99 %), Deferoxamine mesylate (Sigma-Aldrich, ≥92.5 %), Anhydrous triethylamine (TEA) (Sigma-Aldrich, >98 %), Anhydrous dimethylformamide (DMF) (Sigma-Aldrich, >99.8 %), 2-Chloro-4,6-dimethoxy-1,3,5-triazine (CDMT) (Sigma-Aldrich, 97 %), *N*-methylmorpholine (NMM) (Sigma-Aldrich, 99 %), 2-Hydroxyethyl disulfide (Sigma-Aldrich, technical grade), Cysteamine hydrochloride (Sigma-Aldrich, ≥98 %), *N,N′*-Disuccinimidyl carbonate (Sigma-Aldrich, ≥95 %), Doxorubicin hydrochloride (Carbosynth, >98 %). All other solvents were analytical or HPLC grade and purchased from Fisher Scientific and all chemical used as received unless otherwise stated.

2.1.2 Cell Biology

MIA PaCa-2 and Bone Marrow-Derived Mesenchymal Stem Cells (MSCs) were obtained from the CRN NCI-60 cell bank initiative, Cancer Biology Division of Cancer and Stem Cells, School of Medicine, University of Nottingham. The RAW 264.7 macrophage cell line was acquired from the American Type Culture Collection (ATCC, Manassas, VA). Dulbecco's Phosphate Buffer Saline (PBS), L-Glutamine (2 mM), Dulbecco's Modified Eagle Medium (DMEM), Accutase Solution, Live/Dead Cell Double Staining Kit, Dimethyl sulfoxide (DMSO) and Lactic Dehydrogenase (LDH) Toxicology Assay Kit (TOX7 kit) were purchased from Sigma-Aldrich (Dorset, UK). Mesenchymal Stem Cell Medium (MSCM) and Mesenchymal Stem Cell Growth Supplement (MSCGS) were sourced from ScienCell Research Laboratories. Foetal Bovine Serum (FBS) solution was obtained from Invitrogen (Paisley, UK). Trypsin- EDTA was supplied by Gibco, Life Technologies Ltd, (Paisley, UK). Well-plates, Ultra-low attachment (ULA) 96-well round-bottom plates were sourced from Corning (Amsterdam, The Netherlands). Cultrex® Basement Membrane Extract (BME) was acquired from Trevigen (Gaithersburg USA). Hoechst 33342 (NucBlue® Live ReadyProbes® Reagent) was supplied by from Life Technologies Ltd, (Paisley, UK). Paraformaldehyde (PFA) solution (4 %) was purchased from Alfa Aesar, A Johnson Matthey Company (Heysham, UK). Hoechst 33342, PrestoBlue® Cell Viability Reagent and Gibco TrypLE Express (1X) were purchased from Thermo Fisher Scientific. CellTiter-Glo® 3D Cell Viability Assay was purchased from Promega. All chemicals were used as received unless otherwise stated.

2.2 Instrumentation

Silica gel column chromatography. Silica gel column chromatography is an example of a liquid-solid chromatography (LSC).[273] LSC relies on the differential adsorption of compounds to the surface of the stationary phase and competition with components of the mobile phase to separate substances.[274] The commonly used

stationary phase for LSC is silica, including chemically bonded silica phases with 3-aminopropyl, spacer bonded propanediol groups and 3-cyanopropyl.[274] The silica particles are coated with silanol groups (≡Si—OH).[274] These groups are relatively strong proton donors and therefore interact with the solute molecules that contain hydrogen-bond acceptor groups leading to retention of the molecules. Due to this interaction, different molecules will move through the column at different rates, allowing for their separation into fractions which is collected as they elude from the column. In this project, Merck 60 (230-400 mesh) silica gel was used for column chromatography and TLCs were performed using pre-coated silica gel DC-Fertigfolien ALUGRAM SIL G/UV254.

Nuclear Magnetic Resonance (NMR) spectroscopy. NMR is an analytical chemistry technique used to ascertain the purity and molecular structure of a sample.[275] This is achieved through the application of a magnetic field to the atomic nucleus of stable isotopes such as ^{1}H, ^{13}C, ^{19}F and ^{15}N. Radiofrequency pulses are then used to characterise the resulting resonant frequency of that atomic nucleus in accordance with its chemical or environmental surroundings.[276] The electrons of the atom circulates in the direction of the applied magnetic field causing a small opposing magnetic field at the nucleus. Due to the variability in the electron density around nuclei in different molecules as a result of the types of nuclei and bonds it has, differences are observed in the static and opposing magnetic fields.[276] This phenomenon commonly referred to as “chemical shift” (ppm or Hz) is the fundamental information used in the characterisation of the structure of molecules and polymers.[276] The inter-relationship between protons in the same molecule or polymer can also be elucidated based on the principle of “spin-spin coupling”. Spin-spin coupling describes the effect nuclei close to each other (i.e., 3 or fewer bond lengths apart) have on each other’s opposing magnetic field.[276]

All NMR spectra were recorded on a Bruker DPX 400 UltraShield™ Spectrometer (400 MHz) using deuterated solvents from Aldrich. Spectra were processed with MestReNova® 9.0.1 software.

Dynamic light scattering (DLS). DLS is a technique used for rapid determination of size distribution of small particles or droplets in suspension.[277] In DLS measurements, a light source shines a beam of focused light at the particles in solutions.[278] This light is then scattered in all direction as a function of the size and shape of the particles. Due to the Brownian motion of the particles in solution as a result of the continuous bombardment from molecules of the surrounding medium, there is an observed fluctuation in the intensity of the scattered light.[279] This fluctuation in intensity is then analysed and the diffusion coefficient that is related to the hydrodynamic size of macromolecules obtained.[279]

Particle size was measured on Viscotek 802 DLS with a laser wavelength of 830 nm at 20 ^{0}C. Polymer solutions were prepared as 1 mg/mL in water and the data analysed using OmniSIZE software. A minimum of 10 measurements was collected per sample. Zeta potential measurements were taken with Malvern Zetasizer Nano ZS at 25 ^{0}C (scattering angle 173^{0}, laser of 633 nm). All measurements were performed in triplicate.

Fourier Transform Infrared Spectrometer (FTIR). FTIR is an example of vibrational spectroscopy which is used to determine the molecular structure of a compound based on its characteristic absorption of infrared radiation.[280] During an IR spectroscopy, electromagnetic radiation in the IR region is either reflected off the sample's surface or transmitted through it.[276] The photons which correspond to the resonant mode frequencies in the sample is absorbed.[276] As the absorption bands relates to specific functional groups within the molecule, identification of these bands leads to the identification of the functional groups within the molecule.[281] The FTIR

spectra were recorded using an Agilent Cary630 FTIR spectrometer and the data were analysed using MicroLab FTIR Software, Agilent Technologies.

Gel Permeation Chromatography (GPC). GPC is an analytical technique used to determine molecular weight and molecular weight distribution of macromolecules. Briefly, a sample mixture is introduced into a column packed with porous gel and the analyte molecules separated by size based on their elution from the column and their retention time (time at which the sample emerges from the column) measured.[276] The separation process is dependent on the diffusion and permeation of the molecules in and out of the pores of the gel - small molecules easily diffuse in and out of the pores, penetrating deeper than large molecules and hence are eluted last. Thus, retention is easily correlated with molecular size and weight.[282] When coupled with light scattering, UV absorbance and refractive index (RI) detector, the absolute molecular weight, molecular size and intrinsic viscosity can be determined.[283]

Aqueous GPC was performed on a Shimadzu Prominence UPLC fitted with differential RI detector. The eluent was 0.1 M sodium nitrate at a flow rate of 1 $mL \cdot min^{-1}$. The instrument was fitted with a Polymer Labs aquagel-OH guard column (50 × 7.5 mm, 8 μm) followed by three PL aquagel-OH columns (30, 40 and 50; 300 × 7.5 mm, 8 μm). Column calibration was achieved using narrow PEG/PEO standards of known Mp in the range of 200 Da – 130 kDa. Molecular weights and dispersity values were calculated using Shimadzu LabSolutions software with GPC analysis add-on. HBP HPMA was dissolved in 0.1M of sodium nitrate and filtered (4 μm) at a concentration of 5 mg/mL. Mn and Đ were determined by light scattering measurements with a *dn/dc* of 0.159 mL/g (Figure 2-1).

Mass spectrometry. Mass spectrometry is an analytical method used to measure the mass-to-charge (*m/z*) ratio or properties concerning the *m/z* of ions relating to

the compounds in a given sample.[284] The electrospray ionisation (ESI) method uses an energetic electron beam to produce charge species during the ionisation process. During the analysis, a heated metallic filament, (for example, tungsten) is used to generate a beam of electrons which are electrically accelerated to collide with the vapourised sample.[285] This causes the expulsion of electrons from the analytes and the formation of positively charged radical cations.[285] A mass spectrum plot is then generated of ion abundance versus *m/z* and presented as Daltons (Da)/unit charge.[284] ESI TOF Mass Spectrometry measurements were carried out using a Bruker ApexIV FT-ICR spectrometer.

Transmission Electron Microscope (TEM). TEM is one of the best techniques for characterising and determining the size and morphology of nanoparticles.[286] In TEM analysis, an energetic electron beam is transmitted through the sample and the interaction between the sample and the electrons forms an image due to differential absorption of electrons by the material as a consequence of differences its composition or thickness.[286] The morphologies and sizes of polymers were analysed on a Tecnai G2 (FEI, Oregon USA) transmission electron microscope. Samples were dissolved in DI H2O at a concentration of 1 mg/mL and 13 µL was added to copper grids (Formvar/Carbon film 200 mesh Copper (100)). The sample was allowed to settle for 10 min, excess water removed, and images captured without staining.

Flow Cytometry. Flow cytometry is an analytical instrument for quantifying the fluorescence and optical characteristics (such as size, shape and granularity) of a single cell in a fluid stream.[287-289] In flow cytometry, moving cells in a fluid stream passes in front of a light from excitation source such as a laser beam leading to scattering and fluorescence emission.[287] The scattered light correlates directly to morphological and structural properties of the cell and fluorescence emission from a fluorescence probe is proportional to the amount of fluorescent probe bound to or

internalised by the cell or cellular component.[288] All flow cytometry experiments were performed on Coulter FC-500 cytometer (Beckman Coulter) and analysed using Kaluza Analysis 1.5 software.

Fluorescence microscopy. Fluorescence microscopy is an optical imaging technique that selectively examines a specific component of a complex biomolecular specimen.[290] Filtered light of the absorbing wavelength is used to illuminate the fluorescently labelled specimen. This specimen is then viewed using a barrier filter which transmits the longer wavelength of the emitted light but is opaque to the absorbing wavelength.[290] Thus, the structures fluorescently marked will light up against the black background.[290] Fluorescence microscopy images were acquired on an inverted Nikon Eclipse TE 300 microscope. Images were processed using ImageJ software (1.50i).

***In vivo* optical imaging.** *In vivo* optical imaging is a non-invasive technique that utilises differences in near-infrared and visible wavelengths of light in living tissues to monitor biological processes.[291, 292] The optical imaging is achieved through the use of endogenous and/or exogenous imaging agents.[291, 292] Cell lines can be engineered to express one or more of the numerous endogenous luciferase and/or fluorescent proteins that have been identified and characterised to provide information about the structure and function of the living tissue.[291, 293, 294] In contrast, exogenous imaging agents such as organic and inorganic dyes, fluorescently labelled nanoparticles, quantum dots, and fluorescent proteins are injected into the animals prior to injection to monitor and visualise several physiological processes including apoptosis, and proliferation.[295-297] The emission of fluorescence is as a result of the absorption of light of a specific wavelength in order to reach an excited state. This is followed by relaxation to the ground state consequently emitting photons that can be visualised through an emission filter.[298] IVIS® Spectrum

imaging system (Perkin Elmer) was used to obtain data for *in vivo* biodistribution assays. Data analysis was performed using Living Image Software (Perkin Elmer).

Positron Emission Tomography-Computed Tomography (PET-CT). PET is a nuclear medicine imaging technique used to produce functional three-dimensional images of physiological processes.[299] Positron-emitting radionuclide (radiotracer) is introduced into the body with the help of a carrier molecule.[300] This radiotracer then emits gamma rays that are detected and used to form the image of specific targets and biochemical processes in the body.[301] Due to the utilisation of the gamma rays in PET assays, there is negligible background signal in image acquisition and hence it can be employed for the monitoring of disease states through molecular imaging of the radiotracer.[302] PET can also be employed in the study of nanoparticle biodistribution and pharmacokinetics *in vivo* by incorporating the radioisotopes such as ^{64}Cu or ^{89}Zr to the nanoparticle systems using metal-chelating cages (e.g., 1,4,7,10-tetraazacyclododecane-1,4,7,10-tetraacetic acid (DOTA) for or deferoxamine B respectively).[303-305]

X-ray based computed tomography is emerging as a molecular technique owing to developments of specific nanoparticle contrast agents for image enhancement.[306] CT imaging consists of the collection of several two-dimensional radiographic images taken at different angles around a single plane of rotation. These images are then reconstructed into a 3D image to create anatomical information of the differential x-ray absorption between different tissues.[307] PET and CT images can be used in conjunction with one another to precisely align the functional images of PET with the anatomical imaging of CT in order to help interpret data from the studies.[308] Siemens Inveon PET-CT scanner was used to obtain images for the PET-CT biodistribution assay. The images were reconstructed using Feldkamp reconstruction software (Siemens).

2.3 Supplementary Information

The refractive index increment (*dn/dc*) of the hyperbranched HPMA polymers was measured using a refractometer (Abbemat 200). The polymers were dissolved in deionised water at different concentrations. The refractive index values were plotted against concentration and the *dn/dc* was determined from the slope of the linear fitting of the dataset.

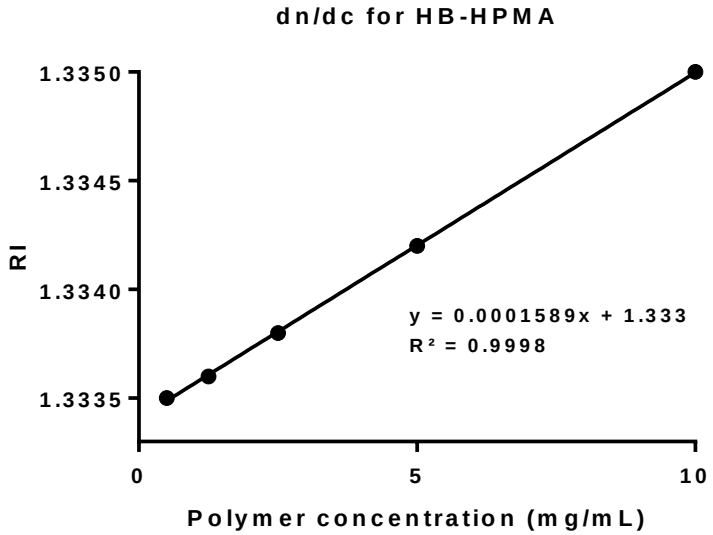


Figure 2-1 Refractive index as a function of HB-HPMA polymer concentration for dn/dc determination.

Chapter 3 Development and characterisation of a 3D Spheroid Model of Pancreatic Cancer

3.1 Introduction

The aim of this study was to develop and characterise the 3D MCTS of the MIA PaCa-2 pancreatic cancer cell line to be used as a model for biological screening of synthesised materials. As mentioned in Chapter 1, pancreatic cancer is stroma-rich cancer with the stroma accounting for approx. 90 % of the tumour volume.[309] The presence of the stroma can impede the delivery of drugs to the tumour cells for treatment.[310-312] Stroma is made up of cancer-associated fibroblasts (CAFs), extracellular matrix (ECM) and immune cells, with CAFs considered an integral part due to their role in the accumulation of ECM and secretion of soluble factors associated with disease progression and chemoresistance.[313-316] The major sources for CAFs in pancreatic cancer are pancreatic stellate cells (PSCs).[265, 313] When activated in tumour cells, PSCs create a fibrotic and hypoxia environment for the growth and metastasis of the tumour as observed in *in vivo* and *in vitro* co-culture models.[314, 317] As a result, PSCs have been used in the past as a model for the investigation of stroma-mediated chemoresistance.[318] In this work, bone marrow-derived mesenchymal stem cells (BM-MSCs) were used in place of PSCs as it has been reported through several *in vitro* and *in vivo* studies that stellate cells are mesenchymal stem cells (MSCs) and therefore should function similarly to PSCs when cocultured with the MIA PaCa-2 pancreatic cancer cells used in this work.[319]

The developed spheroids were characterised for growth rate, cell viability and retention of the mesenchymal stem cells (MSCs) in order to select the optimum conditions, such as seeding density, length of experimental time and MIA PaCa-2/MSCs ratio for all subsequent spheroid experiments. This was to ensure that

viability of cells in the spheroids over the course of the assay will not impact on the administered treatment.

3.2 Experimental

3.2.1 Tissue Culture of the cell monolayer

3.2.1.1 Culturing of the cell monolayer

MIA PaCa-2 (Human Pancreas carcinoma) and BM-MSCs were cultured in T75 culture flask containing Dulbecco's Modified Eagle Medium (DMEM, 15 mL), and ScienCell Mesenchymal Stem Cell Medium (MSCM, 15 mL) respectively. DMEM was supplemented with 10 % (v/v) foetal bovine serum (FBS) and 2 mM L-glutamine, and MSCM was supplemented with ScienCell Mesenchymal Stem Cell Growth Supplement (MSCGS) and FBS. The media were warmed in a 37 °C water bath prior to their use in experiments.

The cells were routinely checked for mycoplasma contamination and passaged at approximately 80 % confluency. The cells were passaged by first washing with Dulbecco's phosphate buffer saline (PBS) before treatment with phenol red-free Gibco TrypLe Express Enzyme (1X, 5 mL) to induce cell detachment at 37 °C for approximately 5 min. The relevant medium was then added (5 mL) and the suspension centrifuged at 300 RCF (Relative Centrifugal Force) for 5 min to collect the cell pellet. The cells were then re-suspended in 5mL medium and passaged into a new T75 flask containing fresh medium at 1:10 dilution. Cells in all cases were incubated in a humidified incubator (5 % CO_2 / 95 % air atmosphere at 37 °C).

3.2.1.2 Freezing cell stocks

Cells at approximately 80 % confluency were harvested as described above. The cell pellet was then resuspended in freezing medium (5 mL) consisting of the relevant medium with Dimethyl sulfoxide (DMSO, 10 %). The suspension was then

aliquoted (1mL) into cryovials and placed in a propane-2-ol containing chamber at -80 °C overnight and kept at -80 °C freezer thereafter.

3.2.1.3 Thawing cell stocks

The cryovial containing frozen cells was removed from -80 °C freezer and immediately placed into a 37 °C water bath. Once thawed, the cell suspension was transferred to the relevant pre-warmed medium (10 mL) and centrifuged at 300 RCF for 5 min. The supernatant was decanted, the cell pellet resuspended in fresh medium, transferred to a T75 flask containing medium (15 mL) and incubated until 80 % confluent. The medium was refreshed every 48 hours until cells were ready for passaging. To ensure full recovery from freezing, all cells were maintained for several passages (1-3) before being used in experiments.

3.2.2 3D Spheroid generation

Corning 7007 Ultra-low attachment (ULA) 96-well round-bottom plates were used in the generation of the 3D spheroids. 80 % confluent monolayer cells were detached, collected and the cell number determined using the Biorad TC20 automated cell counter. A single-cell suspension was diluted accordingly in a suitable medium, in the presence of Cultrex basement membrane extract (Cultrex-BME, 100 µg/mL) to generated different sized spheroids. The final volume of cell suspension in each well was kept constant (100 µL) for each of the different seeding densities (1000, 2000 and 4000 cells per well) at N = 4 replicates. The plates were centrifuged at 300 RCF for 5 min. The spheroids are referred to by their seeding density throughout the text, i.e. 1K, 2K and 4K).

3.2.3 3D Spheroid characterisation

3.2.3.1 Spheroid imaging

Images of the spheroids were taken with a Nikon Ti Eclipse inverted microscope.

3.2.3.2 Growth analysis

The volume of the spheroids was analysed by measuring their cross-sectional area using the in-house open-source macro for the FiJi distribution of ImageJ written by Ivanov.[251, 320] The macro determines the area of each spheroid using an established threshold algorithm.[321] This automated process is relatively robust as less than 5 % variation has been found between the algorithm and manual measurement.[251] The measured area (S) from the macro data of the 2D projection of the spheroid was then used to calculate the radius, $\left(r = \sqrt{\frac{S}{\pi}}\right)$ and subsequently, the volume, $\left(V = \frac{4}{3}\pi r^3\right)$ of an equivalent sphere.[322]

3.2.3.3 Monitoring Cell Viability in the 3D Spheroid

Spheroids of the different seeding densities were generated in 96 well ULA plates. On days 3, 5, 6 and 7 the spheroids were stained in the wells with a working solution of propidium iodide (PI, 5 µL) and calcein acetoxymethyl (AM, 5 µL). Hoechst 33342 solution was also used as a reference stain for the cell nuclei. The spheroids were incubated with the stains for 4 hours, and then the wells were washed with PBS (x3) and resuspended in DMEM. The presence of calcein AM and PI positively stained cells were visualised with the fluorescence microscope. PI stains necrotic cells red, calcein AM stains live cells green and Hoechst 33342 stains the nuclei of the cells blue.

3.2.3.4 Statistical Analysis

Coefficient of variability (CV) was calculated as:

$$CV\ \% = \frac{SD}{Mean} \times 100$$ (Acceptance criteria CV % <20)

where SD = standard deviation.

3.3 Results and Discussion

3.3.1 Monitoring MIA PaCa-2 mono-culture spheroid growth

The MIA PaCa-2 pancreatic cancer cell line was employed as the *in vitro* model of pancreatic cancer for evaluation of all the synthesised polymers in this work. Initially, the cell line was assessed for its ability to form spheroids in the presence of basement membrane extract (BME). It has been reported that to develop an *in vitro* cancer model resembling that in a solid tumour, and to maintain cell physiology, gene expression and morphology, cells need to be cultured in specific culture conditions such as the use of extracellular matrix support and 3D structures. Therefore, to facilitate with rapid spheroid formation and provide ECM needed for cell-matrix interaction observed in physiological paradigm, BME was added to cell suspension in each well.[323-325]

The ULA round-bottom plates used in the spheroid generation were coated with a hydrophilic polymer coating. This acts to prevent cell attachment to the culture plate and hence forces the cells to adhere to one another forming 3D spheroid structures. The seeding of the cells led to the formation of one spheroid in each well of the 96 well ULA round bottom plate. The growth of these spheroids was monitored and characterised over a period of 7 days in order to determine the appropriate density for future experiments. Images were taken off the spheroids from day 1-7 (Figure 3-1) and showed the cells forming compact spheroids on day 3 of the seeding.

The growth of the seeded spheroids, as represented by Figure 3-2A shows a constant increase in the volume of the spheroids over the study period. The percentage volume increase was calculated to be 169 %, 105 % and 81 % for 1K, 2K and 4K cells/well respectively (Figure 3-2B). The low seeding number of 1K spheroids led to significantly higher volume increase over the seven days than 4K.

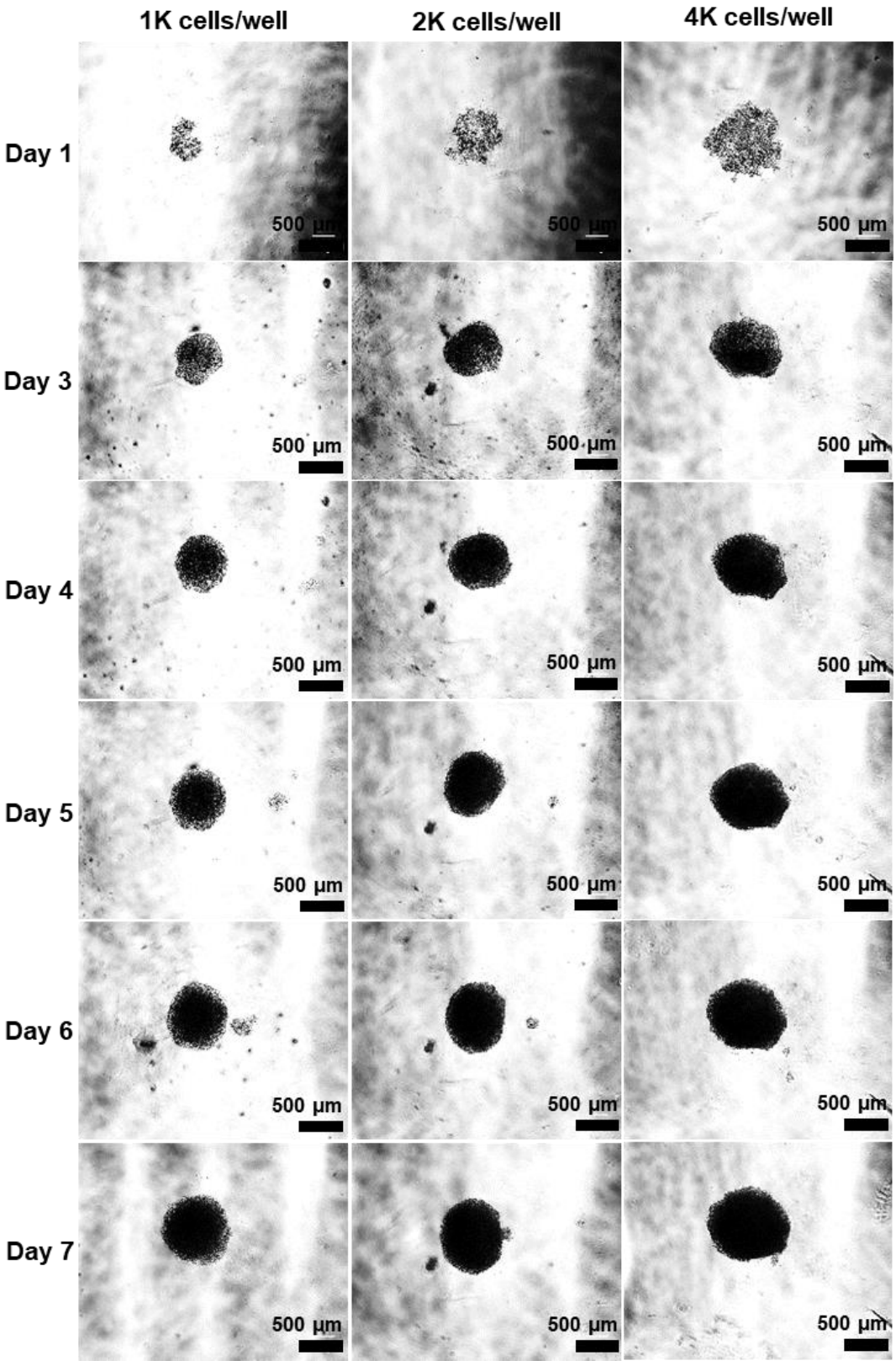


Figure 3-1 Representative brightfield microscope images (x4 objective) of MIA PaCa-2 spheroid formation and growth at different seeding densities (1K, 2K and 4K) over 7 days, (N = 4). Scale bar = 500 µm.

This linear and logical growth of the spheroids over time has also been observed in other studies.[326, 327]

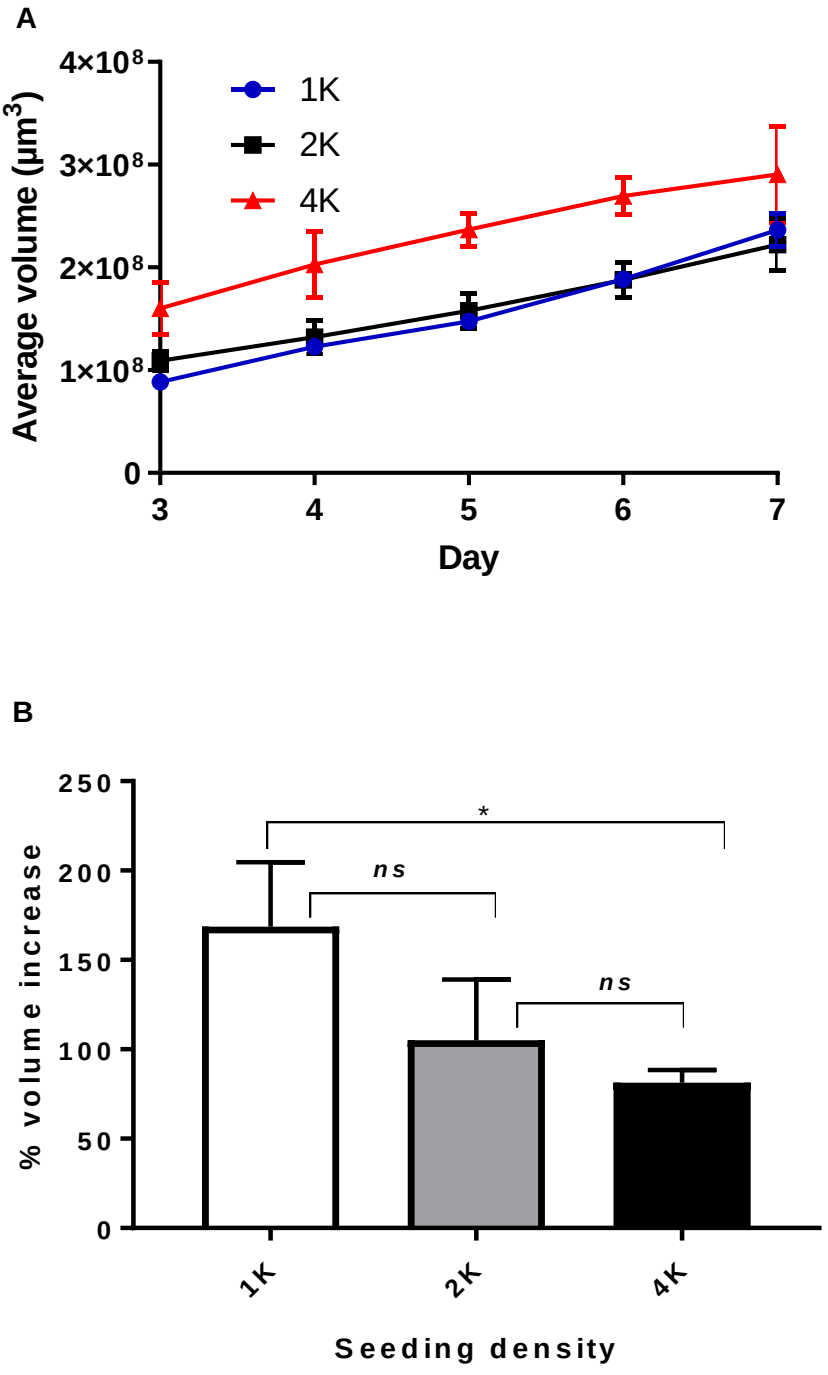


Figure 3-2 Analysis of spheroid growth. A) Growth curve of Mia-PaCa2 spheroids of varying seeding densities (1K, 2K, and 4K) monitored from day 3 to 7; B) Percentage volume increase of spheroids between day 3 and 7. The volume of the spheroids was calculated using the formula $4/3*\pi*r^3$, where the radius 'r' was derived from the analysis of spheroid area in ImageJ. Percentage volume increase was calculated using the equation: (Day7-Day3)/Day3 x *100. P value of <0.05 was considered statistically significant (n=4). (*p < 0.05, two-way ANOVA with Tukey's multiple comparison test).*

The difference in proliferation capacity in relation to seeding density could be due to hindrance in the rate of growth of larger spheroids by the geometry of the well and the constant volume of the medium.[251] Due to the high number of cells in the high seeding density compared with the low seeding density, the availability of nutrients will deplete at a faster rate and as a result impact on the rate of growth – similar results have been described in the literature.[251, 328]

The liquid overlay method proved to be a reliable method for large-scale generation of the MIA PaCa-2 spheroids with high reproducibility, with CV values of spheroid volume of <8 %, <9 % and <16 % for 1K, 2K and 4K respectively on day 3 post-seeding. Different sized spheroids are easily and rapidly produced by varying the number of seeded cells per well; however, it is worth noting that the rate of growth of larger spheroids can be hindered by factors described above.

3.3.2 Monitoring Cell Viability in the 3D Spheroid

It has been shown that increases in spheroid size can lead to the development of a necrotic core due to transport limitation causing the formation of oxygen and nutrient gradients.[329, 330] As the aim of this work is to observe the effect of the drug on cell viability, appropriate seeding density is required in order to avoid any necrosis or cell death in the untreated spheroids in the course of the study. The cell viability in the spheroid was studied using calcein AM (acetoxymethyl) and propidium iodide (PI).

PI intercalates nucleic acids of dead cells giving them a red fluorescence, however, it does not permeate into live cells, therefore, it is often used to detect dead cells in a population.[331, 332] Calcein AM, a non-fluorescent compound is converted to the green-fluorescent calcein in live cells after hydrolysis of acetoxymethyl ester.[333-335]

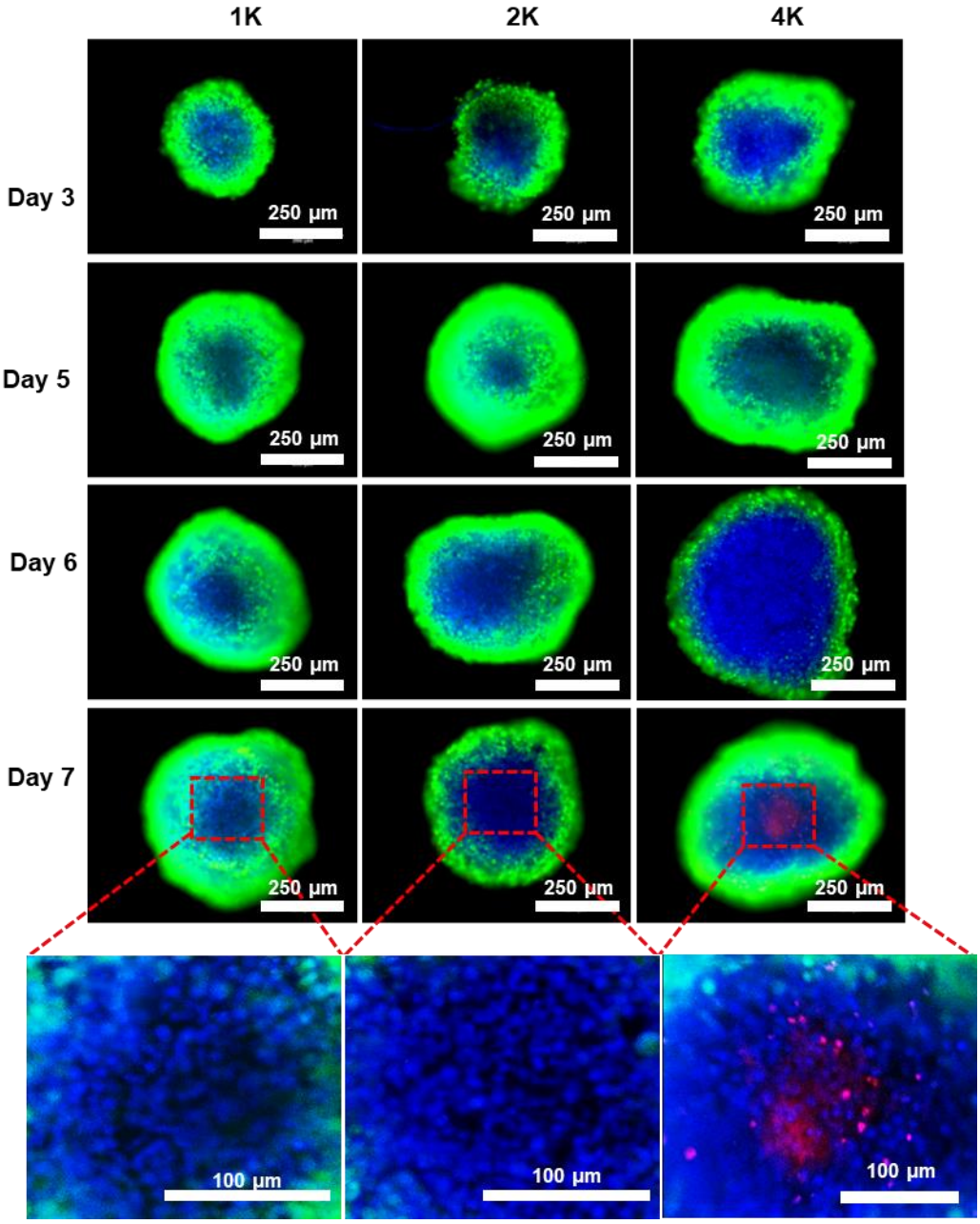


Figure 3-3 Cell viability analysis of MIA PaCa-2 spheroids of varying seeding densities. Representative widefield fluorescence microscope images (x10 objective) of spheroids stained with calcein AM (green), PI (red) and Hoechst (blue) on days 3, 5, 6 and 7 in culture, (n = 4). From the enlarged images, it is clear that the necrotic core is only present in 4K seeding density on day 7 of incubation. Scale bar = 250 µm for original images and 100 µm for enlarged images.

Figure 3-3 shows images of the spheroids on different days at different seeding densities. There were no observable PI-positive cells at all seeding densities on days 3, 5 and 6. However, on day 7, a small percentage of PI-positive cells was detected in the centre of 4K spheroids indicating the formation of a necrotic core.

This observation supports literature findings whereby an increase in spheroid size can lead to the formation of a necrotic core.[336, 337]

The ratio between the green (calcein AM) and red (PI) signals were calculated to provide semi-quantitative data of cell viability in the 3D spheroids across the different seeding densities over time and the results are represented in the graph above (Figure 3-4). From this, no significant difference was observed between the cell viability of the spheroids in each seeding density from day 3 to day 5. The viability of cells in 2K and 4K spheroids gradually decreased from day 5 to day 7 with a significant difference found between 1K and 4K spheroids. Cell viability of 1K spheroids remains constant from day 3 to day 6 and slightly decreases on day 7.

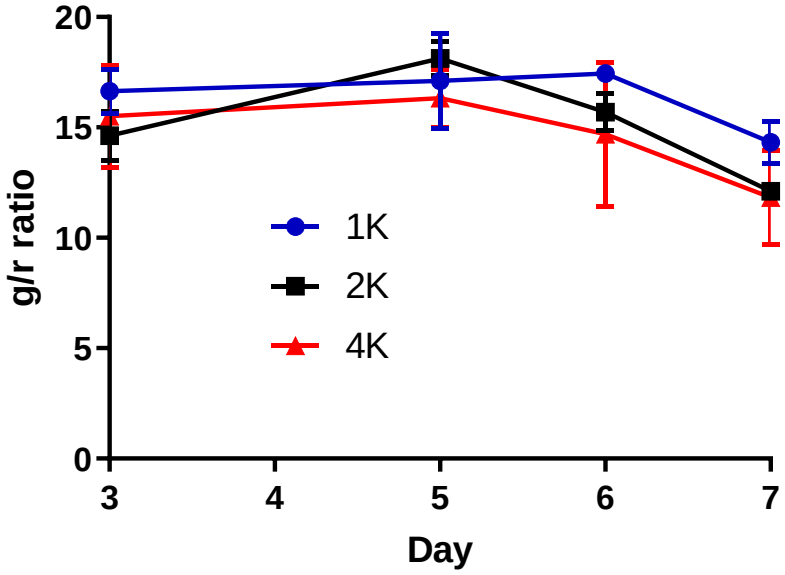


Figure 3-4 Green/red (g/r) ratio of the MIA PaCa-2 spheroids for the different seeding densities on day 3-7. Green represents calcein AM stain for live cells and red represents PI stain for dead cells.

Based on the observed high cell viability of 1K spheroids on days 6 and 7 over 4K spheroids, the lack of necrotic core formation, and the higher growth rate, a seeding density of 1K cells was chosen as the most appropriate for all subsequent spheroid assays. The maximum length of time for 3D spheroid assays was chosen to be 7 days. This was to ensure that the experimental time frame resides within the screening assays, and thus there should be no inadvertent changes in cell viability

as a result of culturing conditions (e.g. time course of the assay and not refreshing the culture medium).

3.3.3 Retention of GFP labelled MSCs in MIA PaCa-2 spheroid co-culture model

In order to establish a 3D spheroid model that mimics the dense stromal characteristic of pancreatic tumour, and to further understand the impact stromal cells have on the treatment of pancreatic cancer, a co-culture of MIA PaCa-2 (1K cell number) with varying ratios of MSCs as the stromal cell model (1:1, 1:2 and 2:1) was developed to study the retention and role of MSCs in the coculture system. Spheroid formation and retention of the MSCs were monitored *via* microscopy images (Figure 3-5). An impact of the ratio of the two cell types can be observed, where the formation of intact spheroids in the co-culture system was successful in the 1:1 ratio compared with the other two ratios where the MIA PaCa-2 cells dissociated from the MSCs. A similar observation was made by Bulin *et. al.* whereby coculture of MIA PaCa-2 with pCAF (pancreatic cancer-associated fibroblasts) cells at 2500 cells/well each led to the formation dense core with a loose periphery of escaping cancer cells.[327] Although a large number of cancer cells in the monoculture can form spheroids, up to 4000 cell/well in this study, the presence of MSCs in co-culture means that seeding density of 3000 cells/well (1:2 and 2:1) inhibits spheroid formation. This may be due to the MSCs inducing invasion in the cancer cells in the higher seeding densities and obscuring spheroid formation. As a detailed investigation of the invasion-inducing properties of MSCs in pancreatic cells was beyond the scope of this work, the subsequent hypotheses tested were based upon the findings of previous studies, which had demonstrated the invasion-inducing nature of MSCs in pancreatic cancer cells, including the MIA PaCa-2 cell line and other cancer cell types.[338-341]

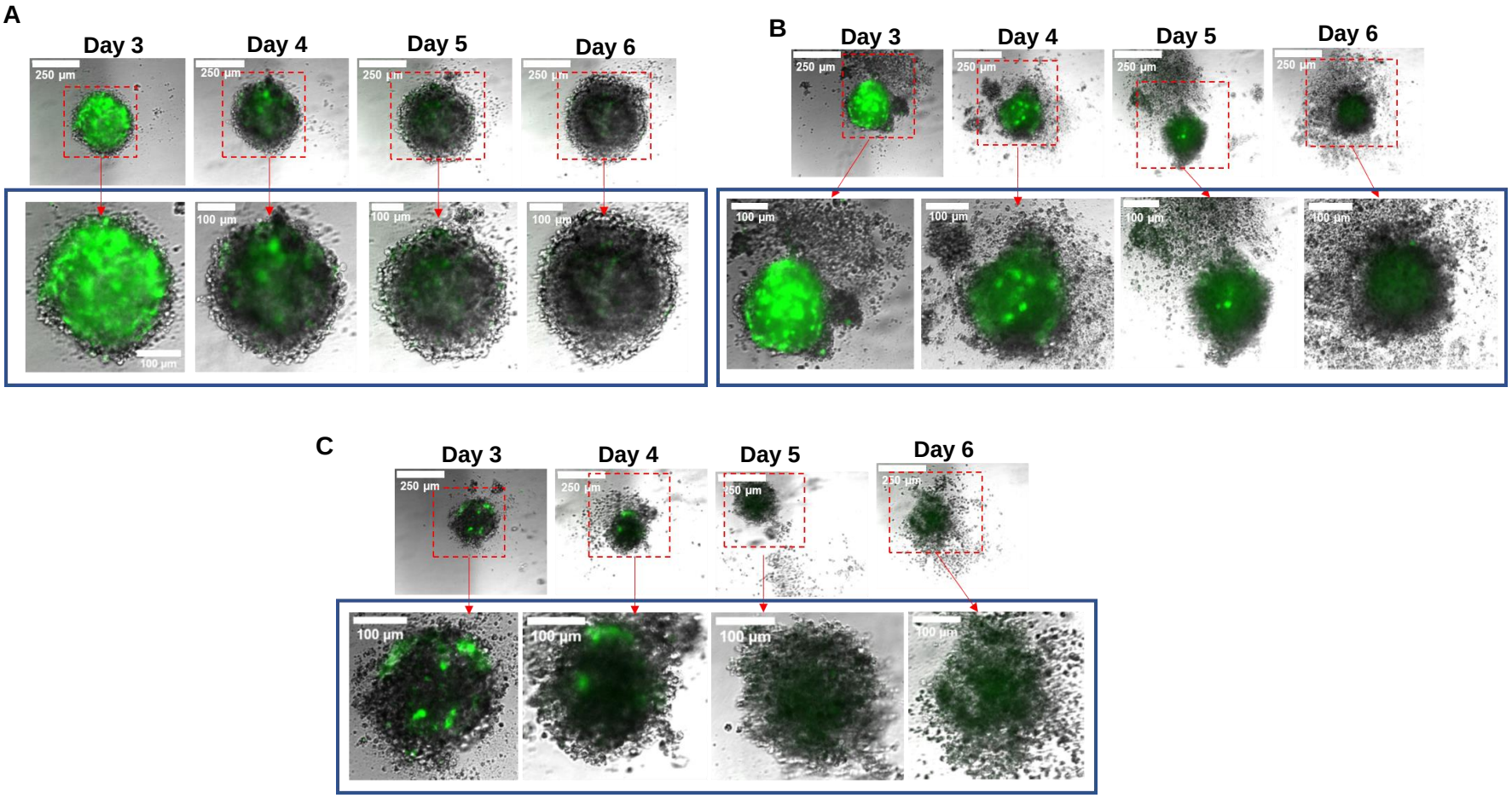


Figure 3-5 Representative widefield fluorescence microscope images (x10 objective) of MIA PaCa-2 cells (1K/well) co-cultured with different ratio of MSCs; A) 1:1, B) 1:2 and C) 2:1 MIA PaCa-2 to MSCs from day 3-6, (N = 4). Scale bar = 250 µm for original images and 100 µm for enlarged images. As depicted, the formation of intact spheroids over the assay period is only present in 1:1 ratio.

To test the hypothesis that the lack of spheroid formation in 1:2 and 2:1 was due the number of cells, the experiment was repeated, keeping the total number of cells per well the same for each condition (2K). The number of cells of MIA PaCa-2 and MSCs was varied in the different conditions to ensure that the total number of cells/well remained 2K, for example in 1:2 MIA PaCa-2 to MSCs ratio, 667 cells/well of MIA PaCa-2 and 1333 cells/well MSCs were seeded. From the images (Figure 3-6), it can be observed that both cell lines are retained in the spheroid over the course of the assay, proving that the lack of spheroid formation in the 1:2 and 2:1 conditions was as a result of the total number of the seeding density.

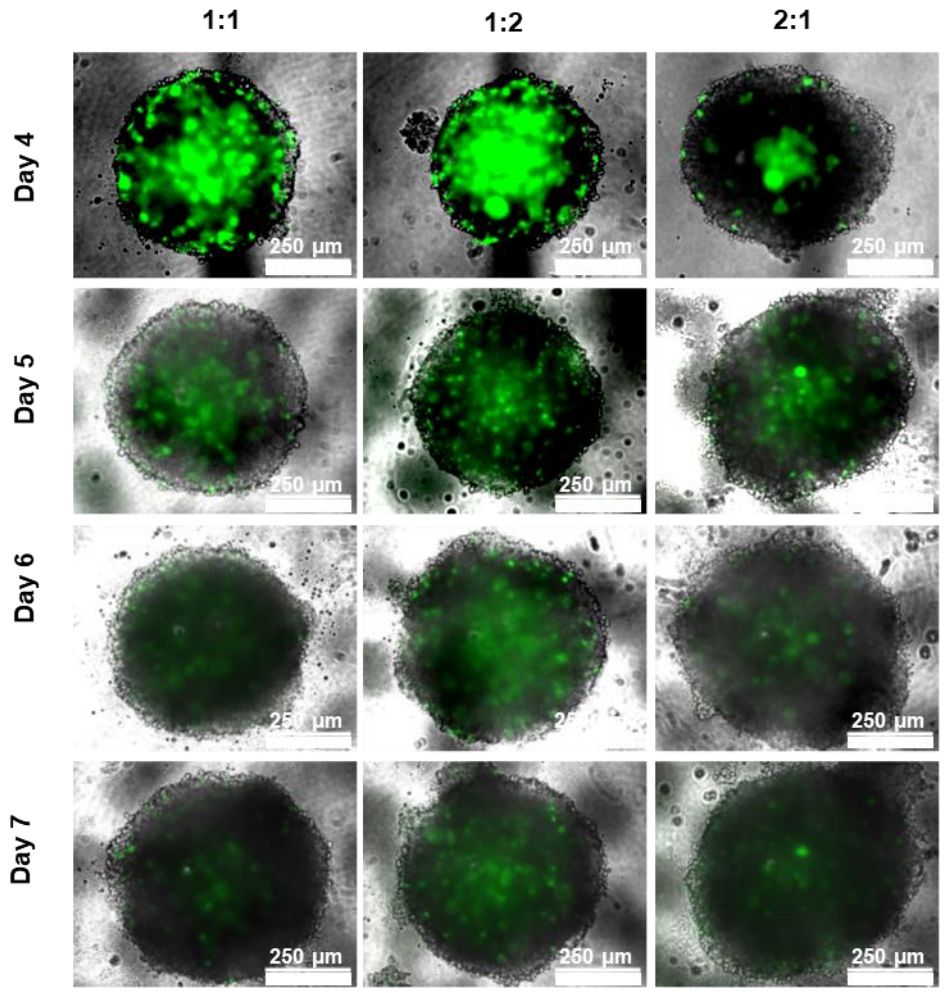


Figure 3-6 Representative widefield fluorescence microscope images (x10 objective) of MIA PaCa-2 cells co-cultured with MSCs at 1:1, 1:2 and 2:1 ratio, (N = 4). The total number of cells/well was kept constant (2K) to study the effect of total cell number on the formation of the co-cultured spheroids. Scale bar =250 µm.

Although 1:2 ratio showed better retention of MSCs (Figure 3-5), its inability to form intact spheroids and also to keep the number of MIA PaCa-2 cells constant between the monoculture and co-culture system (1K), 1:1 ratio was selected for the downstream experiments.

3.4 Conclusions

In this study, we have been able to show the ability of MIA PaCa-2 cells to form spheroids on day 3 of cell seeding with the liquid overlay method. Although there was constant growth in all cases, the different seeding densities exhibited differences in volume, and in percentage volume increase, over the course of the study. There was no significant difference in cell viability in the spheroid between the different seeding densities from day 3 to day 5. However, cell viability in 1K spheroids was found to be significantly higher than 4K on days 6 and 7. Microscope images of the spheroids showed the formation of a necrotic core in 4K spheroids on day 7. Based on these observations, 1K seeding was chosen for downstream studies of MIA PaCa-2 monoculture system.

The co-culturing assay showed that the total number of seeded cells per well had a significant difference in the formation of spheroids with no compact co-culture spheroids observed in 1:2 and 2:1 ratios (both 3000 cells/well). Therefore 1:1 ratio was chosen for subsequent co-culture experiments.

This part of the study thus demonstrated good evidence of MIA PaCa-2 spheroid formation. It also highlighted the importance of thorough characterisation of 3D cell culture models in order to optimise culturing conditions such as seeding density and cell viability to ensure effective *in vitro* screening of bioactive materials.

3.5 Chapter acknowledgements

I would like to thank Pamela Collier and Catherine Probert for the technical support and the periodic testing of the cells for mycoplasma contamination. I would also like to extend my gratitude to Amarnath Pal for the training in spheroid development and characterisation.

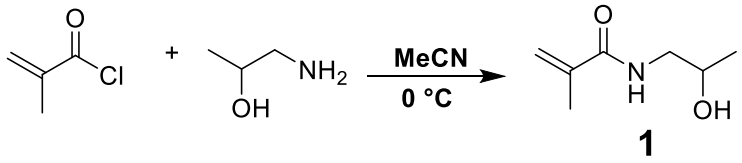
Chapter 4 Size effect on cellular uptake and *in vivo* distribution of non-degradable hyperbranched HPMA polymer

4.1 Introduction

The aim of this part of the thesis work was to investigate how molar masses, size and conformations of hyperbranched HPMA polymers influenced *in vitro* uptake and *in vivo* biodistribution for their subsequent use in the treatment of pancreatic cancer cells. The polymeric backbone was based on the clinically tested HPMA framework, as this has previously been shown to be well tolerated *in vivo* and to circulate well for extended times in the bloodstream following injection. A hyperbranched architecture was chosen as it was hypothesised to provide maximum loading of drugs on the polymer backbone without inducing significant changes in overall solubility. RAFT-based polymerisation techniques were used to provide control in (co-)monomer content and overall polymer molar mass.

4.2 Experimental

4.2.1 Synthesis of hyperbranched HPMA polymer

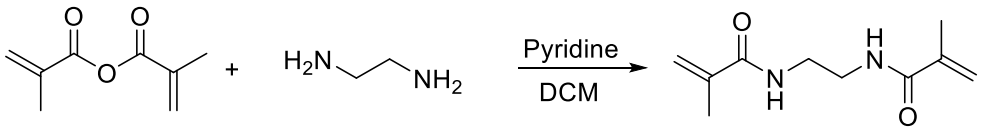


1

***N*-(2-Hydroxypropyl)methacrylamide) (HPMA) 1.**[206] Methacryloyl chloride (14.9 mL, 152.44 mmol) in 40 mL acetonitrile added dropwise over an hour to a solution of 1-amino-2-propanol in 85 mL acetonitrile at 0 °C under vigorous stirring. The reaction mixture was stirred at this temperature for a further 30 min. The precipitated 2-hydroxypropylammonium chloride was removed by filtration and the solvent under reduced pressure. The product (yield = 65 %) was purified by repeated crystallisation from acetone (mp = 58 - 80 °C) and stored at 4 °C. **^{1}H NMR** (400 MHz, $CDCl_3$) δ 6.35 (s, 1H), 5.72 (d, *J* = 1.9 Hz, 1H), 5.35 (d, *J* = 2.7 Hz, 1H) 3.95

(d, *J* = 29.6 Hz, 1H), 3.50 (d, *J* = 23.5 Hz, 1H), 3.17 (d, *J* = 26.8 Hz, 1H), 1.97 (dd, *J* = 1.6, 0.9 Hz, 3H), 1.20 (d, *J* = 6.3 Hz, 3H). **^{13}C NMR** (101 MHz, $CDCl_3$) δ 169.88 (C=O), 140.03 (C-CH), 120.47 (HC=CH), 67.54 (CO), 47.56 (CH_2), 21.31 (CH_3), 19.04 (CH_3). **FT-IR**: v (cm^{-1}) = 3263, 3089, 2974, 1654, 1614, 1545. These data correspond with reported literature on the synthesis of HPMA monomer.[206, 207, 342, 343]

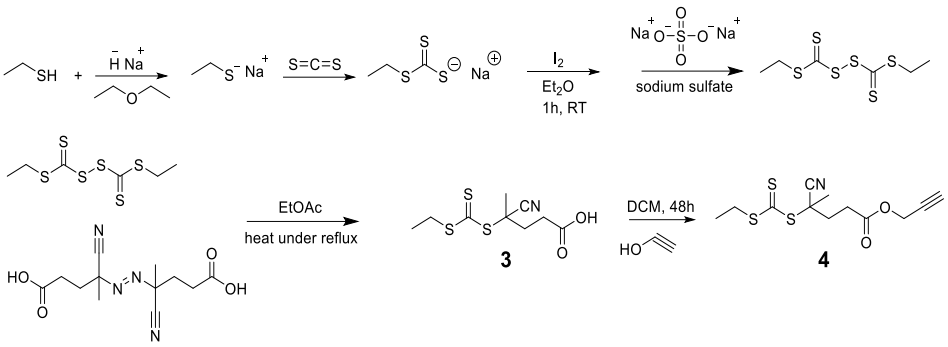
Ethylene Dimethacrylamide (EDMA) 2.



2

A solution of methacrylic anhydride (18 mL, 119.7 mmol) in DCM was added dropwise under vigorous stirring to an ice-cold suspension of ethylenediamine (2 mL, 29.9 mmol) and pyridine (4.8 mL, 59.83 mmol) in 10 mL DCM over 1 h. The reaction mixture was stirred overnight at room temperature. The solid was filtered off and the organic phase washed with deionised water (x3), acidic water (HCl,10 %) (x3), deionised water (x3), a solution of sodium bicarbonate in water (x3) and deionised water (x3). The solvent was removed under reduced pressure using rotary evaporator and oil left at -20 °C for the precipitate to form. The precipitate was further purified *via* precipitation from ethyl acetate to yield an off-white solid (72 %). **^{1}H NMR** (400 MHz, $CDCl_3$) δ 6.62 (s, 2H), 5.74 (s, 2H), 5.35 (s, 2H), 3.55-3.47 (m, 4H), 1.96 (s, 6H). **^{13}C NMR** (101 MHz, $CDCl_3$) δ 170.06 (C=O), 139.81(C=CH), 120.72 (HC=CH), 40.90 (CH_2), 19.02 (CH_3). **FT-IR:** v (cm^{-1}) = 3328, 1652, 1611, 1215. The data presented correspond to reported literature on ethylene dimethacrylamide synthesis.[344]

4-**Cyano-4-(ethylsulfanylthiocarbonyl) sulfanyl pentanoic acid** (CEPA) **3**.



Ethanethiol (4.72 g, 75.97 mmol) was added over 10 min to a stirred suspension of sodium hydride (60 wt. % in mineral oil; 3.17 g, 79.14 mmol) in diethyl ether (150 mL) at 0 °C and the reaction stirred for a further 10 min. Carbon disulfide (6.03 g, 79.14 mmol) was then added slowly to the reaction mixture and crude sodium s-ethyl trithiocarbonate collected by filtration and resuspended in diethyl ether (100 mL). The suspension was treated with the portion-wise addition of solid iodine (6.3 g, 24.82 mmol) and the reaction mixture stirred at room temperature for 1 h. The reaction was filtered after 1 hour and washed with aqueous sodium thiosulfate and dried over sodium sulfate. Crude *bis*(ethylsulfanylthiocarbonyl) disulfide was isolated by rotary evaporation. 4'4'-Azobis(4-cyanovaleric acid) (7.25 g, 25.86 mmol) and *bis*(ethylsulfanylthiocarbonyl) disulfide (4.73 g, 17.24 mmol) were dissolved in ethyl acetate (130 mL) and refluxed for 18 h. The reaction mixture was concentrated on the rotary evaporator and purified by silica flash column chromatography (50:50 hexane: ethyl acetate mobile phase) to yield **4-cyano-4-(ethylsulfanylthiocarbonyl) sulfanyl pentanoic acid** (CEPA) as an orange-red oil (81 %). **^{1}H NMR** (400 MHz, $CDCl_3$) δ 3.38 (q, *J* = 7.4 Hz, 2H), 2.76 – 2.68 (m, 2H), 2.63 – 2.52 (m, 1H), 2.43 (ddd, *J* = 14.2, 9.3, 6.9 Hz, 1H), 1.91 (s, 3H), 1.39 (t, *J* = 7.4 Hz, 3H). **ESI-TOF-MS**: m/z: $[M + H]^+$ $C_9H_{13}NO_2S_3$ calculated, 263.01; found, 264.02. The data is in agreement with a previously reported synthesis of CEPA.[345]

Alkyne-terminated RAFT agent (Alkyne-CTA) 4.

CEPA (7.42 g, 28.17 mmol), propargyl alcohol (4.1 mL, 70.43 mmol), and 4-dimethylaminopyridine (DMAP) (0.69 g, 5.63 mmol) were dissolved in 300 mL of DCM in a 500 mL round bottom flask. The flask was sealed with a rubber septum and bubbled with argon for 30 min in an ice bath. Following this, 1-ethyl-3-(3-dimethylaminopropyl)carbodiimide (EDC) (10.8 g, 56.34 mmol) in 30 mL of DCM was added dropwise into the reaction mixture. The reaction was stirred in the ice bath for 2 hours and then room temperature for 48 hours. After 48 hours, the mixture was filtered to remove insoluble precipitates and washed with water (100 mL x2) and brine (100 mL x2). The organic phase was dried over anhydrous $MgSO_4$. The organic solvent was removed under reduced pressure and the resulting orange oily compound purified by silica gel flash chromatography, (using Pet. Ether/ethyl acetate) at a gradient from 9/1 to 6/4 as the mobile phase to yield the pure product, an orange viscous liquid (53 %). **^{1}H NMR** (400 MHz, $CDCl_3$) δ 4.72 (d, *J* = 2.5 Hz, 2H), 3.36 (q, *J* = 7.4 Hz, 2H), 2.72-2.65 (m, 2H), 2.61 – 2.52 (m, 1H), 2.47 – 2.37 (m, 1H), 1.89 (s, 3H) 1.37 (t, *J* = 7.4 Hz, 3H). **^{13}C NMR** (101 MHz, $CDCl_3$) δ 216.72 (CS), 170.76 (CO), 119.00 (CN), 75.39 (CH), 52.58 (CH_2), 46.35 (C), 33.75 (CH_2), 31.49 (CH_2), 29.66 (CH_2), 24.95 (CH_3), 12.86 (CH_3). **ESI-TOF-MS**: m/z: $[M + Na]^+$ $C_{12}H_{15}NO_2S_3$ calculated, 324.03; found, 324.02. The data reported above is in agreement with a previously reported synthesis of the Alkyne-CTA.[346]

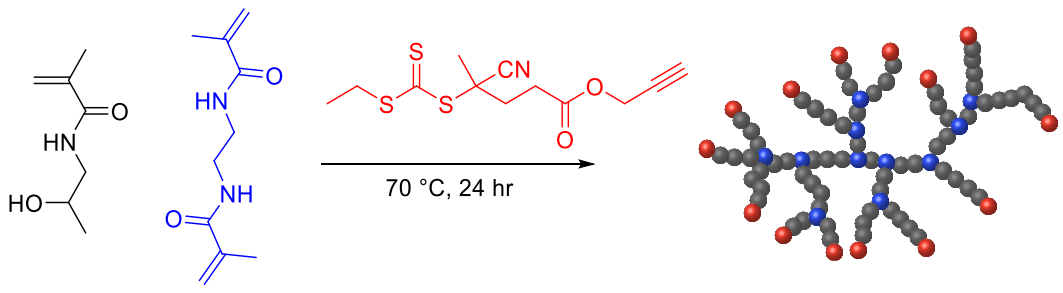


Figure 4-1 Schematic presentation of hyperbranched HPMA polymer synthesis using RAFT polymerisation technique.

Synthesis and purification of HB-HPMA polymer 4. Hyperbranched (HB) polymers were synthesised through RAFT polymerisation, incorporating an alkyne-

CTA and ethylene dimethacrylamide as branching agent, with azobisisobutyronitrile (AIBN) as the radical initiator. HPMA (200 mg, 1.40 mmol), AIBN (2.29 mg, 0.014 mmol), EDMA (13.71 mg, 0.07 mmol) and Alkyne-RAFT agent (21.05 mg, 0.07 mmol) were dissolved in 1:1 ratio of *N,N*-dimethylacetamide (DMAc) and water in a 2 mL tube equipped with a magnetic stirrer bar. The tube was sealed, and the reaction mixture purged with argon for 30 minutes. The vial was placed in an oil bath at 70 °C for 24 h.

After 24 h, the polymer was precipitated dropwise into excess acetone three times, followed by dissolving in Milli Q water and dialysing for 48 hours in a 3.5 kDa molecular weight cut-off pleated snakeskin tubing and subsequently lyophilised.

Table 5 Reaction conditions used for the synthesis of the three hyperbranched HPMA polymers

Polymer	HPMA (mg)	EDMA (mg)	RAFT (mg)	Initiator (mg)	Solvent (mL)	Time (hr)	% conversion
HPMA-HB-7	200	13.71	21	2.3	**1.6**	24	90
HPMA-HB-20	200	13.71	21	2.3	**1.2**	18	93
HPMA-HB-40	200	13.71	21	2.3	**0.8**	14	97

4.2.2 Cyanine 5 (Cy5) conjugation to HB-HPMA polymers

HB-HPMA-Cy5 5. Briefly, 23 mg (0.005 mmol, alkyne unit) of control hyperbranched polymer and 5.6 mg (0.01 mmol) of Cy5-azide were added into the reaction vessel in 2 mL of DMSO. A 100 µL solution of ascorbic acid (2.3 mg/mL) was added and the reaction was purged with nitrogen and left stirring for 30 min. Next, 100 µL of copper (II) sulfate solution (2.9 mg/mL), was added into the reaction and the mixture was stirred overnight at room temperature. The polymer was purified as above to

remove any unreacted dye and subsequently lyophilised. The conjugation efficiency was determined by UV-Vis spectroscopy.

4.2.3 Conjugation of deferoxamine chelator to Cy5 labelled HB-HPMA polymer

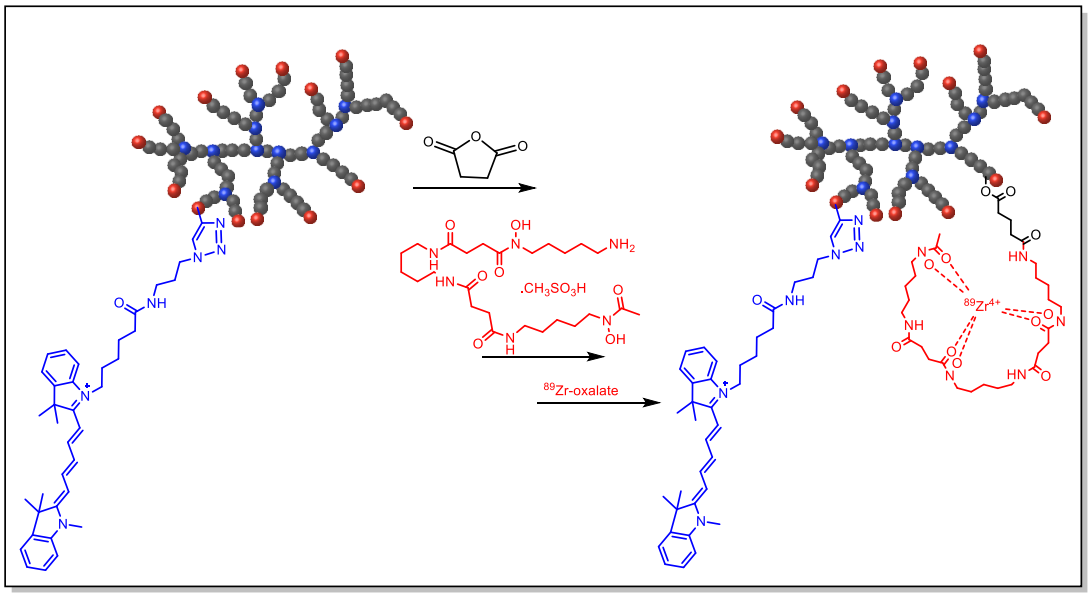


Figure 4-2 Schematic representation of the attachment of the ^{89}Zr chelator, deferoxamine (DFO) to a Cy5-labelled HB-HPMA polymer to enable ^{89}Zr PET imaging.

Synthesis of HB-HPMA acid 6. HB-HPMA (50 mg, 0.35 mmol OH residues) was dissolved in anhydrous pyridine (1 mL) in a test tube. Succinic anhydride (70 mg, 0.70 mmol) was added to the reaction mixture and the solution stirred to allow esterification to proceed at room temperature for 24 hours. The reaction mixture was precipitated into diethyl ether (5 mL); solids re-dissolved in THF, and precipitation repeated into diethyl ether (x3). ^{1}H NMR (400 MHz, D_2O) δ 8.00-7.35 (s, 1H), 5.11-4.87 (s, 1H, conjugated CH), 4.05-3.84 (s, 1H, unconjugated CH), 3.64 - 2.95 (2H), 2.70 (s, 4H), 2.33 - 0.70 (broad, m, 8H, CH_2 and CH_3 of Polymer backbone and $CHCH_3$).

HB-HPMA-DFO synthesis 7. HB-HPMA acid (20 mg, 0.07 mmol acid residues), Deferoxamine mesylate (18.21 mg, 0.03 mmol), triethylamine (TEA) (2.81 mg, 0.03 mmol) and DMAP (1.69 mg, 0.01 mmol) were dissolved in DMSO (1 mL) in a reaction vessel and stirred for 30 min. EDC (15.95 mg, 0.08 mmol) in 1 mL DMSO

was added dropwise to the reaction and stirred for 24 hours. The reaction was diluted in Milli Q water and dialysed for 72 hours in a 3.5 kDa molecular weight cut-off pleated snakeskin tubing and subsequently lyophilised. The ^{1}H NMR (Figure 4-29, SI) spectrum of the resultant polymer shows the characteristic deferoxamine resonance with varied deferoxamine units per HB-HPMA polymer.

^{89}Zr labelling. ^{89}Zr oxalate in 1 M oxalic acid (Perkin Elmer) (91 µL) was neutralised with 1 M Na_2CO_3 (78 µL) solution and 33 µL aliquots of the mixture added to solutions of the Cy5 labelled **HB-HPMA-DFO** polymers (146 µg) in 0.5 M HEPES buffer to give 300-fold excess of the polymers to ^{89}Zr. The reaction mixtures were stirred at room temperature for 2 hours to allow the labelling to proceed. ^{89}Zr-labelled polymers were purified, and buffer exchanged into phosphate-buffered saline using Zeba Spin Desalting Columns (7 kDa MWCO, Thermo Fisher Scientific). To determine the radiochemical yields, 1 µL of each solution were taken and spotted on a thin layer chromatography paper (Agilent iTLC-SG Glass microfiber chromatography paper impregnated with silica gel) and eluted in 50/50 H_2O/EtOH with or without 50 mM diethylenetriaminepentaacetic acid (DTPA). Control experiments were conducted to monitor the elution behaviour of unbound ^{89}Zr for quality control. Plates were imaged on a Bruker *In Vivo* MS FX Pro imaging system using a radioisotopic phosphor screen.

4.2.4 Cell culture

Conditions for culturing cells used in this study are as described in 3.2.

4.2.5 *In vitro* 2D cell viability assay of MIA PaCa-2 cell line

The cytotoxicities of the HB-HPMA polymers were assessed over 72 h using the trypan blue dye exclusion test for cell viability. MIA PaCa-2 cells were cultured in 6-well plates at a seeding density of 2 x 10^5 cells/well for 24 h to allow cells to attach. The cells were then treated with the HB-HPMA polymers dissolved in DMEM culture

medium at the indicated concentrations. After 72 h incubation time, the medium was removed, cells treated with 2 mL phenol red-free TrypLe Express Enzyme (1X) for approximately 5 mins. Cells were collected, centrifuged and resuspended in fresh medium and an equal volume of 0.4 % trypan blue added to each cell suspension. The approximate number of live cells were counted on a TC20 automated cell counter. Percentage cell viability was calculated as follows[347]:

$$\% \text{ viable cell} = (N_T/N_c) \times 100$$

where N_T is the total viable cell after treatment and N_c is the total viable cell of control.

4.2.6 *In vitro* 2D cellular uptake assay in MIA PaCa-2 cell line

The uptake of Cy5-labelled HB-HPMA was studied using the 2D cell culture model. Briefly, cells were cultured in 6-well plates at a seeding density of 2.5 x 10^5 cells/well for 24 h. The medium was replaced with 200 µg/mL solution of Cy5-labelled polymer and the plate incubated for 1 h. The cells were then washed thrice with fresh medium and Hoechst 33342 stain applied and incubated for 30 minutes. Uptake of the polymer by cells was visualised using a Nikon Ti Eclipse inverted microscopy and quantified using flow cytometry.

4.2.7 *In vitro* 3D cell viability assay of MIA PaCa-2 cell line

3D monoculture MIA PaCa-2 (1000 cell/well) spheroids were prepared using a 3D multicellular tumour spheroids (MCTS) model as described in 3.2.2. The three HB-HPMA polymers were prepared as solutions in media at x2 the concentration of 2D cell culture. 100 µL of the sample was added to each well, taking the total volume to 200 µL and the plate incubated for 72 h. 100 µL of fresh complete growth medium was also added to control spheroids to keep the volume of all the wells at 200 µL. Images were taken immediately prior to treatment and every day thereafter for 3 days for spheroid volume analysis.

4.2.8 CellTiter-Glo® 3D cell viability assay in MIA PaCa-2 cell line

The CellTiter-Glo® 3D cell viability assay determines cell viability through quantification of adenosine triphosphate (ATP) levels as a marker of metabolically active cells. 72 h post-treatment of the spheroids, the plate was equilibrated to room temperature for approximately 30 minutes. 100 µL of cell culture medium was taken from each well using a multichannel pipette and the same volume of assay-ready CellTiter-Glo® solution added. The contents of the plate were mixed vigorously for 5 minutes to induce cell lysis. The plate was incubated at room temperature for an additional 25 minutes and analysed for luminescence.

4.2.9 *In vitro* 3D cell uptake assay in MIA PaCa-2 cell line

The cells were incubated for 4 days during which time they aggregated and formed spheroids with diameters of approximately 500 µm (mono-culture) and 620 µm (co-culture). 100 µL of a 400 µg/mL Cy5 labelled HB-HPMA polymers were added to the spheroids (n = 4), taking the concentration to 200 µg/mL and the volume of each well to 200 µL. The plate was then incubated for 2 h, after which the spheroids were washed (x3) with fresh medium and Hoechst 33342 stain applied and incubated for 2 hours. Uptake of the polymer by cells was visualised using a Nikon Ti Eclipse inverted microscope and quantified using flow cytometry (n = 10). 3D MIA PaCa-2 mono and co-culture (with MSCs) spheroids were used for this experiment. Co-cultured MIA PaCa-2 and MSCs 3D spheroids were prepared as described in 3.2.2 with 1000 cells/well each (total cells per well = 2000).

4.2.10 Spheroid dissociation

After polymer uptake and Hoechst 33342 staining, the spheroids were dissociated for uptake quantification using flow cytometry. The spheroids (n = 10 for each polymer) were transferred into 15 mL falcon tubes and allowed to settle to the bottom. The medium was subsequently discarded without disturbance to the

spheroids and washed with PBS (x3) and incubated with accutase (1 mL) for 5 min at 37 °C. This was followed by mechanical dissociation with a pipette to form a single-cell suspension. 2mL of complete growth medium was added to the dissociated cells, centrifuged at 300 xg for 5 min and re-suspended in 1 mL pre-warmed complete medium ready for flow cytometry analysis.

4.2.11 Cytocompatibility evaluation in macrophages

The lactate dehydrogenase (LDH) release assay (Sigma Aldrich, TOX7 kit) and PrestoBlue™ cell viability assay (Thermo Fisher Scientific) were performed to assess particle cytotoxicity. RAW 264.7 cells were seeded at $1x10^4$ cells per well in 96 well plates and cultured for 24 hours prior to assaying. HB-HPMA polymers were exposed to cells for 24 hours and applied in 100 µL phenol red-free DMEM containing 10 % (v/v) FBS and 2 mM L-glutamine. Triton X-100 applied at 1 % (v/v) in phenol red-free medium was used as a cell death (positive) control and a vehicle control containing no nanoparticles used as a negative control. Following exposure, 50 µL of supernatant was collected per well for analysis of LDH content. Cells were then washed twice with warm PBS and 100 µL 10 % (v/v) PrestoBlue™ reagent diluted in phenol red-free medium applied per well for 60 minutes. The resulting fluorescence was measured at 560/600 nm (λex/λem). Relative metabolic activity was calculated by setting values from the negative control as 100 % and positive control values as 0 % metabolic activity. Assessment of LDH release was performed according to the manufacturer's instructions and involved adding 100 µl LDH reagent to collected supernatant samples and incubating at room temperature shielded from light for 25 minutes. Absorbance was then measured at 492 nm. Relative LDH release was calculated with the negative control absorbance at 492 nm taken as 0 %, and the positive control assumed to cause total cell lysis, as 100 %.

4.2.12 Macrophage uptake of particles assessed by spectrophotometry

RAW 264.7 macrophages were plated in 12 well plates at a seeding density of $1.2x10^5$ cells per well and cultured for 48 hours. Culture medium was then removed, and 1 mL of nanoparticles applied in phenol red-free medium. The time-dependent uptake was assessed with a polymer concentration of 50 µg/mL. Following exposure, polymer solutions were removed, and cells washed three times with ice-cold PBS. Five hundred microlitres of 1 % (v/v) Triton X-100 solution applied in PBS was then added per well for 10 minutes at 37°C. To assess nanoparticle uptake, 100 µL of the resulting solution was collected per well and transferred to 96 well plates for the measurement of fluorescence at 640/680 nm (λex/λem). Quantification of nanoparticles uptake was achieved *via* calibration curves of known nanoparticle concentrations diluted in 1 % (v/v) Triton X-100 in PBS solution. Values were normalised to viable cell number per well determined by the trypan blue exclusion test and cell counting on a haemocytometer.

4.2.13 Statistical Analysis

Values obtained from the experiments were analysed in GraphPad Prism 7 software using one-way or two-way analysis of variance (ANOVA). In all cases, differences were considered significant when $p^{***} < 0.001$, $p^{**} < 0.01$, and $p^{*} < 0.05$.

4.2.14 *In vivo* biodistribution studies

In vivo biodistribution experiments were performed to assess distribution, organ accumulation and clearance of the different sized **HB-HPMA** polymers.

4.2.14.1 Fluorescent biodistribution study

The experiments were conducted under the UK Home Office Licence number PPL P435A9CF8. In addition, LASA good practice guidelines, FELASA working group on pain and distress guidelines and ARRIVE reporting guidelines were also followed. In

these studies, 8-9-week-old female immunodeficient CD-1 NuNu mice purchased from Charles River UK were maintained in Individually Ventilated Cages (Tecniplast UK) within a barriered unit, illuminated by fluorescent light set to give a 12-hour light-dark cycle (on 07.00, off 19:00). The air temperature range of the room was maintained at 21 ± 2 ºC with a humidity of 55 % ± 10 %. During the study, the mice were housed in social groups, 3 per cage, with irradiated bedding and autoclaved nesting materials and environmental enrichment (Datesand UK). Sterile irradiated 5V5R rodent diet (IPS Ltd, UK) and autoclaved water were offered *ad libitum*. The condition of the animals was monitored by an experienced technician throughout the study. The mice were randomly assigned to the study groups (6 mice per polymer) by weight after a week's acclimatisation. No power calculation was required for a simple biodistribution assay. After acclimatisation, the mice were warmed in a thermostatically controlled heating box (Datesand UK) and injected intravenously *via* the tail vein with 100 µL of a 500 µg/mL solution of the relevant polymer in PBS. There were no adverse effects observed post-injection and over the course of the study. The concentrations of the experimental formulations were determined from a balance of non-toxicity from *in vitro* analysis as well as sufficient fluorescent intensity for imaging *in vivo*. Images were taken at 1 hr, 4 hrs and 24 hrs post-injection and prior to each study time point, the mice were anaesthetised with an injectable anaesthetic combination (Anaestemine [ketamine]/Sedastart [medetomadine], Animalcare Ltd. UK). Two mice in each group were culled by cervical dislocation, organs dissected out, and imaged *ex vivo* at these time points. The other mice were then allowed to recover from the anaesthetic with appropriate post-procedural monitoring and therapy; including placing mice on a heat pad and provided fluid replacement *via* wet mash once awake. An aliquot (25 µL) of urine along with the excised organs (kidney, liver, spleen, pancreas, lung, heart, bladder, brain and subiliac lymph nodes) were imaged. All images were collected using the IVIS® Spectrum imaging system, PerkinElmer (MA, USA) and fluorescent signals were

quantified using Regions of Interest (ROIs) and quantified as photons emitted using Living Image/Igor Pro Software (Caliper Life Sciences).

4.2.14.2 PET-CT biodistribution study in tumour naïve and tumour bearing mice

Animals. The animal studies were performed in accordance with guidelines of the Animal Ethics Committee of The University of Queensland (UQ), and Australian Code for the Care and Use of Animals for Scientific Purposes for PET-CT biodistribution study. Mice were anaesthetised using 2 % isofluorane in O_2 for all injection and imaging procedures throughout. Female balb/c NuNu mice (approximately 8 weeks of age) were used for both biodistribution studies. Mice in the tumour bearing study were injected (27 G needle, 50 µL PBS) with 2 x 10^6 MIA PaCa-2 cells in the mammary fat pad. Tumours were allowed to develop for 4 weeks before polymer administration at which time they were approximately 5 mm in diameter.

PET-CT imaging. A Siemens Inveon PET-CT scanner with physiological monitoring achieved using a respiratory probe (BioVetTM system, m2m Imaging, Australia) was used for the PET-CT imaging studies. For biodistribution studies, anaesthetized mice were injected with the relevant ^{89}Zr-labelled polymer (2-3 MBq activity per mouse, 150 – 200 µL phosphate-buffered saline). At 24 hours post-injection, the mice were anaesthetised, positioned on the scanner bed and moved to the PET acquisition position and images acquired using 30-90 minutes static acquisitions. Further PET scans were collected on days 2, and 5 for tumour naïve mice studies and days 2, 3, 4, 6 and 8 for tumour bearing mice studies after injection of the radiotracer. Following each PET acquisition, micro-CT scans of the mice were acquired through an x-ray source with a set voltage and current of 80 kV and 500 µA respectively for anatomical co-registration. The scans were performed using 360° rotation with 120 rotation steps with a low magnification and a binning factor of

four. The exposure time was 230 ms with an effective pixel size of 106 µm. The total CT scanning process took approximately 15 minutes and the images were reconstructed using Feldkamp reconstruction software (Siemens). The PET images were reconstructed using an ordered-subset expectation maximization (OSEM2D) algorithm and analysed using the Inveon Research Workplace software (IRW 4.1) (Siemens) which allows fusion of CT and PET images and definition of regions of interest (ROIs). To ensure good overlap of the organs of interest, the CT and PET datasets of each individual animal were aligned using IRW software (Siemens). Three dimensional ROIs were placed within the whole body, as well as all the organs of interest, such as heart, kidney, lungs, bladder, liver, spleen, intestines and tumour, using morphologic CT information to delineate organs. Using a conversion factor obtained by scanning a cylindrical phantom filled with a known activity of ^{89}Zr, the activity per voxel was converted to nci/cc to account for PET scanner efficiency. Activity concentrations were then expressed as a per cent of the decay-corrected injected activity per cm^3 of tissue that can be approximate as percentage injected dose/g (%ID/g).

^{89}Zr-PET imaging *in vivo* biodistribution. PET-CT images were acquired of mice until days 5 (non-tumour bearing) and 8 (tumour bearing) post particle injection. Region-of-interest (ROI) analysis of images allowed for assessment of *in vivo* biodistribution at each time point.

***Ex vivo* biodistribution by λ scintillation counter.** The mice were injected intravenously via the tail vein with 100 µL 1 % (w/v) Evans blue in phosphate-buffered saline using 29 G needle following the PET-CT image acquisition on day 5 and 8 for tumour naïve and tumour bearing mice respectively. The mice were then euthanised by cervical dislocation, blood sampled, and tissue collected and cleaned of excess blood and weighed for ex vivo analysis. Radioactivity in the tissues was measured using a PerkinElmer 2480 Automatic Gamma Counter after calibration

with known ^{89}Zr samples. The measured activity presented as %ID/g based on injected activities.

4.3 Results and discussion

4.3.1 Synthesis and physical characterisation of HB-HPMA polymers

The aim of this work was to investigate the effect of **HB-HPMA** polymer size on the performance of the biomaterial *in vitro* and *in vivo*. To achieve this, the HB polymers were synthesised using the same starting materials but varying the synthetic conditions (Table 5), to provide a water-soluble and biocompatible final polymeric architecture, only differing by physical properties such as molecular weight and particle size. A hyperbranched architecture was chosen for this work due to the presence of abundant functional groups for high drug loading and the demonstrated potential for tumour targeting and *in vivo* particle uptake.[225, 348] The syntheses of the HB polymers were achieved through the use of RAFT-based polymerisation technique, utilising an alkyne terminated RAFT agent (Figure 4-24 and Figure 4-25, SI), a bifunctional ethylene dimethacrylamide (EDMA) monomer (Figure 4-22 and Figure 4-23, SI) and AIBN as the initiator as previously described.[349]

HPMA, the functional monomer of the polymerisation, was synthesised according to the previously described procedure by Kopeček *et al*. and was obtained in a 65 % yield after purification by recrystallisation (Figure 4-3 and Figure 4-21, SI).[206]

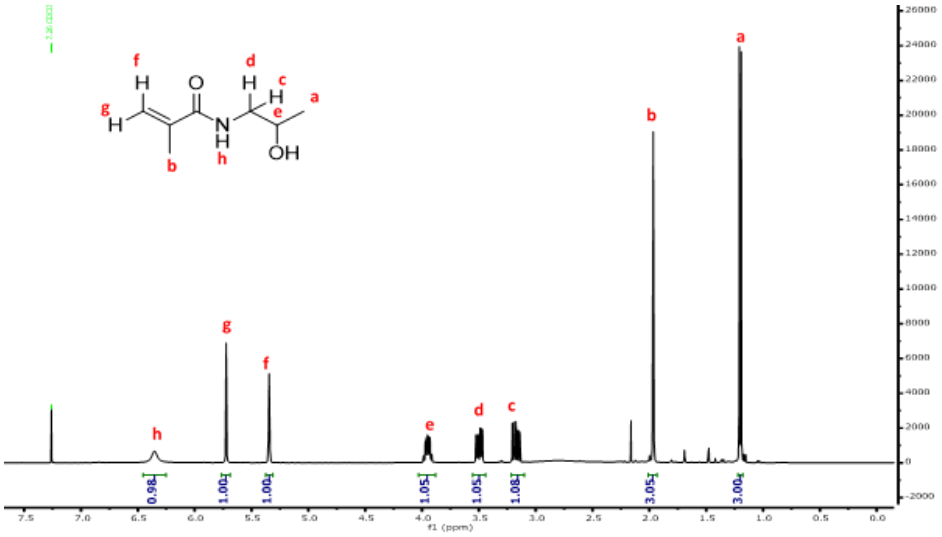


Figure 4-3 ^{1}H NMR spectrum of HPMA monomer in $CDCl_3$.

Finally, a bifunctional methacrylamide unit was incorporated into the polymerisation to induce branching in the macromolecules to yield the unimolecular globular particles.

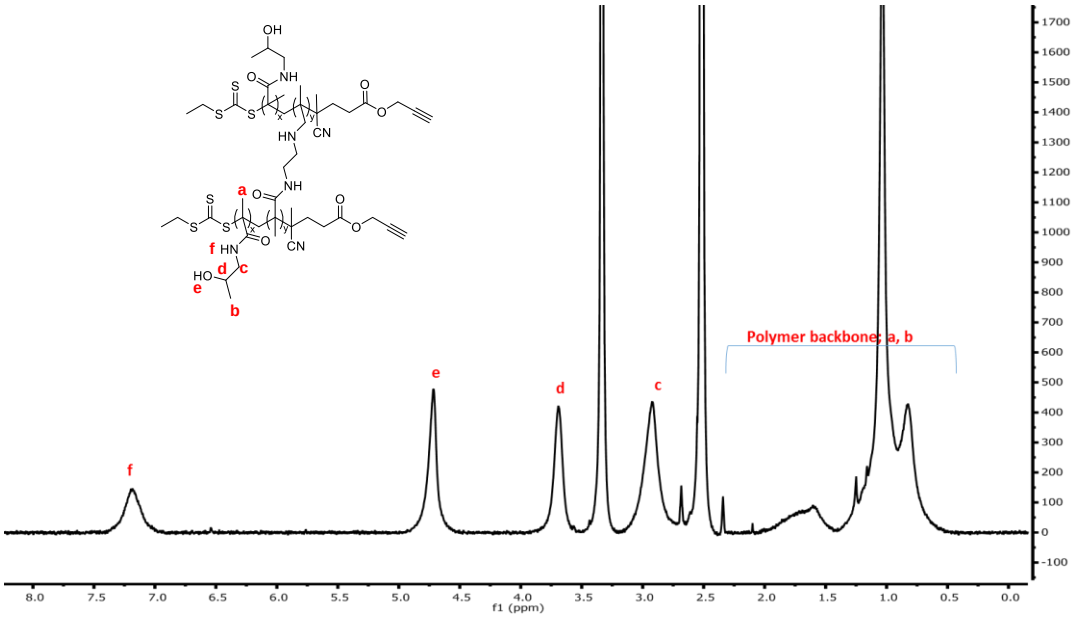


Figure 4-4. Representative ^{1}H NMR spectrum of hyperbranced HPMA polymer (HB-HPMA) in DMSO-d_6.

The bifunctional monomer, EDMA, was synthesised through a reaction of methacrylic anhydride and ethylenediamine in a 1:4 ratio to yield (72 %) the pure monomer. Varying monomer conversion was achieved for the synthesised polymers (90 - 97 %). The synthetic route to generate the **HB-HPMA** polymers is depicted in

Figure 4-1 and the resultant hyperbranched polymers were characterised for their purity (^{1}H NMR, Figure 4-4), molecular weight (aqueous GPC), hydrodynamic radius (DLS, Figure 4-5A), and physical size and morphology (TEM, Figure 4-5B). All the polymers were confirmed to contain no detectable residual monomer due to the absence of vinyl peaks at 5.72 and 5.32 ppm as well as the characteristic broadening of monomer resonances in ^{1}H NMR spectrum (Figure 4-4), indicative of polymeric materials.

Table 6 Physical characterisation of varying size HB-HPMA polymers.

Polymer	HB-HPMA-7	HB-HPMA-20	HB-HPMA-40
M_n by GPC* (g/mol)	2 x 10^4 ± 4 %	1 x 10^5 ± 1 %	2 x 10^6 ± 1 %
Đ	2.1 (±1.1)	2.5 ± 0.5	3.1 ± 1.0
Size by DLS (nm)	7 ±1	20 ±3	40 ± 3
ζ-potential (mV)	-6.9 ± 5.2	-6.3 ± 3.3	-12.7 ± 3.1
Size by TEM (nm)	7.3 ± 1.7	14.8 ± 1.9	30.2 ± 9.5
Cy5/HB polymer (UV-Vis) wt%	5.7	5.1	2.2

*dn/dc = 0.1589.

Monomer conversion was calculated from the ^{1}H NMR spectrum of the crude product by comparing the ratio between the vinyl protons and the polymer resonance at 3.82-3.57 ppm.

The molecular weight analysis using the multi-angle laser light scattering of the GPC (dn/dc = 0.1589 g/mL) was taken as the absolute molecular weight of each of the synthesised polymers due to the complexity of the final architecture. In addition, the peaks corresponding to the alkyne-RAFT agent overlapped with the polymer peaks

and hence, it was not possible to estimate the M_n of the polymer using NMR spectroscopy. As expected, the molecular weight of the polymers increased with increasing monomer concentration in the reaction mixture, i.e., **HB-HPMA-7**, **HB-HPMA-20** and **HB-HPMA-40** had molecular weights of 15 kDa, 110 kDa and 1,800 kDa respectively.[350] In addition to this, the polydispersity of the polymers as measured by GPC, also increased with increasing concentration and hence the size of the polymer. Due to the randomly induced branching in the hyperbranched system compared to dendrimers, these systems often exhibit relatively high polydispersity.[221] However, as can be seen from the data acquired, there also appeared to be a concentration effect whereby high monomer concentration at the start of the reaction led to increased monomer conversion which in turn led to a potential loss of control over the polymerisation increasing the polydispersity.[225]

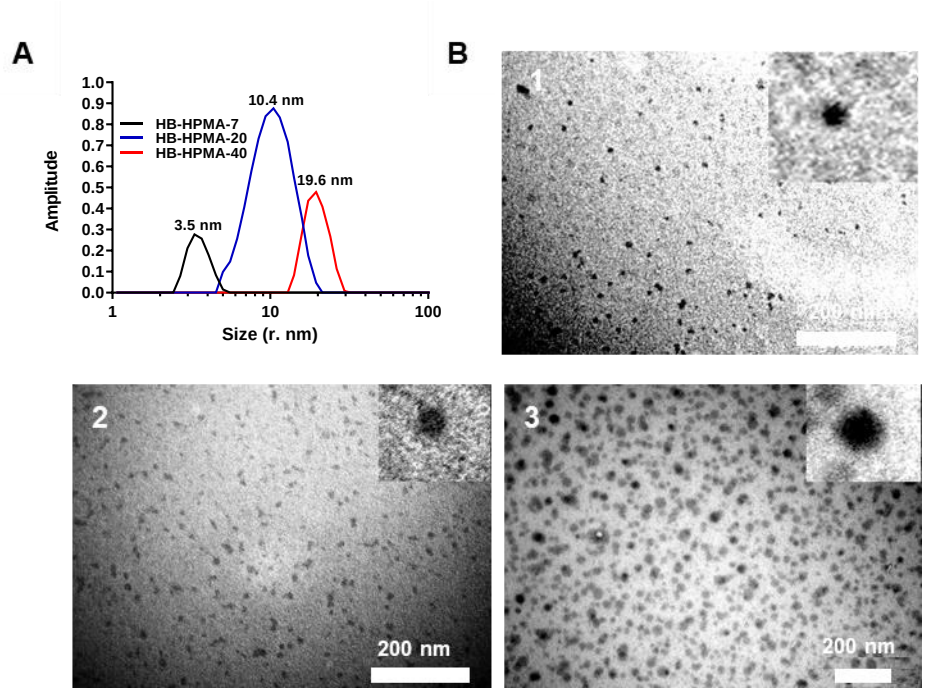


*Figure 4-5 A) Dynamic light scattering measurements of the different size polymers. B) Representative transmission electron microscopy images (scale bar = 200 nm) of (1) **HB-HPMA-7**, (2) **HB-HPMA-20** and (3) **HB-HPMA-40.***

The size of these polymers was analysed using DLS, Figure 4-5. The three polymers showed different hydrodynamic diameters of approx. 7 nm, 20 nm and 40

nm (**HB-HPMA-7**, **HB-HPMA-20** and **HB-HPMA-40** respectively). In addition to DLS, the sizes of the polymers, as well as the morphology, were evaluated using transmission electron microscopy (TEM). From the images (Figure 4-5), it is evident that the polymers exist in a distinct globular structure with sizes differing from those seen in the DLS analysis. The reason for the observed differences is because DLS samples are in contact with a solvent, meaning the particles are measured in motion, therefore, factors such as the liquid layer surrounding the particles are important. In addition, DLS algorithms assume that the particles are spherical and non-interacting, thus

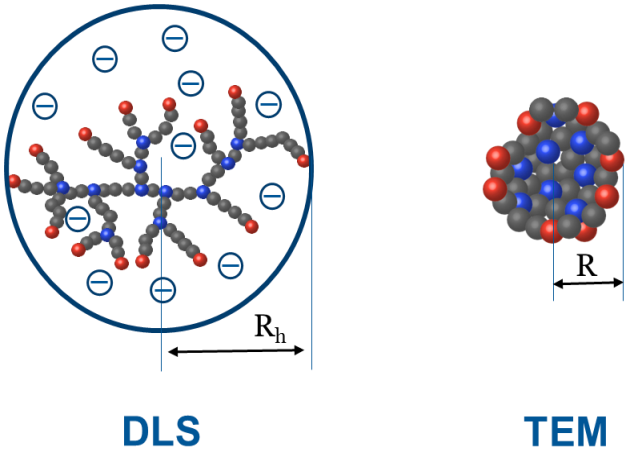


Figure 4-6 Schematic depiction of size differences observed by DLS and TEM.

the radii obtained may not reflect any anisotropy in polymer architecture. Samples in TEM are free of solvent and hence this liquid layer effect is not observed (Figure 4-6). This, therefore, means the number distribution sizes obtained from TEM measurements are smaller than the intensity distribution from DLS, however, these two measurements provide complementary information regarding particle sizing. The physical properties of the final hyperbranched polymers are summarised in Table 6. The data presented here, therefore, showed the successful synthesis and characterisation of a range of **HB-HPMA** polymers with different molecular weights and sizes. These materials were then investigated for the effect these characteristics would have on their *in vitro* and *in vivo* behaviour. In order to provide

a fluorescence label for the biological screening of these materials, Cy5 azide was conjugated to the polymer *via* CuAAC (copper catalysed azide-alkyne 1,3-dipolar cycloaddition) to the alkyne RAFT end group and successful incorporation of the dye characterised by UV-Vis spectroscopy.

4.3.2 *In vitro* toxicity and cellular uptake of synthesised polymers

Experiments were performed in order to evaluate the cytotoxicity and cellular uptake of the hyperbranched polymers.

These polymers are intended to be used as carriers for the delivery of anticancer agents to various cancer cells, particularly pancreatic cancer cell line. Therefore, they were screened in the MIA PaCa-2 pancreatic cancer cell line in both 2D and 3D cell culture models to evaluate their cytocompatibility.

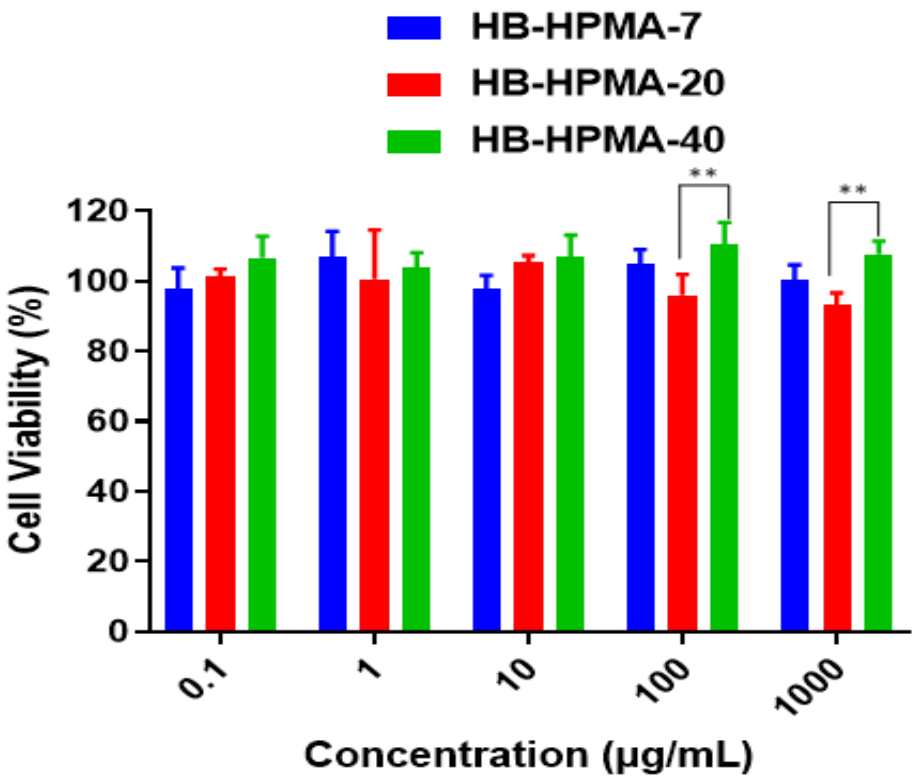


*Figure 4-7 In vitro 2D cell viability assay at 72h post treatment with different concentrations of the three **HB-HPMA** polymers on MIA PaCa-2 pancreatic cancer cell line using trypan blue dye exclusion test of cell viability. Error bars show standard deviation (N = 4). (**p <0.01, two-way ANOVA with Tukey's multiple comparison test).*

The trypan blue dye exclusion test of cell viability was used to determine the cytotoxicity of the polymers in 2D cell culture over 72h. As can be seen from Figure 4-7, all the polymers did not induce any toxic effect on the MIA PaCa-2 cell line at the concentrations tested. The assay was repeated in a MIA PaCa-2 3D cell culture model whereby changes in spheroid volume and CellTiter-Glo® 3D cell viability assays were used to analyse cell viability.

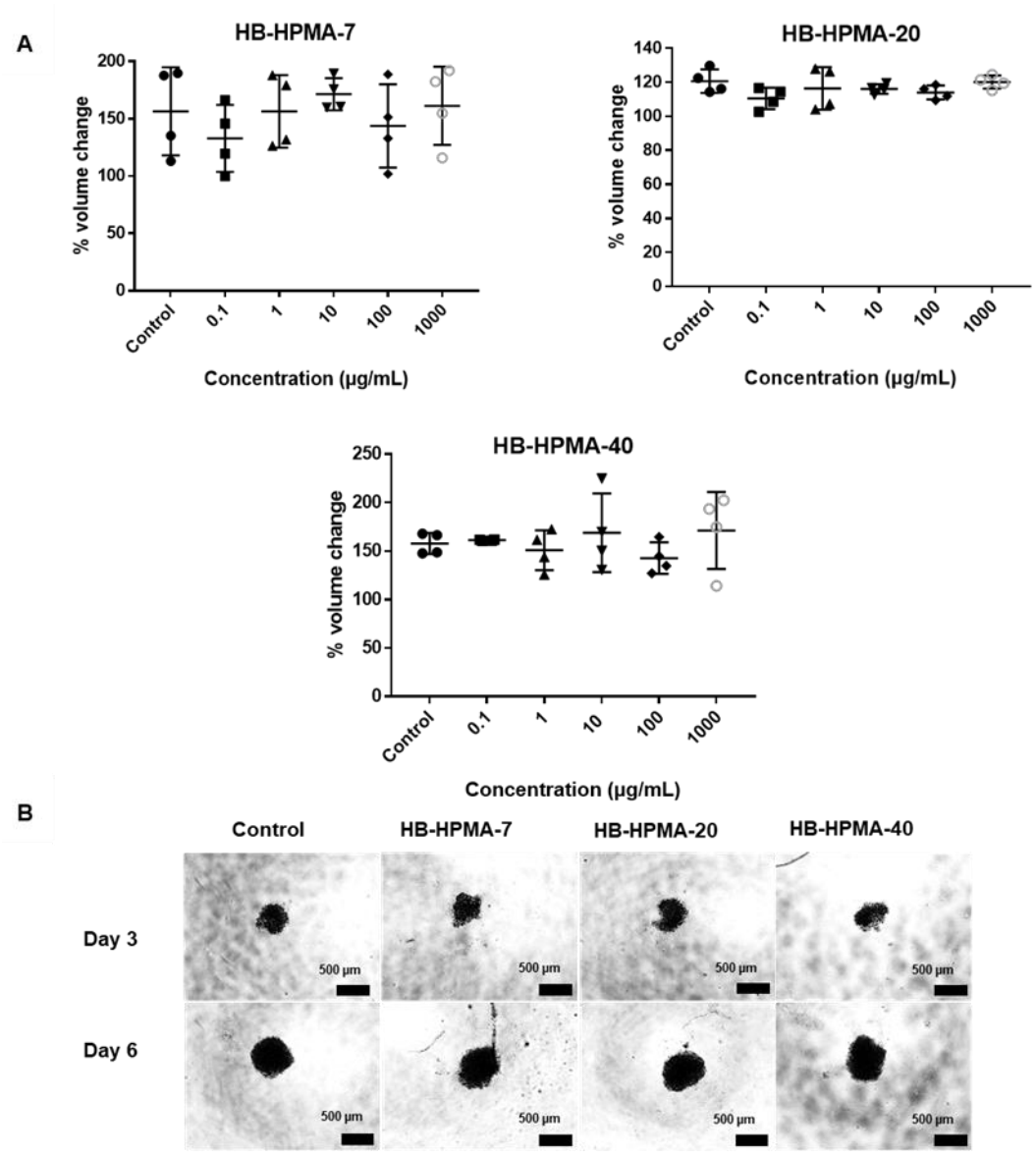


Figure 4-8 3D cell cytocompatibility assay with the three polymers at different concentrations (A) Percentage volume change between day 3 (pre-treatment) and day 6 (72 hours post treatment). (B) Representative brightfield images of control and treated spheroids (1000 µg/mL), demonstrating volume increase over the assay period, (N = 4).

Similar to the 2D cell culture model, no toxic effects were observed in the 3D cell culture assay. The volume of the spheroids (Figure 4-26, SI), in both the control and treated wells, increased at a constant rate over the course of the assay for all three polymers. In addition, the percentage change in volume between day 3 and 6 remained above 100 % for all three polymers at all the tested concentrations. (Figure 4-8A).

To substantiate these data, the spheroids after 72 hours of treatment with the polymers were treated with CellTiter-Glo® 3D cell viability assay solution. From Figure 4-9, at all concentrations tested, the cell viability remained above 90 %, further proving that the polymers alone are not toxic to the cancer line.

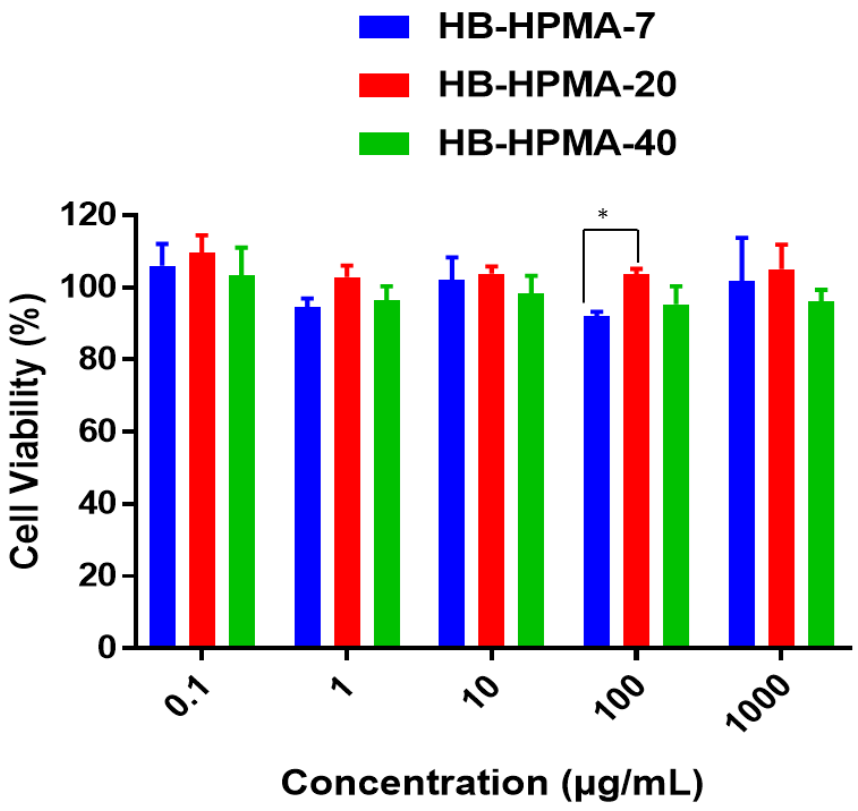


*Figure 4-9 In vitro CellTiter-Glo® 3D cell viability assay for the three HB-HPMA polymers in MIA PaCa-2 pancreatic cancer cell line Error bars show standard deviation (N = 4). (*p <0.05, two-way ANOVA with Tukey's multiple comparison test).*

For the uptake studies, MIA PaCa-2 cells were incubated with the labelled polymer for either 1 hour (2D assay) or 2 hours (3D assay) at a concentration of 200 µg/mL.

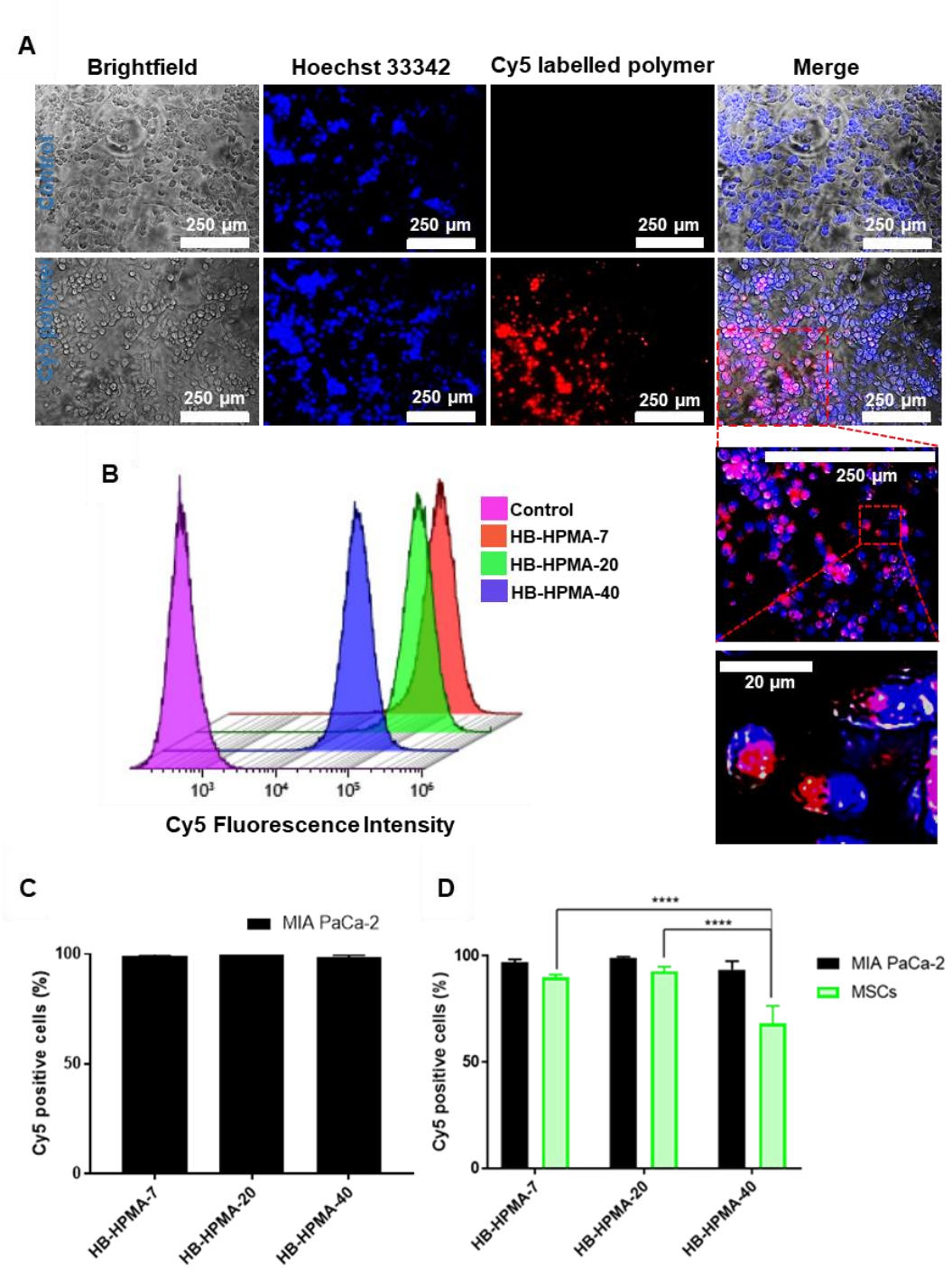


*Figure 4-10 2D cellular uptake of Cy5-labelled HB-HPMA polymers by MIA PaCa-2 pancreatic cancer cells after 1-hour incubation. A) Representative fluorescence microscopy images confirming intracellular localisation of **HB-HPMA-7** polymers during uptake studies (scale bar = 250 µm and 20 µm). B) FACS uptake histograms for all three polymers compared to control. Percentage of Cy5 positive cells of HB-HPMA polymers in C) mono and D) co-cultured spheroids after 2 hours incubation. Data are representative of three experiments (N = 3) (****p ≤ 0.0001 two-way ANOVA with Tukey's multiple comparisons test).*

Microscopy images from both 2D (Figure 4-10A) and 3D (Figure 4-11A & B) cell culture assays showed that there was high uptake of the polymers into the MIA

PaCa-2 cells. This is backed up by the flow cytometry analysis of the cells (Figure 4-10B-D, Figure 4-11C-D).

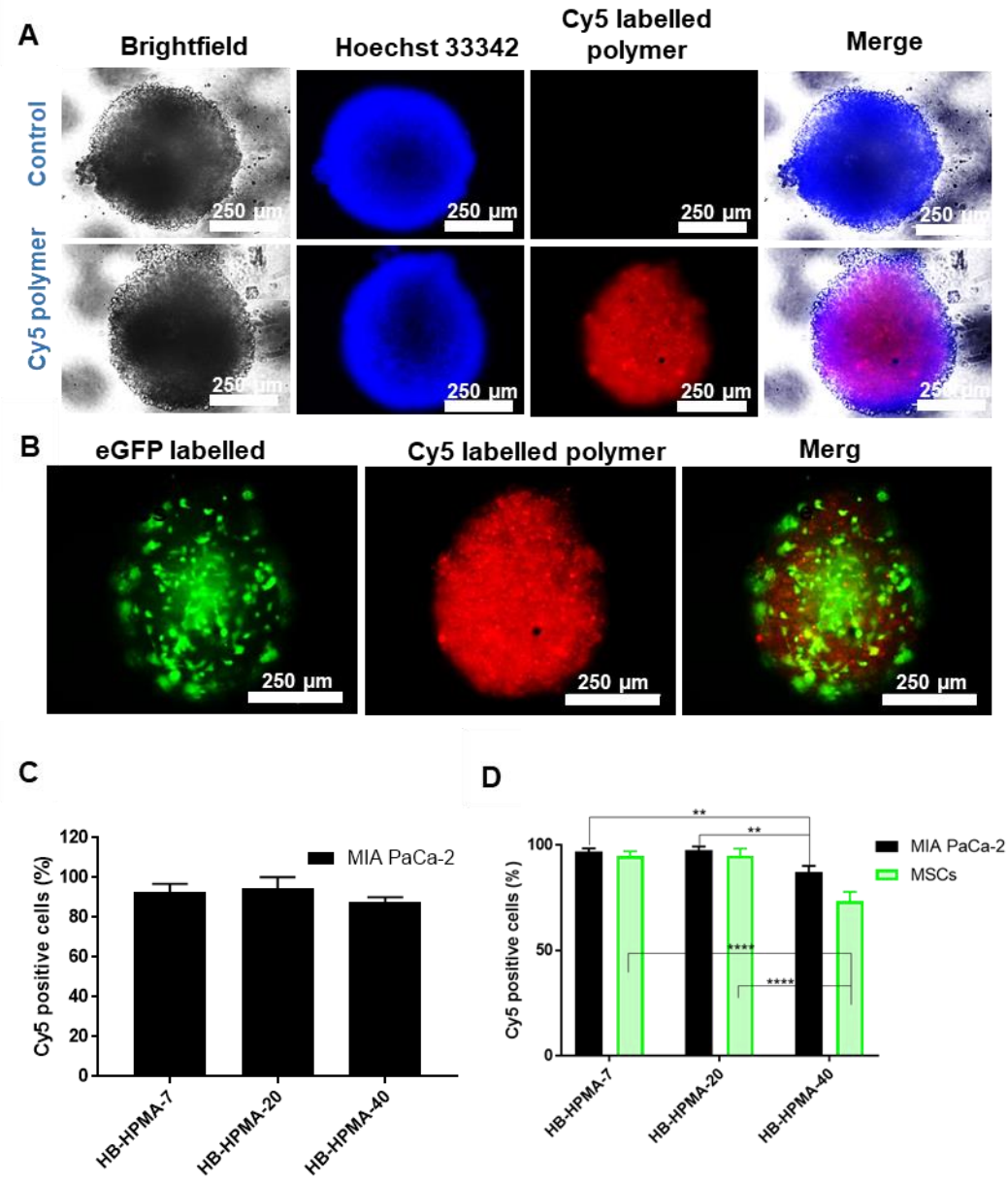


*Figure 4-11 . In vitro cellular uptake of HB-HPMA polymers in 3D MIA PaCa-2 mono and coculture cell models. (A) Representative microscope images of cellular uptake of **HB-HPMA-7** in 3D MIA PaCa-2 monoculture system. (B) Representative microscope images of cellular uptake of **HB-HPMA-7** in co-culture spheroids (cell nuclei stained with Hoechst 33342: blue; MSC: green; Cy5 polymer: red). Percentage of Cy5 positive cells in FACS analyses of **HB-HPMA** polymers in (C) mono and (D) co-cultured spheroids after 2 hours incubation. The scale bar represents 250 µM. Data are represented as a mean (N = 3, n = 10) (**p ≤ 0.01, ****p ≤ 0.0001 two-way ANOVA with Tukey's multiple comparisons test).*

No significant difference was observed in the uptake behaviours of all three polymers in both 2D and 3D monoculture (Figure 4-10C and Figure 4-11C). However, in the coculture experiments, **HB-HPMA-7** and **HB-HPMA-20** performed

better than **HB-HPMA-40** in both cell lines (Figure 4-10D and Figure 4-11D). This could be due to the size differences of the polymers as particles with a size range of less than <30 nm are known to exhibit good tumour penetration properties.[351]

In addition to this, there was no overlap of signals between the Cy5 labelled polymer and the mesenchymal stem cells (Figure 4-11B), suggesting there was preferential uptake of the polymer into the MIA PaCa-2 cell line when in the presence of both cell lines. However, the flow cytometry data analysis showed uptake of the polymers into both cell lines. Therefore, it can be concluded from the 3D uptake studies that the presence of the MSCs did not appear to affect the uptake behaviour of all three polymers. In addition, there was no preferential uptake of the polymer into the pancreatic cancer cell line hence polymer-drug conjugates using these **HB-HPMA** polymers for the treatment of pancreatic cancer cells cocultured with MSCs may induce a toxic effect on both cell lines.

4.3.3 *In vitro* macrophage cytotoxicity and uptake

The backbone of the polymer was based on pHPMA to provide stealth properties to the final polymer-drug conjugate in order to evade macrophage uptake *in vivo*. In drug delivery, ‘stealth’ is used to describe particles that are not recognised by biological systems such as Kupffer cells and the mononuclear phagocyte system (MPS) involved in the clearance of particles from the bloodstream.[352]

RAW 264.7 cells were the *in vitro* macrophage cell line of choice for this investigation. Initially, a cytocompatibility assay was conducted with PrestoBlue™ cell metabolic assay and LDH release assay to determine the effect of the **HB-HPMA** polymers on the macrophage cell line. After 24 hours of treatment, both assays confirmed all polymers tested were compatible with the cell line with no observable toxicity or membrane damage.

Polymer internalisation in the murine macrophage cell line, RAW 264.7, was performed in order to study the immune evasive capabilities of the three polymers, and therefore provide an indication of stealth properties and potential performance in *in vivo* biodistribution experiments.[353, 354] The time-dependent uptake of the particles, Figure 4-12, showed that the fastest rate of internalisation occurred within

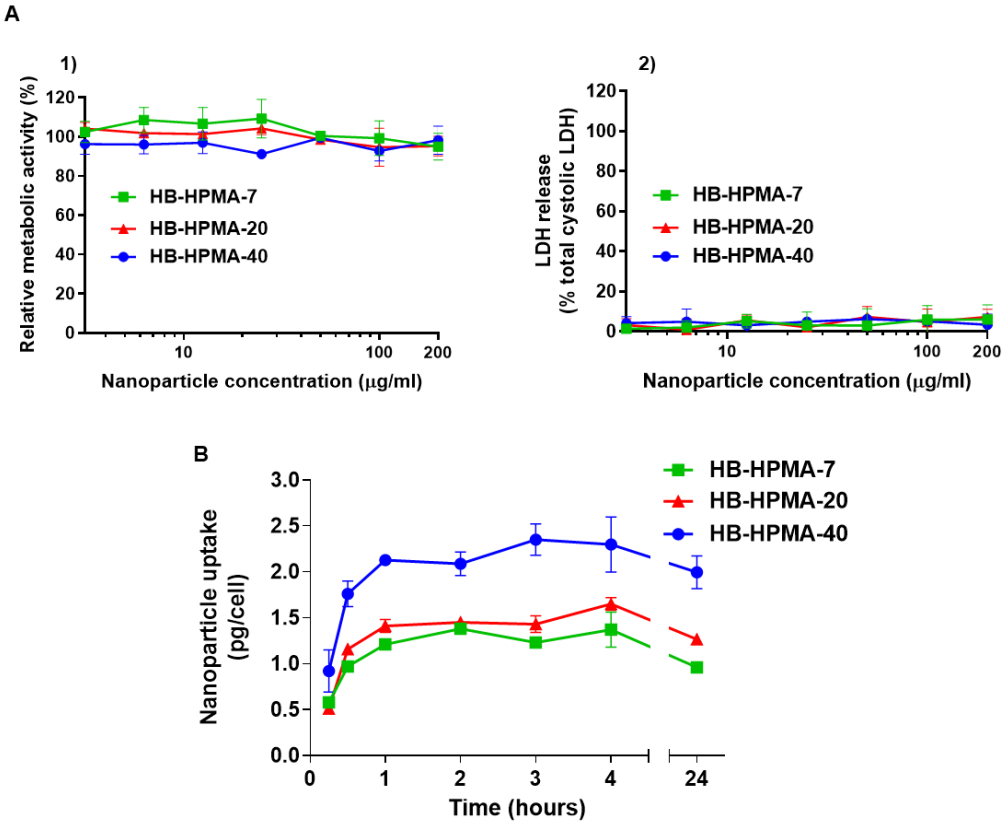


Figure 4-12 In vitro macrophage studies. (A) Evaluation of HB-HPMA polymers biocompatibility in RAW 264.7 macrophages polymers applied in 10 % FBS/DMEM for 24 hours, (1) PrestoBlue™ cell metabolic assay (2) LDH release assay. Data are presented as mean ± S.D (N = 3, n = 3). (B) Time-dependent NP uptake in RAW 264.7 macrophages polymers applied at 50 μg/mL in 10 % FBS/DMEM. Data generated and analysed by Dr Robert Cavanagh.

the first 60 minutes for all three polymers followed by a plateau at 1-24 hours. It is currently unclear what mechanism drives the observed plateau in particle uptake, however, one explanation might involve an existing equilibrium between endocytotic and exocytotic processes, as previously observed and described in the literature.[355, 356] The three polymers displayed differences in uptake behaviour with **HB-HPMA-7** and **HB-HPMA-20** demonstrating the most 'stealth-like' behaviour of the three

polymers with lower levels of particle internalisation after 1 hour (1.21 ± 0.03 pg/cell and 1.41 ± 0.07 pg/cell respectively, compared with **HB-HPMA-40**, 2.13 ± 0.05 pg/cell). This observed difference in macrophage uptake could be due to the differences in polymer physical sizes, as has been reported for iron oxide nanoparticles.[354]

Phagocytosis is a specific form of endocytosis, and a key process performed by macrophages, whereby bacterial, cell debris and other large-sized materials are ingested and removed from the milieu intérieur.[357] Phagocytosis of material can be enhanced *via* a process known as opsonisation. Opsins, such as immunoglobulin and other serum constituents, interact with target material and in turn, increase the material's attraction to cell surface receptors and binding to macrophages.[358] Furthermore, opsonisation can also stimulate phagocytosis via the propagation of signal cascade from opsin-activated receptors on the cell surface.[359]

It has been reported that small particles (i.e. <50 nm) are less likely to undergo opsonisation by serum proteins in the bloodstream and therefore are more likely to evade recognition and uptake by macrophages in organs of the mononuclear phagocytotic systems (MPS).[354, 357, 360, 361] Indeed, nanoparticles in the size range of 250 nm to 3 μM have been shown to be optimal for *in vitro* phagocytosis.[357] Therefore, considering the size of the particles used in this work, it is unlikely that phagocytosis is the predominant pathway for macrophage uptake. More feasible routes for internalisation by macrophages may thus include caveolin-mediated and clathrin-mediated endocytotic pathways, which are well-known routes for nanoparticle uptake in a variety of cell types.[357] Vesicles of the caveolin-mediated pathways are approx. 100 – 150 nm, and the clathrin-mediated route vesicles approx. 150 – 200 nm.[362, 363] Vesicle size, therefore, restricts the pathways nanoparticles can exploit, however, due to the size of our particles, it is possible they utilise both clathrin- and caveolin-mediated endocytotic routes. Regarding

nanoparticle size, a study by Lu *et al* demonstrated that nanoparticles in the range of 30-50 nm are able to bind more effectively to cell membrane receptors and subsequently promote higher levels of clathrin-mediated endocytosis.[364] This may, therefore, help explain our observation that the **HB-HPMA-40** particle (size 40 nm) experienced the highest levels of internalisation compared to **HB-HPMA-20** (size 20 nm) and **HB-HPMA-7** (size 7 nm), both of which are outside the optimal size range.

4.3.4 *In vivo* analysis of organ distribution

4.3.4.1 Fluorescent biodistribution study

In vivo biodistribution studies in immune-deficient tumour naïve mice were performed following confirmation of biocompatibility, good *in vitro* cellular uptake properties in MIA PaCa-2 cells and reduced uptake in RAW 264.7 macrophage cells of all three polymers. The assay was to understand how the different sizes of the three polymers will affect circulation and organ accumulation, especially in the organs of the MPS. Six healthy female CD-1 nude mice were injected *via* the tail vein with 500 µg/mL solution of each polymer. Fluorescence images were acquired at 1, 4- and 24-hours post-injection (Figure 4-13A). Due to the limited penetration abilities of *in vivo* fluorescence imaging, two mice from each group were culled at the different time points and *ex vivo* images taken of the organs (Figure 4-13B) for semi-quantitative analysis of polymer accumulation with focus on the organs involved in particle clearance from the bloodstream. The fluorescence signal of each organ was analysed in detail by expressing it as a percentage of the total organ signal (Figure 4-13C).

From the depicted *in vivo* images of 4 hour time point (Figure 4-13A), it can be seen that the polymers in all cases accumulate predominantly in the kidney, liver and bladder of the mice, characterised by the fluorescent signals in these organs - with the smaller particles accumulating more in the bladder and kidney than the bigger particles. The significantly small diameter of the glomerular capillary could provide

an explanation for the difference observed in the clearance and organ accumulation

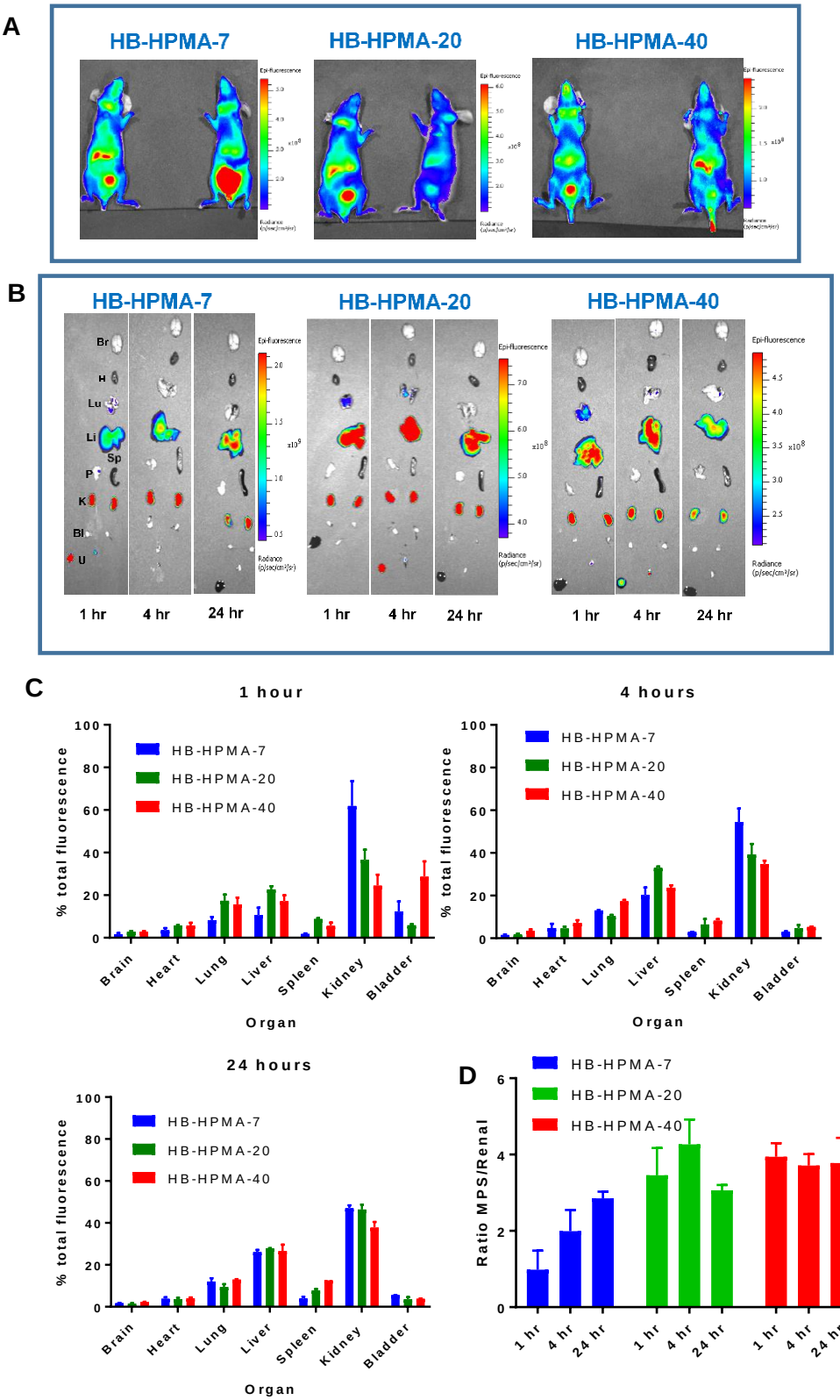


Figure 4-13. A) Representative in vivo images (4 hr post injection), B) Ex vivo images at 1 hr, 4 hr and 24 hr post injection (Br = brain, H = heart, Lu = lungs, Li = liver, P = pancreas, Sp = spleen, K = kidney, U = urine, Bl = bladder). C) Quantitative data to highlight fluorescence signal in nanoparticle clearance organs as a percentage of total organ signal (n = 2) and D) Ratio between signal in MPS organs (spleen, lungs and liver) and renal organs (kidney) over time. Data generated by Alison Ritchie and Dr Phillip Clarke.

of these three particles (Figure 4-13B-C). The small diameter, measuring at 4.5 – 5 nm, leads to a highly specific size filtration whereby particles with a small hydrodynamic diameter, approx. 6 nm, are easily filtered while larger particles, > 8 nm, typically have reduced renal and enhanced hepatic clearance.[365, 366]

As already mentioned, the polydispersity of these polymers increases with increasing molecular weight and therefore physical size. This leads to a broader range of molecular weight and particle size especially in the larger particle population (**HB-HPMA-40**). This was apparent in their clearance behaviour - there was an observed accumulation of **HB-HPMA-20** and **HB-HPMA-40** in the kidneys and bladder of the mice (Figure 4-13 A-C), especially at the earlier time points which could be attributed to the initial clearance of the smaller particle from the sample species.

The ratio of MPS organs to the renal system was calculated to better our understanding of the clearance mechanism of these polymers from the bloodstream (Figure 4-13D). The ratio of the smaller particles (**HB-HPMA-7**) is significantly less than that of the two big particles at 1 hour and 4-hour time points. However, no significant difference was observed at the 24-hour time point. This could be as a result of the **HB-HPMA-7** having a higher percentage of smaller particles and hence being able to utilise the renal clearance system more effectively. However, at 24 hours, most of the small particles have been cleared from the bloodstream and hence the clearance mimics that of the larger particles.

Although differences are seen between **HB-HPMA-7** and **HB-HPMA-20** and **HB-HPMA-40**, it is worth noting that, all three polymers have relatively low MPS to renal ratios and therefore have an overall reduced accumulation in the MPS organs, supporting the data from the macrophage uptake studies. This is expected as it has been shown that hyperbranched HPMA polymers, as a result of the stealth

properties, tend to exhibit a low macrophage uptake and hence demonstrate a reduced MPS organ accumulation.[367]

4.3.4.2 PET-CT biodistribution study in tumour naïve and tumour bearing mice

Samples labelled with ^{89}Zr for longitudinal PET imaging were used to probe the behaviour of these polymers further *in vivo*. ^{89}Zr was the isotope of choice due to its longer half-life compared with ^{64}Cu, i.e. 3.3 days and 12.7 hours respectively.[304]

Table 7 Percentage of DFO units HB-HPMA polymer.

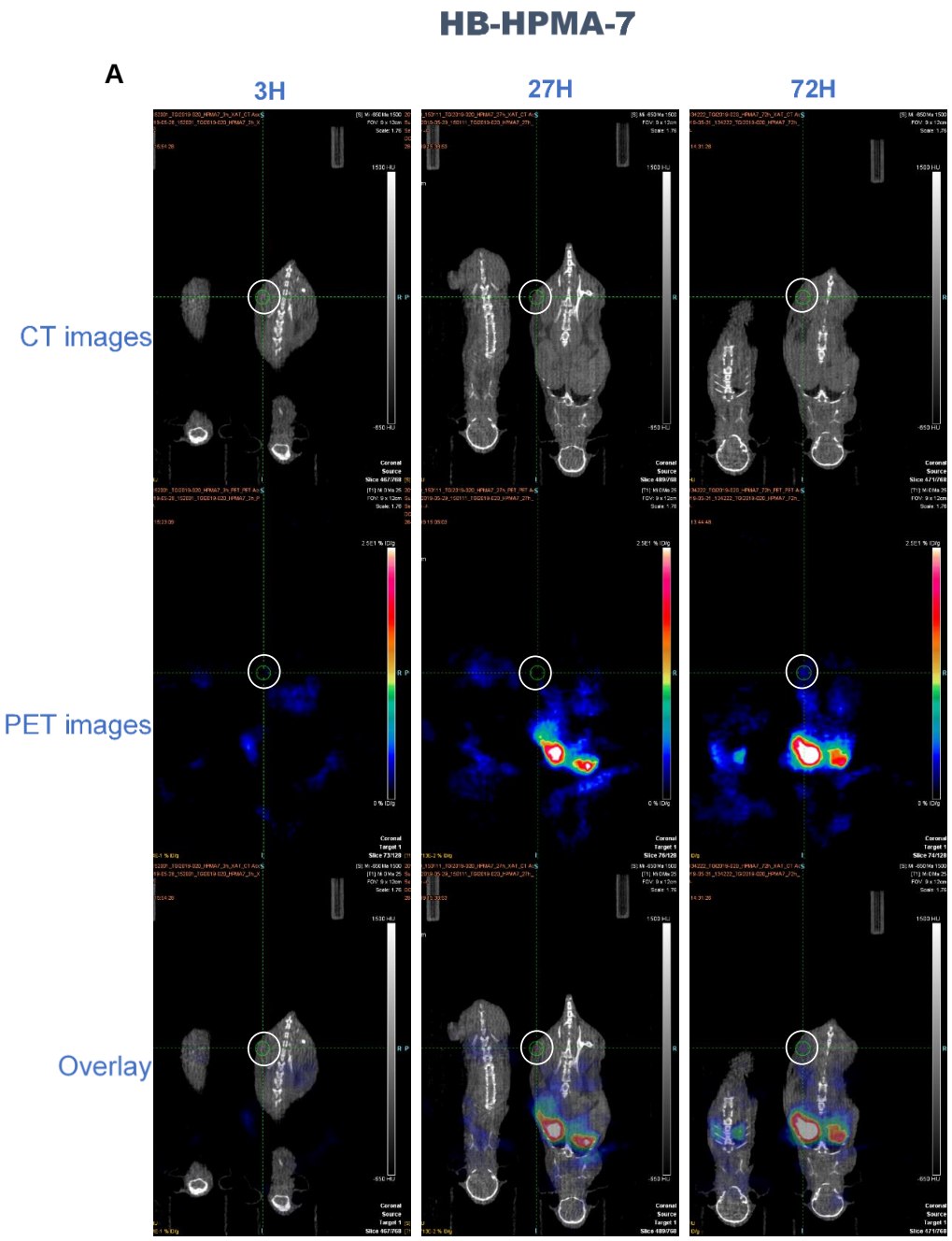
Polymer	DFO/HB-HPMA (^{1}H NMR) (mol/mol%)
HB-HPMA-7	18
HB-HPMA-20	12
HB-HPMA-40	9

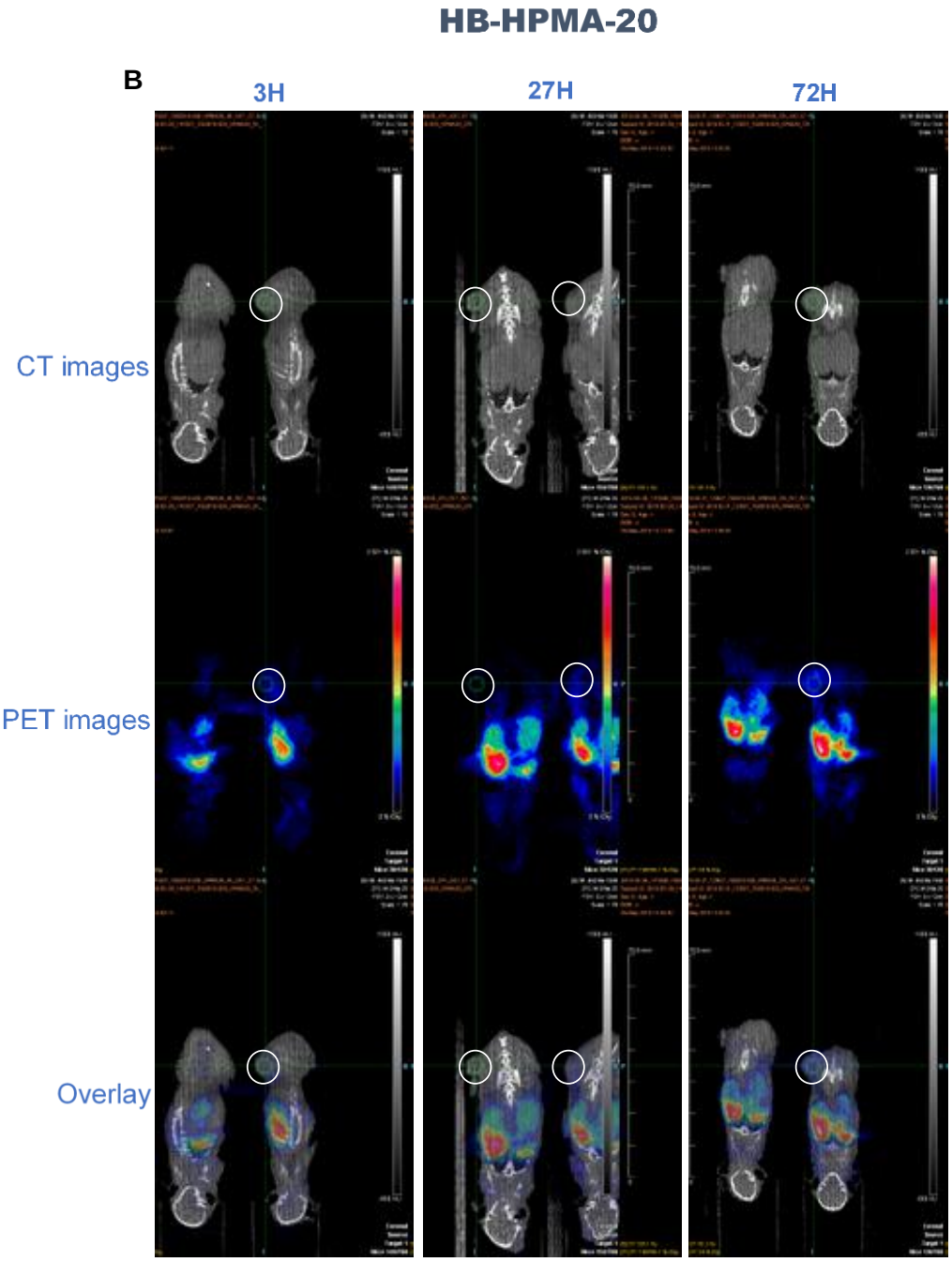
Deferoxamine (DFO) was employed as the chelator for ^{89}Zr for the ^{89}Zr-PET imaging as it has been used in clinical applications.[304, 368, 369] DFO was covalently attached to the **HB-HPMA** polymer backbone through an amide linker. Briefly, the secondary hydroxyl group of HPMA was reacted with succinic anhydride to provide a carboxylic acid handle for the subsequent attachment of DFO *via* the amine functional group to yield the **HB-HPMA-DFO** polymer as confirmed by ^{1}H NMR (Figure 4-29, SI, Table 7). As can be seen from the table, the DFO percentage of the three polymers varied with **HB-HPMA-7** having significantly more DFO units per polymer chain. This reflected in the level of ^{89}Zr labelling on each polymer (Figure 4-30, SI) with **HB-HPMA-7** having the largest level of ^{89}Zr labelling followed by **HB-HPMA-20** and finally **HB-HPMA-40** with the lowest ^{89}Zr label. In addition to this, all three **HB-HPMA** polymers demonstrated successful radiolabelling with ^{89}Zr (>99 %) with no

trace of free chelator as observed on the radiographic thin layer chromatography (TLC, Figure 4-30, SI).

To assess the *in vivo* biodistribution properties of these polymers, the radiolabelled polymers were injected intravenously into Balb/c nude MIA PaCa-2 xenograft mice and tumour naïve mice (n = 4 per group). PET-CT images were acquired at the different time points for the tumour bearing and the non-tumour bearing mice of each polymer.

Figure 4-14 and Figure 4-15 show representative PET-CT images of tumour bearing mice at indicated time points post-injection. From both images, it can be seen that at 3 hours post-injection, the majority of the particles in all cases were in circulation with little accumulation in tissues such as the liver, kidneys and spleen. However, the number of circulating particles decreased by 27 and 72 hours mostly due to liver and spleen retention. The tumour ^{89}Zr signal appeared to increase over the 72-hour time point with **HB-HPMA-20** showing higher ^{89}Zr signals, therefore enhanced particle accumulation in the tumour, particularly at 72 hours post-injection.


HB-HPMA-7
A
3H
27H
72H
CT images
PET images
Overlay


HB-HPMA-20
B
3H
27H
72H
CT images
PET images
Overlay

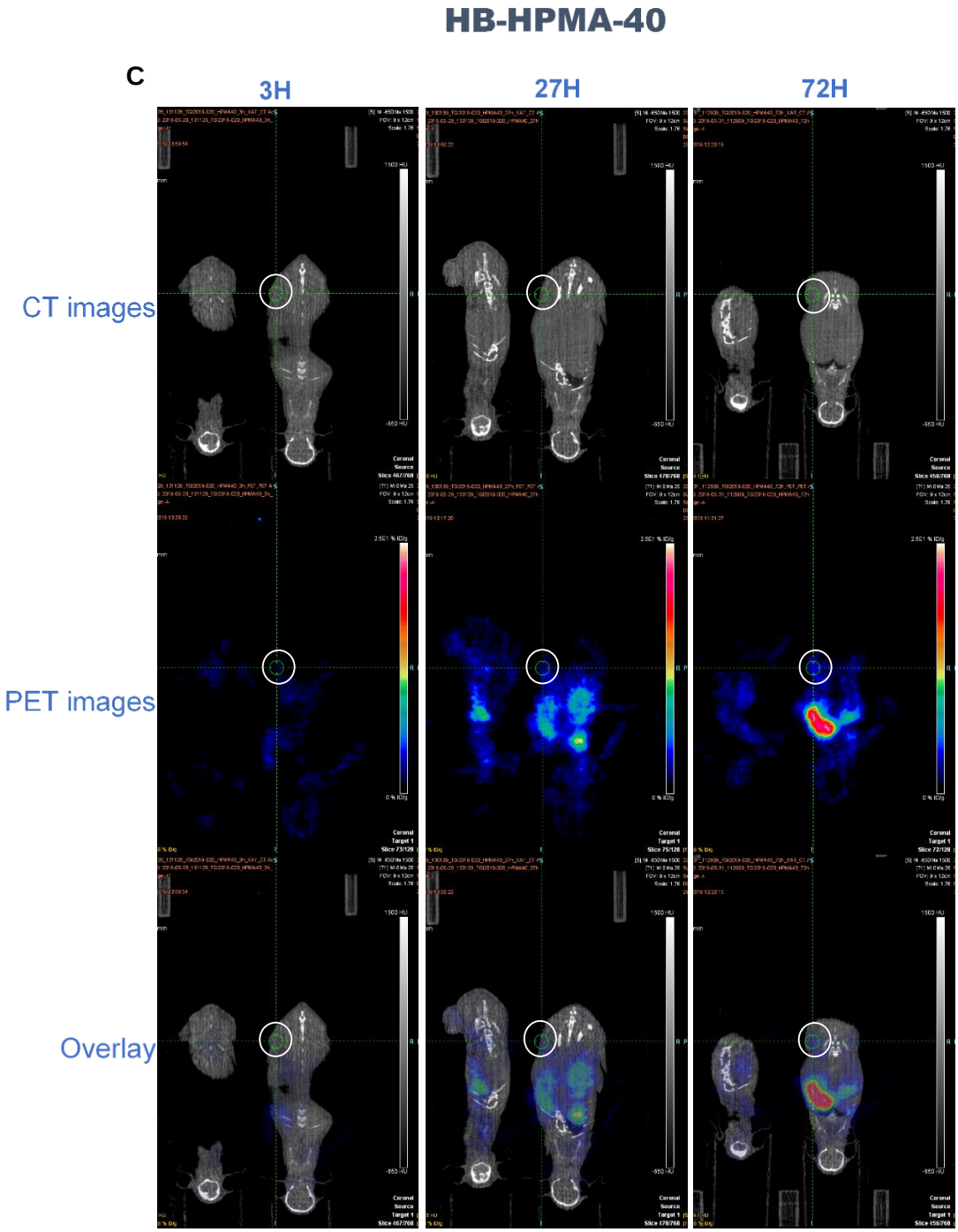


*Figure 4-14 Representative in vivo PET-CT images of the ^{89}Zr-labelled HB-HPMA polymers at 3H, 27H and 72H post-injection in MIA PaCa-2 xenograft mice models. (A-C) Distribution behaviour of **HB-HPMA-7**, **HB-HPMA-20** and **HB-HPMA-40** at the indicated time points post-injection. White circles highlight the tumour location in each image. The intensity bar of the PET images represents the %ID/g whereby black = 0 %, blue = approx. 4 % and red = approx. 16 %. Data generated and analysed by Dr Nicholas Fletcher, Dr Zachary Houston and Theo Crawford.*

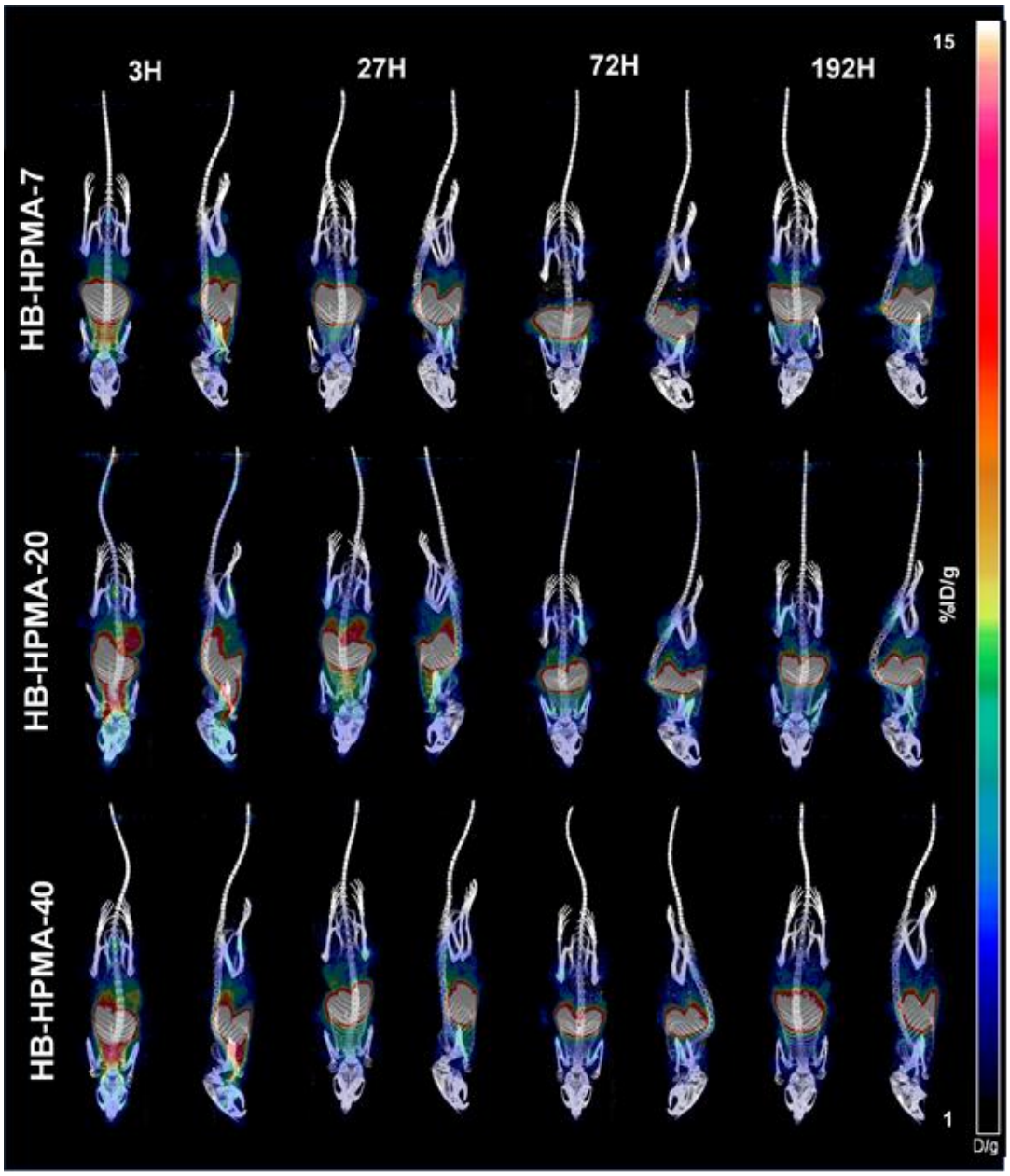


*Figure 4-15 PET-CT imaging of ^{89}Zr-labelled **HB-HPMA** polymers in MIA PaCa-2 xenograft model. Representative two orientation maximum intensity projection (MIP) images of all three polymers showing majority of the particles in circulation at 3 H post injection. This is followed by retention of the particles mostly in the liver in the later timepoints. The intensity bar represents the %ID/g whereby black = 0 %, white = 15 %ID/g, dark blue = 1 %ID/g and red = approx. 10 %ID/g. Data generated and analysed by Dr Nicholas Fletcher, Dr Zachary Houston and Theo Crawford.*

The longitudinal *in vivo* biodistribution behaviour of these particles were also quantified from the region of interest (ROI) analysis of the ^{89}Zr-PET-CT images. The graphical presentation of the distribution patterns of the different particles in the tissues of interest is shown in Figure 4-16. The heart ROI, which is assumed to represent the concentration of circulating particles, given there is no cardiac tissue perfusion, exhibited similar biodistribution profile for all three particles with the

majority of the materials being cleared from the bloodstream over the course of the assay.

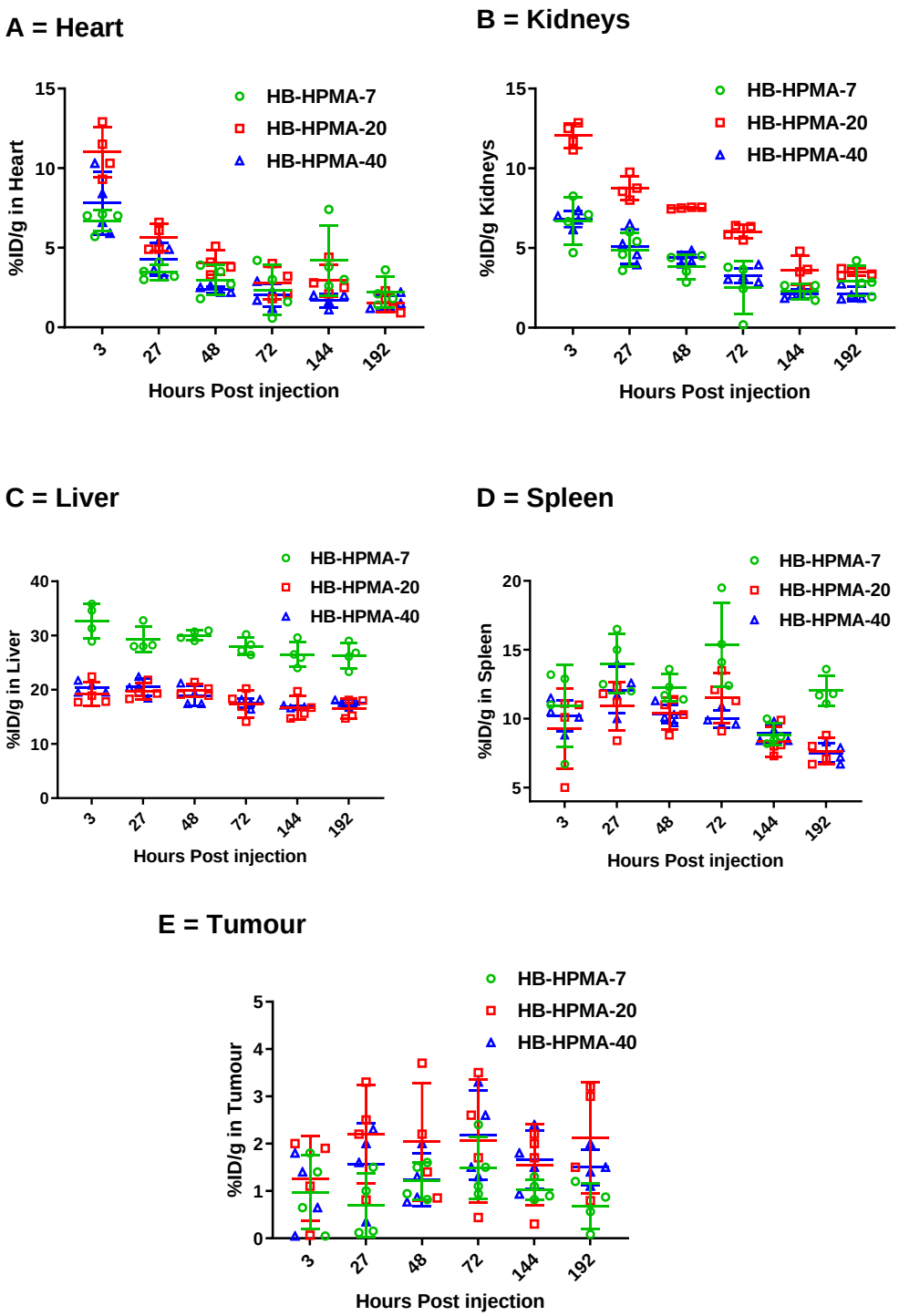


Figure 4-16 PET ROI analysis of in vivo tissues accumulation of HB-HPMA polymers in MIA PaCa-2 xenograft model. A-E) Graphs of hyperbranched HPMA polymer distribution over time in heart, kidneys, liver, spleen and tumour respectively. Data generated by Dr Nicholas Fletcher and Dr Zachary Houston.

The renal profiles of the three polymers resembled those of the heart profiles, further

confirming the gradual clearance of the particles from circulation. As observed from the images, high hepatic and splenic accumulation of the materials were also seen from the ROI analysis of the PET-CT images, particularly at the earlier time points. Interestingly, **HB-HPMA-7** displayed the highest percentage of material accumulation in these tissues compared with **HB-HPMA-20** and **HB-HPMA-40**. This was unexpected as the previous biodistribution with Cy5-labelled polymers showed the **HB-HPMA-7** to be taken up less into liver and spleen tissues and exhibited better MPS/renal ratio than the two bigger particles. In addition to this, HPMA mono and copolymers have been described in the literature to be effective at escaping MPS clearance due to their stealth properties, especially at low molecular weights.[303, 367, 370, 371] The enhanced uptake of these particles, particularly **HB-HPMA-7**, in the MPS tissues may have been due to conformational changes to the particles post DFO conjugation especially as the polymer with the highest uptake into these tissues was **HB-HPMA-7** (18 mol% DFO units compared to 12 mol% and 9 mol% for **HB-HPMA-20** and **HB-HPMA-40** respectively). The likely changes caused by DFO conjugation were increased hydrophobicity, and accordingly the enhanced possibility of inter-polymer aggregates as hydrophobic 'patches' self-assembled. In addition, hydrophobic regions in these polymers could render them prone to opsonisation by serum proteins with increased phagocytosis by macrophage and Kupffer cells. As it is well known that conjugation to the backbone of polymers can cause slight variation in structure and conformational changes that can affect the polymer's physical properties.[372] Unfortunately, it was not possible to assess specifically where in the organs the polymers were accumulating as the tissues post λ-scintillation count were not viable for further analysis. Therefore, to determine if the enhanced accumulation of the particles in the splenic and hepatic tissues was due to increased uptake in macrophages, the uptake studies in the RAW 264.7 cells were repeated with the DFO functionalised **HB-HPMA** particles. The results as presented in Figure 4-17 shows that the conjugation of DFO to the

backbone of the

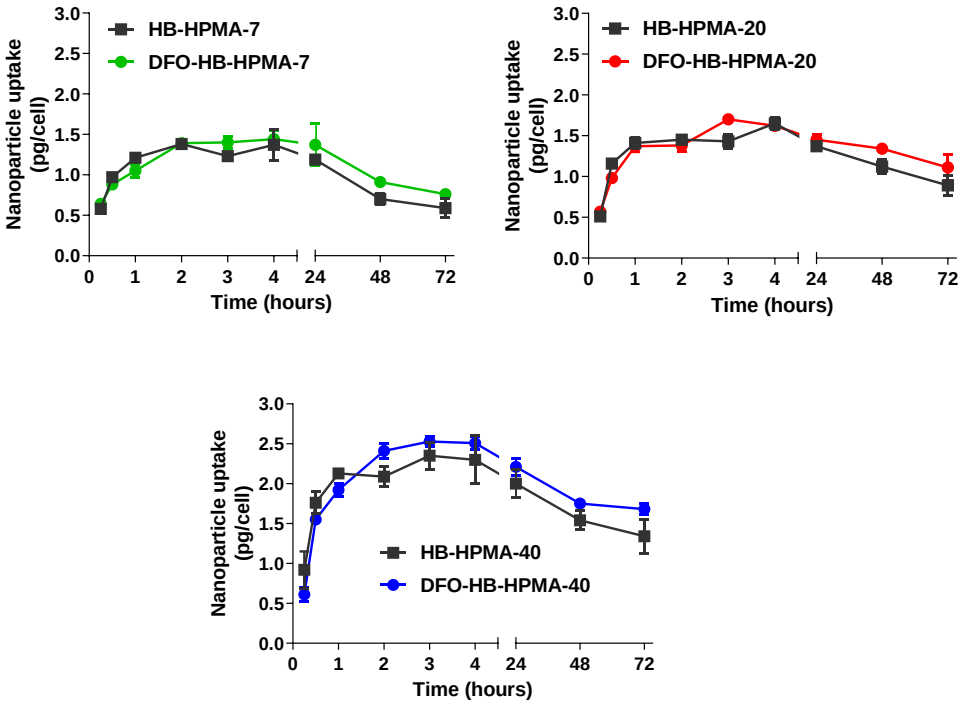


*Figure 4-17 Comparison between the in vitro time-dependent uptake of **HB-HPMA** and **HB-HPMA-DFO** polymers in RAW264.7 macrophage cells at a concentration of 50 µg/m. Cells were cultured for 24h prior to assaying. Hyperbranched polymers were applied in DMEM containing 10 % (v/v) FBS. Data are presented as mean ± S.D (N = 3, n=3). Data generated and analysed by Dr Robert Cavanagh.*

polymer had no significant effect on the uptake of the polymers by the macrophage cells. These cell culture assay might suggest that accumulation of the particles in spleen and liver was not a result of enhanced clearance by organs of the MPS, but it should be noted that 2D macrophage culture assays are not able to replicate fully macrophage behaviour *in vivo*. Additionally, the behaviour of both sets of polymers once in the tissues has not been studied. It is possible that the DFO particles may experience increased retention as a result of reduced exocytosis from hepatocytes, splenic monocytes and liver and spleen macrophages triggering the enhanced liver and spleen accumulation observed in the PET studies. As a result, further studies into the exocytosis behaviour of these particles in addition to a detailed analysis of the *ex vivo* tissues are needed to understand the changes in the distribution profile of **HB-HPMA** polymers in the PET-CT studies.

Finally, there was no significant difference between the tumour accumulation profiles of the different sized particles. However, as was observed from the PET-CT images in Figure 4-14, the ROI analysis confirmed **HB-HPMA-20** to have slightly higher tumour accumulation than **HB-HPMA-7** and **HB-HPMA-40,** especially at the earlier time points. The percentage of accumulated particles in the tumour for all three polymers is comparable with literature findings of nontargeted nanoparticles.[304, 370, 373]

In addition to the ROI analysis, *ex vivo* λ-scintillation counting was used to validate the biodistribution behaviour of the particles 8 days post-injection (Figure 4-18).

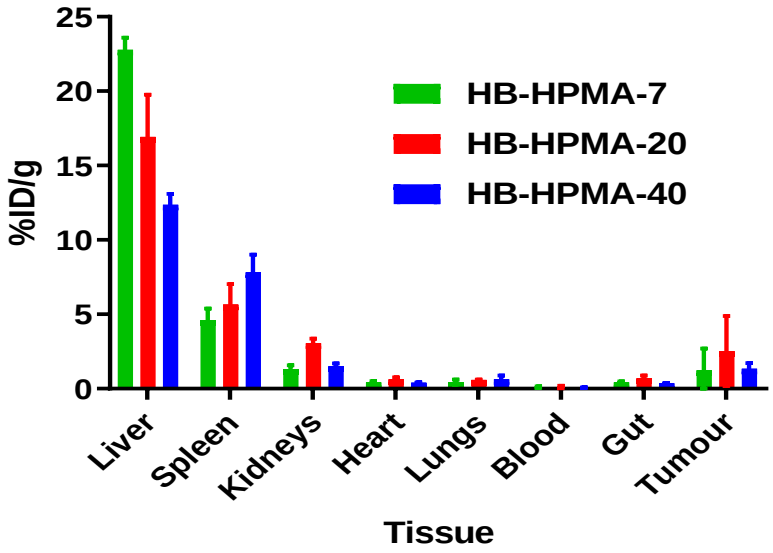


Figure 4-18 Ex vivo λ-scintillation biodistribution data across all tissues 8 days post injection. Data generated by Dr Nicholas Fletcher and Dr Zachary Houston.

These data confirmed the enhanced liver and spleen uptake and retention behaviour observed in the ROI analysis and the images of all three polymers, particularly **HB-HPMA-7**. Accumulation of the particles in the tumour tissues was also shown, with

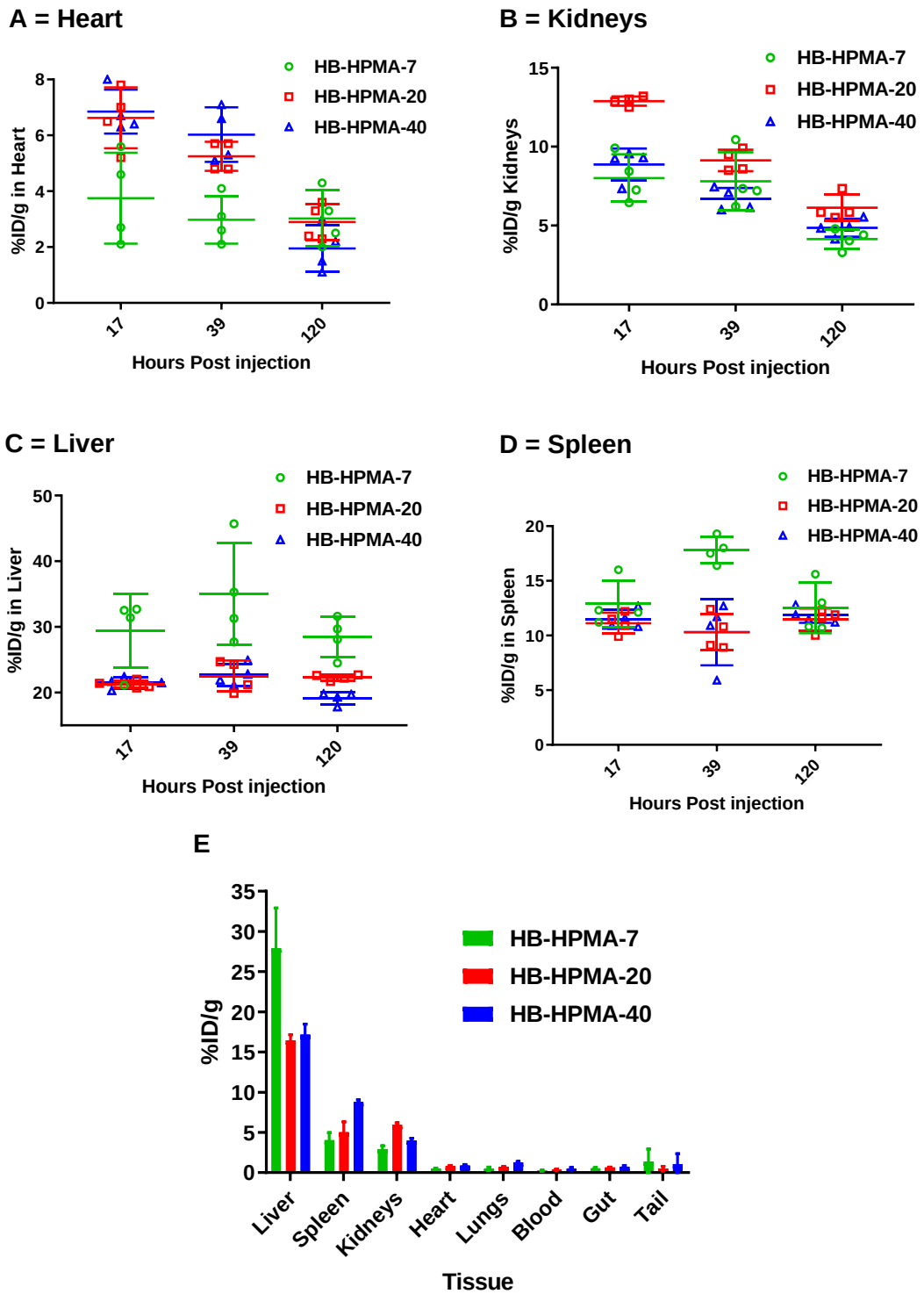


Figure 4-19 PET ROI analysis of in vivo tissues accumulation of HB-HPMA polymers in tumour naïve mice. A-D) Graphs of hyperbranched HPMA polymer distribution over time in heart, kidneys, liver and spleen respectively. E) Ex vivo λ-scintillation biodistribution data across all tissues 5 days post injection. Data generated by Dr Nicholas Fletcher and Dr Zachary Houston.

HB-HPMA-20 having the highest levels of tumour association. The biodistribution profiles of the particles in the tumour-bearing and non-tumour bearing mice

resembled each other (Figure 4-19, Figure 4-31, SI) and the presence of the tumours had no observable effect on the distribution pattern of these particles in the various tissues.

4.4 Conclusions

The data presented here demonstrate the successful synthesis of the hyperbranched HPMA polymers *via* RAFT polymerisation. These polymers were characterised by NMR, GPC, DLS, TEM etc. and were found to differ by molecular weight and physical size. The resultant materials displayed desirable *in vitro* biocompatibility and cellular uptake in both 2D and 3D MIA PaCa-2 cell culture models.

The *in vivo* fluorescence biodistribution studies of these polymers demonstrated reduced uptake into the macrophage processing organs such as the spleen and lungs which were in agreement with the *in vitro* macrophage cellular uptake findings. There were observable differences in the renal and hepatic clearance of the three fluorescently-labelled polymers whereby **HB-HPMA-7** was found to utilise the renal clearance system more effectively than the **HB-HPMA-20** and **HB-HPMA-40**.

We further functionalised these polymers with DFO to quantify their longitudinal PET-CT biodistribution behaviour past their biological half-life. There were observable differences between the PET and fluorescence biodistribution assays for all particles. These differences were attributed to the possible conformational changes from the DFO conjugation to the polymeric backbone. However, further studies are required to confirm this hypothesis.

All three polymers showed desirable *in vitro* characteristics with **HB-HPMA-7** and **HB-HPMA-20** exhibiting the most ‘stealth-like’ properties in the fluorescence biodistribution assay. However, **HB-HPMA-7** had the highest accumulation in the spleen and liver tissues with relatively low tumour uptake in the PET-CT

biodistribution assay. Based on these findings, **HB-HPMA-20** was selected as the particles size of choice for the development of HB-HPMA-Drug conjugate system for the delivery of chemotherapeutic drugs to pancreatic cancer cells.

4.5 Chapter acknowledgements

I would like to acknowledge Dr Robert Cavanagh for macrophage cytotoxicity and uptake work, Dr Phillip Clarke and Alison Ritchie for the fluorescence *in vivo* biodistribution assay, Dr Nicholas Fletcher, Dr Zachary Houston and Theo Crawford for the PET-CT biodistribution assays and Programme Grant for Next Generation Biomaterials Discovery for funding my trip to Brisbane for the PET-CT work.

4.6 Supplementary Information

Stock solutions of Cy5 (1, 2, 2.5, 5, 10, 20, 30 and 40 µg/mL) were prepared in DMSO for standard calibration curve. The absorbance of each solution was recorded at 670 nm on a UV-Vis spectrophotometer at room temperature. A standards curve (Figure 4-20, SI) (regression equation: $y = 0.02065x + 0.04962$, $R^2 = 0.9994$) was obtained by plotting the UV absorbance against Cy5 concentration.

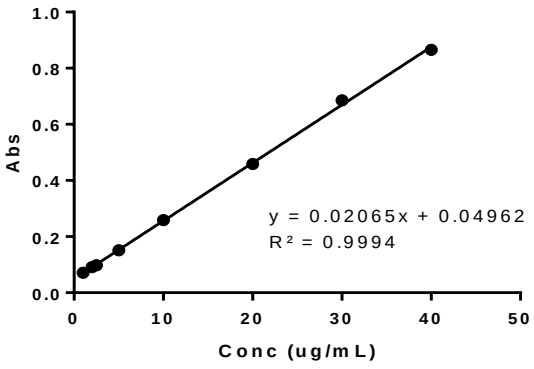


Figure 4-20 Standard calibration curve of Cy5 stock solutions. Absorbance was measure at 670 nm.

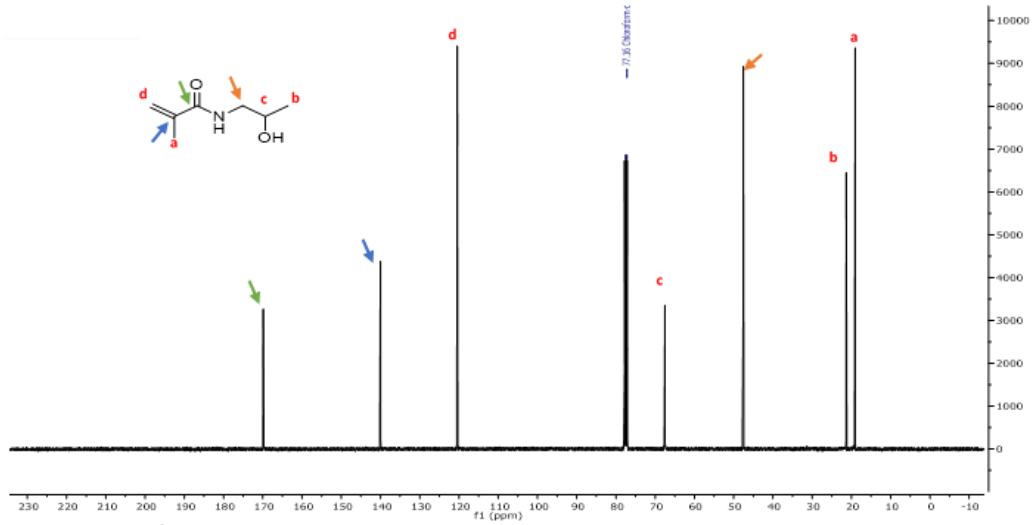


Figure 4-21 ^{13}C NMR spectrum of HPMA monomer in $CDCl_3$.

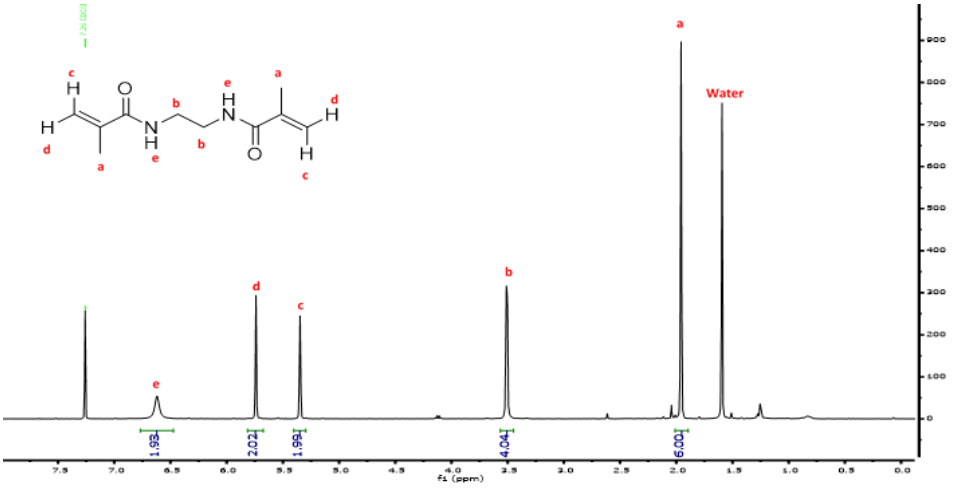


Figure 4-22 ^{1}H NMR spectrum of EDMA in $CDCl_3$.

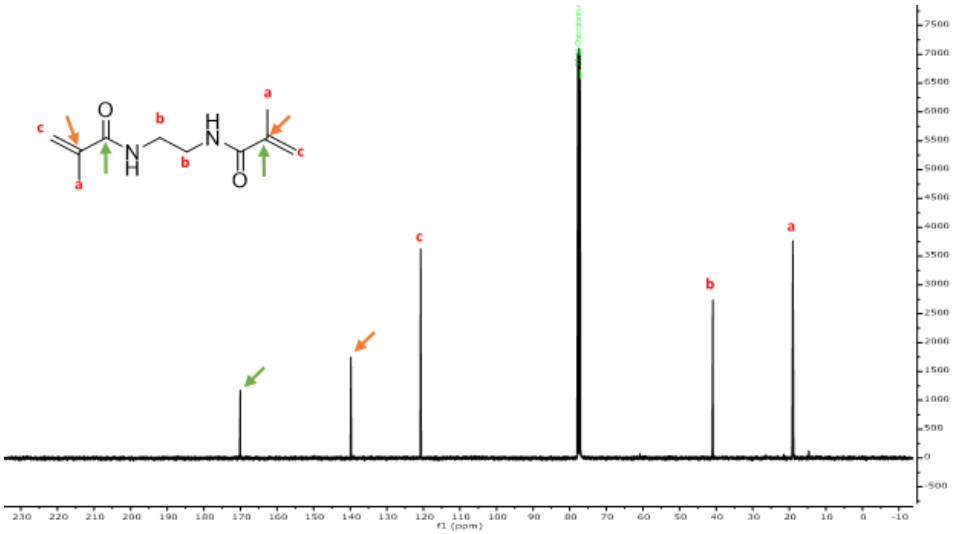


Figure 4-23 ^{13}C NMR spectrum of EDMA in $CDCl_3$.

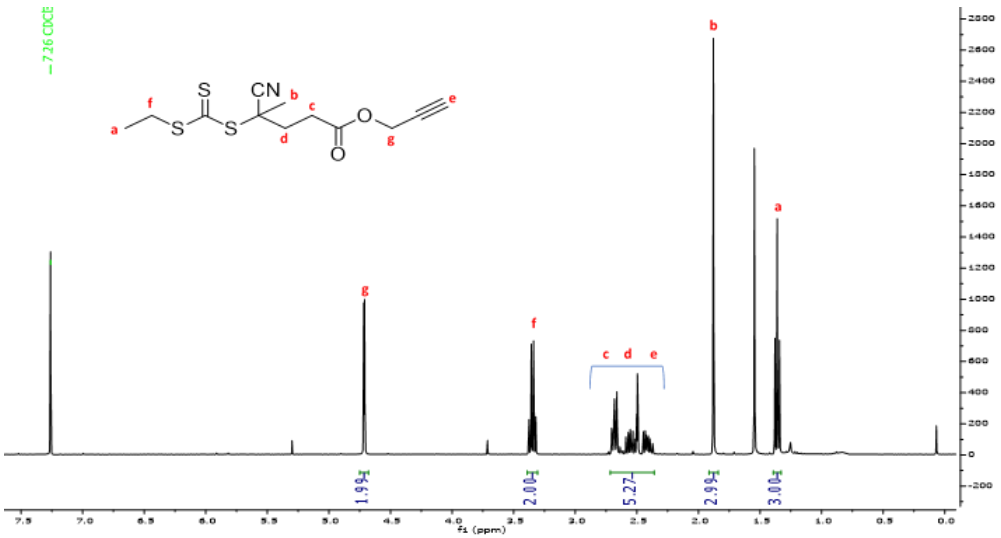


Figure 4-24. ^{1}H NMR spectrum of Alkyne-CTA in $CDCl_3$.

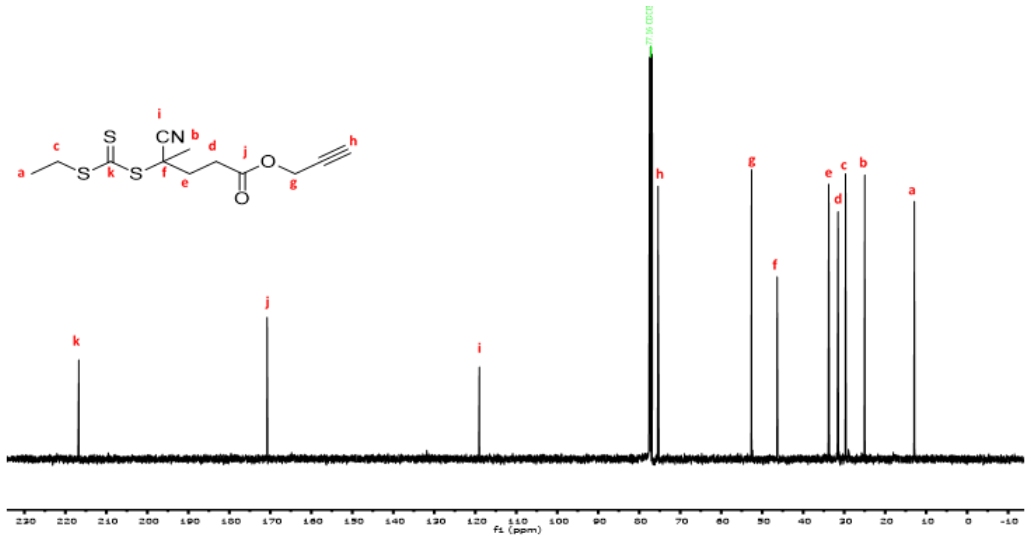


Figure 4-25 ^{13}C NMR spectrum of Alkyne-CTA in $CDCl_3$.

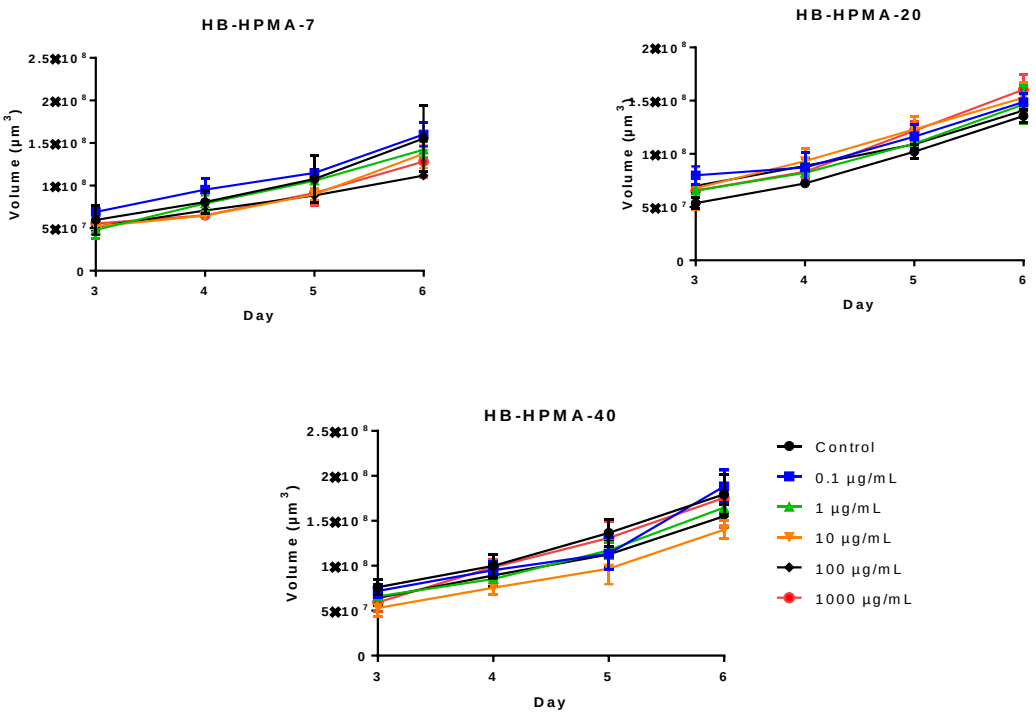


*Figure 4-26. Graphs showing changes in spheroid volume over the 72 hours incubation with the three **HB-HPMA** polymers, (N = 4).*

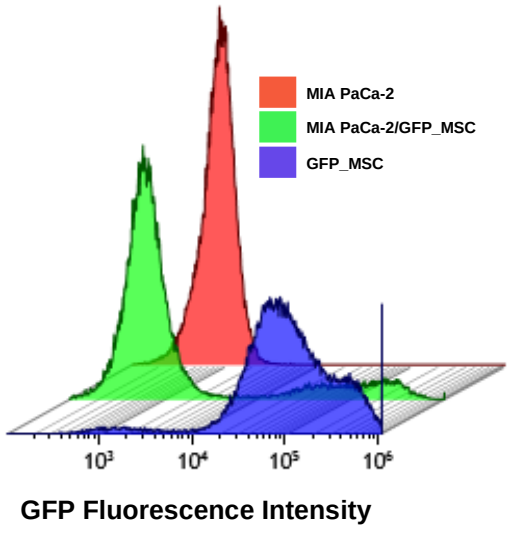


Figure 4-27 FACS histograms showing control MIA PaCa-2 only, mixed MIA PaCa-2/GFP_MSC and GFP_MSC only cell populations.

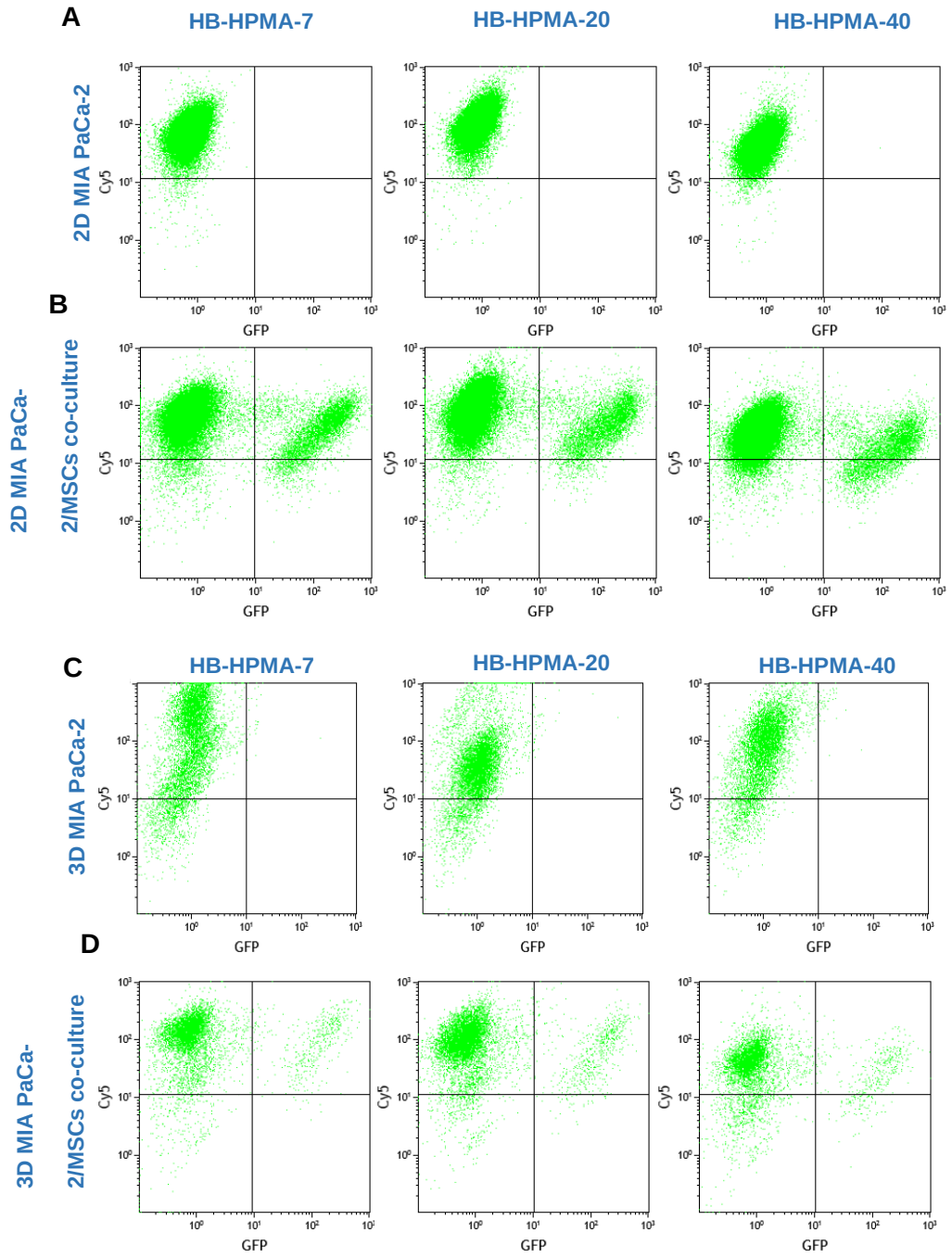


Figure 4-28 Representative FACS quadrants of cellular uptakes of Cy5-labelled HB-HPMA polymers in A) 2D MIA PaCa-2 cells, B) 2D MIA PaCa-2/MSC cocultured cells C) 3D MIA PaCa-2 cells and D) 3D MIA PaCa-2/MSC cocultured cells.

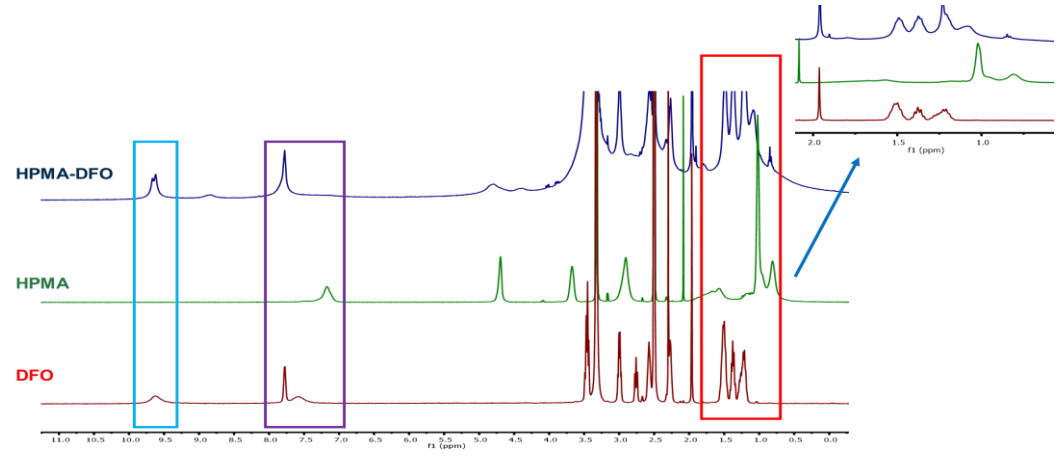


Figure 4-29 Representative ^{1}H NMR spectra for HPMA-DFO conjugation. Top) HPMA-DFO polymer. Middle) HPMA polymer and Bottom) DFO. The comparison between the different spectrum shows succesful conjugation of DFO to the backbone of the polymer.

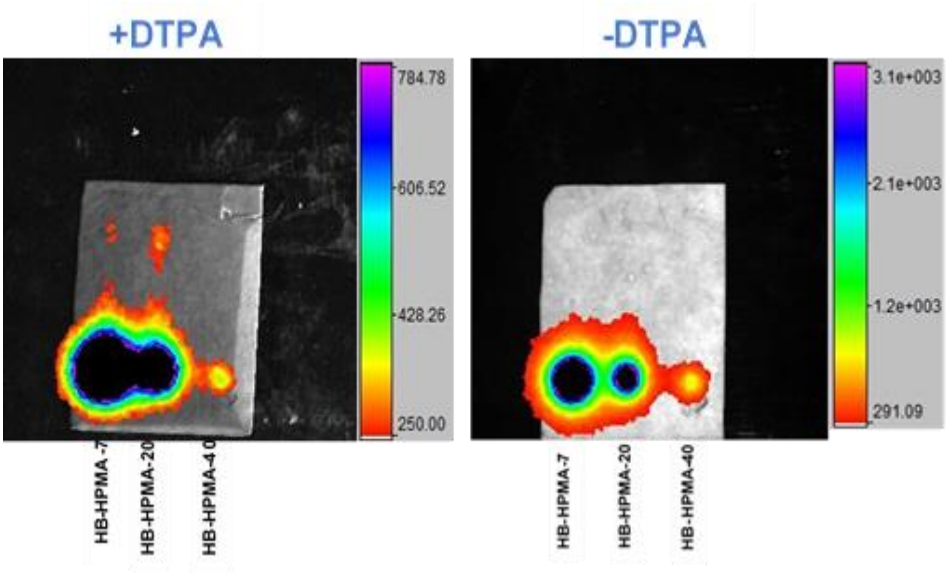


Figure 4-30 Radiographic TLC of all three polymers post ^{89}Zr labelling +/-DTPA. The signals at the bottom of the TLC represent polymer bound radioisotope and any movement up the plate represents unbound ^{89}Zr (+DTPA plate) or free DFO in the sample bound to ^{89}Zr (-DTPA plate). From the TLC plates, it is clear that the polymer solutions injected for the biodistribution assay were free from unconjugated DFO.

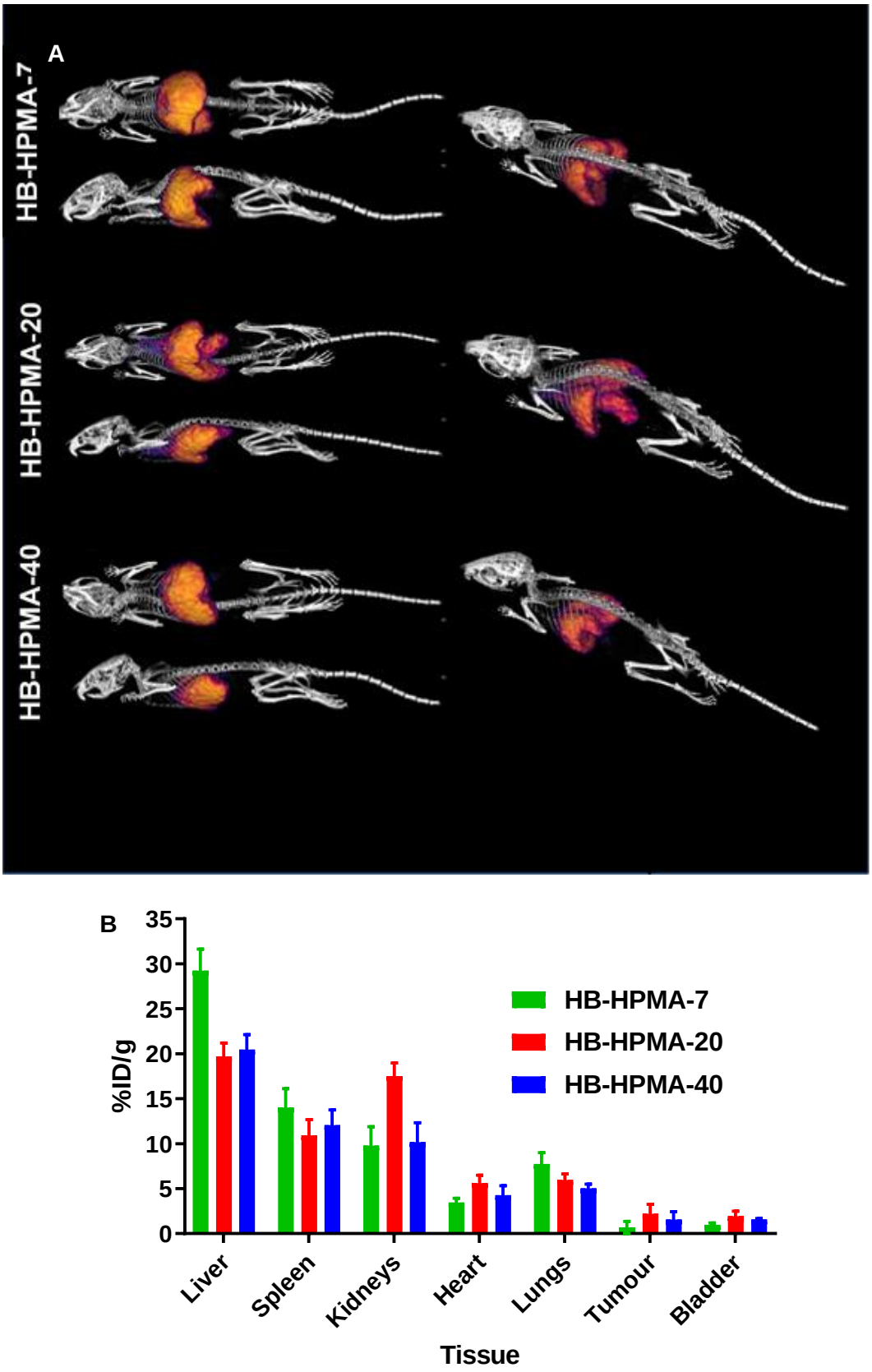


Figure 4-31 PET-CT imaging of ^{89}Zr-labelled HB-HPMA polymers in MIA PaCa-2 xenograft model. A) 3 orientations of 3D rendering of the distribution of all three polymers at 27 H post injection. B) The corresponding biodistribution profile as determined by ROI analysis of PET-CT images (n=4).

Chapter 5 Development, *in vitro* and *in vivo* evaluation of synthesised HPMA-GEM polymer

5.1 Introduction

Nucleoside analogues such as gemcitabine are one of the most important classes of chemotherapeutic drugs in the clinic.[374] Although gemcitabine is a very effective treatment option for pancreatic cancer and various other solid tumours such a breast, non-small cell lung cancer (NSCLC), ovarian and bladder cancers, the poor bioavailability of the drug dictates the administration of high doses which restricts its clinical applicability.[375-379] High doses of GEM have been associated with several serious side effects in patients such as neutropenia, myelosuppression, thrombocytopenia and anaemia which can affect treatment.[380, 381] In addition to this, patients can develop acquired resistance to GEM through deficiencies in dCK and nucleoside transport activities.[379] Therefore, there is a need to improve the pharmacokinetic properties of GEM in order to enhance its therapeutic index and decrease adverse side effects. Previous reports have demonstrated that modifications of the chemical structure of GEM, such as the formation of polymeric prodrugs through either the 5'-OH or the amino position can result in an improvement in enzymatic stability and blood circulation time compared to the parent drug.[149, 150] There is accordingly, a strong argument for developing chemistries and delivery mechanisms to enhance the bioavailability of GEM.

5.1.1 GEM prodrugs

Prodrug approaches for GEM involve conjugation of various moieties to the 4-amino and/or 5'-OH groups (Figure 5-1) to obtain the corresponding amide and/or ester in order to protect against deamination, prolong the release of the active molecule and

improve storage stability.

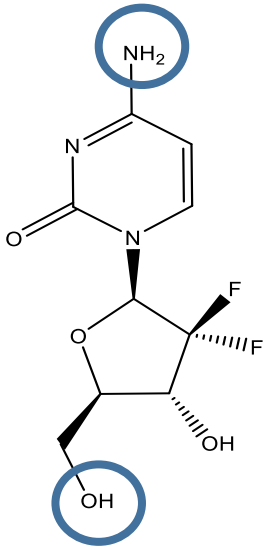


Figure 5-1 Circled groups in the structure of gemcitabine illustrates site for chemical modification.

One of these GEM prodrugs reported in the literature is the valproic acid GEM-conjugate (Figure 5-2A), which was synthesised to improve the oral bioavailability of the drug by reducing the first-pass metabolism through the inhibition of the site termination of dFdU. This conjugate was found to be chemically and enzymatically stable in systemic circulation and had comparative *in vivo* anticancer activity in HCT-116 bearing mice as intraperitoneal (*i.p.*) delivery even at a reduced dose, 7.55 mg/kg/dose and 160 mg/kg/dose for 14 days respectively.[382]

Another group covalently coupled poly(ethylene glycol) (PEG) to GEM at the amino position (Figure 5-2B) and found this conjugate to have significantly reduced clearance (21 times) compared with the parent drug after 1 hour *i.v.* administration. They also observed an enhanced intracellular localisation and increased cytotoxicity

in pancreatic cancer cell lines.[383]

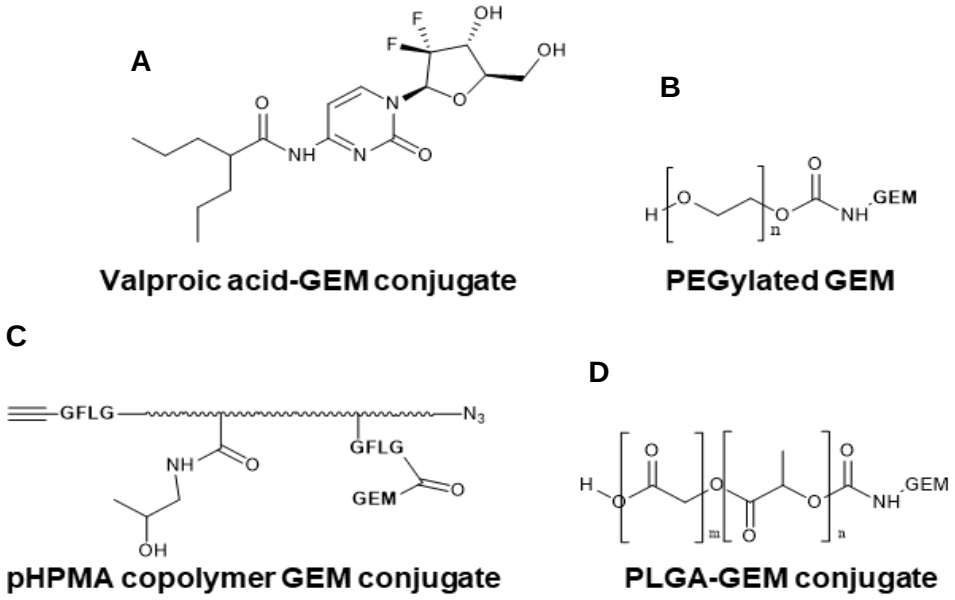


Figure 5-2 Examples of gemcitabine (GEM) prodrugs and polymer conjugates.

In a similar approach, Yang *et. al.* developed a multiblock copolymer of polyHPMA GEM conjugates (Figure 5-2C) with potential for enhanced intravascular half-life and improvement in cancer therapeutic efficacy.[384] Conjugation to the *N*-4-position of GEM is said to protect against enzymatic degradation. Khare *et. al.* demonstrated this effect when their poly(lactic-co-glycolic) acid (PLGA) GEM conjugate (Figure 5-2D) was found to be more stable against CDA present in plasma than the free drug after 72 h (approx. 40 % and 7 % respectively).[385] They also found the PLGA-GEM conjugate did not utilise the nucleoside transporters for entry into the cells and hence were less likely to succumb to the acquired resistance due to deficiencies in nucleoside transport activity commonly seen with GEM treatment.[379] These examples demonstrate how GEM prodrugs, especially through polymeric modification could improve circulation time, bioavailability, protect against enzymatic degradation with concomitant improvement in therapeutic index.

5.2 Aims

The aim of this chapter was to develop a GEM polymeric prodrug for pancreatic cancer therapy. The polymeric prodrug was based on the hyperbranched polymer platform synthesised from *N*-(2-hydroxypropyl)methacrylamide) (HPMA) *via* reversible addition-fragmentation chain-transfer (RAFT) polymerisation (Figure 5-3).

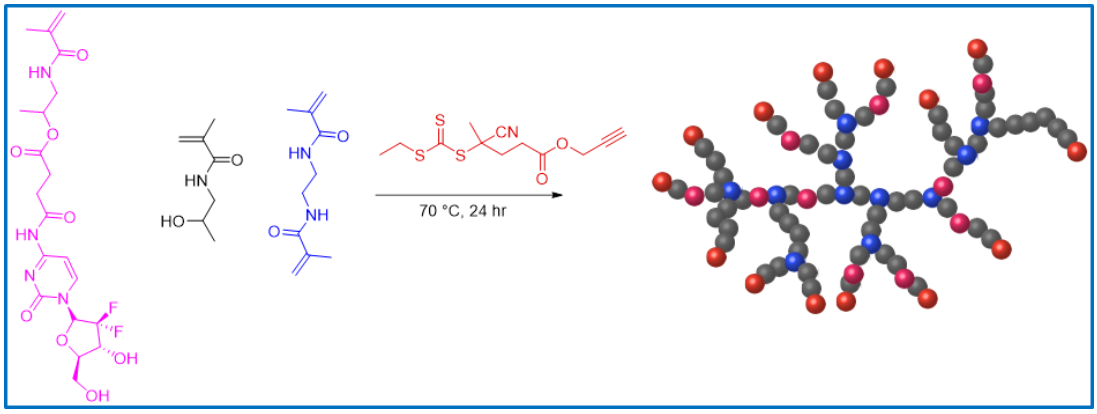


Figure 5-3 Schematic representation of the HPMA-GEM hyperbranched system.

The drug was covalently attached to the polymer at the N-4-position of GEM through an amide linker. A hyperbranched polymer architecture was chosen for high drug loading due to the possibility for attaching high numbers of drug molecules to the abundant side-chains without adversely affecting solubility, which is often a limiting factor with linear polymers. The relatively high acidic nature of the TME and upregulation of certain proteases was expected to trigger the release of the drug from the polymer backbone after an initial internalisation of the particles by the cell, which would then illicit its toxic effect. The efficacy of the polymer prodrug was extensively evaluated *in vitro* in both 2D cell culture and 3D multicellular spheroids of a pancreatic cell line. Due to the dense stromal tissue shown to surround pancreatic tumours, co-cultures of MIA PaCa-2 3D spheroids with mesenchymal stem cells were also developed to probe further the effects of stromal tissues on pancreatic cancer treatment.[310, 386, 387]

5.3 Experimental

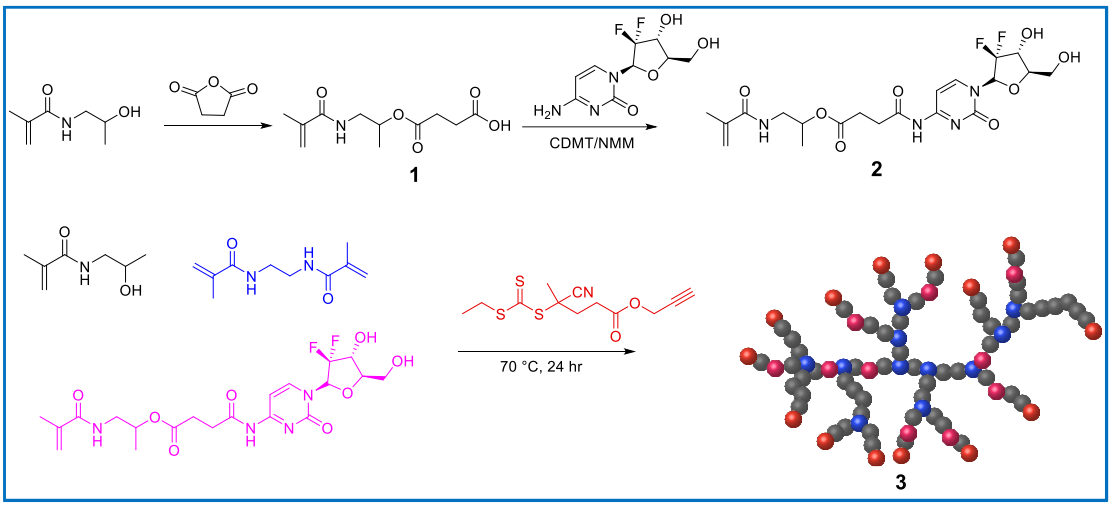


Figure 5-4 Experimental procedure for the synthesis of HPMA-GEM polymer.

5.3.1 Synthesis of 4-((1-methacrylamidopropan-2-yl)oxy)-4-oxobutanoic acid (HPMA Acid)

HPMA acid 1. HPMA (1 g, 7 mmol) was dissolved in $CHCl_3$ (5 mL) and succinic anhydride (1.05 g, 10.5 mmol) was added to the solution along with triethylamine (1.41 g, 14 mmol), 4-dimethylaminopropylamine (DMAP) (171 mg, 1.4 mmol) and DMF (1.5 mL). The reaction was stirred at room temperature and stopped after the solution turned purple. The crude was washed with 1 M HCl (50 mL) and saturated brine (3 x 50 mL) and the organic phase filtered through a silica plug first eluting with $CHCl_3$ and then with 5 % MeOH in $CHCl_3$ to yield a viscous clear gel (1.2 g, 71 %). **^{1}H NMR** (400 MHz, DMSO-d_6) δ 12.19 (s, 1H), 7.96 (s, 2H), 5.61 (s, 1H), 5.31 (s, 1H), 4.90 (td, *J* = 6.7, 5.0 Hz, 1H), 3.34 – 3.11 (m, 2H), 2.47 (s, 4H), 1.84 (s, 3H), 1.12 (d, *J* = 6.4 Hz, 3H). **^{13}C NMR** (101 MHz, DMSO-d_6) δ 173.53 (C=O), 171.67 (C=O), 167.85 (C=O), 139.87 (CH), 119.08 (HC=CH), 69.16 (CO), 43.05 (CH_2), 28.86 (CH_2), 18.63(CH_3), 17.47 (CH_3). **ESI-TOF-MS**: m/z: $[M - H]^-$ $C_{11}H_{17}NO_5$ calculated, 242.11; found, 242.10.

5.3.2 Synthesis of HPMA-GEM monomer

HPMA-GEM monomer 2. Gemcitabine hydrochloride (474 mg, 1.58 mmol) was dissolved in dry dimethylformamide (DMF) (5 mL) and HPMA acid (350 mg, 1.44 mmol) was added followed by 2-chloro-4,6-dimethoxy-1,3,5-triazine (CDMT) (278 mg, 1.58 mmol). The mixture was stirred at room temperature for 5 minutes, following which *N*-methylmorpholine (NMM) (400 mg, 4 mmol) was added over 2 minutes and the reaction stirred overnight. The mixture was concentrated onto silica gel and eluted with ethyl acetate, followed by 10% methanol in dichloromethane to yield the product as a white solid (yield 2.39 g, 68 %). **^{1}H NMR** (400 MHz, DMSO-d_6) δ 11.08 (s, 1H), 8.24 (d, *J* = 7.6 Hz, 1H), 7.95 (t, *J* = 6.0 Hz, 1H), 7.23 (d, *J* = 7.6 Hz, 1H), 6.31 (d, *J* = 6.5 Hz, 1H), 6.17 (t, *J* = 7.4 Hz, 1H), 5.61 (s, 1H), 5.30 (s, 2H), 4.89 (m, 1H), 4.17 (dd, *J* = 16.9, 10.3 Hz, 1H), 3.94 – 3.60 (m, 3H), 3.25 – 3.12 (m, 2H), 2.75 – 2.65 (m, 2H), 1.83 (s, 3H), 1.23 (s, 1H), 1.11 (d, *J* = 6.4 Hz, 3H). **^{13}C NMR** (101 MHz, DMSO-d_6) δ 173.37 (C=O), 172.12 (C=O), 168.28 (C=O), 162.99 (CN), 154.64 (C=O), 145.20 (C=CH), 140.31 (CF), 119.52 (HC=CH), 96.35 (CH), 81.48 (CO), 69.66 (CO), 43.53 (CO), 31.81 (CH_2), 28.83 (CH_2), 19.09 (CH_3), 17.93 (CH_3). **ESI-TOF-MS:** m/z: $C_{20}H_{26}F_2N_4O_8$ $[M + H]^+$ calculated, 489.17; found, 489.18.

5.3.3 Synthesis and purification of HPMA-GEM hyperbranched polymer conjugate

The syntheses of HPMA monomer, RAFT agent and EDMA are as described in 4.2.1.

HPMA-GEM polymer 3. Hyperbranched (HB) polymers were synthesised through RAFT polymerisation, incorporating an alkyne-CTA and ethylene dimethacrylamide as branching agent, with AIBN as the radical initiator. 2-Hydroxypropyl methacrylamide (HPMA) (117.67 mg, 0.82 mmol), HPMA-GEM (100.3 mg, 0.21 mmol), AIBN (1.35 mg, 0.008 mmol), EDMA (8.06 mg, 0.041 mmol) and Alkyne-CTA (12.39 mg, 0.041 mmol) were dissolved in 50:50 *N,N*-dimethylacetamide

(DMAc) and deionised water (1.3 mL) in a 2 mL tube equipped with a magnetic stirrer bar. The tube was sealed, and the reaction mixture purged with argon for 30 minutes. The vial was placed in an oil bath at 70 °C for 24 h.

After 24 h, the polymer was precipitated dropwise into excess acetone (x3), followed by dissolving in Milli Q water and dialysing for 48 hours in a 3.5 kDa molecular weight cut-off pleated snakeskin tubing and subsequently lyophilised. The polymer was then characterised by NMR, GPC, DLS and FT-IR.

5.3.4 *In vitro* 2D cell viability assay

The activity of GEM hydrochloride (HCl) and **HPMA-GEM** polymer were measured for 72 h using a trypan blue dye exclusion test for cell viability. The cells were cultured in 24-well plates at a seeding density of 2.5 x 10^5 cells/well for 24 h. The cells were treated with either GEM HCl or **HPMA-GEM** polymer dissolved in phenol red-free DMEM culture medium at different concentrations. The culture medium in the well plates was replaced with 500 µL of sample solutions. After 72 h incubation, the medium was removed, cells treated with 400 µL phenol red-free TrypLe Express Enzyme (1X) for approximately 5 mins and diluted with 600 µL fresh medium. The suspension was then centrifuged and redissolved in 100 µL of fresh medium. An equal volume of trypan blue was added to each cell suspension and cell viability determined on a TC20 automated cell counter. Percentage cell viability was calculated as follows[347]:

$$\% \text{ viable cell} = (N_T/N_c) \times 100$$

Equation 1: where N_T is the total viable cell after treatment and N_c is total viable cell of control.

5.3.5 *In vitro* 3D cell viability assay

GEM HCl and **HPMA-GEM** polymer were prepared as solutions in media at x2 the concentration of 2D cell culture. 100 µL of the sample was added to each well containing 1 spheroid in 100 µL of the medium, taking the total volume to 200 µL

and the plate incubated for 72 h. Images were taken immediately prior to treatment and every day thereafter for 3 days for spheroid volume analysis. For co-culture experiments, MIA PaCa-2 and MSC cells were seeded at 1 x10^3 cells each/well. Seeding density and times were predetermined *via* optimisation of the MIA PaCa-2 and MIA PaCa-2/MSC co-culture spheroid formation (Chapter 3).

5.3.6 CellTiter-Glo® 3D cell viability assay

CellTiter-Glo® 3D cell viability assay determines cell viability through quantification of adenosine triphosphate (ATP) levels as a marker of metabolically active cells. At a time period of 72 h post-treatment of the spheroids, the plate was equilibrated to room temperature for approximately 30 minutes. 100 µL of cell culture medium was taken from each well and replaced with an equal volume of assay-ready CellTiter-Glo® 3D solution. The contents of the plate were mixed vigorously for 5 minutes to induce cell lysis, the plate incubated at room temperature for an additional 25 minutes and analysed for luminescence.

5.4 Results and discussion

5.4.1 Synthesis of HPMA-GEM polymer conjugate

In order to produce a polymerisable gemcitabine prodrug with similar reactivity to the backbone of the polymer, a strategy was devised to modify the secondary hydroxyl group of HPMA to serve as a functional handle for covalent attachment of the drug.

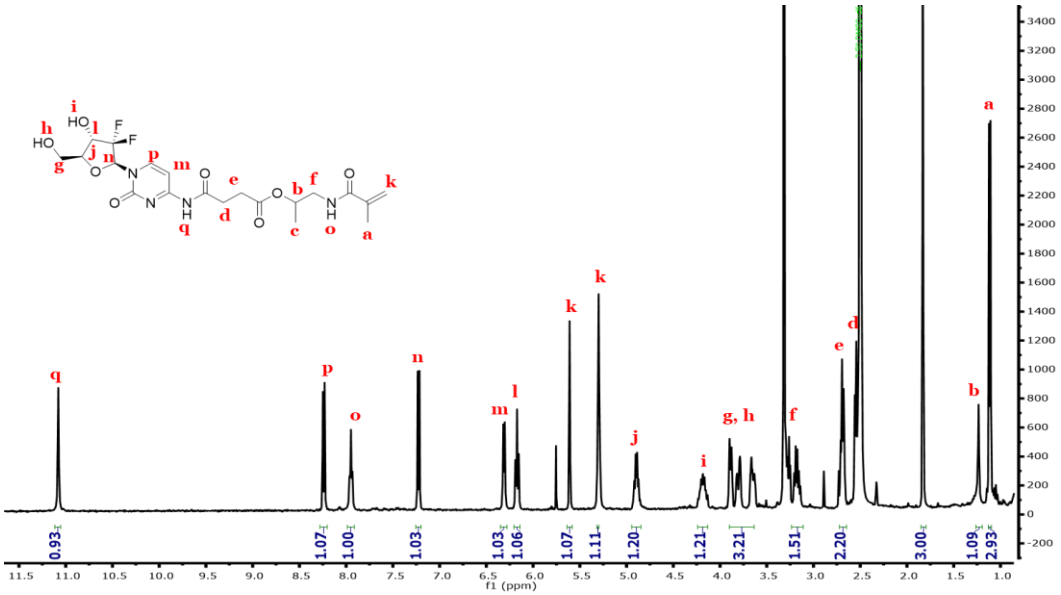


*Figure 5-5 ^{1}H NMR of **HPMA-GEM** monomer in DMSO-d_6.*

In addition, a spacer group was introduced between the backbone of HPMA and GEM such that hydrolytic cleavage of the drug from the polymer might be less sterically hindered, and that reaction at the alkenic sites during polymerisation might also be less sterically encumbered. The final prodrug monomer was therefore designed to be analogous to HPMA in terms of polymerisation reactivity, but with the possibility of drug release from the polymer *via* two distinct mechanisms. Drug release could occur either by ester hydrolysis close to the HPMA backbone or at the amide directly formed at the exocyclic amine of GEM. The former reaction would be less favoured again due to steric reasons, while the amide cleavage was expected to occur more readily than conventional amide hydrolyses owing to the less basic nature of the exocyclic amine. It is also of note that pancreatic tumours are rich in neutrophil-derived proteases suggesting a potential for enhanced *in situ* release of GEM from amide-linked carrier polymers.[388] For the synthesis of the monomer, HPMA was reacted with succinic anhydride to provide a carboxylic acid functional group, which was subsequently activated with CDMT in the presence of NMM. The active ester HPMA was then coupled to gemcitabine through the formation of an amide bond with the N-4 amino group. The crude reaction mixture was purified by flash column chromatography on silica gel to obtain the desired monomer. The

purity of the final product was confirmed through ^{1}H NMR

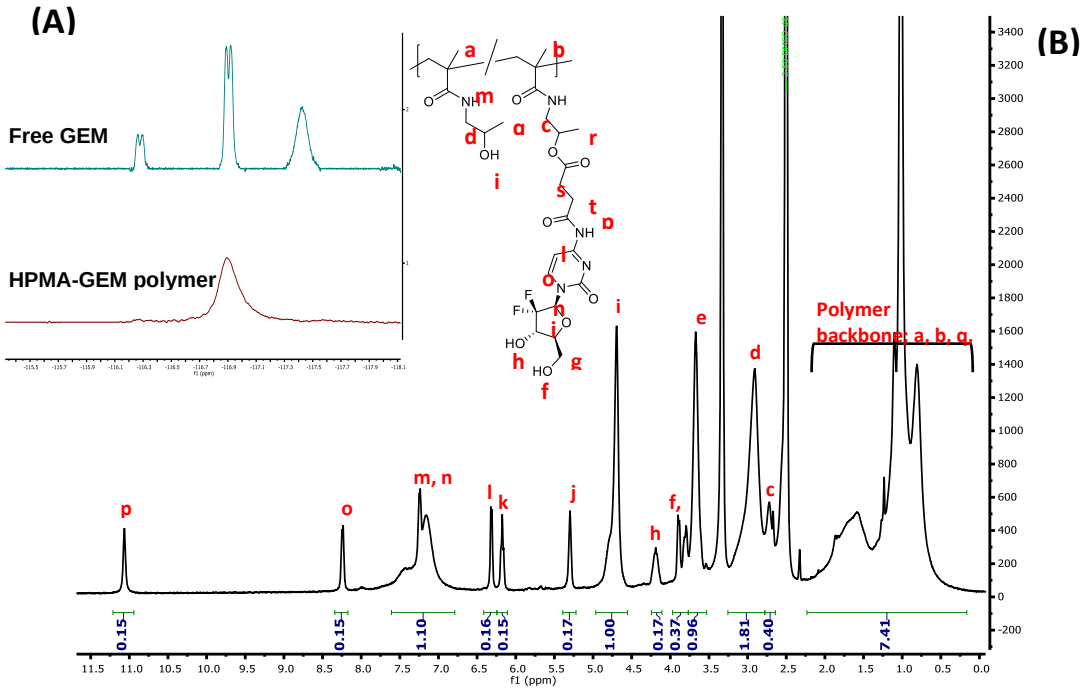


Figure 5-6 NMR spectra of HPMA-GEM polymer conjugate in DMSO-d_6. A) ^{19}F NMR showing the broadening of the fluorine peaks post polymerisation. B) ^{1}H NMR exhibiting successful polymerisation of PMA-GEM conjugate.

(Figure 5-5), ^{13}C NMR (Figure 5-13, SI) and mass spectroscopy (MW 488.17 Da) which demonstrated the presence of a single monomer species with no traces of free gemcitabine.

The final hyperbranched **HPMA-GEM** polymer conjugate was synthesised through RAFT polymerisation of the required functional monomers in 50:50 water/DMF solvent ratio to provide a final water-soluble hyperbranched polymeric architecture with high drug loading. The target functional GEM monomer compared to HPMA content per polymer chain was set at 20 mol/mol% to provide a sufficient dose while maintaining the overall water solubility and stealth properties of HPMA polymers.[389] High monomer conversion was achieved for the polymer synthesis (94 %) and the resultant hyperbranched polymer was characterised by ^{19}F NMR (Figure 5-6A), ^{1}H NMR (Figure 5-6B) and FT-IR (Figure 5-8). The physical properties of the final hyperbranched polymer are summarised in Table 8. ^{1}H NMR confirmed there was no residual monomer in the polymer product due to the absence of vinyl peaks at

5.72 and 5.32 ppm as well as the characteristic broadening of monomer resonances, indicative of polymeric materials. Monomer conversion was calculated from the ^{1}H NMR spectrum of the crude product by comparing the ratio between the vinyl protons and the polymer resonance at 3.82-3.57 ppm, the proton adjacent to the hydroxyl group. The M_n of the polymer by GPC was measured through light scattering with a dn/dc value of 0.1589 and was found to be approx. 49 kDa with a relatively narrow molecular weight distribution of 2 M_w/M_n for a hyperbranched polymer system.[390] Although it was not possible to determine the M_n of the polymer by NMR spectroscopy due to the overlap of the RAFT agent peaks with the peaks of the residues of the polymeric chain, this did not pose a problem because the *Mn* measured by GPC was taken to be the absolute molecular weight of the polymers due to their hyperbranched nature.

*Table 8 Characteristics of **HPMA-GEM** polymer.*

Polymer characteristics	
***M*$_n$ by GPC (kDa)**	49 ± 2 %
Đ (GPC)	2.1 ± 3.6 %
D$_h$ (DLS) (nm)	16.4 ± 1.8
ζ-potential (mV)	-14.9 ± -3.9
Size by TEM (nm)	17.9 ± 3.5

DLS was used to measure the size distribution and zeta potential of the **HPMA-GEM** polymer. The hydrodynamic diameter of the polymer was found to be 16.4 ± 1.8 nm with a slightly high zeta potential of -14.9 ± 3.9 mV compared with the control polymers (-6.3 ± 3.3 mV). This means that the polymer conjugate has a bigger repulsive force and therefore likely to be more stable from aggregation than control polymers.[391] The morphology of the hyperbranched polymer was also assessed

using TEM (Figure 5-7A). Similar to the control polymers, the **HPMA-GEM** polymer samples displayed spherical morphologies and low dispersity populations, therefore, were expected to be good candidates for penetration and accumulation in tumour TME.[392, 393]

The effect of the polymer conjugation on GEM was assessed by polarised optical microscopy (Figure 5-7). Conjugation of the drug to the polymeric backbone appeared to change the physical characteristic of the drug from crystalline to amorphous.

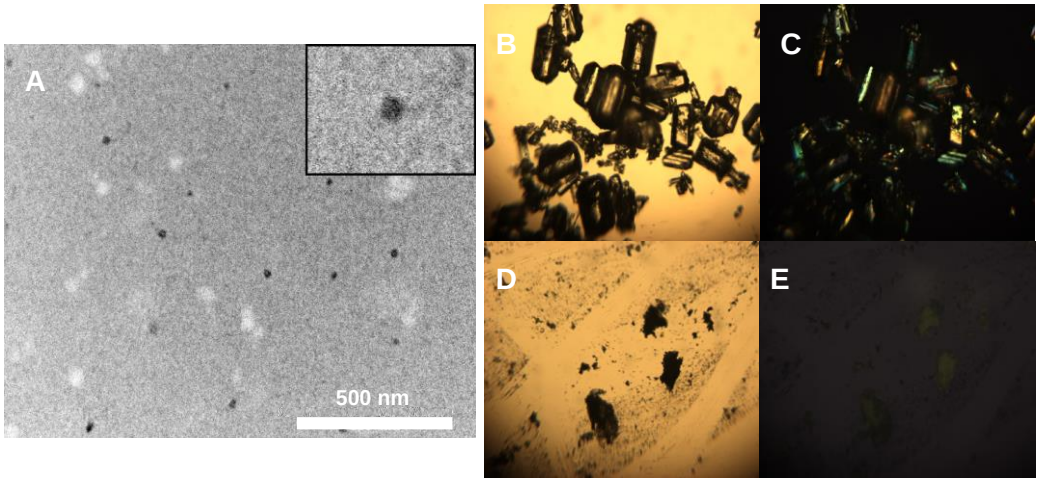


*Figure 5-7 Representative microscope images of free and conjugate GEM. (A) TEM images showing the morphology of the **HPMA-GEM** polymer. Scale = 500 nm (B) Polarised optical microscopy images of: (B) Free GEM with filter, (C) Free GEM without filter, (D) HPMA-GEM polymer with filter, (E) HPMA-GEM polymer without filter. Images were acquired at room temperature. The optical images show free GEM as crystals, however when conjugated to the polymeric backbone, the drug changes physical traits to amorphous due to the lack of birefringence (E).*

As can be seen from the optical microscope images, there is a clear and distinctive crystal structure of the free gemcitabine as confirmed by a strong birefringence (Figure 5-7C). However, in the polymeric prodrug form, the material's aspect changes from crystals to powder with a clear lack of organised structure and amorphicity confirmed by no light birefringence (Figure 5-7E). Amorphous forms of drugs have been shown to have an improved dissolution and hence bioavailability as they are more readily soluble than the crystalline form due to the high Gibbs free energy.[394, 395] This, therefore, supports the theory that polymer-conjugates have the

ability to improve the aqueous solubility of small drug molecules and as a result, enhance their bioavailability.[167]

The characteristic peaks of the main functional groups of GEM can be seen from the FT-IR spectrum of the **HPMA-GEM** polymer (Figure 5-8A). The OH and NH stretching transitions are present at 3400 and 3200 cm^{-1} respectively. The C=O stretching of the cyclic urea group can also be seen at 1750 cm^{-1}. In addition, all the transitions appear as sharp peaks typical of a crystalline molecule, as confirmed by the optical microscope analysis.

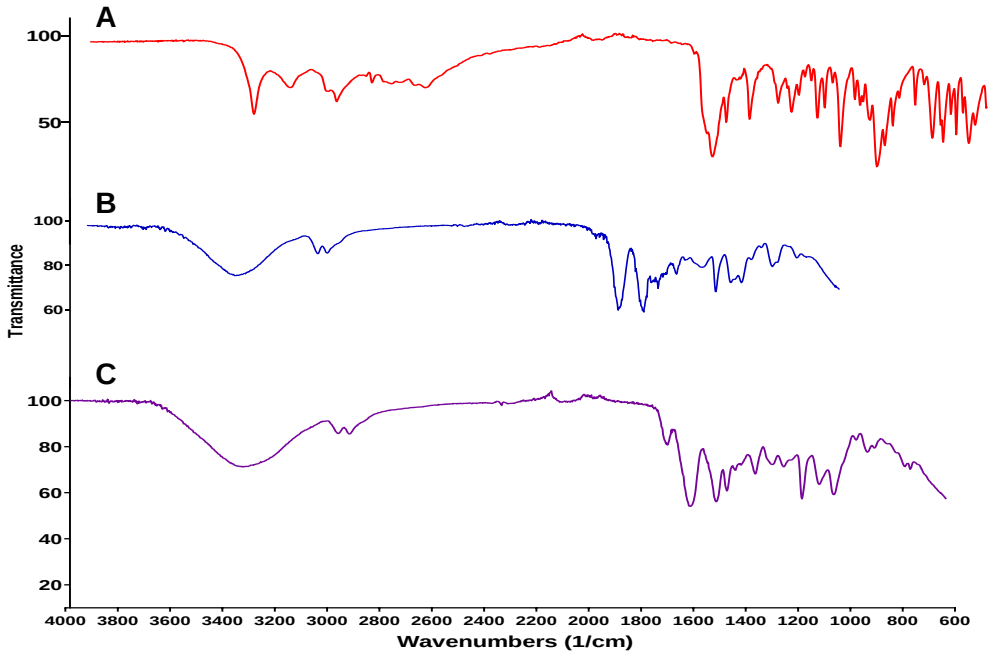


*Figure 5-8 FT-IR spectra of (A) GEM, (B) control HPMA polymer and (C) **HPMA-GEM** prodrug polymer.*

Both **B** and **C** displayed broad OH stretching peaks at around 3300-3400 cm^{-1} due to the hydrogen bond networks and the amorphicity of the systems which also aligns with the optical microscope analysis. Moreover, both **B** and **C** spectra showed the typical double peak of the C=O and CN stretching of the amide groups at 1700 and 1550 cm^{-1} respectively. In the **C** spectrum, an additional group at 1750 cm^{-1} related to the drug can be noticed confirming the conjugation of the GEM to the polymer.

Based on these characteristic features of the **HPMA-GEM** polymer, the conjugated materials were considered suitable for further evaluation in preliminary *in vitro* models.

5.4.2 *In vitro* cytotoxicity assay

The cytotoxicity of the polymer-drug conjugate compared with the free drug was tested against the MIA PaCa-2 pancreatic cancer cell line in both 2D (Figure 5-9) and 3D cell culture (Figure 5-10, Figure 5-11 and Figure 5-15, SI) (n=4 for both assays). The trypan blue dye exclusion test was used to determine the cytotoxicity of the conjugated polymer and free drug in 2D cell culture.

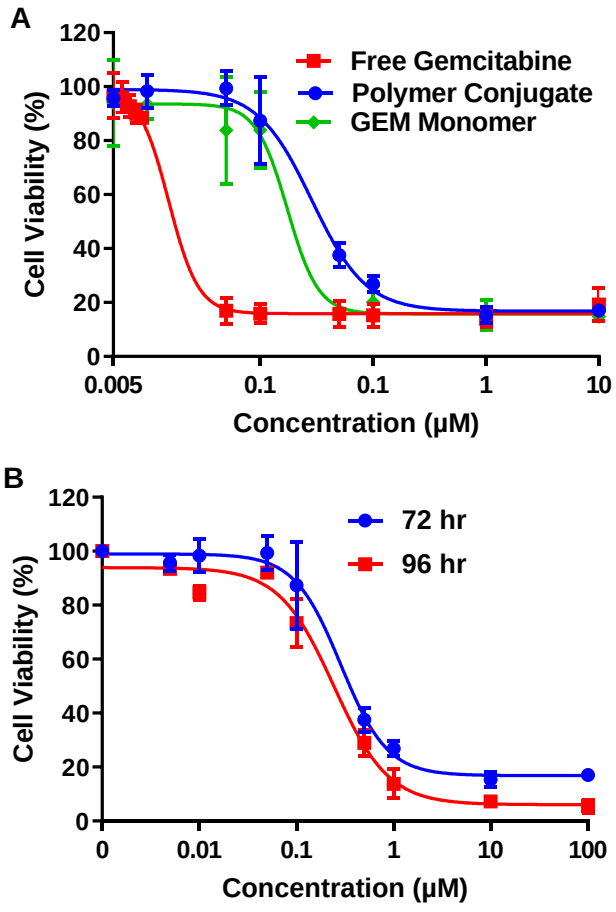


Figure 5-9 2D MIA PaCa-2 cytotoxicity assay of (A) Free and HPMA-GEM polymer conjugate incubated for 72 hours at different concentrations (the concentration of GEM was kept constant between the free drug and HPMA-GEM to allow for direct comparison between the two treatment groups). (B) Time dependent assay of HPMA-GEM - the MIA PaCa-2 cells were treated varying concentrations of HPMA-GEM and incubated for 72 or 96 hours to study the effect of incubation time on the toxicity of the polymer conjugate.

From the experimental data, the IC_{50} of the free drug and the polymer conjugate were found to be 0.015 μM and 0.286 μM (Table 9) respectively after 72 hours incubation time. This difference was expected as the drug is attached to the polymer through an amide bond, and thus requires release through gradual hydrolysis to be active.[184, 277] This effect has been observed previously for amide conjugated gemcitabine prodrugs.[184] In order to confirm the hypothesis that longer time point assays would detect increased toxicity of the conjugates, the assay was repeated with the cells incubated with the polymer-conjugate for 96 h at the same concentrations as previous experiments. It can be seen (Figure 5-9B) that the IC_{50} of the polymer-conjugate unit reduced with increased incubation time, from 0.286 ± 0.073 μM to 0.243 ± 0.057 μM, supporting the hypothesis that increased exposure of the polymer-conjugate to the cells increased the efficacy of the prodrug.

*Table 9 IC_{50} of free and **HPMA-GEM** polymer conjugate in 2D cell culture assay.*

	IC_{50} (μM)
Free Drug	0.015 (± 0.004)
GEM Monomer	0.174 (± 0.111)
Polymer Conjugate 72 hr	0.286 (± 0.073)
Polymer Conjugate 96 hr	0.243 (± 0.057)

As noted earlier, in the absence of peptidase enzymes, the hydrolysis of the drug from the polymer backbone was favoured to occur *via* the ester bond rather than the amide, this means the drug could be released with the amine group still protected. Although this has been shown not to inhibit the activity of gemcitabine but rather block the CDA-induced inactivation of gemcitabine, it could, however, alter the

efficacy of the drug against the MIA PaCa-2 cell line.[396] To assess the potential effect the protected amine could have on the toxicity of the prodrug, the cell viability assay was repeated with the GEM monomer for 72 hours and the IC_{50} calculated to be 0.174 ± 0.111 µM which was found to be higher than the IC_{50} of the free drug (0.015 ± 0.004 µM). The difference observed between the IC_{50} of the **HPMA-GEM** monomer and free drug can be attributed to the protection of the amine group in the GEM monomer assay. Given the release of the drug is *via* ester hydrolysis, leaving the amine group still protected, then the increase in IC_{50} of the **HPMA-GEM** monomer offers further explanation for the reduced efficacy of our developed polymeric prodrug in the 2D cell viability assay. However, the high uptake and the increased circulation time of the **HB-HPMA** polymer would be expected to deliver a higher concentration of the drug to the TME and hence mitigate this negative effect. Additionally, due to the dynamic physiological environment *in vivo*, the **HPMA-GEM** polymer would be exposed to different and more cells types and enzymes such as peptidases, not present in *in vitro* models. This in addition to the steric effect as described above may contribute to enhanced drug release *via* amide hydrolysis, therefore, the effect of the amine protection on the IC_{50} will be diminished. Moreover, the difference in IC_{50} between the **HPMA-GEM** monomer and polymer was expected as the monomer does not require a release to be active.

The cell-killing efficacy of both free and conjugated GEM was also evaluated in a 3D MIA PaCa-2 spheroid model. A decrease in cell viability was indicated by changes in the volume of the spheroid over the course of the treatment (Figure 5-10) and (Figure 5-15, SI), as well as the CellTiter-Glo® 3D cell viability assay at the end of the study (Figure 5-11). Initially, the assays were conducted with 3D MIA PaCa-2 monoculture spheroids treated with either free or conjugated GEM. Following this, the assays were repeated with spheroids from MIA PaCa-2 cells co-cultured with eGFP labelled MSCs to investigate whether stromal cells would have an impact on

the cytotoxicity profiles of the free and conjugated drug. Baseline microscopy images of the spheroids were taken on day 4 of growth immediately before treatment. Images were then taken every day for 72 h of treatment, and the volume was calculated for each spheroid (as described in 3.2.3.2) at the different doses.

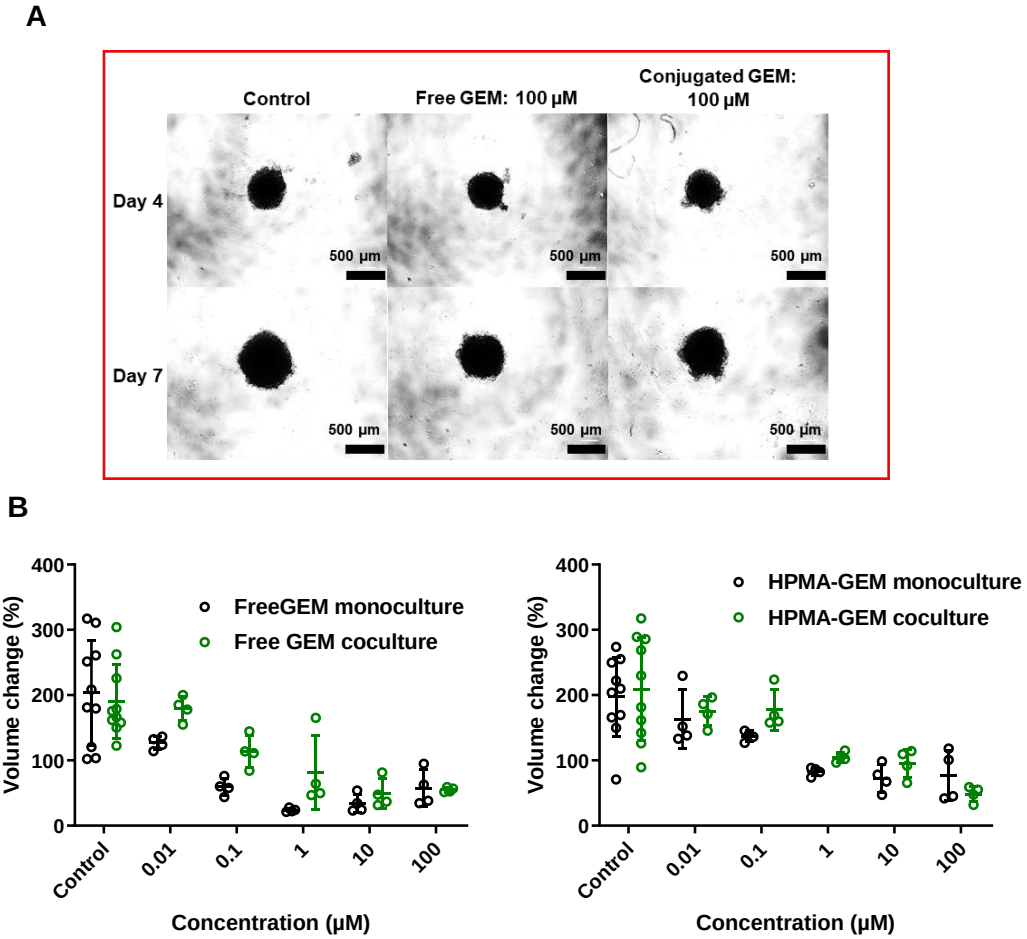


Figure 5-10 3D MIA PaCa-2 spheroids cytotoxicity assay. A). Representative microscope images of different drug concentrations to show differences in volume on day 4 and day 7 of the co-cultured population, (N = 4). B) Graph showing changes in the spheroid volume between days 4 and 7 expressed as a percentage; 1) Free GEM and 2) HPMA-GEM. The scale bar represents 500 µM.

For the lowest concentration of the free drug and the 2 lowest doses of polymer-drug, there is a constant increase in volume of the mono-cultured spheroids over the course of the assay (Figure 5-15, SI). These results are comparable with the 2D cell culture, where it was observed that too little drug was released at the lower concentrations to have significant cell toxicity. However, there was an observed reduction in cell viability at higher concentrations. When comparing the effect of the

conjugated drug on the spheroid volume in both mono and co-culture, there are no significant differences in treatment efficacy (Figure 5-11B).

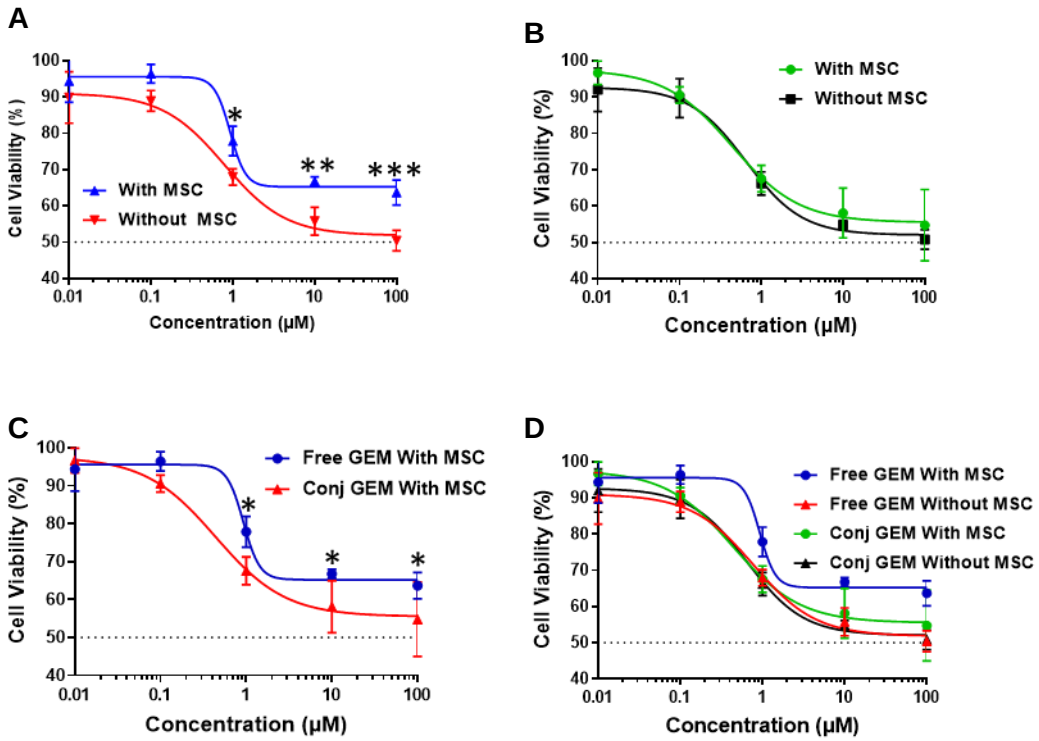


*Figure 5-11 CellTiter-Glo® 3D Cell viability assay of MIA PaCa-2 cells in mono and cocultured systems with (A) Free GEM and (B) Conjugated **HPMA-GEM** polymer. (C) MSC effect on free and conjugated **HPMA-GEM** polymer; and (D) 3D spheroid cytotoxicity. Error bars show standard deviation (N = 4). (*p ≤ 0.05, **p ≤0.01, ***p ≤ 0.001, two-way ANOVA with Sidak's multiple comparison test).*

The cytotoxicity was further evaluated by the CellTiter-Glo® 3D cell viability assay with free GEM and conjugated GEM in both mono and co-cultured (with MSC) MIA PaCa-2 spheroid models. From the data (Figure 5-11A) it was clear that the free GEM had a reduced efficacy against the cocultured compared to the monoculture system as significant differences were observed between the mono and cocultured systems of free GEM whereas no significant difference was seen between both systems with **HPMA-GEM** polymer. As MSCs are employed in the cocultured system to be a mimic for the stromal outer layer present in pancreatic cancer, it can, therefore, be concluded that the presence of the stroma negatively affects the efficacy of free GEM compared with **HPMA-GEM** polymer conjugates.

In addition, significant differences were seen between the data for conjugated and free GEM in the cocultured system (Figure 5-11C), whereby the conjugated GEM appeared to be more potent at the same concentration and incubation time. Therefore it is reasonable to assume that the delivery of GEM using the polymer is able to mitigate some of the deleterious effects stromal cells have on pancreatic cancer treatment, potentially as a result of the enhanced penetration of the polymer material.[397]

Furthermore, it was apparent that the effects of the free drug and conjugate were different between the 2D and 3D assays. It was not possible to determine the IC_{50} value for both the free and conjugated GEM in the spheroid model since, at the highest concentration (100 µM), more than 50 % of the cells were still viable. This outcome was also described by a group that studied the effect of gemcitabine in both 2D and 3D cell culture models.[326] It has been reported that a fast initial drug release, and thus exposure of the spheroids to the high concentration of free drug primarily, can lead to possible cessation of cellular uptake of further drug molecules due to apoptotic peripheral cells. This can, therefore, lead to reduced exposure of the drug to the cells at the core of the spheroid hence higher IC_{50} of chemotherapeutic agents observed in 3D cell culture model over 2D.[350] Moreover, it has been reported that 3D cell culture of pancreatic cancer cells has been shown to have an increased expression of some resistance genes leading to increased drug resistance in 3D cell culture compared with 2D.[398] Therefore, the increased IC_{50} in 3D spheroids could also be attributed to upregulation of these genes conferring drug resistance, in addition to increase in pro-surviving signals and reduction in penetration of the anticancer drugs.[399-401] It is for this reason that, 2D cell culture models may not replicate pathophysiological events as observed in *in vivo* models and hence do not provide an effective method for the evaluation of chemosensitivity in comparison to more realistic results from 3D cell culture.

The reduced sensitivity of GEM to the 3D model compared with 2D was more pronounced with the free drug cohort. This could be because the polymer conjugate is able to exploit cellular transport pathways that are not available to free drugs.[402, 403] Macromolecules are known to utilise several transport mechanisms across biological barriers for tissue access, such as using the transcytosis pathways followed by natural macromolecules in addition to endocytosis, the primary entry route for polymer therapeutics.[404] These mechanisms working together can increase the accumulation of the polymer conjugate intracellularly over the free GEM. For example, transcytosis mechanism may be exploited in the **HPMA-GEM** polymer assay to shuttle the conjugate deep into the core of the spheroid increasing the availability of the attached GEM to all cells. This transcellular penetration of macromolecules was also described by Lu *et. al.* in the delivery of doxorubicin to pancreatic multicellular tumour spheroids.[402] However, as described in 1.2.3, the transport of free GEM intracellularly is *via* nucleoside transporters and in addition to its low molecular weight, this phenomenon will not be observed in free drug treatment group affecting the efficacy of the treatment as can be seen from the cell viability assay data (Figure 5-11).

Lastly, the PET-CT biodistribution assay as described in Chapter 4 showed an enhanced uptake of all particles in the liver and spleen which may be problematic in the use of these polymers for the treatment of pancreatic cancer due to the potential

for hepatic and splenic toxicities.

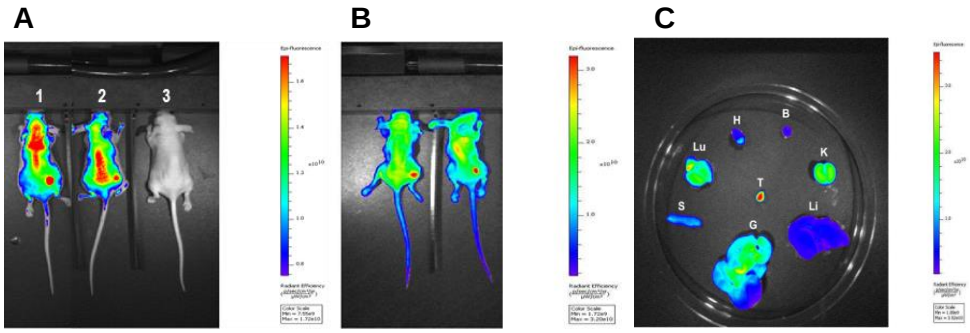


Figure 5-12 Optical images of mice, organs and tumour. A) In vivo images acquired at 72 hours post administration of the first dose of HPMA-GEM (1-2) and free GEM group (3). B) In vivo images acquired at 72 hours post injection of HPMA-GEM second dose C) Following excision from representative mouse 72 hours post administration of the second dose of HPMA-GEM. H heart, Lu lungs, S spleen, T tumour, Li liver, G gut, K kidneys, B blood.

However, preliminary data from the *in vivo* therapeutic assay with the **HPMA-GEM** polymer displays a reduced Cy5 fluorescence (low accumulation) within these organs and all imaged organs compared with the tumour (greater accumulation of **HPMA-GEM** polymers). This indicates that the potential for hepatic and splenic toxicity should be less than expected due to the reduced uptake of the **HPMA-GEM** particles in the organs.

5.5 Conclusions

In this work, we have demonstrated the design, synthesis and evaluation of an **HPMA-GEM** hyperbranched system for activity against pancreatic cancer cells *in vitro*. The polymeric materials were produced *via* RAFT polymerisation using a bifunctional monomer, **HPMA** and an **HPMA-GEM** prodrug. *In vitro* cell cytotoxicity assays with the pancreatic MIA PaCa-2 cell line showed good polymer uptake in both 2D and 3D cell culture models. The cytotoxicity assay showed differences between the 2D and 3D models with the difference being attributed to the possible cessation of free drug uptake in the 3D spheroids assay due to apoptotic peripheral cells. In addition to this, the polymer conjugate appeared to fare better than the free GEM, potentially due to enhanced accumulation and penetration of the conjugates

in the spheroid model compared to the free GEM as a result of the transport mechanisms utilised by the polymer such as endocytosis and transcytosis. The efficacy of the polymer-drug conjugate, particularly in the 3D cell culture, indicates **HPMA-GEM** as a promising treatment option for pancreatic cancer. Finally, this work has highlighted the importance of adopting 3D cell culture models for the preclinical screening of cancer therapeutics.

5.6 Supplementary Information

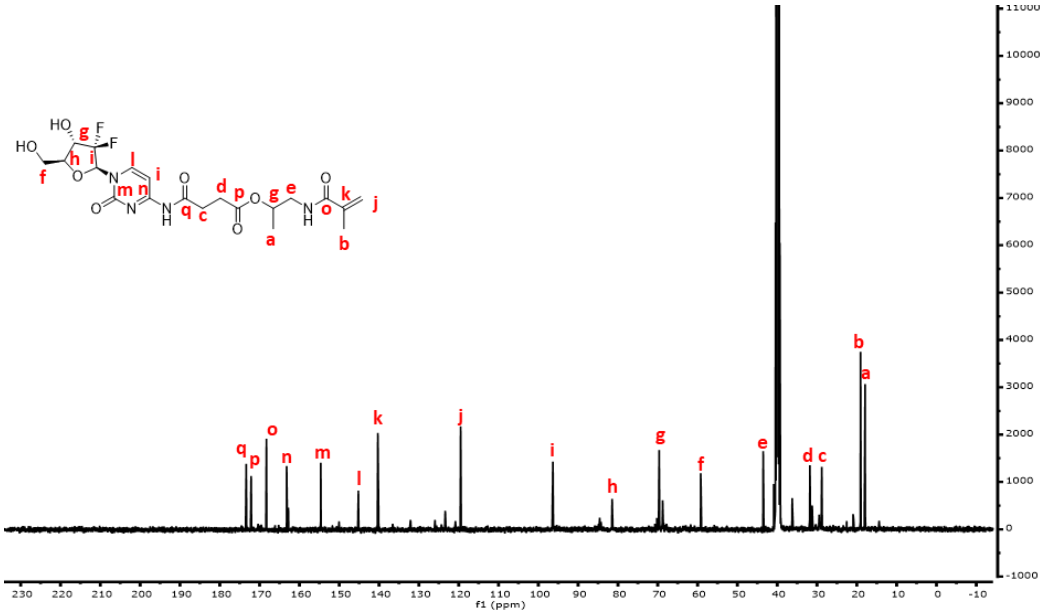


Figure 5-13 ^{13}C NMR of HPMA-GEM monomer in DMSO-d_6.

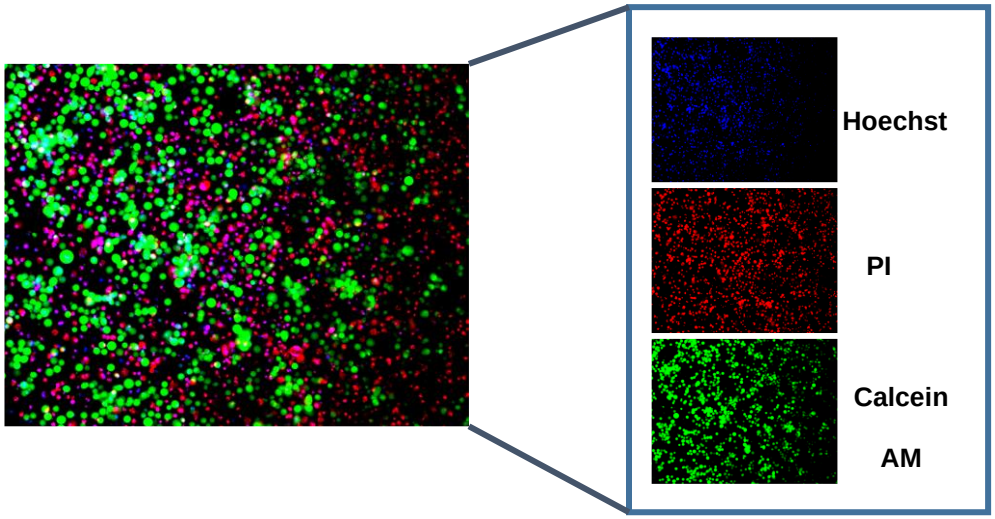


Figure 5-14 Microscopy images of 2D MIA PaCa-2 cells post 72-hour incubation with HPMA-GEM polymer (1 μM concentration). Hoechst = nuclei stain, PI = apoptotic cells and Calcein AM = viable cells. The stains were applied for approx. 20 min before imaging.

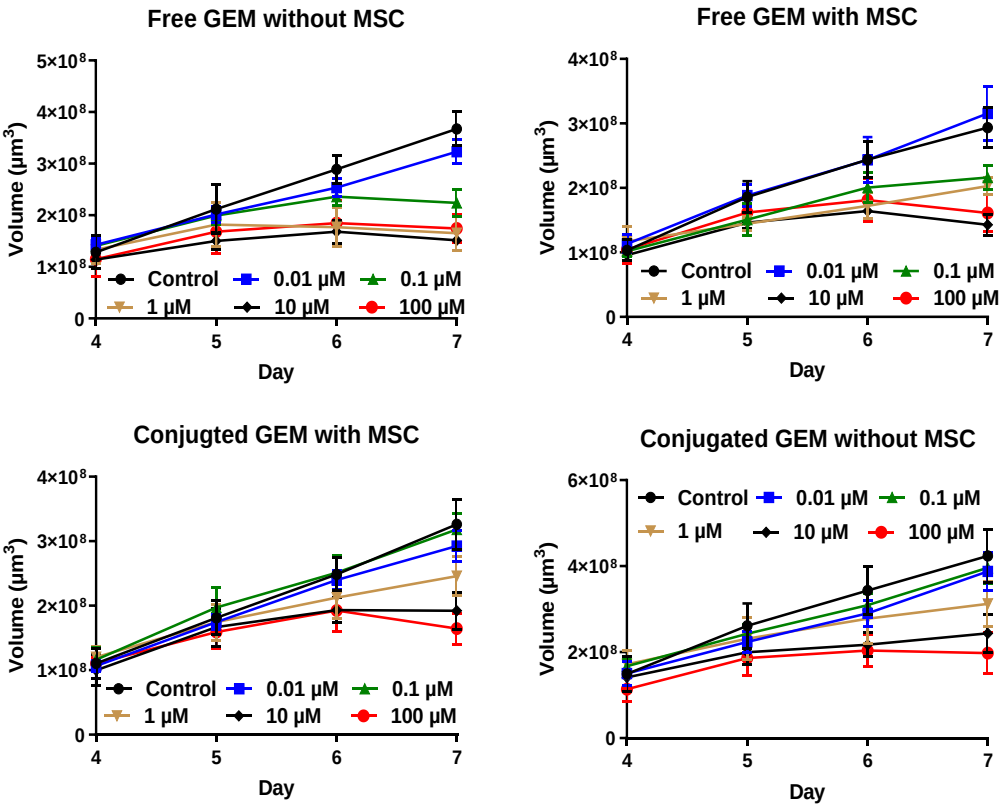


Figure 5-15 Graphs showing changes in spheroid volume over the 72 hours incubation period with free GEM and conjugated HPMA-GEM polymer, (N = 4).

Chapter 6 Combination therapy

6.1 Introduction

Combination therapy, whereby two or more therapeutic agents are given for the treatment of a disease is often the best approach for the treatment of most cancers such as pancreatic cancer.[405-407] The rationale behind combination therapy is to use drugs with different mechanisms of action thus reducing the likelihood of resistant cancer cells.[408] As already described, gemcitabine is a pyrimidine antimetabolite, primarily inducing apoptosis in cells undergoing DNA synthesis. However, doxorubicin, a topoisomerase II inhibitor, interacts with DNA through intercalation inhibiting macromolecular biosynthesis and progression of topoisomerase II, an enzyme needed to reverse supercoils in DNA transcription.[409] Due to the differences in their mechanism of action, this combination has been widely studied in the treatment of cancers such as advanced breast cancer, advanced hepatocellular carcinoma and prostate carcinoma.[410-413]

In this work, we synthesised an **HB-HPMA** based polymer conjugate carrying both gemcitabine and doxorubicin for preliminary evaluation in *in vitro* 2D and 3D pancreatic cancer models. Doxorubicin was chosen for the combination therapy with gemcitabine as a proof of concept because as mentioned above, this combination has been extensively studied. However, it should be noted that this combination is not currently used clinically for the treatment of pancreatic cancer therefore upon the establishment of this system, combinations containing drugs closer to the existing standard of care combinations, (FOLFIRINOX (5-FU, leucovorin, irinotecan and oxaliplatin) or gemcitabine with paclitaxel would be tested.

6.2 Experimental

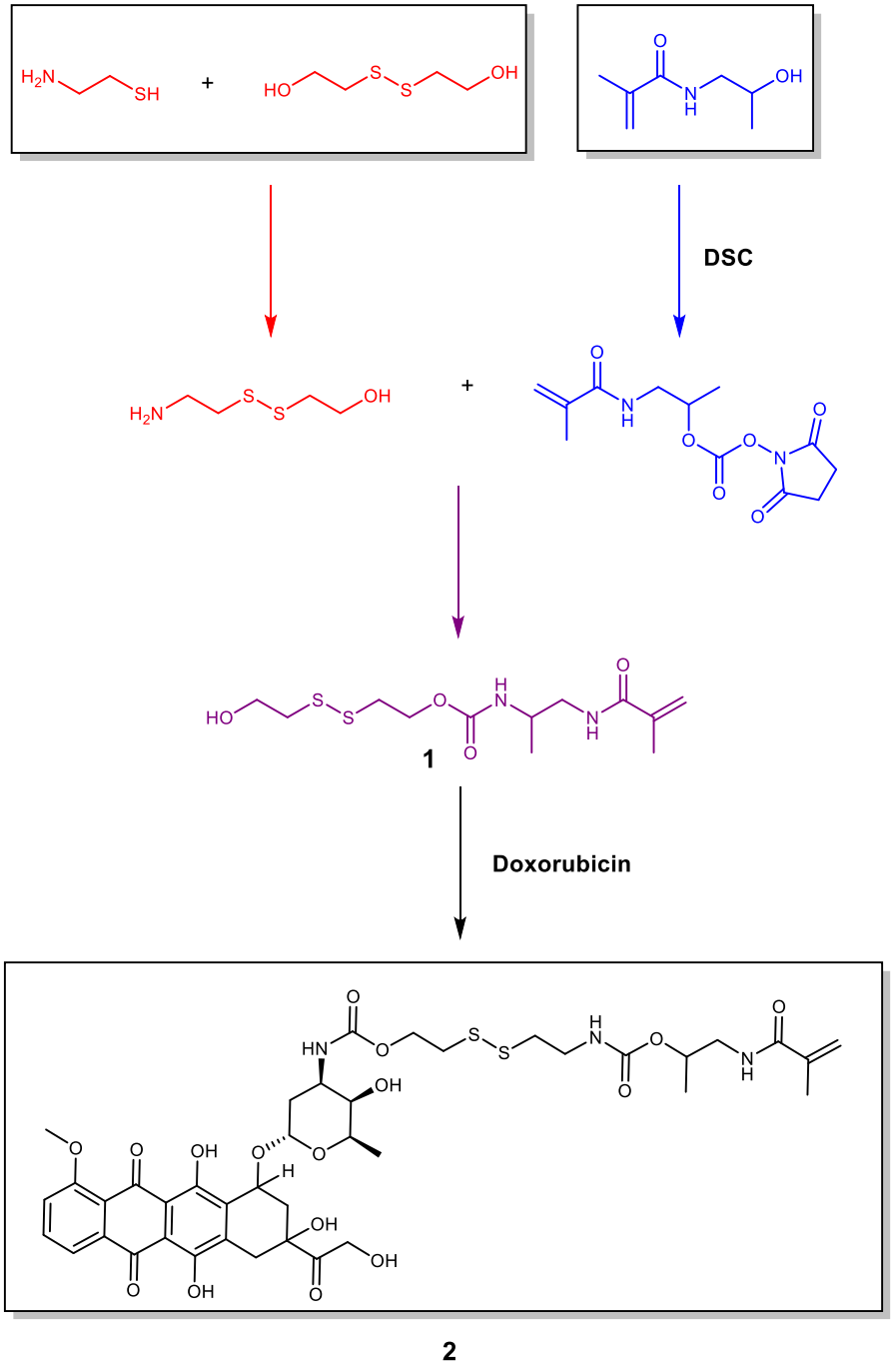


*Figure 6-1 Schematic representation of the synthesis of **HPMA-DOX** monomer.*

6.2.1 Synthesis of HPMA-aminoethyl-2' -Hydroxyethyl disulfide (HPMA-Disulfide)

HPMA-Disulfide 1. A solution of 2-hydroxyethyl disulfide (5 g, 32.4 mmol) and triethylamine (6.6 g, 64.8 mmol, 9 mL) in methanol (13 mL) was added to an ice-cold solution of cysteamine hydrochloride (3.7 g, 32.4 mmol) in methanol (20 mL) and the

solution stirred overnight at room temperature (Flask 1). The mixture was then concentrated in vacuo and resuspended in acetonitrile.

In parallel, *N,N'*-disuccinimidyl carbonate (12.5 g, 48.6 mmol) and triethylamine (4.9 g, 48.6 mmol, 6.7 mL) were added at room temperature to a solution of HPMA (4.6 g, 32.4 mmol) in acetonitrile (80 mL) and stirred overnight (Flask 2). The crude was then added dropwise to the resuspended reaction mixture in Flask 1 and stirred overnight. The reaction mixture was concentrated in vacuo, redissolved in ethyl acetate and washed with a saturated aqueous sodium hydrogen carbonate solution and a saturated saline solution. The organic layer was collected, dried with anhydrous magnesium sulfate and concentrated in vacuo. The crude was then purified by silica gel column chromatography (50:50 ethyl acetate in hexane, followed by ethyl acetate) yielding a viscous clear liquid (52 %). **^{1}H NMR** (400 MHz, DMSO-d_6) δ 7.91 (t, *J* = 5.8 Hz, 1H), 7.17 (t, *J* = 5.7 Hz, 1H), 5.63 (t, *J* = 1.3 Hz, 1H), 5.32 (q, *J* = 1.6 Hz, 1H), 4.86 (t, *J* = 5.5 Hz, 1H), 4.77 (q, *J* = 6.3 Hz, 1H), 3.62 (q, *J* = 6.3 Hz, 2H), 3.22 (ddd, *J* = 23.5, 11.9, 5.9 Hz, 4H), 2.77 (dt, *J* = 12.2, 6.6 Hz, 4H), 1.85 (s, 3H), 1.11 (d, *J* = 6.4 Hz, 3H). **^{13}C NMR** (101 MHz, DMSO-d_6) δ 168.18 (C=O), 156.34 (C=CH2), 140.46 (C=O), 119.47 (HC=CH), 69.52 (CO), 60.21 (CO), 44.05 (CH2), 41.51 (CH2), 38.00 (CH2), 19.05 (CH3), 18.50 (CH3). **ESI-TOF-MS:** m/z: $C_{12}H_{22}N_2O_4S_2$ $[M + H]^+$ calculated, 323.10; found, 323.11.

6.2.2 Synthesis of HPMA-DOX monomer

HPMA-DOX monomer 2. *N,N'*-Disuccinimidyl carbonate (DSC, 930.5 mg, 3.6 mmol) and triethylamine (367.6 mg, 3.6 mmol, 0.5 mL) were added at room temperature to a solution of HPMA-Disulfide (**1**) (780 mg, 2.4 mmol) in acetonitrile (5 mL) and stirred for 2 hours. The crude was added dropwise to a solution of doxorubicin hydrochloride (1.5 g, 2.7 mmol) and triethylamine (229.5 mg, 2.7 mmol, 0.4 mL) in DMF (20 mL) and the reaction mixture stirred overnight. The reaction mixture was concentrated in vacuo and purified by silica gel column chromatography

(ethyl acetate in hexane at a gradient from 50:50 to 100 % ethyl acetate, followed by methanol in DCM at a gradient of 1 % to 5 %) to yield the pure product as a red solid (42 %). **^{1}H NMR** (400 MHz, DMSO-d_6) δ 14.02 (s, 1H), 13.25 (s, 1H), 8.03 – 7.79 (m, 3H), 7.71 – 7.57 (m, 1H), 7.17 (t, *J* = 5.9 Hz, 1H), 6.80 (d, *J* = 8.0 Hz, 1H), 5.62 (d, *J* = 8.6 Hz, 1H), 5.45 (s, 1H), 5.37 – 5.28 (m, 1H), 5.22 (d, *J* = 3.6 Hz, 1H), 4.90 (dt, *J* = 30.1, 5.3 Hz, 2H), 4.79 – 4.66 (m, 2H), 4.58 (d, *J* = 4.6 Hz, 2H), 4.13 (dp, *J* = 17.3, 6.0, 5.2 Hz, 3H), 3.98 (s, 3H), 3.82 – 3.53 (m, 2H), 3.26 – 3.11 (m, 4H), 2.96 (d, *J* = 9.1 Hz, 2H), 2.88 (t, *J* = 6.5 Hz, 2H), 2.74 (t, *J* = 6.7 Hz, 2H), 2.25 – 2.07 (m, 2H), 1.85 (s, 1H), 1.83 (s, 3H), 1.47 (dd, *J* = 12.7, 4.6 Hz, 1H), 1.11 (dd, *J* = 16.1, 6.3 Hz, 6H). **^{13}C NMR** (101 MHz, DMSO-d_6) δ 213.80 (C=O), 186.56 (C=O), 167.70 (C=O), 160.81 (CO), 156.13 (CO), 155.87 (CO), 155.12 (C=O), 139.89 (CH), 135.55 (CH), 134.69 (CH), 134.11 (CH), 120.02 (C=CH), 119.75 (HC=CH), 110.66 (C=C), 100.31 (CO), 74.97 (CO), 69.90 (CO), 68.81 (CO), 67.98 (CO), 66.68 (CO), 63.69 (CO), 61.76 (CO), 43.56 (CN), 37.41 (CS), 36.93 (CS), 29.81 (CH_2), 25.24 (CH_2), 18.65 (CH_2), 18.62 (CH_3), 18.07 (CH_3), 17.03 (CH_3). **ESI-TOF-MS:** m/z: $C_{40}H_{49}N_3O_{16}S_2$ $[M + Na]^+$ calculated, 914.26; found, 914.24.

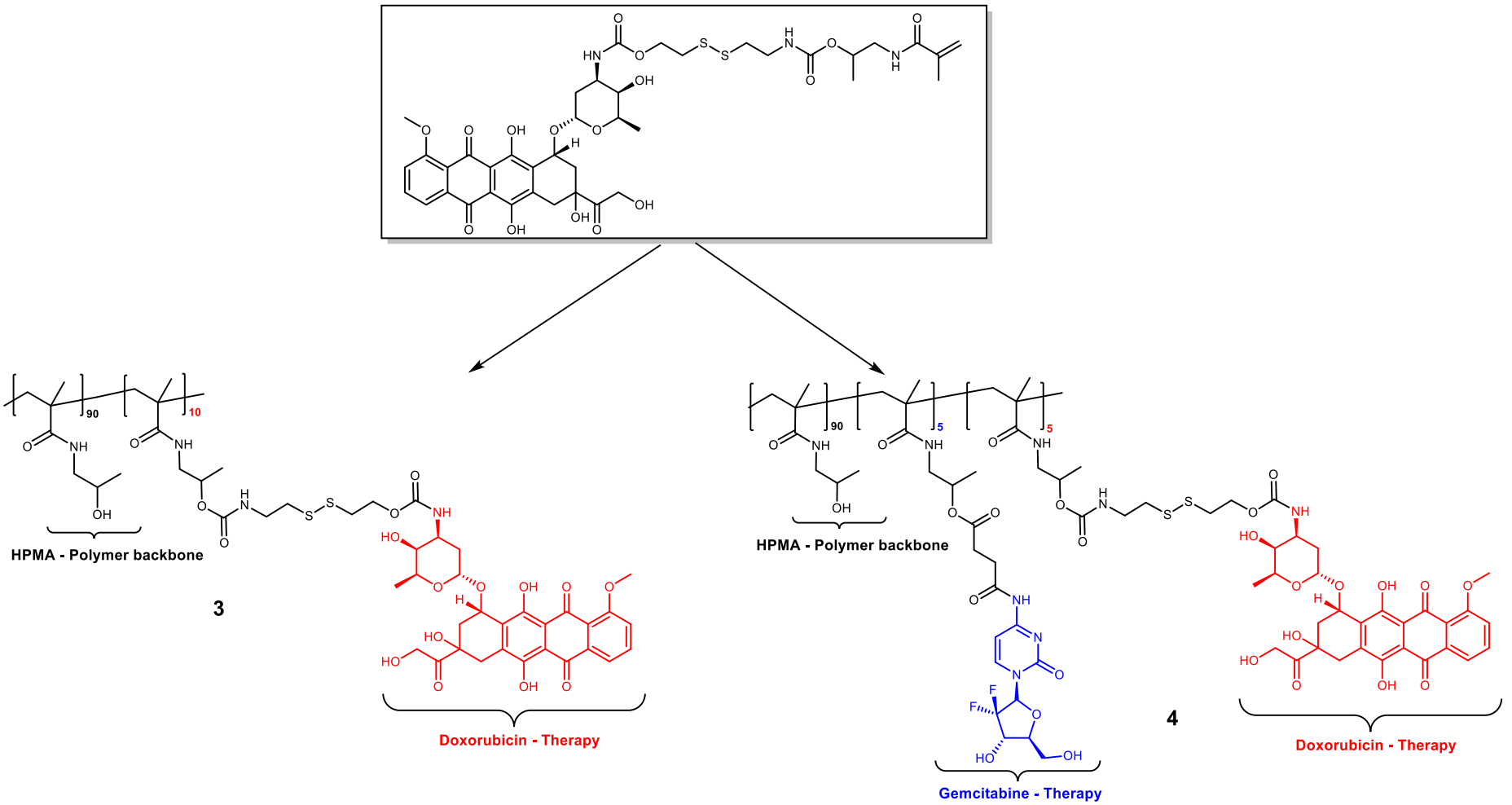


*Figure 6-2 Schematic representation of **HPMA-DOX** and **HPMA-DOX-GEM** polymers.*

6.2.3 Synthesis, characterisation and purification of HPMA-DOX

Synthesis and purification of **HPMA-DOX** polymer (**3**) were similar to **HPMA-GEM** polymer as described in section 5.3.3, substituting **HPMA-GEM** prodrug monomer with **HPMA-DOX** prodrug monomer.

6.2.4 Synthesis and purification of HPMA-DOX-GEM polymer

The combinational polymer (**4**) was synthesised as follows: HPMA (38.4 mg, 0.27 mmol), **HPMA-GEM** monomer (16.4 mg, 0.03 mmol), **HPMA-DOX** monomer (29.9 mg, 0.03 mmol), AIBN (0.44 mg, 0.003 mmol), EDMA (2.6 mg, 0.013 mmol) and Alkyne-CTA (4.1 mg, 0.013 mmol) were dissolved in 50:50 *N,N*-Dimethylacetamide (DMAc) and deionised water (0.51 mL) in a 2 mL tube equipped with a magnetic stirrer bar. The tube was sealed, and the reaction mixture purged with argon for 30 minutes. The vial was placed in an oil bath at 70 °C for 24 h.

*Table 10 Reaction conditions used in the synthesis of **HPMA-DOX** and **HPMA-DOX-GEM** polymers.*

Polymer	HPMA (mg)	HPMA-DOX (mg)	HPMA-GEM (mg)	Solvent (mL)	% conversion
HPMA-DOX	17	26.5	-	0.26	90
HPMA-DOX-GEM	38.4	29.9	16.4	0.51	93

The reaction mixture was precipitated dropwise into excess acetone (x3) after 24 hours, dissolved in Milli Q water, dialysed for 48 hours in a 3.5 kDa molecular weight cut-off pleated snakeskin tubing and subsequently lyophilised. The resultant polymer was characterised by ^{1}H NMR, DLS, GPC and TEM.

6.2.5 *In vitro* 2D cell viability assay

As described in section 5.3.4.

6.2.6 *In vitro* 3D cell viability assay

As described in sections 5.3.5 and 5.3.6

6.3 Results and discussion

6.3.1 Synthesis of the prodrug HPMA polymers

The **HPMA-DOX** monomer was synthesised through DSC coupling of DOX to the HPMA monomer *via* a disulfide linker as shown in Figure 6-1. The disulfide linker was covalently attached to the secondary hydroxyl group of the HPMA monomer through the amine end using DSC coupling and the reaction mixture purified to yield HPMA-Disulfide as a pure product (Figure 6-14 and Figure 6-15, SI).

The reaction was repeated to introduce DOX to the hydroxyl end of the linker forming a carbamate bond. The crude product was purified by flash column chromatography on silica gel to obtain the desired monomer, as depicted in the ^{1}H NMR (Figure 6-3) and ^{13}C NMR spectra (Figure 6-16, SI).

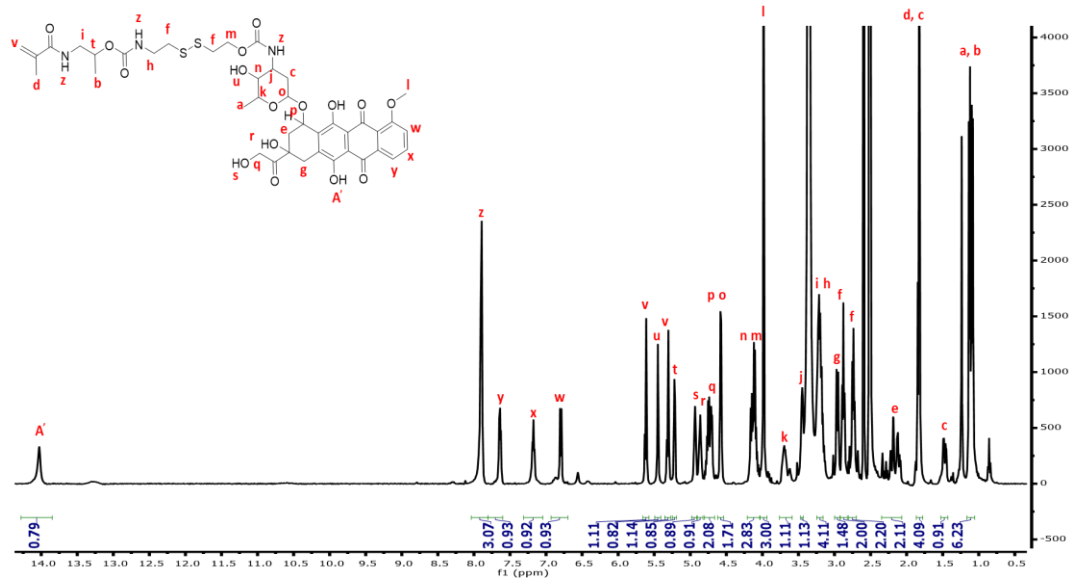


*Figure 6-3 ^{1}H NMR spectrum of **HPMA-DOX** monomer in DMSO-d_6 .*

The **HPMA-DOX** and the combinational **HPMA-DOX-GEM** polymers were

synthesised using RAFT polymerisation as described in previous chapters ensuring the percentage of HPMA monomer in the final polymer remained above 80 mol/mol% to maintain the water solubility properties of the pHPMA.

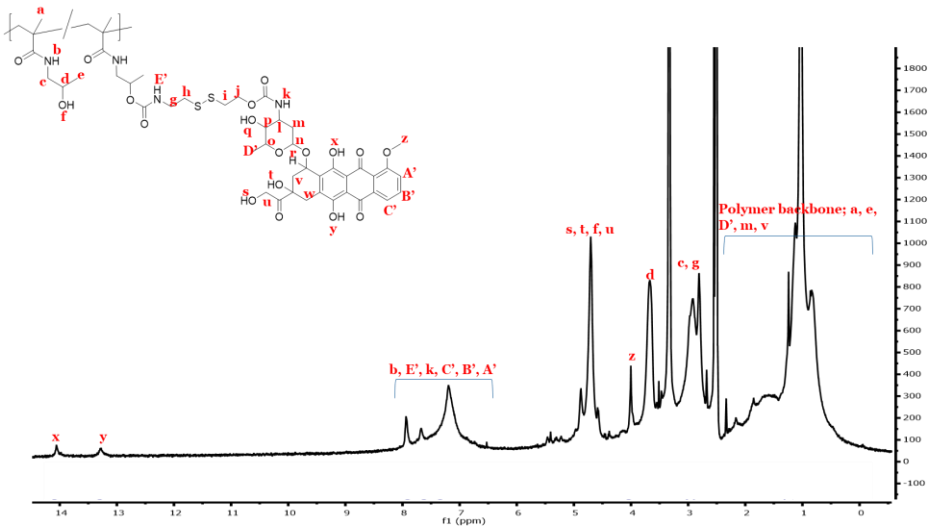


*Figure 6-4 ^{1}H NMR spectrum of **HPMA-DOX** polymer in DMSO-d_6.*

RAFT polymerisation technique was employed as conditions used for RAFT polymerisation have been shown to have no effect on the stability of the disulfide linkage.[414]

*Table 11 Physical characteristics of the synthesised **HPMA-DOX** and **HPMA-DOX-GEM** polymers.*

Polymer characteristics	**HPMA-DOX**	**HPMA-DOX-GEM**
***Mn* by GPC (kDa)**	58 ± 3 %	61 ± 2 %
Đ (GPC)	4.4 ± 3.2 %	2.1 ± 2.6 %
Dh (DLS) (nm)	14.6 ± 3.0	15.8 ± 2.0
ζ-potential (mV)	-9.6 ± -0.8	-3.9 ± -0.3
Size by TEM (nm)	12.1 ± 3.1	17.4 ± 3.7

The polymers were characterised by ^{1}H NMR (Figure 6-4 and Figure 6-5), GPC (Table 11), TEM (Figure 6-6A), and DLS (Figure 6-6B). The ^{1}H NMR traces of both polymers showed the characteristic broad polymer peaks. The characterisation data of the HPMA-DOX and HPMA-DOX-GEM polymers are summarised in Table 11.

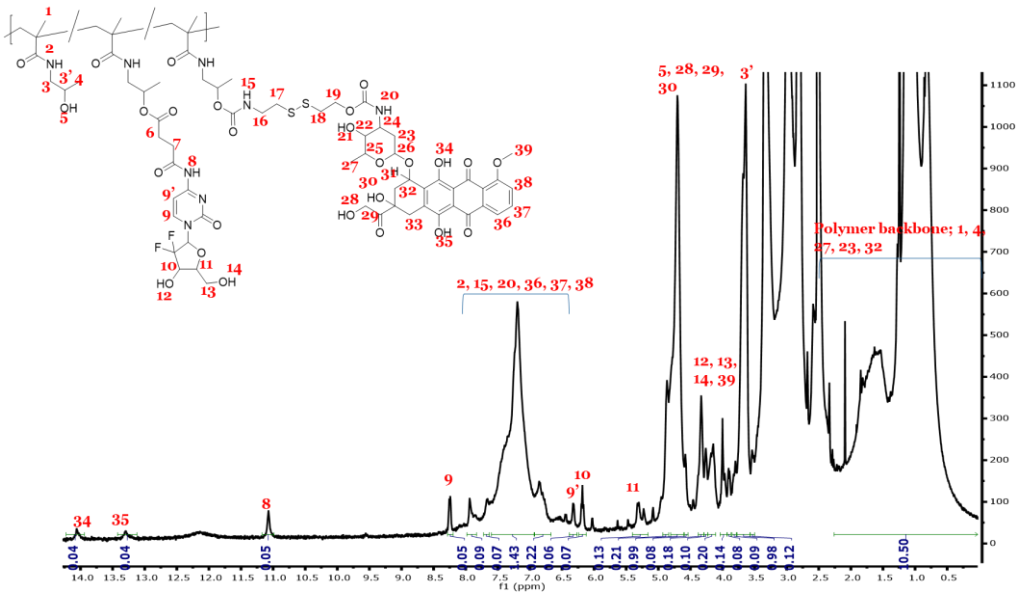


Figure 6-5 ^{1}H NMR spectrum of HPMS-DOX-GEM polymer in DMSO-d_6.

The molar masses of **HPMA-DOX** and **HPMA-DOX-GEM** were obtained from the GPC analysis of the polymers and found to b 58 kDa and 61 kDa respectively. **HPMA-DOX-GEM** afforded a narrower molecular weight distribution than **HPMA-DOX** according to the GPC traces, of 2.1 and 4.4 respectively. The hydrodynamic diameter and zeta potential of the polymers were measured by dynamic light scattering and the morphology determined using TEM. There was no significant difference between the sizes of the two polymers by DLS and TEM. The hydrodynamic diameter as measured by DLS for **HPMA-DOX** and **HPMA-DOX-GEM** was 14.6 ± 3.0 nm and 15.8 ± 2.0 nm respectively. Similar to the **HB-HPMA** and **HPMA-GEM** polymers, the TEM images of the **HPMA-DOX** and the combination polymers presented in Figure 6-6A showed spherical morphologies.

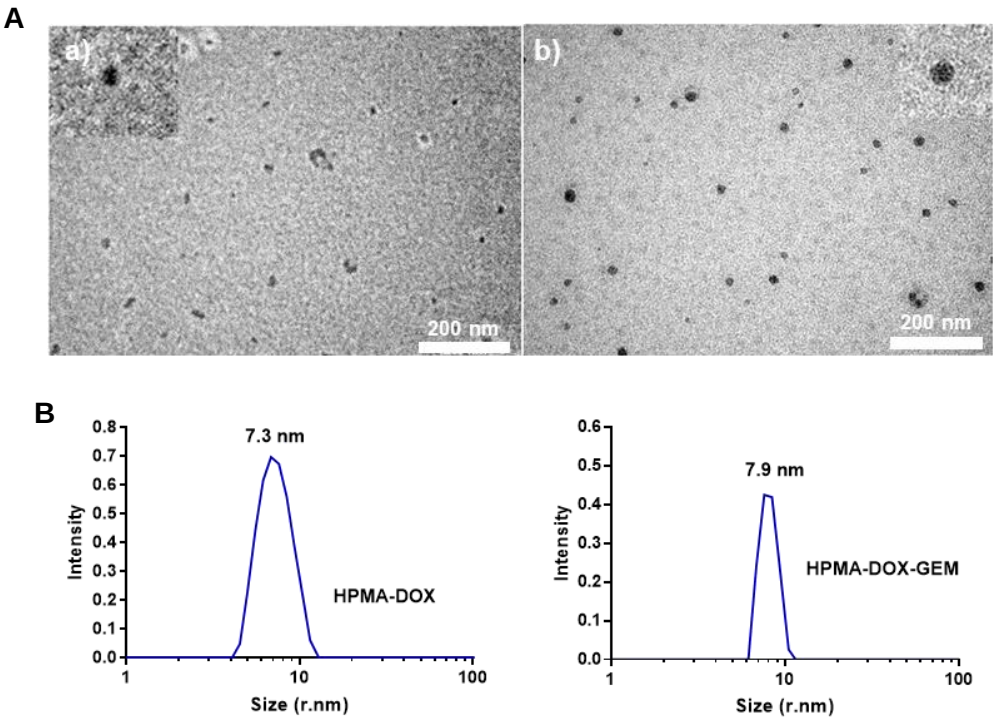


*Figure 6-6 Physical characteristics of **HPMA-DOX** and **HPMA-DOX-GEM** hyperbranched polymers. A) Representative transmission electron microscopy images of a) **HPMA-DOX** and b) **HPMA-DOX-GEM**. B) Dynamic Light scattering measurements. Scale bar= 200 nm for TEM images.*

These observations, therefore, suggested that the polymers synthesised in this work may perform similarly to the **HMPA-GEM** polymer and hence be suitable for drug delivery to the pancreatic cancer cells.

6.3.2 *In vitro* 2D cytotoxicity assay

The *in vitro* 2D cytotoxic effects of the **HPMA-DOX, HPMA-DOX-GEM-c** (HPMA-DOX-GEM-conjugated) and **HPMA-DOX-GEM-m** (HPMA-DOX-GEM-mixed) polymers on MIA PaCa-2 pancreatic cancer cell line were evaluated using trypan blue dye exclusion assay and the results shown in Figure 6-7. In all cases, the cells were exposed to the different drug concentrations for 72 hours and the viability calculated as a percentage of the control.

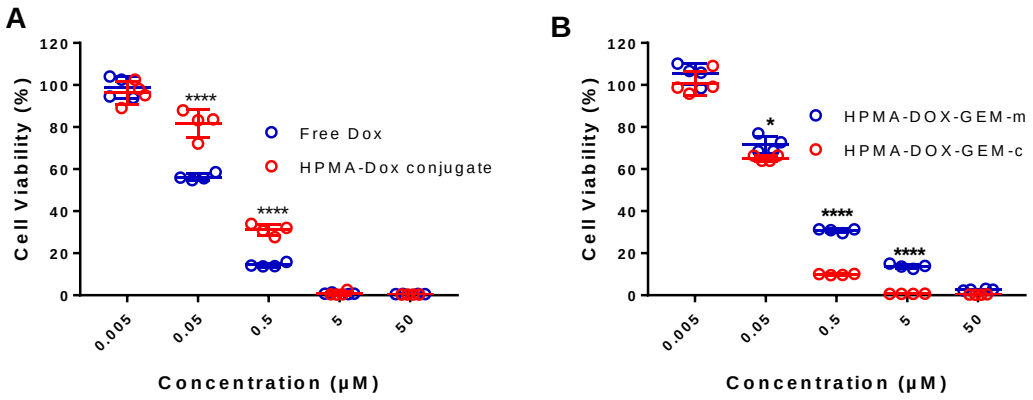


Figure 6-7 2D cell viability acitvities of MIA PaCa-2 cells incubated with free and conjugarted DOX. Error bars show standard deviation (n = 4). (p ≤ 0.05, ****p <0.0001, two-way ANOVA with Sidak's multiple comparison test).*

In the **HPMA-DOX** experiment, the IC_{50} of the free drug and the polymer conjugate were found to be 0.05 ± 0.01 μM and 0.25 ± 0.06 μM respectively (Table 12). This increase in IC_{50} of the polymer conjugate compared to the free drug is in line with the 2D cell viability data of **HPMA-GEM**. Like the **HPMA-GEM** polymer conjugate, the DOX requires a release from the polymer backbone to exert its cytotoxic effect. This release is time-dependent therefore affecting the IC_{50} of the conjugate compared with the readily available free drug in the *in vitro* 2D cell culture assay set up. As with the **HPMA-GEM** conjugate, we predict the toxic effects of the **HPMA-DOX** polymer conjugate to be time-dependent, thus acting as a controlled release system. The **HPMA-DOX** polymer is hypothesised to undergo an intracellular disulfide reshuffling which in turn triggers the release of the drug through intracellular decomposition.[414] The overall redox property of the human blood is oxidative, meaning disulfide-linked polymer-drug conjugates such as the **HPMA-DOX** remain stable in circulation.[414] Upon uptake into the cells, the overall redox potential switches to the reductive state leading to reduction of the disulfide bond to generate a free thiol group for the subsequent decomposition of the carbamate. The reshuffling and the consequent release of the drug is a favoured process due to the

formation of the stable five-membered thiocarbonate side-product (Figure 6-8).[415, 416]

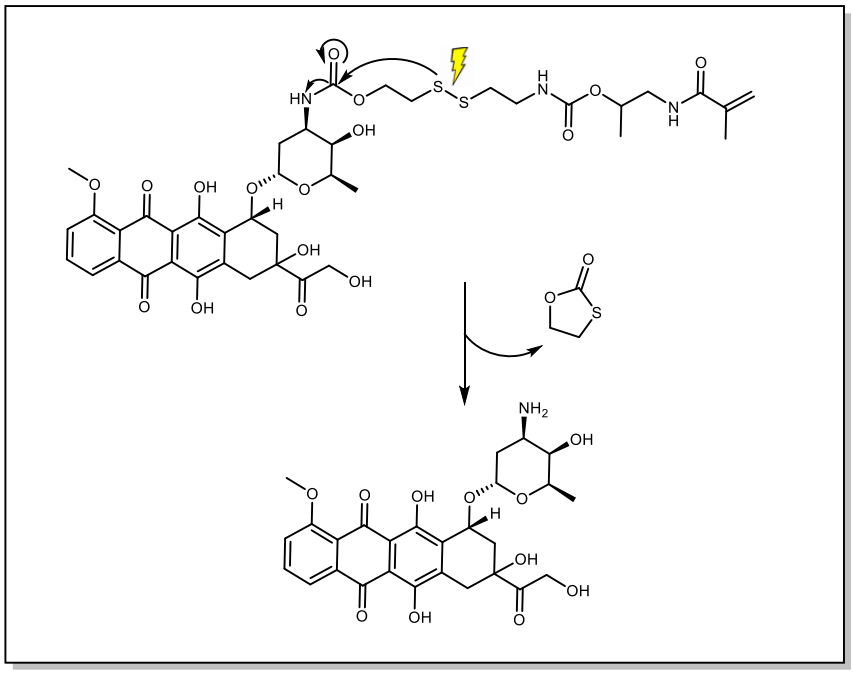


Figure 6-8 Proposed mechanism for the self-immolative DOX release from the backbone of the HPMA polymer.

The assay was then repeated with the conjugated and mixed **HPMA-DOX-GEM** to assess the effect combination therapy will have on the IC_{50} of the pancreatic cancer cell line.

*Table 12 IC_{50} values for the 2D cell viability assays of free DOX, **HPMA-DOX** conjugate and conjugated and mixed **HPMA-DOX-GEM**.*

	IC_{50} (μM) (2D)
Free DOX	0.05 (± 0.01)
HPMA-DOX polymer	0.25 (± 0.06)
HPMA-DOX-GEM-m	0.14 (± 0.07)
HPMA-DOX-GEM-c	0.15 (± 0.02)

The doses used for the combination therapy were based on the concentration of GEM of the conjugated polymer. Table 13 below details the concentration of both

GEM and DOX at each dose. The concentration of DOX and GEM used in the mixed system was the same as the conjugated system.

Table 13 Dosing regimen for 2D cell viability assay of the combination therapy.

Dose	GEM concentration (μM)	DOX concentration (μM)	Total dose (μM)
1	0.01	0.0048	0.0148
2	0.1	0.048	0.148
3	1	0.48	1.48
4	10	4.8	14.8
5	100	48	148

The cytotoxicity data acquired from the experiment (Figure 6-7B, Table 12) suggested an improvement in IC_{50} values from 0.29 ± 0.07 μM (**HPMA-GEM**) and 0.25 ± 0.06 μM (**HPMA-DOX**) to 0.15 ± 0.02 μM (**HPMA-DOX-GEM-c**) and 0.14 ± 0.07 μM (**HPMA-DOX-GEM-m**). No significant difference was seen between the cell viability profiles of the conjugated and mixed systems which shows that conjugation of both drugs to the same polymer backbone has no bearing on the efficacy of the drugs.

To evaluate the effect of the drug combination on the MIA PaCa-2 cells, the combination index values of the **HPMA-DOX-GEM-c** and **HPMA-DOX-GEM-m** polymer conjugate were calculated (Table 14) using the computer simulation software, CompuSyn.[417] This software uses the Chou-Talalay method to determine CI value of a drug combination whereby CI <1, =1 and >1 indicate synergism, additive and antagonism effect.[418] The conjugated DOX-GEM combination was found to display a synergistic effect (CI = 0.62) which provides an explanation for the reduction in IC_{50} value when compared with **HPMA-GEM** and **HPMA-DOX**

monotherapies. Similar observations have been reported previously for other cell line and combinational therapies, which is attributed to the different therapeutic mechanisms of the two drugs.[413, 419-421] The mixed DOX-GEM combination, however, was found to display an antagonistic effect as shown by the CI value of >1.

Table 14 Dose-effect parameters and mean combination index (CI) values as a function of cell viability of GEM and DOX individually and as a combination of MIA PaCa-2 pancreatic cancer cell line.

	Dose-effect parameters			**CI value**	**Effect**
	Dm (μM)	*M*	*r*	IC_{50}	
GEM	1.47	-0.43	-0.87	-	-
DOX	0.22	-0.86	-0.99	-	-
DOX-GEM conjugated	0.18	-0.95	-0.98	0.62	Synergism
DOX-GEM mixed	2.02	-1.03	-0.93	6.87	Antagonism

The parameters Dm, m and r are the slope, antilog of x-intercept and linear correlation coefficient of the median-effect plot which describes the potency (IC_{50}), the shape of the curve and the conformity of the data to mass-action law as calculated by CompuSyn. Dm and m values are used to calculate the CI values.

This observation was not expected due to the synergistic effect as described by the conjugated system. Liu *et. al.* reported on the combinational effect of GEM and DOX against several cell line and found the combination to be synergistic in most cases, according to their CI values.[413] However, they observed an antagonistic effect in one case which they attributed to the delivery of the drugs. They explained that the antagonistic effect of the combination could transform to synergism when both drugs are delivered together in the same micelle or delivery carrier rather than separately. This offers an explanation to the antagonistic effect displayed by **HPMA-DOX-GEM-m** because both drugs, in this case, are on separate polymers and hence their

combined delivery to each cell at the same time cannot be guaranteed. This consequently can affect the displayed effect of this combination therapy. These findings show that it may be advantageous to conjugate both drugs to the same polymeric backbone in order to utilise the synergism both drugs provide.[422]

6.3.3 *In vitro* 3D cytotoxicity assay

The efficacy of the **HPMA-DOX**, **HPMA-DOX-GEM-c** and **HPMA-DOX-GEM-m** against the mono and cocultured pancreatic cancer models was assessed *via* volume analysis and CellTiter-Glo® 3D cell viability assay. The concentrations of DOX and GEM (where applicable) were kept the same as the concentrations used in the efficacy studies in the 2D assay described in 6.3.2.

6.3.3.1 HPMA-DOX 3D assay

In the **HPMA-DOX** assay, the spheroids were treated with the different concentrations of the formulations, however, the concentration of DOX was kept constant between the free DOX and the **HPMA-DOX** to allow for comparison between the efficacy of the two treatments.

Initially, the volume of the spheroids over the course of the assay was measured to evaluate the effect the treatments have on the growing 3D spheroids. The volume was determined from the ROI of the microscope images acquired pre and post-treatment on the different days, as described in Chapter 5. As seen in Figure 6-9A-B, there were differences in the spheroid volume between days 4 and 7 for the media control, free DOX and conjugated DOX in both mono and cocultured systems. The volume in the media control had an approx. 200 % increase between day 4 and 7 in both mono and cocultured spheroids for both treatment groups (Figure 6-9C-D). However, the percentage change between day 4 and 7 for the two treatment groups decreased with increasing concentration as depicted in Figure 6-9C-D. Significant differences were observed in the mono and cocultured assays of

the free DOX at 0.005, 0.05 and 50 µM concentrations with an enhanced toxicity effect observed in the monoculture system compared to the coculture system. This effect was also seen in the free GEM 3D assay implying the presence of the MSCs affects the efficacy of both free drugs tested in this project. The effect was less prominent with the conjugated system, with no significant difference in volume between the two systems other than at the highest DOX concentration (50 µM). Furthermore, it was not possible to determine the volume of the highest free DOX concentration (50 µM) in the monoculture assay as the spheroid had completely disintegrated by day 7, therefore, the volume was taken to be zero. This could be as a result of the significant toxicity effect of the free DOX at the highest concentration, an effect that was not seen in the coculture system. These data further confirmed the effect of MSCs in the coculture system regarding the reduced activity of free drugs compared to the polymer conjugates.

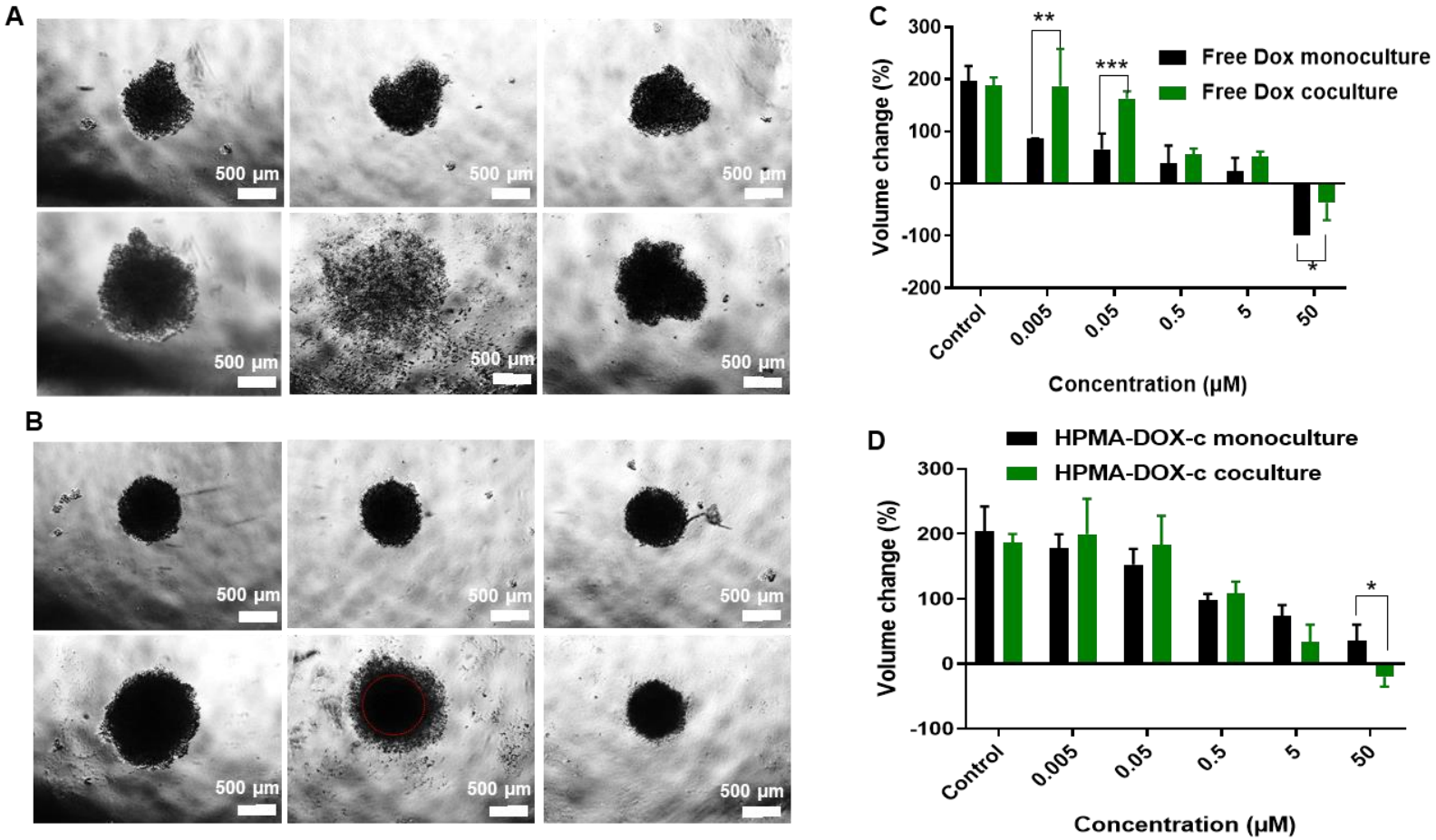


*Figure 6-9 3D MIA PaCa-2 spheroids cytotoxicity assay. A&B). Representative microscope images of different drug concentrations to show differences in volume on day 4 and day 7 of the mono and co-cultured systems respectively. C&D) Graphs showing changes in the spheroid volume between days 4 and 7 expressed as a percentage (C) Free GEM and (D) HPMA-GEM. The scale bar represents 500 µm. Error bars show standard deviation (n = 4). (*p ≤ 0.05, **p <0.01, p*** ≤0.001, two-way ANOVA with Sidak's multiple comparison test).*

CellTiter-Glo® 3D assay was used to further investigate the efficacy of the free DOX and **HPMA-DOX** in the 3D spheroids. The percentage of cell viability was determined from the control and the results of the analysis presented in Figure 6-10. In general, the free and conjugated DOX decreased the cell viability of the spheroids as measured by the amount of ATP released upon cell lysis. In both treatment groups, no significant difference was observed between the mono and cocultured systems at the lowest concentration (0.005 µM).

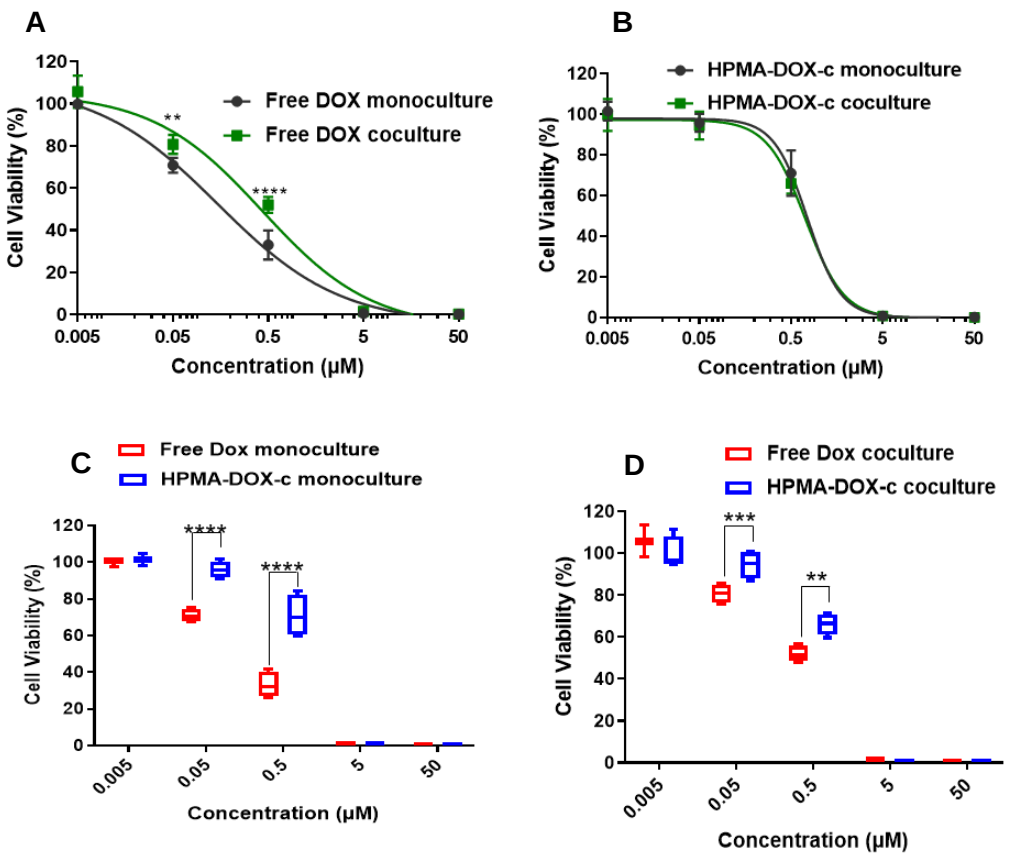


*Figure 6-10 CellTiter-Glo® 3D Cell viability assay (A) Free DOX, (B) Conjugated **HPMA-DOX** polymer, (C) Comparison between free and conjugated DOX in monocultured spheroid and D) Comparison between free and conjugated DOX in cocultured system. Error bars show standard deviation (n = 4). (**p ≤0.01, ***p ≤ 0.001, ****p ≤0.0001, two-way ANOVA with Sidak's multiple comparison test).*

However, increasing the concentration of DOX (0.05 and 0.5 µM) had a significant effect on the toxicity of the free DOX group between the mono and cocultured systems. The free DOX appeared to be more toxic against the monoculture system compared to the cocultured system. This outcome was however not observed in the

HPMA-DOX treatment group (Figure 6-10B) as no significant difference was found between the mono and cocultured systems at all concentrations tested; indicating that the presence of MSC has a negative effect on the efficacy of the free DOX. This effect was also observed in the **HPMA-GEM** assay whereby a significant difference was seen in the CellTiter-Glo® 3D assay of the free GEM and not the GEM conjugate. As stated before, this effect could be due to the potentiated delivery of DOX conjugate to the cells in the spheroid.

Furthermore, the free DOX was found to be significantly more toxic than the conjugated system at 0.005 and 0.5 µM concentrations in the monoculture assay (Figure 6-10C). However, the significant differences in the cocultured system at the same concentrations were found to be slightly less (Figure 6-10D) further displaying the negative impact of the cocultured system on free DOX efficacy.

Table 15 Comparison between the IC_{50} of the 2D and 3D cytotoxicity assay of free and conjugated DOX in the pancreatic cancer cell line.

	IC_{50} (µM) (3D)	**IC_{50} (µM) (2D)**
Free DOX monoculture	0.15 (± 0.07)	0.05 (± 0.01)
Free Dox coculture	0.43 (± 0.22)	-
HPMA-DOX monoculture	0.75 (± 0.46)	0.25 (± 0.06)
HPMA-DOX coculture	0.72 (± 0.26)	-

Table 15 describes the IC_{50} values of the CellTiter-Glo® 3D assay of free DOX and **HPMA-DOX**. The difference in IC_{50} between the mono and cocultured systems in the free DOX (0.15 ± 0.07 µM and 0.43 ± 0.22 µM respectively) was relatively bigger than that observed in the **HPMA-DOX** assays (0.75 ± 0.46 µM and 0.72 ± 0.26 µM respectively). As already mentioned, this could be due to the DOX in the polymer

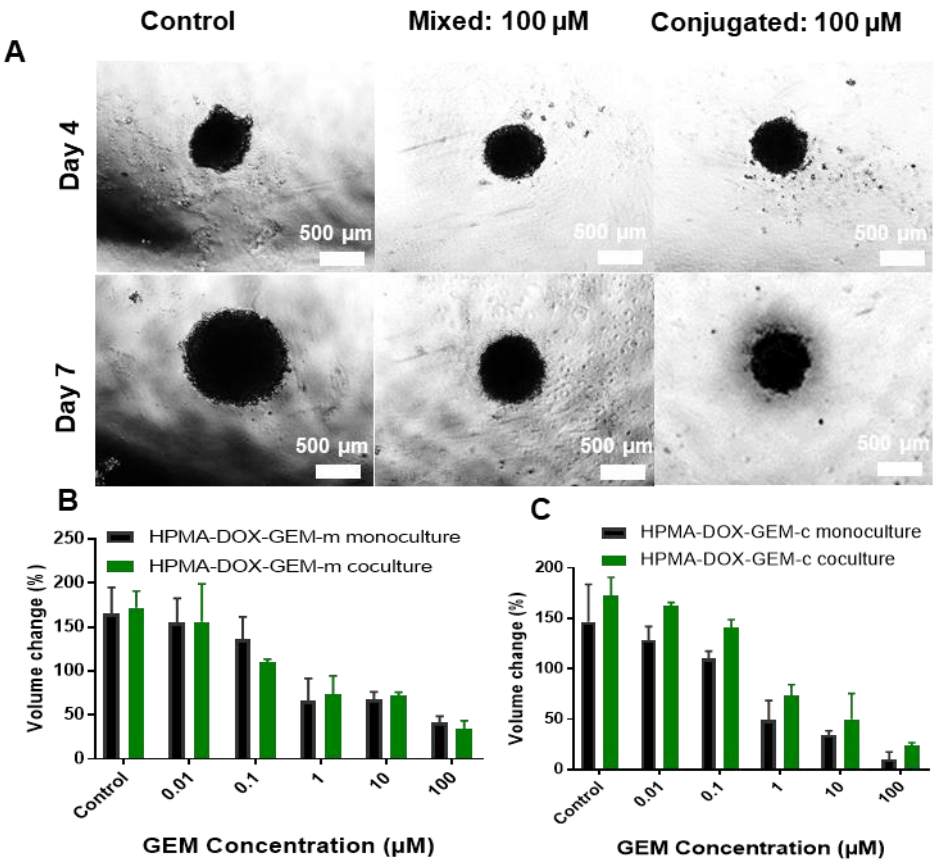
conjugate not being readily available to induce toxicity as it requires a release from the polymeric backbone, unlike the free drug.

Although different methods were used to assess the cell viability of the 2D and 3D assays, it is possible to make comparisons between the normalised data. The main observation made between the two assays is that, in general, there is a reduced efficacy of both formulations in the 3D culture compared to 2D. When comparing the IC_{50} values for the 3D and 2D assays (Table 15), there appear to be approx. 3-fold increase in all cases which is attributable to the structural difference between the 2D monolayer and 3D spheroid models affecting the exposure of the drugs to the cells. From the IC_{50} values, the efficacy of DOX in the 3D model was equally reduced in both the free and conjugated DOX treatment groups. This is different from the observations from the 3D assay of the GEM conjugate whereby the conjugate was seen to fare better in the 3D spheroid model than the free drug. This could be due to the differences in the transport mechanisms of GEM and DOX. In addition to protein-mediated transportation intracellularly, DOX also undergoes passive diffusion across cell membranes.[402, 423, 424] This could improve the penetration ability of the drug within the spheroid, a process that is not feasible with the hydrophilic GEM molecule.

6.3.3.2 Combinational therapy 3D assay

The biological effect of **HPMA-DOX-GEM-c** and **HPMA-DOX-GEM-m** polymers were further evaluated in the 3D spheroid models. As with the other 3D *in vitro* efficacy studies, there were observable differences between the spheroid volumes on days 4 and 7 of the control and treatment groups (Figure 6-11A). The volume of the untreated spheroids averaged at approx. 150 % bigger on day 7 when compared to day 4 (pre-treatment). However, the volume of the treated mono and cocultured spheroids in both **HPMA-DOX-GEM-c** and **HPMA-DOX-GEM-m** were significantly lower at the highest concentration on day 7 compared to the control (Figure 6-11B-

D).



D

Comparison	Significance	Adjusted P-value
Mixed Monoculture		
Control vs. 1	****	<0.0001
Control vs. 10	****	<0.0001
Control vs. 100	****	<0.0001
Mixed coculture		
Control vs. 0.1	***	0.0009
Control vs. 1	****	<0.0001
Control vs. 10	****	<0.0001
Control vs. 100	****	<0.0001
Conjugated monoculture		
Control vs. 0.1	*	0.0233
Control vs. 1	****	<0.0001
Control vs. 10	****	<0.0001
Control vs. 100	****	<0.0001
Conjugated coculture		
Control vs. 0.1	*	0.0330
Control vs. 1	****	<0.0001
Control vs. 10	****	<0.0001
Control vs. 100	****	<0.0001

*Figure 6-11 3D MIA PaCa-2 spheroid cytotoxicity od combination therapy. A) Microscope images of the spheroids on days 4 and 7 in culture. B) Percentage volume changes between days 4 and 7 of mixed **HPMA-GEM** and **HPMA-DOX** treatment. C) Percentage volume changes between days 4 and 7 of conjugated **HPMA-DOX-GEM**. D) Table depicting statistically significant resutls of the percentage volume change analysis. Error bars show standard deviation (n = 4). (*p ≤0.05, ***p ≤0.001, ****p ≤ 0.0001, two-way ANOVA with Dunnett's multiple comparisons test.*

It was also observed that increasing the concentration of GEM and DOX led to an improvement in the inhibition of spheroid growth as shown by the constant reduction in spheroid volume as a factor of concentration in Figure 6-11B-C. As expected, there appeared to be no significant difference in the percentage volume change between the mono and coculture spheroids in both treatment groups because both treatment groups have the same polymeric backbone and it has been shown in the previous 3D assays that, conjugation of drugs to the **HB-HPMA** polymer backbone helps to overcome the reduced efficacy effect of free drugs observed in the cocultured system.

To substantiate the results obtained from the analysis of the spheroid volume after treatment with the combination polymers, the cell viability of the spheroids was evaluated using the CellTiter-Glo® 3D cell viability assay solution.

Table 16 IC_{50} values for the 3D cell culture assessment of DOX and GEM combinational therapy.

	IC_{50} (μM) (3D) Combinational
HPMA-DOX-GEM-m monoculture	1.66 (± 0.88)
HPMA-DOX-GEM-m coculture	1.74 (± 0.67)
HPMA-DOX-GEM-c monoculture	2.01 (± 0.87)
HPMA-DOX-GEM-c coculture	2.38 (± 0.75)
HPMA-DOX monoculture	0.75 (± 0.46)
HPMA-DOX coculture	0.72 (± 0.26)

We observed that the activity of both **HMPA-DOX-GEM** drug combinations resulted in increased toxicity to the 3D spheroids compared with **HPMA-GEM** alone as it was not possible to obtain an IC_{50} for the latter in the cell viability assay. However, this

was not the case for **HPMA-DOX** as the IC_{50} appear to increase in the combination therapy meaning the presence of GEM reduces the effectiveness of the DOX (Table 16). This effect was not observed in the 2D cell viability assay as the IC_{50} of both **HPMA-GEM** and **HPMA-DOX** (0.29 ± 0.07 and 0.25 ± 0.06 µM respectively) were found to be higher than **HPMA-DOX-GEM-c** and **HPMA-DOX-GEM-m** (0.15 ± 0.02 and 0.14 ± 0.07 µM respectively).

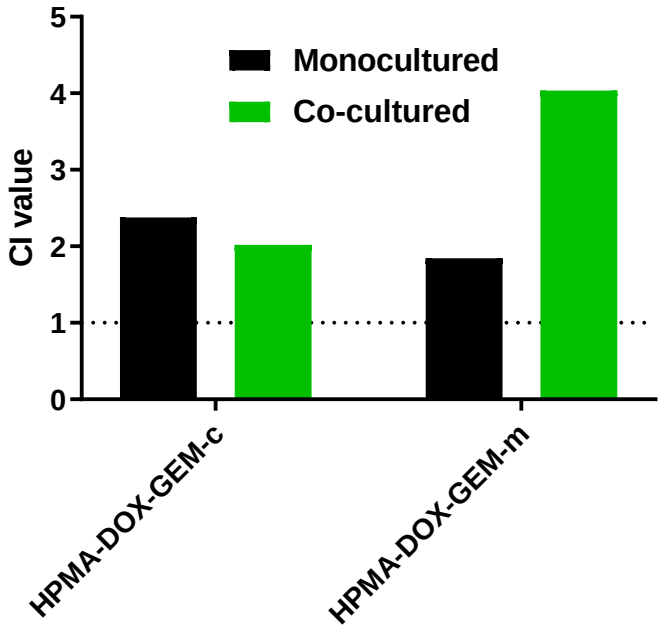


Figure 6-12 Combination index of DOX and GEM against MIA PaCa-2 cell line in 3D cell culture assay.

This could be due to the antagonistic effect of both formulations in the 3D cell culture (Figure 6-12). The CI values of **HPMA-DOX-GEM-c** and **HPMA-DOX-GEM-m** in both mono and cocultured systems were found to be above 1 indicating that the transformation from antagonism to synergism as explained by Liu *et. al.* does not occur in the 3D system. Another group also witnessed this change in CI value when comparing 2D and 3D results.[425] They found the CI value increased by a factor of 4.7-7.8 in the 3D spheroid assay compared to 2D. These observations further show the need to adopt 3D cell culture models for the biological screening of

therapeutics. The data from the volume assays also demonstrated no differences between the mono and coculture systems of both treatment groups. Again, these data indicate the benefit of using the **HB-HPMA** delivery system, particularly in the co-culture spheroids. Finally, no significant difference was found between the efficacy of the conjugated and the mixed population as presented by the cell viability graphs from Figure 6-13C-D.

Although in the 2D cell viability assay we found **HPMA-DOX-GEM-c** to have a synergistic effect in the MIA PaCa-2 cell line, the 3D cell culture as mentioned before resembles the *in vivo* cell environment better than 2D.

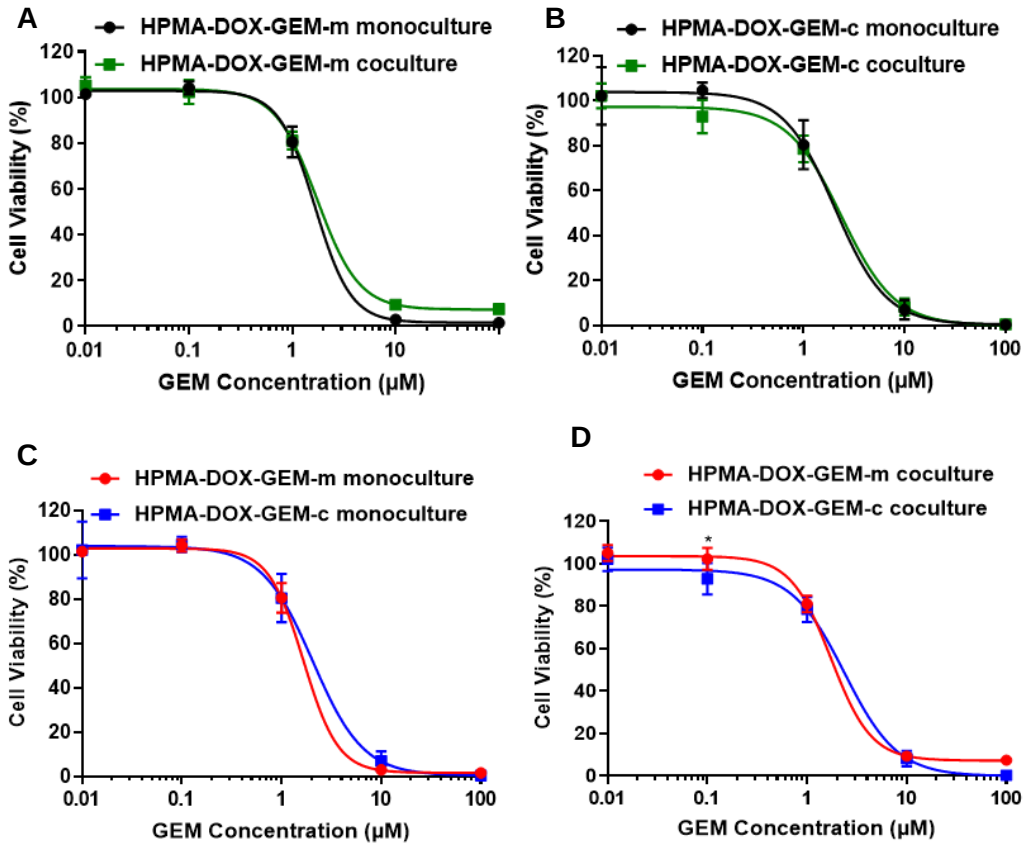


*Figure 6-13 CellTiter-Glo® 3D Cell viability assay 72 hours post treatment with (A) **HPMA-DOX-GEM-m**, (B) **HPMA-DOX-GEM-c**. C) Comparison between mixed and conjugated **HPMA-DOX-GEM** in monoculture spheroid D) Comparison between mixed and conjugated **HPMA-DOX-GEM** in coculture system. Error bars show standard deviation (n = 4). (*p ≤0.05, two-way ANOVA with Sidak's multiple comparisons test).*

Therefore we believe the antagonistic effect seen between DOX and GEM in the MIA PaCa-2 pancreatic cancer line better describes the potential effect *in vivo*.

However, further experiments such as *in vivo* efficacy studies are needed to confirm this observation. As mentioned previously, neither DOX nor DOX-GEM combinations are currently indicated in pancreatic cancer treatment; doxorubicin was primarily employed for this work as a well-established fluorescent anticancer drug to develop methodologies. Future work will, therefore, adopt these methods to investigate a more clinically relevant combination such as gemcitabine and capecitabine.

6.4 Conclusions

In this chapter, we have demonstrated the successful synthesis of gemcitabine and doxorubicin conjugated hyperbranched HPMA polymer for co-delivery to pancreatic cancer cell line. **HPMA-DOX** and **HPMA-DOX-GEM** polymers were synthesised by RAFT polymerisation ensuring incorporating >80 mol/mol% of HPMA units to maintain the good water solubility of the polymer. The DOX was attached to the polymer backbone *via* a carbamate bond to a disulfide linker for a self-immolative release of the drug through a reduction of the disulfide bond.

The toxicity profiles of these polymers were assessed in *in vitro* 2D and 3D cell culture assays. Observed toxicity data of **HPMA-DOX** in both cell culture models showed that the polymers could effectively deliver DOX to the pancreatic cancer cell lines. The need for drug release in the polymer conjugate means differences were observed between **HPMA-DOX** and free drug assays in both 2D and 3D cell culture. However, the potential improvement in the biodistribution profile of the DOX in the polymer conjugate would be expected to enhance the therapeutic window of doxorubicin in an *in vivo* setting.

The combinational effects of DOX and GEM on the pancreatic cancer cell line were also evaluated. Both drugs, when conjugated to the same polymer, were found to produce a synergistic effect on the MIA PaCa-2 cell line in the 2D assay. However,

in the 3D assay, the drugs were found to be antagonistic in effect. The differences seen could be due to the lack of complexity in the 2D model leading to the generation of unrepresentative results. To the best of our knowledge, studies showing synergism between GEM and DOX in cancer cell lines have been conducted before only in 2D cell models and therefore may not correctly reflect the *in vivo* behaviour.[412, 413] Thus further work is needed to ascertain the effect of DOX and GEM in pancreatic cancer treatment.

Overall, this study has demonstrated that the **HB-HPMA** polymer can be a promising system for the attachment and subsequent delivery of anticancer agents for mono and combinational therapy in the treatment of pancreatic cancer. Additionally, it has further highlighted the differences that exist between 2D and 3D cell culture methods in both mono and combinational therapies aimed at MIA PaCa-2 cell line.

6.5 Supplementary Information

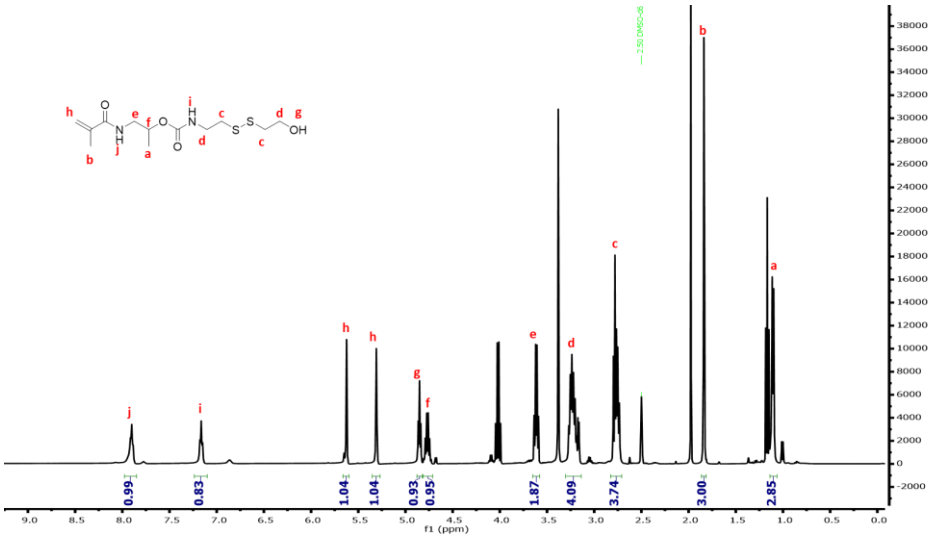


Figure 6-14 ^{1}H NMR of HPMA-Disulfide in DMSO-d_6.

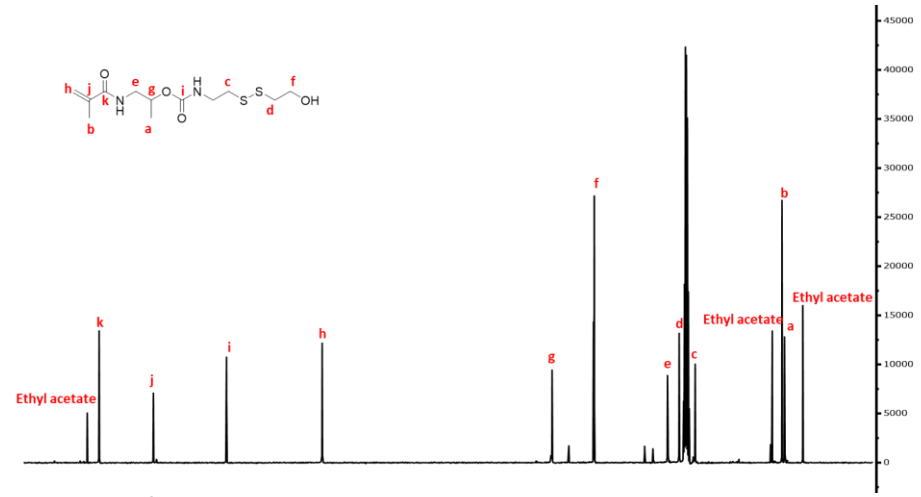


Figure 6-15 ^{13}C NMR of HPMA-Disulfide in DMSO-d_6.

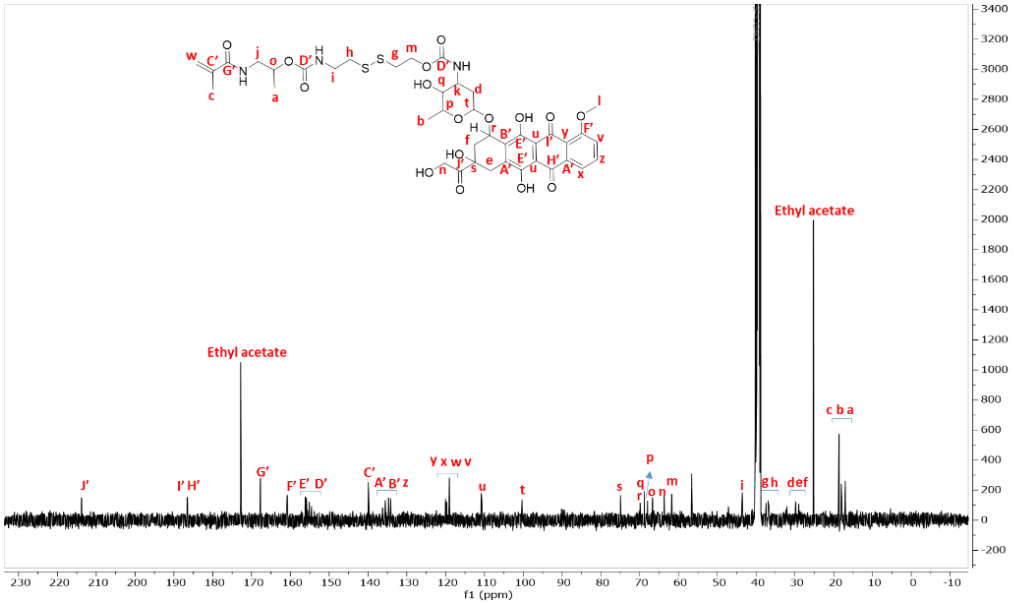


*Figure 6-16 ^{13}C NMR of **HPMA-DOX** monomer in DMSO-d_6.*

Chapter 7 Summary and outlook

7.1 Summary

The scientific work presented here shows the role polymer conjugates can play in the delivery of drugs for the treatment of pancreatic cancer. As previously described, gemcitabine, a nucleoside analogue is the first-line treatment for patients with advanced or metastatic adenocarcinoma of the pancreas. However, the efficacy of the drug is affected by metabolism and reduced cellular uptake of the drug by the stromal dense pancreatic tumour. In this work, a hyperbranched polymer conjugate approach based on 2-hydroxypropyl methacrylamide (HPMA) polymer backbone was designed and synthesised to enhance the delivery of chemotherapeutic agents to the pancreatic cancer cells.

Preclinical screening of therapeutics is often initiated with 2D monolayer cell culture models. However, studies have shown that these models are not representative of the *in vivo* environment, especially in the tumour microenvironment (TME). Therefore, in chapter 3, 3D pancreatic cancer model based on MIA PaCa-2 cell line was developed and characterised to be used as a model for biological screening of synthesised materials. The properties of the spheroids in terms of seeding density, growth period and development of necrotic core was to be used as guidelines for all future pancreatic cancer 3D spheroid studies. From this work, we were able to show the formation of intact spheroids of the MIA PaCa-2 cell line at day 3 in culture. We were also able to establish that the development of pathological features such as the formation of the necrotic core was dependent on seeding density and time in culture. As a result, 1K seeding density was chosen for downstream studies of MIA PaCa-2 monoculture system.

In addition to this, mesenchymal stem cells (MSCs) were coculture with MIA PaCa-2 as a mimic for the stroma outer layer present in pancreatic cancer. In this assay, we

established that the seeding density had a significant effect on the spheroid formation, whereby a high seeding density of 3000 cells/well did not yield compact spheroids. This was thought to be due to the potential invasion-inducing nature of MSCs in pancreatic cancer cells. Therefore 1:1 ratio (1000 cells each per well) was chosen for subsequent co-culture experiments.

To develop our polymer-drug conjugates, it was important to establish the potential effect size of the hyperbranched HPMA (HB-HPMA) polymer will have on the uptake and biodistribution of the potential delivery system *in vivo*. As it is well known, the size of nanomaterials is crucial for circulation and uptake purposes. Therefore, the second part of the work was focused on the synthesis of three **HB-HPMA** polymers of varying size (7, 20 and 40 nm by DLS) for *in vitro* and *in vivo* evaluation with the idea of selecting the better performing particle by size for subsequent drug conjugation. The polymers were synthesised by RAFT polymerisation with an alkyne terminated chain transfer agent (CTA). These polymers displayed desirable biocompatibility and uptake behaviour in both 2D and 3D cell culture models. In addition to this, these polymers were found to exhibit 'stealth-like' properties as shown by the macrophage uptake studies. However, differences were observed in the fluorescent *in vivo* biodistribution assay. The smaller polymer appeared to accumulate preferentially in the kidneys whereas the larger polymer mostly accumulated in the liver. This was expected as larger particles are known to have reduced renal clearance and enhanced hepatic clearance due to the small diameter of glomerular capillary. The PET-CT biodistribution assay results, however, contradict the result of the fluorescent assay, whereby all polymers had enhanced liver and splenic accumulation with the **HB-HPMA-7** displaying the most enhanced effect. This was speculated to be due to potential difference in the exocytosis behaviour of the polymers out of the hepatocytes and splenic monocytes, as well as the macrophages, following deferoxamine conjugation**.** Based on the data from this

assay, 20 nm was chosen as the preferred target size for our polymer conjugate system.

The secondary hydroxyl group of the HB-HPMA polymer was functionalised to introduce a carboxylic acid linker for the successful conjugation of gemcitabine for the treatment of pancreatic cancer cells. *In vitro* analysis of the polymer conjugate in both 2D and 3D cell culture assays confirm the ability of the polymer to successfully deliver the chemotherapeutic to the dividing cancer cells as shown by the cytotoxicity profiles. The differences found in the efficacy of the conjugate and free GEM in the 3D assay was not as profound as that observed in the 2D assay. This was attributed to the polymer conjugate potentially exploiting cellular transport pathways not available to free drugs, enabling them to penetrate further into the spheroids. In addition to this, free drugs could become entrapped in the periphery of the spheroids as a result of apoptosis of the outer cells of the spheroids. Owning to the ability of 3D spheroids to more realistically predict *in vivo* behaviour, we believe this system is a viable candidate for pancreatic cancer therapy.

Whilst the work presented in this chapter shows the potential benefit for the use of **HB-HPMA** polymer system for delivery of GEM to pancreatic cancer cells, in order to demonstrate the ability of the system to act as a therapeutic agent, studies are currently underway to assess the efficacy of the **HPMA-GEM** polymer through a 28-day tumour regression experiment in mice. The mice are being monitored for changes in tumour volume and body weight compared to free GEM.

Chapter 6 further explores the potential use of the HB system in the delivery of chemotherapeutic agents for pancreatic cancer treatment. Doxorubicin was conjugated to the backbone of the polymer for mono and combinational therapy with GEM for the treatment of MIA PaCa-2 pancreatic cancer cells. The data presented was a preliminary assessment of these polymers in *in vitro* 2D and 3D cell culture

models. Like **HPMA-GEM**, the **HPMA-DOX** was found to elicit a toxic effect in the pancreatic cancer line, thus showing the effective delivery of the drug to the dividing cells. The combinational therapy appeared to improve the effectiveness of both drugs on the MIA PaCa-2 cells as the IC_{50} was found to be lower than the IC_{50} of both **HPMA-GEM** and **HPMA-DOX**. This synergistic effect in the 2D cell culture assay was also backed up with the calculated combinational index value (CI) of <1. However, in 3D cell culture assay, the IC_{50} of the combination was much higher than the IC_{50} of **HPMA-DOX** alone reflecting the reduced effectiveness of the DOX in the combination therapy and hence drug antagonism. Once more, this antagonistic effect was confirmed by a >1 CI value. The observed difference could be due to the inability of the 2D cell culture in accurately predicting the *in vivo* behaviour as a result of the lack of complexity of the model. Therefore, it's essential to adopt a better *in vitro* screening model such as 3D spheroids for the biological evaluation of therapeutics.

The work presented in this thesis highlights the potential benefit of **HB-HPMA** system in the delivery of chemotherapeutics for pancreatic cancer treatment. HPMA, as shown in Chapter 1, has been extensively studied in the clinics as a drug delivery vector for cancer treatment. However, these clinical trials failed mostly due to the no perceived benefit of the drug delivery system compared to free drug mainly owing to low drug loading. Here, we have developed a hyperbranched polymer system for high drug loading to overcome this problem. This thesis consequently has established a significant foundation for further investigation into the development of these hyperbranched HPMA polymer systems for cancer delivery.

7.2 Future work

7.2.1 Short term

In chapter 4, we observed differences in the *in vivo* organ distribution of the polymer in fluorescent and PET-CT biodistribution assays. This was thought to be due to the possible conformational changes caused by DFO conjugations. Therefore, additional future experiments should focus on understanding the potential structural differences that exist between the polymers used in both assays. For example, small-angle neutron scattering (SANS) can be used to provide an understanding of the solution conformation of both sets of particles to help predict their biological behaviour.[422, 426] Additionally, endo and exocytosis behaviour of the polymers should be extensively studied especially in macrophages, hepatocytes and splenic monocytes. To further predict how these systems may interact with different tissues such as the liver and kidneys in the body and to gain a better understanding of particle disposition and toxicity, the organs-on-chip technique should be employed to further evaluate the control polymers and polymer-drug conjugates.[427]

Further particles characterisation should include the use of techniques such as asymmetrical flow field-flow fractionations (AF4) to separate out highly branched polymers from linear and hyperbranched polymers with a low degree of branching (DP) in order to improve the uniformity of test samples and their clinical application.[428, 429] Time-of-Flight Secondary Ion Mass Spectrometry (ToF-SIMS) can also be employed to study the different metabolites present spheroid slices after treatment with the polymer-drug conjugates. This will provide information on the mechanism of drug release from our systems and any potentially toxic metabolites produced as a result of the degradation of the polymer backbone.[430]

The *in vitro* drug release profiles of the polymer therapeutics should also be studied. In **HPMA-GEM** assay, the dialysis method in buffered release media (pH 7.4, pH 5.5

and pH 5.5 with a protease such as cathepsin B) could be used to understand the mechanism through which GEM is released from the polymer backbone to exert its toxic effect. Similarly, the dialysis method could also be used to study the *in vitro* drug release of **HPMA-DOX**. The buffered release medium (pH 7.4) should contain 10 mM solution of glutathione (GSH) to mimic the intracellular redox conditions within cancer cells. In the combination therapy release assay, the pH of the buffered medium will be adjusted to pH 5.5 with the addition of cathepsin B to trigger GEM release. The concentrations of both drugs at each time point would be determined by comparing it to their respective calibration curves. The cumulative percentage drug release would then be calculated based on the initial concentrations of the drugs at the start of the study.

Finally, conclusion and analysis of the *in vivo* tumour regression studies of the **HPMA-GEM** should be undertaken to evaluate the efficacy of polymer in tumour bearing mice against the free drug. As stated above, the mice are being monitored for changes in tumour volume and body weight.

7.2.2 Long term

The differences in combination effect observed between 2D and 3D cell culture models should be further explored. *In vivo* studies with the DOX-GEM combination should be undertaken to determine the real effect of this combination on MIA PaCa-

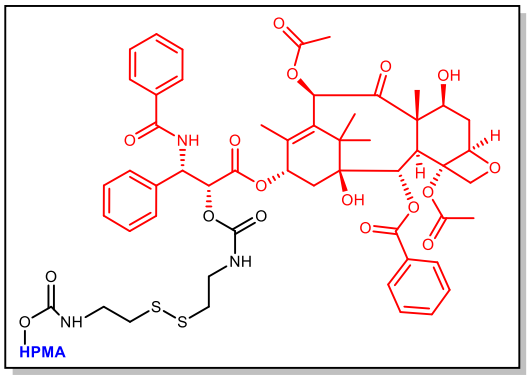


Figure 7-1 Proposed mechanism for attachment of Paclitaxel to HPMA backbone using cystamine as the linker.

2 pancreatic cancer cells. In addition to this, the developed methodology should be applied to the synthesis of combinations containing drugs closer to the existing standard of care combinations such as gemcitabine and paclitaxel. Cystamine linker could be used to conjugate the paclitaxel to the backbone of the HPMA polymer (Figure 7-1).

The resultant polymers would undergo *in vitro* drug release as explained above, in addition to an evaluation in MIA PaCa-2 pancreatic cancer cells. Upon demonstration of *in vitro* cytotoxic effect, *in vivo* tumour regression assay would be used to assess efficacy.

Chapter 8 References

1. Jemal, A.; Bray, F.; Center, M. M.; Ferlay, J.; Ward, E.; Forman, D., Global cancer statistics. *CA: a cancer journal for clinicians* **2011,** *61* (2), 69-90.

2. Urruticoechea, A.; Alemany, R.; Balart, J.; Villanueva, A.; Vinals, F.; Capella, G., Recent Advances in Cancer Therapy: An Overview. *Current Pharmaceutical Design* **2010,** *16* (1), 3-10.

3. Borghaei, H.; Smith, M. R.; Campbell, K. S., Immunotherapy of cancer. *Eur J Pharmacol* **2009,** *625* (1-3), 41-54.

4. Hoelder, S.; Clarke, P. A.; Workman, P., Discovery of small molecule cancer drugs: successes, challenges and opportunities. *Mol Oncol* **2012,** *6* (2), 155-176.

5. Adusumilli, P. S.; Cha, E.; Cornfeld, M.; Davis, T.; Diab, A.; Dubensky, T. W.; Evans, E.; Grogan, J. L.; Irving, B. A.; Leidner, R. S.; Olwill, S. A.; Soon-Shiong, P.; Triebel, F.; Tuck, D.; Bot, A.; Dansey, R. D.; Drake, C. G.; Freeman, G. J.; Ibrahim, R.; Patel, S.; Chen, D. S., New Cancer Immunotherapy Agents in Development: a report from an associated program of the 31stAnnual Meeting of the Society for Immunotherapy of Cancer, 2016. *Journal for ImmunoTherapy of Cancer* **2017,** *5* (1), 50.

6. Zhang, H.; Chen, J., Current status and future directions of cancer immunotherapy. *J Cancer* **2018,** *9* (10), 1773-1781.

7. Kruger, S.; Ilmer, M.; Kobold, S.; Cadilha, B. L.; Endres, S.; Ormanns, S.; Schuebbe, G.; Renz, B. W.; D'Haese, J. G.; Schloesser, H.; Heinemann, V.; Subklewe, M.; Boeck, S.; Werner, J.; von Bergwelt-Baildon, M., Advances in cancer immunotherapy 2019 – latest trends. *Journal of Experimental & Clinical Cancer Research* **2019,** *38* (1), 268.

8. Subramaniam, D. S.; Liu, S. V.; Giaccone, G., Novel approaches in cancer immunotherapy. *Discovery medicine* **2016,** *21* (116), 267-74.

9. Lesterhuis, W. J.; Haanen, J. B.; Punt, C. J., Cancer immunotherapy--revisited. *Nat Rev Drug Discov* **2011,** *10* (8), 591-600.

10. Dranoff, G., Cytokines in cancer pathogenesis and cancer therapy. *Nature reviews. Cancer* **2004,** *4* (1), 11-22.

11. Lakshmi Narendra, B.; Eshvendar Reddy, K.; Shantikumar, S.; Ramakrishna, S., Immune system: a double-edged sword in cancer. *Inflammation research : official journal of the European Histamine Research Society ... [et al.]* **2013,** *62* (9), 823-34.

12. Ventola, C. L., Cancer Immunotherapy, Part 2: Efficacy, Safety, and Other Clinical Considerations. *P T* **2017,** *42* (7), 452-463.

13. Weiner, L. M., Cancer immunology for the clinician. *Clinical advances in hematology & oncology : H&O* **2015,** *13* (5), 299-306.

14. Alatrash, G.; Jakher, H.; Stafford, P. D.; Mittendorf, E. A., Cancer immunotherapies, their safety and toxicity. *Expert Opin Drug Saf* **2013,** *12* (5), 631-45.

15. Zugazagoitia, J.; Guedes, C.; Ponce, S.; Ferrer, I.; Molina-Pinelo, S.; Paz-Ares, L., Current Challenges in Cancer Treatment. *Clinical therapeutics* **2016,** *38* (7), 1551-66.

16. Altmann, D. M., A Nobel Prize-worthy pursuit: cancer immunology and harnessing immunity to tumour neoantigens. *Immunology* **2018,** *155* (3), 283-284.

17. Paz-Ares, L.; Luft, A.; Vicente, D.; Tafreshi, A.; Gumus, M.; Mazieres, J.; Hermes, B.; Cay Senler, F.; Csoszi, T.; Fulop, A.; Rodriguez-Cid, J.; Wilson, J.; Sugawara, S.; Kato, T.; Lee, K. H.; Cheng, Y.; Novello, S.; Halmos, B.; Li, X.; Lubiniecki, G. M.; Piperdi, B.; Kowalski, D. M., Pembrolizumab plus Chemotherapy for Squamous Non-Small-Cell Lung Cancer. *N Engl J Med* **2018,** *379* (21), 2040-2051.

18. Gandhi, L.; Rodríguez-Abreu, D.; Gadgeel, S.; Esteban, E.; Felip, E.; De Angelis, F.; Domine, M.; Clingan, P.; Hochmair, M. J.; Powell, S. F.; Cheng, S. Y.-S.; Bischoff, H. G.; Peled, N.; Grossi, F.; Jennens, R. R.; Reck, M.; Hui, R.; Garon, E. B.; Boyer, M.; Rubio-Viqueira, B.; Novello, S.; Kurata, T.; Gray, J. E.; Vida, J.; Wei, Z.; Yang, J.; Raftopoulos, H.; Pietanza, M. C.; Garassino, M. C., Pembrolizumab plus Chemotherapy in Metastatic Non–Small-Cell Lung Cancer. *New England Journal of Medicine* **2018,** *378* (22), 2078-2092.

19. Schmid, P.; Adams, S.; Rugo, H. S.; Schneeweiss, A.; Barrios, C. H.; Iwata, H.; Dieras, V.; Hegg, R.; Im, S. A.; Shaw Wright, G.; Henschel, V.; Molinero, L.; Chui, S. Y.; Funke, R.; Husain, A.; Winer, E. P.; Loi, S.; Emens, L. A., Atezolizumab and Nab-Paclitaxel in Advanced Triple-Negative Breast Cancer. *N Engl J Med* **2018,** *379* (22), 2108-2121.

20. Burtness, B.; Harrington, K. J.; Greil, R.; Soulières, D.; Tahara, M.; De Castro, G., Jr; Psyrri, A.; Baste Rotllan, N.; Neupane, P. C.; Bratland, Å.; Fuereder, T.; Hughes, B. G. M.; Mesia, R.; Ngamphaiboon, N.; Rordorf, T.; Wan Ishak, W. Z.; Roy, A.; Cheng, J.; Jin, F.; Rischin, D., LBA8_PRKEYNOTE-048: Phase III study of first-line pembrolizumab (P) for recurrent/metastatic head and neck squamous cell carcinoma (R/M HNSCC). *Annals of Oncology* **2018,** *29* (suppl_8).

21. Zhang, F.; Qi, X.; Wang, X.; Wei, D.; Wu, J.; Feng, L.; Cai, H.; Wang, Y.; Zeng, N.; Xu, T.; Zhou, A.; Zheng, Y., Structural basis of the therapeutic anti-PD-L1 antibody atezolizumab. *Oncotarget* **2017,** *8* (52), 90215-90224.

22. Scapin, G.; Yang, X.; Prosise, W. W.; McCoy, M.; Reichert, P.; Johnston, J. M.; Kashi, R. S.; Strickland, C., Structure of full-length human anti-PD1 therapeutic IgG4 antibody pembrolizumab. *Nature structural & molecular biology* **2015,** *22* (12), 953-8.

23. Maude, S. L.; Laetsch, T. W.; Buechner, J.; Rives, S.; Boyer, M.; Bittencourt, H.; Bader, P.; Verneris, M. R.; Stefanski, H. E.; Myers, G. D.; Qayed, M.; De Moerloose, B.; Hiramatsu, H.; Schlis, K.; Davis, K. L.; Martin, P. L.; Nemecek, E. R.; Yanik, G. A.; Peters, C.; Baruchel, A.; Boissel, N.; Mechinaud, F.; Balduzzi, A.; Krueger, J.; June, C. H.; Levine, B. L.; Wood, P.; Taran, T.; Leung, M.; Mueller, K. T.; Zhang, Y.; Sen, K.; Lebwohl, D.; Pulsipher, M. A.; Grupp, S. A., Tisagenlecleucel in Children and Young Adults with B-Cell Lymphoblastic Leukemia. *New England Journal of Medicine* **2018,** *378* (5), 439-448.

24. Schuster, S. J.; Bishop, M. R.; Tam, C. S.; Waller, E. K.; Borchmann, P.; McGuirk, J. P.; Jager, U.; Jaglowski, S.; Andreadis, C.; Westin, J. R.; Fleury, I.; Bachanova, V.; Foley, S. R.; Ho, P. J.; Mielke, S.; Magenau, J. M.; Holte, H.; Pantano, S.; Pacaud, L. B.; Awasthi, R.; Chu, J.; Anak, O.; Salles, G.; Maziarz, R. T., Tisagenlecleucel in Adult Relapsed or Refractory Diffuse Large B-Cell Lymphoma. *N Engl J Med* **2019,** *380* (1), 45-56.

25. Neelapu, S. S.; Locke, F. L.; Bartlett, N. L.; Lekakis, L. J.; Miklos, D. B.; Jacobson, C. A.; Braunschweig, I.; Oluwole, O. O.; Siddiqi, T.; Lin, Y.; Timmerman, J. M.; Stiff, P. J.; Friedberg, J. W.; Flinn, I. W.; Goy, A.; Hill, B. T.; Smith, M. R.; Deol, A.; Farooq, U.; McSweeney, P.; Munoz, J.; Avivi, I.; Castro, J. E.; Westin, J. R.; Chavez, J. C.; Ghobadi, A.; Komanduri, K. V.; Levy, R.; Jacobsen, E. D.; Witzig, T. E.; Reagan, P.; Bot, A.; Rossi, J.; Navale, L.; Jiang, Y.; Aycock, J.; Elias, M.; Chang, D.; Wiezorek, J.; Go, W. Y., Axicabtagene Ciloleucel CAR T-Cell Therapy in Refractory Large B-Cell Lymphoma. *New England Journal of Medicine* **2017,** *377* (26), 2531-2544.

26. Tang, J.; Shalabi, A.; Hubbard-Lucey, V. M., Comprehensive analysis of the clinical immuno-oncology landscape. *Annals of oncology : official journal of the European Society for Medical Oncology* **2018,** *29* (1), 84-91.

27. Sasaki, T.; Koivunen, J.; Ogino, A.; Yanagita, M.; Nikiforow, S.; Zheng, W.; Lathan, C.; Marcoux, J. P.; Du, J.; Okuda, K.; Capelletti, M.; Shimamura, T.; Ercan, D.; Stumpfova, M.; Xiao, Y.; Weremowicz, S.; Butaney, M.; Heon, S.; Wilner, K.; Christensen, J. G.; Eck, M. J.; Wong, K. K.; Lindeman, N.; Gray, N. S.; Rodig, S. J.; Janne, P. A., A novel ALK secondary mutation and EGFR signaling cause resistance to ALK kinase inhibitors. *Cancer Res* **2011,** *71* (18), 6051-60.

28. Poulikakos, P. I.; Persaud, Y.; Janakiraman, M.; Kong, X.; Ng, C.; Moriceau, G.; Shi, H.; Atefi, M.; Titz, B.; Gabay, M. T.; Salton, M.; Dahlman, K. B.; Tadi, M.; Wargo, J. A.; Flaherty, K. T.; Kelley, M. C.; Misteli, T.; Chapman, P. B.; Sosman, J. A.; Graeber, T. G.; Ribas, A.; Lo, R. S.; Rosen, N.; Solit, D. B., RAF inhibitor resistance is mediated by

dimerization of aberrantly spliced BRAF(V600E). *Nature* **2011,** *480* (7377), 387-390.

29. Rodrik-Outmezguine, V. S.; Chandarlapaty, S.; Pagano, N. C.; Poulikakos, P. I.; Scaltriti, M.; Moskatel, E.; Baselga, J.; Guichard, S.; Rosen, N., mTOR kinase inhibition causes feedback-dependent biphasic regulation of AKT signaling. *Cancer Discov* **2011,** *1* (3), 248-59.

30. Nazarian, R.; Shi, H.; Wang, Q.; Kong, X.; Koya, R. C.; Lee, H.; Chen, Z.; Lee, M. K.; Attar, N.; Sazegar, H.; Chodon, T.; Nelson, S. F.; McArthur, G.; Sosman, J. A.; Ribas, A.; Lo, R. S., Melanomas acquire resistance to B-RAF(V600E) inhibition by RTK or N-RAS upregulation. *Nature* **2010,** *468* (7326), 973-7.

31. Johannessen, C. M.; Boehm, J. S.; Kim, S. Y.; Thomas, S. R.; Wardwell, L.; Johnson, L. A.; Emery, C. M.; Stransky, N.; Cogdill, A. P.; Barretina, J.; Caponigro, G.; Hieronymus, H.; Murray, R. R.; Salehi-Ashtiani, K.; Hill, D. E.; Vidal, M.; Zhao, J. J.; Yang, X.; Alkan, O.; Kim, S.; Harris, J. L.; Wilson, C. J.; Myer, V. E.; Finan, P. M.; Root, D. E.; Roberts, T. M.; Golub, T.; Flaherty, K. T.; Dummer, R.; Weber, B. L.; Sellers, W. R.; Schlegel, R.; Wargo, J. A.; Hahn, W. C.; Garraway, L. A., COT drives resistance to RAF inhibition through MAP kinase pathway reactivation. *Nature* **2010,** *468* (7326), 968-72.

32. Kola, I.; Landis, J., Can the pharmaceutical industry reduce attrition rates? *Nat Rev Drug Discov* **2004,** *3* (8), 711-5.

33. Campbell, F. V., C., *Pathology of the Pancreas*. 1 ed.; Springer London, 2013; p 3-20.

34. Longnecker, D., Anatomy and Histology of the Pancreas. *Pancreapedia: Exocrine Pancreas Knowledge Base* **2014**.

35. Chandra, R.; Liddle, R. A., Neural and hormonal regulation of pancreatic secretion. *Curr Opin Gastroenterol* **2009,** *25* (5), 441-446.

36. Krull, D. L.; Peterson, R. A., Chapter 11 - Preclinical Applications of Quantitative Imaging Cytometry to Support Drug Discovery. In *Methods in Cell Biology*, Darzynkiewicz, Z.; Holden, E.; Orfao, A.; Telford, W.; Wlodkowic, D., Eds. Academic Press: 2011; Vol. 102, pp 291-308.

37. Veite-Schmahl, M. J.; Regan, D. P.; Rivers, A. C.; Nowatzke, J. F.; Kennedy, M. A., Dissection of the Mouse Pancreas for Histological Analysis and Metabolic Profiling. *J Vis Exp* **2017,** (126).

38. Adsay, N. V.; Basturk, O.; Cheng, J. D.; Andea, A. A., Ductal neoplasia of the pancreas: nosologic, clinicopathologic, and biologic aspects. *Seminars in radiation oncology* **2005,** *15* (4), 254-64.

39. Kopp, J. L.; von Figura, G.; Mayes, E.; Liu, F.-F.; Dubois, C. L.; Morris, J. P. t.; Pan, F. C.; Akiyama, H.; Wright, C. V. E.; Jensen, K.; Hebrok, M.; Sander, M., Identification of Sox9-dependent acinar-to-ductal

reprogramming as the principal mechanism for initiation of pancreatic ductal adenocarcinoma. *Cancer Cell* **2012,** *22* (6), 737-750.

40. Jaster, R., Molecular regulation of pancreatic stellate cell function. *Mol Cancer* **2004,** *3*, 26.

41. Tirado, C.; S Shabsovich, D.; Ji, J.; Dawson, D., *Solid Tumour Section Atlas of Genetics and Cytogenetics in Oncology and Haematology Pancreatic tumors: an overview*. 2014; Vol. 18.

42. Bilici, A., Prognostic factors related with survival in patients with pancreatic adenocarcinoma. *World J Gastroenterol* **2014,** *20* (31), 10802-10812.

43. staff, B. c., Medical gallery of Blausen Medical 2014. *WikiJournal of Medicine* **2014,** *1* (2).

44. Artinyan, A.; Soriano, P. A.; Prendergast, C.; Low, T.; Ellenhorn, J. D. I.; Kim, J., The anatomic location of pancreatic cancer is a prognostic factor for survival. *HPB (Oxford)* **2008,** *10* (5), 371-376.

45. Schneider, G.; Siveke, J. T.; Eckel, F.; Schmid, R. M., Pancreatic cancer: basic and clinical aspects. *Gastroenterology* **2005,** *128* (6), 1606-25.

46. Hruban, R. H.; Adsay, N. V.; Albores-Saavedra, J.; Compton, C.; Garrett, E. S.; Goodman, S. N.; Kern, S. E.; Klimstra, D. S.; Kloppel, G.; Longnecker, D. S.; Luttges, J.; Offerhaus, G. J., Pancreatic intraepithelial neoplasia: a new nomenclature and classification system for pancreatic duct lesions. *Am J Surg Pathol* **2001,** *25* (5), 579-86.

47. Iacobuzio-Donahue, C. A., Genetic evolution of pancreatic cancer: lessons learnt from the pancreatic cancer genome sequencing project. *Gut* **2012,** *61* (7), 1085-1094.

48. Koorstra, J. B.; Feldmann, G.; Habbe, N.; Maitra, A., Morphogenesis of pancreatic cancer: role of pancreatic intraepithelial neoplasia (PanINs). *Langenbecks Arch Surg* **2008,** *393* (4), 561-70.

49. Maitra, A.; Fukushima, N.; Takaori, K.; Hruban, R. H., Precursors to invasive pancreatic cancer. *Adv Anat Pathol* **2005,** *12* (2), 81-91.

50. Hruban, R. H.; Goggins, M.; Parsons, J.; Kern, S. E., Progression Model for Pancreatic Cancer. *Clinical Cancer Research* **2000,** *6* (8), 2969-2972.

51. Hruban, R. H.; Maitra, A.; Goggins, M., Update on pancreatic intraepithelial neoplasia. *Int J Clin Exp Pathol* **2008,** *1* (4), 306-316.

52. Go, V. L. W., Tumors of the Pancreas (Atlas of Tumor Pathology Series 4). *Pancreas* **2007,** *35* (4), 388.

53. Winter, J. M.; Cameron, J. L.; Campbell, K. A.; Arnold, M. A.; Chang, D. C.; Coleman, J.; Hodgin, M. B.; Sauter, P. K.; Hruban, R. H.; Riall, T. S.; Schulick, R. D.; Choti, M. A.; Lillemoe, K. D.; Yeo, C. J., 1423 pancreaticoduodenectomies for pancreatic cancer: A single-institution experience. *J Gastrointest Surg* **2006,** *10* (9), 1199-210; discussion 1210-1.

54. Adsay, N. V.; Merati, K.; Andea, A.; Sarkar, F.; Hruban, R. H.; Wilentz, R. E.; Goggins, M.; Iocobuzio-Donahue, C.; Longnecker, D. S.; Klimstra, D. S., The dichotomy in the preinvasive neoplasia to invasive carcinoma sequence in the pancreas: differential expression of MUC1 and MUC2 supports the existence of two separate pathways of carcinogenesis. *Mod Pathol* **2002,** *15* (10), 1087-95.

55. Matthaei, H.; Schulick, R. D.; Hruban, R. H.; Maitra, A., Cystic precursors to invasive pancreatic cancer. *Nature Reviews Gastroenterology &Amp; Hepatology* **2011,** *8*, 141.

56. Rahma, O. E.; Duffy, A.; Liewehr, D. J.; Steinberg, S. M.; Greten, T. F., Second-line treatment in advanced pancreatic cancer: a comprehensive analysis of published clinical trials. *Annals of oncology : official journal of the European Society for Medical Oncology* **2013,** *24* (8), 1972-9.

57. Cancer Research UK, Pancreatic cancer statistics. https://www.cancerresearchuk.org/health-professional/cancer-statistics/statistics-by-cancer-type/pancreatic-cancer (accessed 20 June 2019).

58. Cancer Research UK, Pancreatic cancer incidence statistics. https://www.cancerresearchuk.org/health-professional/cancer-statistics/statistics-by-cancer-type/pancreatic-cancer/incidence?_ga=2.124287503.429803634.1561043410-1627763986.1561043410#ref-0 (accessed 20 June 2019).

59. Vincent, A.; Herman, J.; Schulick, R.; Hruban, R. H.; Goggins, M., Pancreatic cancer. *Lancet* **2011,** *378* (9791), 607-620.

60. Raimondi, S.; Maisonneuve, P.; Lowenfels, A. B., Epidemiology of pancreatic cancer: an overview. *Nat Rev Gastroenterol Hepatol* **2009,** *6* (12), 699-708.

61. Amundadottir, L.; Kraft, P.; Stolzenberg-Solomon, R. Z.; Fuchs, C. S.; Petersen, G. M.; Arslan, A. A.; Bueno-de-Mesquita, H. B.; Gross, M.; Helzlsouer, K.; Jacobs, E. J.; LaCroix, A.; Zheng, W.; Albanes, D.; Bamlet, W.; Berg, C. D.; Berrino, F.; Bingham, S.; Buring, J. E.; Bracci, P. M.; Canzian, F.; Clavel-Chapelon, F.; Clipp, S.; Cotterchio, M.; de Andrade, M.; Duell, E. J.; Fox, J. W., Jr.; Gallinger, S.; Gaziano, J. M.; Giovannucci, E. L.; Goggins, M.; Gonzalez, C. A.; Hallmans, G.; Hankinson, S. E.; Hassan, M.; Holly, E. A.; Hunter, D. J.; Hutchinson, A.; Jackson, R.; Jacobs, K. B.; Jenab, M.; Kaaks, R.; Klein, A. P.; Kooperberg, C.; Kurtz, R. C.; Li, D.; Lynch, S. M.; Mandelson, M.; McWilliams, R. R.; Mendelsohn, J. B.; Michaud, D. S.; Olson, S. H.; Overvad, K.; Patel, A. V.;

Peeters, P. H.; Rajkovic, A.; Riboli, E.; Risch, H. A.; Shu, X. O.; Thomas, G.; Tobias, G. S.; Trichopoulos, D.; Van Den Eeden, S. K.; Virtamo, J.; Wactawski-Wende, J.; Wolpin, B. M.; Yu, H.; Yu, K.; Zeleniuch-Jacquotte, A.; Chanock, S. J.; Hartge, P.; Hoover, R. N., Genome-wide association study identifies variants in the ABO locus associated with susceptibility to pancreatic cancer. *Nat Genet* **2009,** *41* (9), 986-90.

62. Wolpin, B. M.; Chan, A. T.; Hartge, P.; Chanock, S. J.; Kraft, P.; Hunter, D. J.; Giovannucci, E. L.; Fuchs, C. S., ABO blood group and the risk of pancreatic cancer. *J Natl Cancer Inst* **2009,** *101* (6), 424-31.

63. Blackford, A.; Parmigiani, G.; Kensler, T. W.; Wolfgang, C.; Jones, S.; Zhang, X.; Parsons, D. W.; Lin, J. C.; Leary, R. J.; Eshleman, J. R.; Goggins, M.; Jaffee, E. M.; Iacobuzio-Donahue, C. A.; Maitra, A.; Klein, A.; Cameron, J. L.; Olino, K.; Schulick, R.; Winter, J.; Vogelstein, B.; Velculescu, V. E.; Kinzler, K. W.; Hruban, R. H., Genetic mutations associated with cigarette smoking in pancreatic cancer. *Cancer Res* **2009,** *69* (8), 3681-8.

64. Petersen, G. M.; de Andrade, M.; Goggins, M.; Hruban, R. H.; Bondy, M.; Korczak, J. F.; Gallinger, S.; Lynch, H. T.; Syngal, S.; Rabe, K. G.; Seminara, D.; Klein, A. P., Pancreatic cancer genetic epidemiology consortium. *Cancer Epidemiol Biomarkers Prev* **2006,** *15* (4), 704-10.

65. Maisonneuve, P.; Marshall, B. C.; Lowenfels, A. B., Risk of pancreatic cancer in patients with cystic fibrosis. *Gut* **2007,** *56* (9), 1327-1328.

66. Reichert, M.; Rustgi, A. K., Pancreatic ductal cells in development, regeneration, and neoplasia. *J Clin Invest* **2011,** *121* (12), 4572-4578.

67. Chuvin, N.; Vincent, D. F.; Pommier, R. M.; Alcaraz, L. B.; Gout, J.; Caligaris, C.; Yacoub, K.; Cardot, V.; Roger, E.; Kaniewski, B.; Martel, S.; Cintas, C.; Goddard-Léon, S.; Colombe, A.; Valantin, J.; Gadot, N.; Servoz, E.; Morton, J.; Goddard, I.; Couvelard, A.; Rebours, V.; Guillermet, J.; Sansom, O. J.; Treilleux, I.; Valcourt, U.; Sentis, S.; Dubus, P.; Bartholin, L., Acinar-to-Ductal Metaplasia Induced by Transforming Growth Factor Beta Facilitates KRAS(G12D)-driven Pancreatic Tumorigenesis. *Cell Mol Gastroenterol Hepatol* **2017,** *4* (2), 263-282.

68. Evans, J.; Chapple, A.; Salisbury, H.; Corrie, P.; Ziebland, S., "It can't be very important because it comes and goes"--patients' accounts of intermittent symptoms preceding a pancreatic cancer diagnosis: a qualitative study. *BMJ Open* **2014,** *4* (2), e004215-e004215.

69. Takhar, A. S.; Palaniappan, P.; Dhingsa, R.; Lobo, D. N., Recent developments in diagnosis of pancreatic cancer. *BMJ* **2004,** *329* (7467), 668-673.

70. Bornman, P. C.; Beckingham, I. J., ABC of diseases of liver, pancreas, and biliary system. Pancreatic tumours. *BMJ* **2001,** *322* (7288), 721-723.

71. Zhu, Z.; Friess, H.; diMola, F. F.; Zimmermann, A.; Graber, H. U.; Korc, M.; Buchler, M. W., Nerve growth factor expression correlates with perineural invasion and pain in human pancreatic cancer. *J Clin Oncol* **1999,** *17* (8), 2419-28.

72. Tummala, P.; Junaidi, O.; Agarwal, B., Imaging of pancreatic cancer: An overview. *J Gastrointest Oncol* **2011,** *2* (3), 168-174.

73. Callery, M. P.; Chang, K. J.; Fishman, E. K.; Talamonti, M. S.; William Traverso, L.; Linehan, D. C., Pretreatment assessment of resectable and borderline resectable pancreatic cancer: expert consensus statement. *Ann Surg Oncol* **2009,** *16* (7), 1727-33.

74. Feldman, M. K.; Gandhi, N. S., Imaging Evaluation of Pancreatic Cancer. *Surg Clin North Am* **2016,** *96* (6), 1235-1256.

75. Rickes, S.; Unkrodt, K.; Neye, H.; Ocran, K. W.; Wermke, W., Differentiation of pancreatic tumours by conventional ultrasound, unenhanced and echo-enhanced power Doppler sonography. *Scand J Gastroenterol* **2002,** *37* (11), 1313-20.

76. Bhutani, M. S.; Gress, F. G.; Giovannini, M.; Erickson, R. A.; Catalano, M. F.; Chak, A.; Deprez, P. H.; Faigel, D. O.; Nguyen, C. C., The No Endosonographic Detection of Tumor (NEST) Study: a case series of pancreatic cancers missed on endoscopic ultrasonography. *Endoscopy* **2004,** *36* (5), 385-9.

77. Jailwala, J.; Fogel, E. L.; Sherman, S.; Gottlieb, K.; Flueckiger, J.; Bucksot, L. G.; Lehman, G. A., Triple-tissue sampling at ERCP in malignant biliary obstruction. *Gastrointest Endosc* **2000,** *51* (4 Pt 1), 383-90.

78. Siddiqui, A. A.; Brown, L. J.; Hong, S. K.; Draganova-Tacheva, R. A.; Korenblit, J.; Loren, D. E.; Kowalski, T. E.; Solomides, C., Relationship of pancreatic mass size and diagnostic yield of endoscopic ultrasound-guided fine needle aspiration. *Dig Dis Sci* **2011,** *56* (11), 3370-5.

79. Gress, F. G.; Hawes, R. H.; Savides, T. J.; Ikenberry, S. O.; Cummings, O.; Kopecky, K.; Sherman, S.; Wiersema, M.; Lehman, G. A., Role of EUS in the preoperative staging of pancreatic cancer: a large single-center experience. *Gastrointest Endosc* **1999,** *50* (6), 786-91.

80. Saftoiu, A.; Vilmann, P., Role of endoscopic ultrasound in the diagnosis and staging of pancreatic cancer. *J Clin Ultrasound* **2009,** *37* (1), 1-17.

81. Chang, K. J.; Wiersema, M. J., Endoscopic ultrasound-guided fine-needle aspiration biopsy and interventional endoscopic ultrasonography. Emerging technologies. *Gastrointest Endosc Clin N Am* **1997,** *7* (2), 221-35.

82. Gu, M.; Ghafari, S.; Lin, F.; Ramzy, I., Cytological diagnosis of endocrine tumors of the pancreas by endoscopic ultrasound-guided fine-needle aspiration biopsy. *Diagn Cytopathol* **2005,** *32* (4), 204-10.

83. Rosch, T.; Lightdale, C. J.; Botet, J. F.; Boyce, G. A.; Sivak, M. V., Jr.; Yasuda, K.; Heyder, N.; Palazzo, L.; Dancygier, H.; Schusdziarra, V.; et al., Localization of pancreatic endocrine tumors by endoscopic ultrasonography. *N Engl J Med* **1992,** *326* (26), 1721-6.

84. Palazzo, L.; Roseau, G.; Gayet, B.; Vilgrain, V.; Belghiti, J.; Fekete, F.; Paolaggi, J. A., Endoscopic ultrasonography in the diagnosis and staging of pancreatic adenocarcinoma. Results of a prospective study with comparison to ultrasonography and CT scan. *Endoscopy* **1993,** *25* (2), 143-50.

85. Rosch, T.; Lorenz, R.; Braig, C.; Feuerbach, S.; Siewert, J. R.; Schusdziarra, V.; Classen, M., Endoscopic ultrasound in pancreatic tumor diagnosis. *Gastrointest Endosc* **1991,** *37* (3), 347-52.

86. Hidalgo, M., Pancreatic cancer. *N Engl J Med* **2010,** *362* (17), 1605-17.

87. Cong, L.; Liu, Q.; Zhang, R.; Cui, M.; Zhang, X.; Gao, X.; Guo, J.; Dai, M.; Zhang, T.; Liao, Q.; Zhao, Y., Tumor size classification of the 8(th) edition of TNM staging system is superior to that of the 7(th) edition in predicting the survival outcome of pancreatic cancer patients after radical resection and adjuvant chemotherapy. *Sci Rep* **2018,** *8* (1), 10383-10383.

88. Pawlik, T. M.; Laheru, D.; Hruban, R. H.; Coleman, J.; Wolfgang, C. L.; Campbell, K.; Ali, S.; Fishman, E. K.; Schulick, R. D.; Herman, J. M., Evaluating the impact of a single-day multidisciplinary clinic on the management of pancreatic cancer. *Ann Surg Oncol* **2008,** *15* (8), 2081-8.

89. Bachmann, J.; Michalski, C. W.; Martignoni, M. E.; Büchler, M. W.; Friess, H., Pancreatic resection for pancreatic cancer. *HPB (Oxford)* **2006,** *8* (5), 346-351.

90. Buchler, M. W.; Wagner, M.; Schmied, B. M.; Uhl, W.; Friess, H.; Z'Graggen, K., Changes in morbidity after pancreatic resection: toward the end of completion pancreatectomy. *Arch Surg* **2003,** *138* (12), 1310-4; discussion 1315.

91. Oettle, H.; Neuhaus, P.; Hochhaus, A.; Hartmann, J. T.; Gellert, K.; Ridwelski, K.; Niedergethmann, M.; Zulke, C.; Fahlke, J.; Arning, M. B.; Sinn, M.; Hinke, A.; Riess, H., Adjuvant chemotherapy with gemcitabine and long-term outcomes among patients with resected pancreatic cancer: the CONKO-001 randomized trial. *Jama* **2013,** *310* (14), 1473-81.

92. Neoptolemos, J. P.; Kerr, D. J.; Beger, H.; Link, K.; Pederzoli, P.; Bassi, C.; Dervenis, C.; Fernandez-Cruz, L.; Lacaine, F.; Friess, H.; Buchler, M., ESPAC-1 trial progress report: the European randomized adjuvant study comparing radiochemotherapy, 6 months chemotherapy and combination therapy versus observation in pancreatic cancer. *Digestion* **1997,** *58* (6), 570-7.

93. Neoptolemos, J. P.; Moore, M. J.; Cox, T. F.; Valle, J. W.; Palmer, D. H.; McDonald, A. C.; Carter, R.; Tebbutt, N. C.; Dervenis, C.; Smith, D.; Glimelius, B.; Charnley, R. M.; Lacaine, F.; Scarfe, A. G.; Middleton, M. R.; Anthoney, A.; Ghaneh, P.; Halloran, C. M.; Lerch, M. M.; Olah, A.; Rawcliffe, C. L.; Verbeke, C. S.; Campbell, F.; Buchler, M. W., Effect of adjuvant chemotherapy with fluorouracil plus folinic acid or gemcitabine vs observation on survival in patients with resected periampullary adenocarcinoma: the ESPAC-3 periampullary cancer randomized trial. *Jama* **2012,** *308* (2), 147-56.

94. McGuigan, A.; Kelly, P.; Turkington, R. C.; Jones, C.; Coleman, H. G.; McCain, R. S., Pancreatic cancer: A review of clinical diagnosis, epidemiology, treatment and outcomes. *World J Gastroenterol* **2018,** *24* (43), 4846-4861.

95. Neoptolemos, J. P.; Palmer, D. H.; Ghaneh, P.; Psarelli, E. E.; Valle, J. W.; Halloran, C. M.; Faluyi, O.; O'Reilly, D. A.; Cunningham, D.; Wadsley, J.; Darby, S.; Meyer, T.; Gillmore, R.; Anthoney, A.; Lind, P.; Glimelius, B.; Falk, S.; Izbicki, J. R.; Middleton, G. W.; Cummins, S.; Ross, P. J.; Wasan, H.; McDonald, A.; Crosby, T.; Ma, Y. T.; Patel, K.; Sherriff, D.; Soomal, R.; Borg, D.; Sothi, S.; Hammel, P.; Hackert, T.; Jackson, R.; Buchler, M. W., Comparison of adjuvant gemcitabine and capecitabine with gemcitabine monotherapy in patients with resected pancreatic cancer (ESPAC-4): a multicentre, open-label, randomised, phase 3 trial. *Lancet* **2017,** *389* (10073), 1011-1024.

96. Conroy, T.; Hammel, P.; Hebbar, M.; Abdelghani, M. B.; Wei, A. C.-c.; Raoul, J.-L.; Chone, L.; Francois, E.; Artru, P.; Biagi, J. J.; Lecomte, T.; Assenat, E.; Faroux, R.; Ychou, M.; Volet, J.; Sauvanet, A.; Jouffroy-Zeller, C.; RAT, P.; Castan, F.; Bachet, J.-B., Unicancer GI PRODIGE 24/CCTG PA.6 trial: A multicenter international randomized phase III trial of adjuvant mFOLFIRINOX versus gemcitabine (gem) in patients with resected pancreatic ductal adenocarcinomas. *Journal of Clinical Oncology* **2018,** *36* (18_suppl), LBA4001-LBA4001.

97. Ducreux, M.; Cuhna, A. S.; Caramella, C.; Hollebecque, A.; Burtin, P.; Goere, D.; Seufferlein, T.; Haustermans, K.; Van Laethem, J. L.; Conroy, T.; Arnold, D., Cancer of the pancreas: ESMO Clinical Practice Guidelines for diagnosis, treatment and follow-up. *Annals of oncology : official journal of the European Society for Medical Oncology* **2015,** *26 Suppl 5*, v56-68.

98. Raufi, A. G.; Manji, G. A.; Chabot, J. A.; Bates, S. E., Neoadjuvant Treatment for Pancreatic Cancer. *Semin Oncol* **2019,** *46* (1), 19-27.

99. Gillen, S.; Schuster, T.; Meyer Zum Buschenfelde, C.; Friess, H.; Kleeff, J., Preoperative/neoadjuvant therapy in pancreatic cancer: a systematic review and meta-analysis of response and resection percentages. *PLoS Med* **2010,** *7* (4), e1000267.

100. D'Angelo, F.; Antolino, L.; Farcomeni, A.; Sirimarco, D.; Kazemi Nava, A.; De Siena, M.; Petrucciani, N.; Nigri, G.; Valabrega, S.; Aurello, P.; Ramacciato, G., Neoadjuvant treatment in pancreatic cancer: Evidence-based medicine? A systematic review and meta-analysis. *Med Oncol* **2017,** *34* (5), 85.

101. Versteijne, E.; Vogel, J. A.; Besselink, M. G.; Busch, O. R. C.; Wilmink, J. W.; Daams, J. G.; van Eijck, C. H. J.; Groot Koerkamp, B.; Rasch, C. R. N.; van Tienhoven, G., Meta-analysis comparing upfront surgery with neoadjuvant treatment in patients with resectable or borderline resectable pancreatic cancer. *Br J Surg* **2018,** *105* (8), 946-958.

102. Suker, M.; Beumer, B. R.; Sadot, E.; Marthey, L.; Faris, J. E.; Mellon, E. A.; El-Rayes, B. F.; Wang-Gillam, A.; Lacy, J.; Hosein, P. J.; Moorcraft, S. Y.; Conroy, T.; Hohla, F.; Allen, P.; Taieb, J.; Hong, T. S.; Shridhar, R.; Chau, I.; van Eijck, C. H.; Koerkamp, B. G., FOLFIRINOX for locally advanced pancreatic cancer: a systematic review and patient-level meta-analysis. *The Lancet Oncology* **2016,** *17* (6), 801-810.

103. Mokdad, A. A.; Minter, R. M.; Zhu, H.; Augustine, M. M.; Porembka, M. R.; Wang, S. C.; Yopp, A. C.; Mansour, J. C.; Choti, M. A.; Polanco, P. M., Neoadjuvant Therapy Followed by Resection Versus Upfront Resection for Resectable Pancreatic Cancer: A Propensity Score Matched Analysis. *Journal of Clinical Oncology* **2017,** *35* (5), 515-522.

104. Tienhoven, G. V.; Versteijne, E.; Suker, M.; Groothuis, K. B. C.; Busch, O. R.; Bonsing, B. A.; Hingh, I. H. J. T. d.; Festen, S.; Patijn, G. A.; Vos-Geelen, J. d.; Zwinderman, A. H.; Punt, C. J. A.; Eijck, C. H. J. v.; Group, a. a. o. i. o. t. i. p. i. t. t. o. b. o. t. D. P. C., Preoperative chemoradiotherapy versus immediate surgery for resectable and borderline resectable pancreatic cancer (PREOPANC-1): A randomized, controlled, multicenter phase III trial. *Journal of Clinical Oncology* **2018,** *36* (18_suppl), LBA4002-LBA4002.

105. Kleeff, J.; Reiser, C.; Hinz, U.; Bachmann, J.; Debus, J.; Jaeger, D.; Friess, H.; Büchler, M. W., Surgery for recurrent pancreatic ductal adenocarcinoma. *Ann Surg* **2007,** *245* (4), 566-572.

106. Burris, H. A., 3rd; Moore, M. J.; Andersen, J.; Green, M. R.; Rothenberg, M. L.; Modiano, M. R.; Cripps, M. C.; Portenoy, R. K.; Storniolo, A. M.; Tarassoff, P.; Nelson, R.; Dorr, F. A.; Stephens, C. D.; Von Hoff, D. D., Improvements in survival and clinical benefit with gemcitabine as first-line therapy for patients with advanced pancreas cancer: a randomized trial. *J Clin Oncol* **1997,** *15* (6), 2403-13.

107. el-Kamar, F. G.; Grossbard, M. L.; Kozuch, P. S., Metastatic pancreatic cancer: emerging strategies in chemotherapy and palliative care. *Oncologist* **2003,** *8* (1), 18-34.

108. Stark, A.; Hines, O. J., Endoscopic and operative palliation strategies for pancreatic ductal adenocarcinoma. *Semin Oncol* **2015,** *42* (1), 163-76.

109. Kneuertz, P. J.; Cunningham, S. C.; Cameron, J. L.; Torrez, S.; Tapazoglou, N.; Herman, J. M.; Makary, M. A.; Eckhauser, F.; Wang, J.; Hirose, K.; Edil, B. H.; Choti, M. A.; Schulick, R. D.; Wolfgang, C. L.; Pawlik, T. M., Palliative surgical management of patients with unresectable pancreatic adenocarcinoma: trends and lessons learned from a large, single institution experience. *Journal of gastrointestinal surgery : official journal of the Society for Surgery of the Alimentary Tract* **2011,** *15* (11), 1917-1927.

110. Perone, J. A.; Riall, T. S.; Olino, K., Palliative Care for Pancreatic and Periampullary Cancer. *The Surgical clinics of North America* **2016,** *96* (6), 1415-1430.

111. World Health Organisation. WHO Definition of Palliative Care. https://www.who.int/cancer/palliative/definition/en/ (accessed 11/07/2019).

112. Nakakura, E. K.; Warren, R. S., Palliative care for patients with advanced pancreatic and biliary cancers. *Surg Oncol* **2007,** *16* (4), 293-7.

113. Wong, G. Y.; Schroeder, D. R.; Carns, P. E.; Wilson, J. L.; Martin, D. P.; Kinney, M. O.; Mantilla, C. B.; Warner, D. O., Effect of neurolytic celiac plexus block on pain relief, quality of life, and survival in patients with unresectable pancreatic cancer: a randomized controlled trial. *Jama* **2004,** *291* (9), 1092-9.

114. Fazal, S.; Saif, M. W., Supportive and palliative care of pancreatic cancer. *Jop* **2007,** *8* (2), 240-53.

115. Jiang, X.; Li, J.; Zhang, R.; Zhu, Y.; Shen, J., An Improved Preparation Process for Gemcitabine. *Organic Process Research & Development* **2008,** *12* (5), 888-891.

116. de Sousa Cavalcante, L.; Monteiro, G., Gemcitabine: metabolism and molecular mechanisms of action, sensitivity and chemoresistance in pancreatic cancer. *Eur J Pharmacol* **2014,** *741*, 8-16.

117. Veltkamp, S. A.; Beijnen, J. H.; Schellens, J. H., Prolonged versus standard gemcitabine infusion: translation of molecular pharmacology to new treatment strategy. *Oncologist* **2008,** *13* (3), 261-76.

118. Noble, S.; Goa, K. L., Gemcitabine. A review of its pharmacology and clinical potential in non-small cell lung cancer and pancreatic cancer. *Drugs* **1997,** *54* (3), 447-72.

119. Abbruzzese, J. L.; Grunewald, R.; Weeks, E. A.; Gravel, D.; Adams, T.; Nowak, B.; Mineishi, S.; Tarassoff, P.; Satterlee, W.; Raber, M. N., A phase I clinical, plasma, and cellular pharmacology study of gemcitabine. *Journal of Clinical Oncology* **1991,** *9* (3), 491-498.

120. Ciccolini, J.; Serdjebi, C.; Peters, G. J.; Giovannetti, E., Pharmacokinetics and pharmacogenetics of Gemcitabine as a mainstay in adult and pediatric oncology: an EORTC-PAMM perspective. *Cancer Chemother Pharmacol* **2016,** *78* (1), 1-12.

121. Mackey, J. R.; Mani, R. S.; Selner, M.; Mowles, D.; Young, J. D.; Belt, J. A.; Crawford, C. R.; Cass, C. E., Functional nucleoside transporters are required for gemcitabine influx and manifestation of toxicity in cancer cell lines. *Cancer Res* **1998,** *58* (19), 4349-57.

122. Spratlin, J.; Sangha, R.; Glubrecht, D.; Dabbagh, L.; Young, J. D.; Dumontet, C.; Cass, C.; Lai, R.; Mackey, J. R., The Absence of Human Equilibrative Nucleoside Transporter 1 Is Associated with Reduced Survival in Patients With Gemcitabine-Treated Pancreas Adenocarcinoma. *Clinical Cancer Research* **2004,** *10* (20), 6956-6961.

123. Ritzel, M. W.; Ng, A. M.; Yao, S. Y.; Graham, K.; Loewen, S. K.; Smith, K. M.; Hyde, R. J.; Karpinski, E.; Cass, C. E.; Baldwin, S. A.; Young, J. D., Recent molecular advances in studies of the concentrative Na+-dependent nucleoside transporter (CNT) family: identification and characterization of novel human and mouse proteins (hCNT3 and mCNT3) broadly selective for purine and pyrimidine nucleosides (system cib). *Mol Membr Biol* **2001,** *18* (1), 65-72.

124. van Haperen, V. W.; Veerman, G.; Vermorken, J. B.; Pinedo, H. M.; Peters, G., Regulation of phosphorylation of deoxycytidine and 2',2'-difluorodeoxycytidine (gemcitabine); effects of cytidine 5'-triphosphate and uridine 5'-triphosphate in relation to chemosensitivity for 2',2'-difluorodeoxycytidine. *Biochem Pharmacol* **1996,** *51* (7), 911-8.

125. Ohhashi, S.; Ohuchida, K.; Mizumoto, K.; Fujita, H.; Egami, T.; Yu, J.; Toma, H.; Sadatomi, S.; Nagai, E.; Tanaka, M., Down-regulation of deoxycytidine kinase enhances acquired resistance to gemcitabine in pancreatic cancer. *Anticancer Res* **2008,** *28* (4b), 2205-12.

126. Heinemann, V.; Hertel, L. W.; Grindey, G. B.; Plunkett, W., Comparison of the cellular pharmacokinetics and toxicity of 2',2'-difluorodeoxycytidine and 1-beta-D-arabinofuranosylcytosine. *Cancer Res* **1988,** *48* (14), 4024-31.

127. Bouffard, D. Y.; Laliberte, J.; Momparler, R. L., Kinetic studies on 2',2'-difluorodeoxycytidine (Gemcitabine) with purified human deoxycytidine kinase and cytidine deaminase. *Biochem Pharmacol* **1993,** *45* (9), 1857-61.

128. Hatzis, P.; Al-Madhoon, A. S.; Jüllig, M.; Petrakis, T. G.; Eriksson, S.; Talianidis, I., The Intracellular Localization of Deoxycytidine Kinase. *Journal of Biological Chemistry* **1998,** *273* (46), 30239-30243.

129. Van Rompay, A. R.; Johansson, M.; Karlsson, A., Phosphorylation of Deoxycytidine Analog Monophosphates by UMP-CMP Kinase: Molecular Characterization of the Human Enzyme. *Molecular Pharmacology* **1999,** *56* (3), 562-569.

130. Wong, A.; Soo, R. A.; Yong, W.-P.; Innocenti, F., Clinical pharmacology and pharmacogenetics of gemcitabine. *Drug Metabolism Reviews* **2009,** *41* (2), 77-88.

131. Huang, P.; Chubb, S.; Hertel, L. W.; Grindey, G. B.; Plunkett, W., Action of 2',2'-difluorodeoxycytidine on DNA synthesis. *Cancer Res* **1991,** *51* (22), 6110-7.

132. Gandhi, V.; Legha, J.; Chen, F.; Hertel, L. W.; Plunkett, W., Excision of 2',2'-difluorodeoxycytidine (gemcitabine) monophosphate residues from DNA. *Cancer Res* **1996,** *56* (19), 4453-9.

133. Heinemann, V.; Xu, Y. Z.; Chubb, S.; Sen, A.; Hertel, L. W.; Grindey, G. B.; Plunkett, W., Cellular elimination of 2',2'-difluorodeoxycytidine 5'-triphosphate: a mechanism of self-potentiation. *Cancer Res* **1992,** *52* (3), 533-9.

134. Heinemann, V.; Xu, Y. Z.; Chubb, S.; Sen, A.; Hertel, L. W.; Grindey, G. B.; Plunkett, W., Inhibition of ribonucleotide reduction in CCRF-CEM cells by 2',2'-difluorodeoxycytidine. *Mol Pharmacol* **1990,** *38* (4), 567-72.

135. Xu, H.; Faber, C.; Uchiki, T.; Racca, J.; Dealwis, C., Structures of eukaryotic ribonucleotide reductase I define gemcitabine diphosphate binding and subunit assembly. *Proc Natl Acad Sci U S A* **2006,** *103* (11), 4028-33.

136. Sarup, J. C.; Johnson, M. A.; Verhoef, V.; Fridland, A., Regulation of purine deoxynucleoside phosphorylation by deoxycytidine kinase from human leukemic blast cells. *Biochem Pharmacol* **1989,** *38* (16), 2601-7.

137. Ferreira, C. G.; Span, S. W.; Peters, G. J.; Kruyt, F. A.; Giaccone, G., Chemotherapy triggers apoptosis in a caspase-8-dependent and mitochondria-controlled manner in the non-small cell lung cancer cell line NCI-H460. *Cancer Res* **2000,** *60* (24), 7133-41.

138. Habiro, A.; Tanno, S.; Koizumi, K.; Izawa, T.; Nakano, Y.; Osanai, M.; Mizukami, Y.; Okumura, T.; Kohgo, Y., Involvement of p38 mitogen-activated protein kinase in gemcitabine-induced apoptosis in human pancreatic cancer cells. *Biochem Biophys Res Commun* **2004,** *316* (1), 71-7.

139. Chandler, N. M.; Canete, J. J.; Callery, M. P., Caspase-3 drives apoptosis in pancreatic cancer cells after treatment with gemcitabine. *J Gastrointest Surg* **2004,** *8* (8), 1072-8.

140. Kummer, J. L.; Rao, P. K.; Heidenreich, K. A., Apoptosis induced by withdrawal of trophic factors is mediated by p38 mitogen-activated protein kinase. *J Biol Chem* **1997,** *272* (33), 20490-4.

141. Xu, Y. Z.; Plunkett, W., Modulation of deoxycytidylate deaminase in intact human leukemia cells. Action of 2',2'-difluorodeoxycytidine. *Biochem Pharmacol* **1992,** *44* (9), 1819-27.

142. Hodge, L. S.; Taub, M. E.; Tracy, T. S., The deaminated metabolite of gemcitabine, 2',2'-difluorodeoxyuridine, modulates the rate of gemcitabine transport and intracellular phosphorylation via deoxycytidine kinase. *Drug Metab Dispos* **2011,** *39* (11), 2013-6.

143. Veltkamp, S. A.; Pluim, D.; van Eijndhoven, M. A.; Bolijn, M. J.; Ong, F. H.; Govindarajan, R.; Unadkat, J. D.; Beijnen, J. H.; Schellens, J. H., New insights into the pharmacology and cytotoxicity of gemcitabine and 2',2'-difluorodeoxyuridine. *Mol Cancer Ther* **2008,** *7* (8), 2415-25.

144. Rudin, D.; Li, L.; Niu, N.; Kalari, K. R.; Gilbert, J. A.; Ames, M. M.; Wang, L., Gemcitabine Cytotoxicity: Interaction of Efflux and Deamination. *J Drug Metab Toxicol* **2011,** *2* (107), 1-10.

145. Bergman, A. M.; Giaccone, G.; van Moorsel, C. J.; Mauritz, R.; Noordhuis, P.; Pinedo, H. M.; Peters, G. J., Cross-resistance in the 2',2'-difluorodeoxycytidine (gemcitabine)-resistant human ovarian cancer cell line AG6000 to standard and investigational drugs. *Eur J Cancer* **2000,** *36* (15), 1974-83.

146. Hunsucker, S. A.; Spychala, J.; Mitchell, B. S., Human Cytosolic 5′-Nucleotidase I: CHARACTERIZATION AND ROLE IN NUCLEOSIDE ANALOG RESISTANCE. *Journal of Biological Chemistry* **2001,** *276* (13), 10498-10504.

147. Hunsucker, S. A.; Mitchell, B. S.; Spychala, J., The 5'-nucleotidases as regulators of nucleotide and drug metabolism. *Pharmacol Ther* **2005,** *107* (1), 1-30.

148. Aksoy, P.; Zhu, M. J.; Kalari, K. R.; Moon, I.; Pelleymounter, L. L.; Eckloff, B. W.; Wieben, E. D.; Yee, V. C.; Weinshilboum, R. M.; Wang, L., Cytosolic 5'-nucleotidase III (NT5C3): gene sequence variation and functional genomics. *Pharmacogenet Genomics* **2009,** *19* (8), 567-76.

149. Amrutkar, M.; Gladhaug, I. P., Pancreatic Cancer Chemoresistance to Gemcitabine. *Cancers* **2017,** *9* (11), 157.

150. Moysan, E.; Bastiat, G.; Benoit, J. P., Gemcitabine versus Modified Gemcitabine: a review of several promising chemical modifications. *Molecular pharmaceutics* **2013,** *10* (2), 430-44.

151. Funamizu, N.; Okamoto, A.; Kamata, Y.; Misawa, T.; Uwagawa, T.; Gocho, T.; Yanaga, K.; Manome, Y., Is the resistance of gemcitabine for pancreatic cancer settled only by overexpression of deoxycytidine kinase? *Oncol Rep* **2010,** *23* (2), 471-5.

152. Pearce, A.; Blok, A.; Yilmaz, G.; Singh, N.; Cavanagh, R.; Abelha, T.; Taresco, V.; Alexander, C., *Functional Polymers For Drug Delivery – Prospects and Challenges*. 2018; Vol. 36.

153. Duncan, R., The dawning era of polymer therapeutics. *Nature Reviews Drug Discovery* **2003,** *2* (5), 347-360.

154. Liechty, W. B.; Kryscio, D. R.; Slaughter, B. V.; Peppas, N. A., Polymers for drug delivery systems. *Annu Rev Chem Biomol Eng* **2010,** *1*, 149-173.

155. Colomer, R.; Alba, E.; González-Martin, A.; Paz-Ares, L.; Martín, M.; Llombart, A.; Rodríguez Lescure, A.; Salvador, J.; Albanell, J.; Isla, D.; Lomas, M.; Rodríguez, C. A.; Trigo, J. M.; Germà, J. R.; Bellmunt, J.; Tabernero, J.; Rosell, R.; Aranda, E.; Cubedo, R.; Baselga, J.; Spanish Society of Medical, O., Treatment of cancer with oral drugs: a position statement by the Spanish Society of Medical Oncology (SEOM). *Annals of oncology : official journal of the European Society for Medical Oncology* **2010,** *21* (2), 195-198.

156. Schmaljohann, D., Thermo- and pH-responsive polymers in drug delivery. *Advanced Drug Delivery Reviews* **2006,** *58* (15), 1655-1670.

157. Priya James, H.; John, R.; Alex, A.; Anoop, K. R., Smart polymers for the controlled delivery of drugs – a concise overview. *Acta Pharmaceutica Sinica B* **2014,** *4* (2), 120-127.

158. Jain, R. K., Delivery of molecular medicine to solid tumors: lessons from in vivo imaging of gene expression and function. *Journal of Controlled Release* **2001,** *74* (1), 7-25.

159. Seymour, L. W., Passive tumor targeting of soluble macromolecules and drug conjugates. *Crit Rev Ther Drug Carrier Syst* **1992,** *9* (2), 135-87.

160. Brigger, I.; Dubernet, C.; Couvreur, P., Nanoparticles in cancer therapy and diagnosis. *Advanced Drug Delivery Reviews* **2002,** *54* (5), 631-651.

161. Maeda, H.; Sawa, T.; Konno, T., Mechanism of tumor-targeted delivery of macromolecular drugs, including the EPR effect in solid tumor and clinical overview of the prototype polymeric drug SMANCS. *J Control Release* **2001,** *74* (1-3), 47-61.

162. Yuan, F.; Leunig, M.; Huang, S. K.; Berk, D. A.; Papahadjopoulos, D.; Jain, R. K., Mirovascular Permeability and Interstitial Penetration of Sterically Stabilized (Stealth) Liposomes in a Human Tumor Xenograft. *Cancer Research* **1994,** *54* (13), 3352-3356.

163. Matsumura, Y.; Maeda, H., A new concept for macromolecular therapeutics in cancer chemotherapy: mechanism of tumoritropic accumulation of proteins and the antitumor agent smancs. *Cancer Res* **1986,** *46* (12 Pt 1), 6387-92.

164. Clark, A. J.; Wiley, D. T.; Zuckerman, J. E.; Webster, P.; Chao, J.; Lin, J.; Yen, Y.; Davis, M. E., CRLX101 nanoparticles localize in human tumors and not in adjacent, nonneoplastic tissue after intravenous dosing. *Proceedings of the National Academy of Sciences* **2016,** *113* (14), 3850-3854.

165. Golombek, S. K.; May, J.-N.; Theek, B.; Appold, L.; Drude, N.; Kiessling, F.; Lammers, T., Tumor targeting via EPR: Strategies to enhance patient responses. *Advanced drug delivery reviews* **2018,** *130*, 17-38.

166. Ringsdorf, H., Structure and properties of pharmacologically active polymers. *Journal of Polymer Science: Polymer Symposia* **1975,** *51* (1), 135-153.

167. Larson, N.; Ghandehari, H., Polymeric conjugates for drug delivery. *Chemistry of materials : a publication of the American Chemical Society* **2012,** *24* (5), 840-853.

168. Seymour, L. W.; Ulbrich, K.; Steyger, P. S.; Brereton, M.; Subr, V.; Strohalm, J.; Duncan, R., Tumour tropism and anti-cancer efficacy of polymer-based doxorubicin prodrugs in the treatment of subcutaneous murine B16F10 melanoma. *Br J Cancer* **1994,** *70* (4), 636-41.

169. Gianasi, E.; Wasil, M.; Evagorou, E. G.; Keddle, A.; Wilson, G.; Duncan, R., HPMA copolymer platinates as novel antitumour agents: in vitro properties, pharmacokinetics and antitumour activity in vivo. *Eur J Cancer* **1999,** *35* (6), 994-1002.

170. Van, S.; Das, S. K.; Wang, X.; Feng, Z.; Jin, Y.; Hou, Z.; Chen, F.; Pham, A.; Jiang, N.; Howell, S. B.; Yu, L., Synthesis, characterization, and biological evaluation of poly(L-gamma-glutamyl-glutamine)- paclitaxel nanoconjugate. *International journal of nanomedicine* **2010,** *5*, 825-37.

171. Zhou, P.; Li, Z.; Chau, Y., Synthesis, characterization, and in vivo evaluation of poly(ethylene oxide-co-glycidol)-platinate conjugate. *European journal of pharmaceutical sciences : official journal of the European Federation for Pharmaceutical Sciences* **2010,** *41* (3-4), 464-72.

172. Lipinski, C., Poor aqueous solubility-an industry wide problem in drug discovery. *American Pharmaceutical Reviews* **2002,** *5* (3), 82-85.

173. Taresco, V.; Alexander, C.; Singh, N.; Pearce, A. K., Stimuli-Responsive Prodrug Chemistries for Drug Delivery. *Advanced Therapeutics* **2018,** *1* (4), 1800030.

174. Wang, Y.; Kohane, D. S., External triggering and triggered targeting strategies for drug delivery. *Nature Reviews Materials* **2017,** *2*, 17020.

175. Manzoor, A. A.; Lindner, L. H.; Landon, C. D.; Park, J. Y.; Simnick, A. J.; Dreher, M. R.; Das, S.; Hanna, G.; Park, W.; Chilkoti, A.; Koning, G. A.; ten Hagen, T. L.; Needham, D.; Dewhirst, M. W., Overcoming limitations in nanoparticle drug delivery: triggered, intravascular release to improve drug penetration into tumors. *Cancer Res* **2012,** *72* (21), 5566-75.

176. Zhang, Y.; Yang, C.; Wang, W.; Liu, J.; Liu, Q.; Huang, F.; Chu, L.; Gao, H.; Li, C.; Kong, D.; Liu, Q.; Liu, J., Co-delivery of doxorubicin and curcumin by pH-sensitive prodrug nanoparticle for combination therapy of cancer. **2016,** *6*, 21225.

177. Lv, S.; Tang, Z.; Zhang, D.; Song, W.; Li, M.; Lin, J.; Liu, H.; Chen, X., Well-defined polymer-drug conjugate engineered with redox and pH-

sensitive release mechanism for efficient delivery of paclitaxel. *Journal of Controlled Release* **2014,** *194*, 220-227.

178. Mura, S.; Nicolas, J.; Couvreur, P., Stimuli-responsive nanocarriers for drug delivery. *Nat Mater* **2013,** *12* (11), 991-1003.

179. Ganta, S.; Devalapally, H.; Shahiwala, A.; Amiji, M., A review of stimuli-responsive nanocarriers for drug and gene delivery. *J Control Release* **2008,** *126* (3), 187-204.

180. Vaupel, P.; Kallinowski, F.; Okunieff, P., Blood flow, oxygen and nutrient supply, and metabolic microenvironment of human tumors: a review. *Cancer Res* **1989,** *49* (23), 6449-65.

181. Kato, Y.; Ozawa, S.; Miyamoto, C.; Maehata, Y.; Suzuki, A.; Maeda, T.; Baba, Y., Acidic extracellular microenvironment and cancer. *Cancer Cell Int* **2013,** *13* (1), 89-89.

182. Gillies, E. R.; Goodwin, A. P.; Fréchet, J. M. J., Acetals as pH-Sensitive Linkages for Drug Delivery. *Bioconjugate Chemistry* **2004,** *15* (6), 1254-1263.

183. Parrott, M. C.; Finniss, M.; Luft, J. C.; Pandya, A.; Gullapalli, A.; Napier, M. E.; DeSimone, J. M., Incorporation and controlled release of silyl ether prodrugs from PRINT nanoparticles. *J Am Chem Soc* **2012,** *134* (18), 7978-82.

184. Joubert, F.; Martin, L.; Perrier, S.; Pasparakis, G., Development of a Gemcitabine-Polymer Conjugate with Prolonged Cytotoxicity against a Pancreatic Cancer Cell Line. *ACS Macro Letters* **2017,** *6* (5), 535-540.

185. Zhou, Z.; Li, L.; Yang, Y.; Xu, X.; Huang, Y., Tumor targeting by pH-sensitive, biodegradable, cross-linked N-(2-hydroxypropyl) methacrylamide copolymer micelles. *Biomaterials* **2014,** *35* (24), 6622-35.

186. Jia, T.; Huang, S.; Yang, C.; Wang, M., Unimolecular Micelles of Amphiphilic Cyclodextrin-Core Star-Like Copolymers with Covalent pH-Responsive Linkage of Anticancer Prodrugs. *Molecular pharmaceutics* **2017,** *14* (8), 2529-2537.

187. Deng, B.; Ma, P.; Xie, Y., Reduction-sensitive polymeric nanocarriers in cancer therapy: a comprehensive review. *Nanoscale* **2015,** *7* (30), 12773-12795.

188. Wu, G.; Fang, Y. Z.; Yang, S.; Lupton, J. R.; Turner, N. D., Glutathione metabolism and its implications for health. *J Nutr* **2004,** *134* (3), 489-92.

189. Balendiran, G. K.; Dabur, R.; Fraser, D., The role of glutathione in cancer. *Cell Biochem Funct* **2004,** *22* (6), 343-52.

190. Schafer, F. Q.; Buettner, G. R., Redox environment of the cell as viewed through the redox state of the glutathione disulfide/glutathione couple. *Free Radical Biology and Medicine* **2001,** *30* (11), 1191-1212.

191. Kuppusamy, P.; Li, H.; Ilangovan, G.; Cardounel, A. J.; Zweier, J. L.; Yamada, K.; Krishna, M. C.; Mitchell, J. B., Noninvasive imaging of tumor redox status and its modification by tissue glutathione levels. *Cancer Res* **2002,** *62* (1), 307-12.

192. Lv, H.; Zhen, C.; Liu, J.; Yang, P.; Hu, L.; Shang, P., Unraveling the Potential Role of Glutathione in Multiple Forms of Cell Death in Cancer Therapy. *Oxid Med Cell Longev* **2019,** *2019*, 3150145.

193. Cho, H.; Bae, J.; Garripelli, V. K.; Anderson, J. M.; Jun, H.-W.; Jo, S., Redox-sensitive polymeric nanoparticles for drug delivery. *Chemical Communications* **2012,** *48* (48), 6043-6045.

194. Sun, T.; Zhu, C.; Xu, J., Multiple stimuli-responsive selenium-functionalized biodegradable starch-based hydrogels. *Soft Matter* **2018,** *14* (6), 921-926.

195. Gong, H.; Xie, Z.; Liu, M.; Zhu, H.; Sun, H., Redox-sensitive mesoporous silica nanoparticles functionalized with PEG through a disulfide bond linker for potential anticancer drug delivery. *RSC Advances* **2015,** *5* (73), 59576-59582.

196. Peterson, G. I.; Larsen, M. B.; Boydston, A. J., Controlled Depolymerization: Stimuli-Responsive Self-Immolative Polymers. *Macromolecules* **2012,** *45* (18), 7317-7328.

197. Shenoy, D.; Little, S.; Langer, R.; Amiji, M., Poly(ethylene oxide)-modified poly(beta-amino ester) nanoparticles as a pH-sensitive system for tumor-targeted delivery of hydrophobic drugs: part 2. In vivo distribution and tumor localization studies. *Pharm Res* **2005,** *22* (12), 2107-14.

198. Blencowe, C. A.; Russell, A. T.; Greco, F.; Hayes, W.; Thornthwaite, D. W., Self-immolative linkers in polymeric delivery systems. *Polymer Chemistry* **2011,** *2* (4), 773-790.

199. Wong, A. D.; Güngör, T. M.; Gillies, E. R., Multiresponsive Azobenzene End-Cap for Self-Immolative Polymers. *ACS Macro Letters* **2014,** *3* (11), 1191-1195.

200. Eom, T.; Yoo, W.; Lee, Y.-D.; Park, J. H.; Choe, Y.; Bang, J.; Kim, S.; Khan, A., An activatable anticancer polymer–drug conjugate based on the self-immolative azobenzene motif. *Journal of Materials Chemistry B* **2017,** *5* (24), 4574-4578.

201. Amir, R. J.; Pessah, N.; Shamis, M.; Shabat, D., Self-Immolative Dendrimers. *Angewandte Chemie International Edition* **2003,** *42* (37), 4494-4499.

202. Liu, D.; Yang, F.; Xiong, F.; Gu, N., The Smart Drug Delivery System and Its Clinical Potential. *Theranostics* **2016,** *6* (9), 1306-1323.

203. Ferrari, M., Frontiers in cancer nanomedicine: directing mass transport through biological barriers. *Trends in biotechnology* **2010,** *28* (4), 181-8.

204. Tucker, B. S.; Sumerlin, B. S., Poly(N-(2-hydroxypropyl) methacrylamide)-based nanotherapeutics. *Polymer Chemistry* **2014,** *5* (5), 1566-1572.

205. Barz, M.; Luxenhofer, R.; Zentel, R.; Vicent, M. J., Overcoming the PEG-addiction: well-defined alternatives to PEG, from structure–property relationships to better defined therapeutics. *Polymer Chemistry* **2011,** *2* (9), 1900-1918.

206. Kopeček, J.; Bažilová, H., Poly[N-(2-hydroxypropyl)methacrylamide]—I. Radical polymerization and copolymerization. *European Polymer Journal* **1973,** *9* (1), 7-14.

207. Scales, C. W.; Vasilieva, Y. A.; Convertine, A. J.; Lowe, A. B.; McCormick, C. L., Direct, controlled synthesis of the nonimmunogenic, hydrophilic polymer, poly(N-(2-hydroxypropyl)methacrylamide) via RAFT in aqueous media. *Biomacromolecules* **2005,** *6* (4), 1846-1850.

208. Teodorescu, M.; Matyjaszewski, K., Atom Transfer Radical Polymerization of (Meth)acrylamides. *Macromolecules* **1999,** *32* (15), 4826-4831.

209. Zhou, Y.; Yang, J.; Rhim, J. S.; Kopecek, J., HPMA copolymer-based combination therapy toxic to both prostate cancer stem/progenitor cells and differentiated cells induces durable anti-tumor effects. *J Control Release* **2013,** *172* (3), 946-53.

210. Zhou, Y.; Yang, J.; Kopecek, J., Selective inhibitory effect of HPMA copolymer-cyclopamine conjugate on prostate cancer stem cells. *Biomaterials* **2012,** *33* (6), 1863-72.

211. Vasey, P. A.; Kaye, S. B.; Morrison, R.; Twelves, C.; Wilson, P.; Duncan, R.; Thomson, A. H.; Murray, L. S.; Hilditch, T. E.; Murray, T.; Burtles, S.; Fraier, D.; Frigerio, E.; Cassidy, J., Phase I Clinical and Pharmacokinetic Study of PK1 [N-(2-Hydroxypropyl)methacrylamide Copolymer Doxorubicin]: First Member of a New Class of Chemotherapeutic Agents—Drug-Polymer Conjugates. *Clinical Cancer Research* **1999,** *5* (1), 83-94.

212. Yang, J.; Kopeček, J., The Light at the End of the Tunnel-Second Generation HPMA Conjugates for Cancer Treatment. *Curr Opin Colloid Interface Sci* **2017,** *31*, 30-42.

213. Seymour, L. W.; Ferry, D. R.; Anderson, D.; Hesslewood, S.; Julyan, P. J.; Poyner, R.; Doran, J.; Young, A. M.; Burtles, S.; Kerr, D. J.,

Hepatic drug targeting: phase I evaluation of polymer-bound doxorubicin. *J Clin Oncol* **2002,** *20* (6), 1668-76.

214. Meerum Terwogt, J. M.; ten Bokkel Huinink, W. W.; Schellens, J. H.; Schot, M.; Mandjes, I. A.; Zurlo, M. G.; Rocchetti, M.; Rosing, H.; Koopman, F. J.; Beijnen, J. H., Phase I clinical and pharmacokinetic study of PNU166945, a novel water-soluble polymer-conjugated prodrug of paclitaxel. *Anticancer Drugs* **2001,** *12* (4), 315-23.

215. Schoemaker, N. E.; van Kesteren, C.; Rosing, H.; Jansen, S.; Swart, M.; Lieverst, J.; Fraier, D.; Breda, M.; Pellizzoni, C.; Spinelli, R.; Grazia Porro, M.; Beijnen, J. H.; Schellens, J. H.; ten Bokkel Huinink, W. W., A phase I and pharmacokinetic study of MAG-CPT, a water-soluble polymer conjugate of camptothecin. *Br J Cancer* **2002,** *87* (6), 608-14.

216. Rademaker-Lakhai, J. M.; Terret, C.; Howell, S. B.; Baud, C. M.; De Boer, R. F.; Pluim, D.; Beijnen, J. H.; Schellens, J. H.; Droz, J. P., A Phase I and pharmacological study of the platinum polymer AP5280 given as an intravenous infusion once every 3 weeks in patients with solid tumors. *Clin Cancer Res* **2004,** *10* (10), 3386-95.

217. Campone, M.; Rademaker-Lakhai, J. M.; Bennouna, J.; Howell, S. B.; Nowotnik, D. P.; Beijnen, J. H.; Schellens, J. H., Phase I and pharmacokinetic trial of AP5346, a DACH-platinum-polymer conjugate, administered weekly for three out of every 4 weeks to advanced solid tumor patients. *Cancer Chemother Pharmacol* **2007,** *60* (4), 523-33.

218. Etrych, T.; Šírová, M.; Starovoytova, L.; Říhová, B.; Ulbrich, K., HPMA Copolymer Conjugates of Paclitaxel and Docetaxel with pH-Controlled Drug Release. *Molecular pharmaceutics* **2010,** *7* (4), 1015-1026.

219. Duncan, R.; Vicent, M.; Greco, F.; I Nicholson, R., Polymer-drug conjugates: Towards a novel approach for the treatment of endrocine-related cancer. *Endocrine-related cancer* **2005,** *12 Suppl 1*, S189-99.

220. Duncan, R.; Vicent, M. J.; Greco, F.; Nicholson, R. I., Polymer–drug conjugates: towards a novel approach for the treatment of endrocine-related cancer. **2005,** *12* (Supplement_1), S189.

221. Gao, C.; Yan, D., Hyperbranched polymers: from synthesis to applications. *Progress in Polymer Science* **2004,** *29* (3), 183-275.

222. Ma, Y.; Mou, Q.; Wang, D.; Zhu, X.; Yan, D., Dendritic Polymers for Theranostics. *Theranostics* **2016,** *6* (7), 930-947.

223. Kim, Y. H.; Webster, O. W., Hyperbranched polyphenylenes. *Macromolecules* **1992,** *25* (21), 5561-5572.

224. Kim, Y. H.; Webster, O. W., Water soluble hyperbranched polyphenylene: "a unimolecular micelle?". *Journal of the American Chemical Society* **1990,** *112* (11), 4592-4593.

225. Zheng, Y.; Li, S.; Weng, Z.; Gao, C., Hyperbranched polymers: advances from synthesis to applications. *Chemical Society Reviews* **2015,** *44* (12), 4091-4130.

226. Graeme Moad, E. R., and San H. Thang, Reversible Addition Fragmentation Chain Transfer (RAFT) Polymerization. *Material Matters* **2010,** *5.1* (2).

227. Moad, G.; Rizzardo, E.; Thang, S. H., Toward Living Radical Polymerization. *Accounts of Chemical Research* **2008,** *41* (9), 1133-1142.

228. Semsarilar, M.; Perrier, S., 'Green' reversible addition-fragmentation chain-transfer (RAFT) polymerization. *Nat Chem* **2010,** *2* (10), 811-820.

229. Keddie, D. J., A guide to the synthesis of block copolymers using reversible-addition fragmentation chain transfer (RAFT) polymerization. *Chemical Society Reviews* **2014,** *43* (2), 496-505.

230. Willcock, H.; O'Reilly, R. K., End group removal and modification of RAFT polymers. *Polymer Chemistry* **2010,** *1* (2), 149-157.

231. Costa, E. C.; Moreira, A. F.; de Melo-Diogo, D.; Gaspar, V. M.; Carvalho, M. P.; Correia, I. J., 3D tumor spheroids: an overview on the tools and techniques used for their analysis. *Biotechnology Advances* **2016,** *34* (8), 1427-1441.

232. Breslin, S.; O'Driscoll, L., Three-dimensional cell culture: the missing link in drug discovery. *Drug Discovery Today* **2013,** *18* (5), 240-249.

233. Nath, S.; Devi, G. R., Three-dimensional culture systems in cancer research: Focus on tumor spheroid model. *Pharmacology & Therapeutics* **2016,** *163*, 94-108.

234. Unger, C.; Kramer, N.; Walzl, A.; Scherzer, M.; Hengstschlager, M.; Dolznig, H., Modeling human carcinomas: physiologically relevant 3D models to improve anti-cancer drug development. *Adv Drug Deliv Rev* **2014,** *79-80*, 50-67.

235. Ricci, C.; Moroni, L.; Danti, S., *Cancer tissue engineering—New perspectives in understanding the biology of solid tumors—A critical review*. 2013; Vol. 1, p 1-7.

236. Mueller-Klieser, W., Three-dimensional cell cultures: from molecular mechanisms to clinical applications. *The American journal of physiology* **1997,** *273* (4 Pt 1), C1109-23.

237. Kunz-Schughart, L. A.; Kreutz, M.; Knuechel, R., Multicellular spheroids: a three-dimensional in vitro culture system to study tumour biology. *Int J Exp Pathol* **1998,** *79* (1), 1-23.

238. Mathis, C.; Poussin, C.; Weisensee, D.; Gebel, S.; Hengstermann, A.; Sewer, A.; Belcastro, V.; Xiang, Y.; Ansari, S.; Wagner, S.; Hoeng, J.;

Peitsch, M. C., Human bronchial epithelial cells exposed in vitro to cigarette smoke at the air-liquid interface resemble bronchial epithelium from human smokers. *Am J Physiol Lung Cell Mol Physiol* **2013,** *304* (7), L489-503.

239. Unger, C.; Kramer, N.; Walzl, A.; Scherzer, M.; Hengstschläger, M.; Dolznig, H., Modeling human carcinomas: Physiologically relevant 3D models to improve anti-cancer drug development. *Advanced Drug Delivery Reviews* **2014,** *79-80*, 50-67.

240. Ritter, C. A.; Perez-Torres, M.; Rinehart, C.; Guix, M.; Dugger, T.; Engelman, J. A.; Arteaga, C. L., Human Breast Cancer Cells Selected for Resistance to Trastuzumab In vivo Overexpress Epidermal Growth Factor Receptor and ErbB Ligands and Remain Dependent on the ErbB Receptor Network. *Clinical Cancer Research* **2007,** *13* (16), 4909-4919.

241. Joshi, P.; Lee, M.-Y., High Content Imaging (HCI) on Miniaturized Three-Dimensional (3D) Cell Cultures. *Biosensors* **2015,** *5*, 768-790.

242. Albanese, M.; Jajodia, S.; Jhawar, R.; Piuri, V. In *Reliable mission deployment in vulnerable distributed systems*, 2013 43rd Annual IEEE/IFIP Conference on Dependable Systems and Networks Workshop (DSN-W), 24-27 June 2013; 2013; pp 1-8.

243. Esch, E. W.; Bahinski, A.; Huh, D., Organs-on-chips at the frontiers of drug discovery. *Nature Reviews Drug Discovery* **2015,** *14*, 248.

244. Alessandri, K.; Sarangi, B. R.; Gurchenkov, V. V.; Sinha, B.; Kießling, T. R.; Fetler, L.; Rico, F.; Scheuring, S.; Lamaze, C.; Simon, A.; Geraldo, S.; Vignjević, D.; Doméjean, H.; Rolland, L.; Funfak, A.; Bibette, J.; Bremond, N.; Nassoy, P., Cellular capsules as a tool for multicellular spheroid production and for investigating the mechanics of tumor progression in vitro. *Proceedings of the National Academy of Sciences* **2013,** *110* (37), 14843-14848.

245. Tsai, H.-F.; Trubelja, A.; Shen, A. Q.; Bao, G., Tumour-on-a-chip: microfluidic models of tumour morphology, growth and microenvironment. *J R Soc Interface* **2017,** *14* (131), 20170137.

246. Menon, J., 3D tumor models for cancer drug discovery: Current status and outlook. **2018,** *2*, 1-2.

247. Baal, N.; Widmer-Teske, R.; McKinnon, T.; Preissner, K. T.; Zygmunt, M. T., In vitro spheroid model of placental vasculogenesis: does it work? *Laboratory Investigation* **2008,** *89*, 152.

248. Wenzel, C.; Riefke, B.; Grundemann, S.; Krebs, A.; Christian, S.; Prinz, F.; Osterland, M.; Golfier, S.; Rase, S.; Ansari, N.; Esner, M.; Bickle, M.; Pampaloni, F.; Mattheyer, C.; Stelzer, E. H.; Parczyk, K.; Prechtl, S.; Steigemann, P., 3D high-content screening for the identification of compounds that target cells in dormant tumor spheroid regions. *Exp Cell Res* **2014,** *323* (1), 131-43.

249. Nyga, A.; Cheema, U.; Loizidou, M., 3D tumour models: novel in vitro approaches to cancer studies. *J Cell Commun Signal* **2011,** *5* (3), 239-248.

250. Breslin, S.; O'Driscoll, L., Three-dimensional cell culture: the missing link in drug discovery. *Drug Discov Today* **2013,** *18* (5-6), 240-9.

251. Ivanov, D. P.; Parker, T. L.; Walker, D. A.; Alexander, C.; Ashford, M. B.; Gellert, P. R.; Garnett, M. C., Multiplexing Spheroid Volume, Resazurin and Acid Phosphatase Viability Assays for High-Throughput Screening of Tumour Spheroids and Stem Cell Neurospheres. *PLOS ONE* **2014,** *9* (8), e103817.

252. Ivascu, A.; Kubbies, M., Rapid generation of single-tumor spheroids for high-throughput cell function and toxicity analysis. *J Biomol Screen* **2006,** *11* (8), 922-32.

253. Tchoryk, A.; Taresco, V.; Argent, R. H.; Ashford, M.; Gellert, P. R.; Stolnik, S.; Grabowska, A.; Garnett, M. C., Penetration and Uptake of Nanoparticles in 3D Tumor Spheroids. *Bioconjugate Chemistry* **2019,** *30* (5), 1371-1384.

254. Ivanov, D. P.; Parker, T. L.; Walker, D. A.; Alexander, C.; Ashford, M. B.; Gellert, P. R.; Garnett, M. C., In vitro co-culture model of medulloblastoma and human neural stem cells for drug delivery assessment. *J Biotechnol* **2015,** *205*, 3-13.

255. Pergolini, I.; Morales-Oyarvide, V.; Mino-Kenudson, M.; Honselmann, K. C.; Rosenbaum, M. W.; Nahar, S.; Kem, M.; Ferrone, C. R.; Lillemoe, K. D.; Bardeesy, N.; Ryan, D. P.; Thayer, S. P.; Warshaw, A. L.; Fernández-del Castillo, C.; Liss, A. S., Tumor engraftment in patient-derived xenografts of pancreatic ductal adenocarcinoma is associated with adverse clinicopathological features and poor survival. *PLOS ONE* **2017,** *12* (8), e0182855.

256. Reyes, G.; Villanueva, A.; Garcia, C.; Sancho, F. J.; Piulats, J.; Lluis, F.; Capella, G., Orthotopic xenografts of human pancreatic carcinomas acquire genetic aberrations during dissemination in nude mice. *Cancer Res* **1996,** *56* (24), 5713-9.

257. Rajeshkumar, N. V.; Yabuuchi, S.; Pai, S. G.; De Oliveira, E.; Kamphorst, J. J.; Rabinowitz, J. D.; Tejero, H.; Al-Shahrour, F.; Hidalgo, M.; Maitra, A.; Dang, C. V., Treatment of Pancreatic Cancer Patient–Derived Xenograft Panel with Metabolic Inhibitors Reveals Efficacy of Phenformin. *Clinical Cancer Research* **2017,** *23* (18), 5639-5647.

258. Lee, J. W.; Komar, C. A.; Bengsch, F.; Graham, K.; Beatty, G. L., Genetically Engineered Mouse Models of Pancreatic Cancer: The KPC Model (LSL-Kras(G12D/+) ;LSL-Trp53(R172H/+) ;Pdx-1-Cre), Its Variants, and Their Application in Immuno-oncology Drug Discovery. *Curr Protoc Pharmacol* **2016,** *73*, 14.39.1-14.39.20.

259. Herreros-Villanueva, M.; Hijona, E.; Cosme, A.; Bujanda, L., Mouse models of pancreatic cancer. *World J Gastroenterol* **2012,** *18* (12), 1286-1294.

260. Lee, E. Y. H. P.; Muller, W. J., Oncogenes and tumor suppressor genes. *Cold Spring Harb Perspect Biol* **2010,** *2* (10), a003236-a003236.

261. Lampreht Tratar, U.; Horvat, S.; Cemazar, M., Transgenic Mouse Models in Cancer Research. *Front Oncol* **2018,** *8*, 268-268.

262. A. Pérez-Mancera, P., Mouse Models of Pancreatic Exocrine Cancer. 2017; pp 1-30.

263. Morton, C. L.; Houghton, P. J., Establishment of human tumor xenografts in immunodeficient mice. *Nat Protoc* **2007,** *2* (2), 247-50.

264. Garber, K., Realistic rodents? Debate grows over new mouse models of cancer. *J Natl Cancer Inst* **2006,** *98* (17), 1176-8.

265. Duner, S.; Lopatko Lindman, J.; Ansari, D.; Gundewar, C.; Andersson, R., Pancreatic cancer: the role of pancreatic stellate cells in tumor progression. *Pancreatology* **2010,** *10* (6), 673-81.

266. Kyriazis, A. P.; Kyriazis, A. A.; Scarpelli, D. G.; Fogh, J.; Rao, M. S.; Lepera, R., Human pancreatic adenocarcinoma line Capan-1 in tissue culture and the nude mouse: morphologic, biologic, and biochemical characteristics. *Am J Pathol* **1982,** *106* (2), 250-60.

267. Lohr, M.; Trautmann, B.; Gottler, M.; Peters, S.; Zauner, I.; Maillet, B.; Kloppel, G., Human ductal adenocarcinomas of the pancreas express extracellular matrix proteins. *Br J Cancer* **1994,** *69* (1), 144-51.

268. Tang, L.; Yang, X.; Yin, Q.; Cai, K.; Wang, H.; Chaudhury, I.; Yao, C.; Zhou, Q.; Kwon, M.; Hartman, J. A.; Dobrucki, I. T.; Dobrucki, L. W.; Borst, L. B.; Lezmi, S.; Helferich, W. G.; Ferguson, A. L.; Fan, T. M.; Cheng, J., Investigating the optimal size of anticancer nanomedicine. *Proceedings of the National Academy of Sciences* **2014,** *111* (43), 15344-15349.

269. Peer, D., Harnessing RNAi nanomedicine for precision therapy. *Mol Cell Ther* **2014,** *2*, 5-5.

270. England, R. M.; Hare, J. I.; Barnes, J.; Wilson, J.; Smith, A.; Strittmatter, N.; Kemmitt, P. D.; Waring, M. J.; Barry, S. T.; Alexander, C.; Ashford, M. B., Tumour regression and improved gastrointestinal tolerability from controlled release of SN-38 from novel polyoxazoline-modified dendrimers. *Journal of Controlled Release* **2017,** *247*, 73-85.

271. Kaistha, B. P.; Krattenmacher, A.; Fredebohm, J.; Schmidt, H.; Behrens, D.; Widder, M.; Hackert, T.; Strobel, O.; Hoheisel, J. D.; Gress, T. M.; Buchholz, M., The deubiquitinating enzyme USP5 promotes pancreatic

cancer via modulating cell cycle regulators. *Oncotarget* **2017,** *8* (39), 66215-66225.

272. Gulfam, M.; Matini, T.; Monteiro, P. F.; Riva, R.; Collins, H.; Spriggs, K.; Howdle, S. M.; Jérôme, C.; Alexander, C., Bioreducible cross-linked core polymer micelles enhance in vitro activity of methotrexate in breast cancer cells. *Biomaterials Science* **2017,** *5* (3), 532-550.

273. Gunawan, S.; Ismadji, S.; Ju, Y.-H., Design and operation of a modified silica gel column chromatography. *Journal of the Chinese Institute of Chemical Engineers* **2008,** *39* (6), 625-633.

274. Snyder, L. R.; Dolan, J. W., Chapter 8 - Liquid-solid chromatography. In *Liquid Chromatography (Second Edition)*, Fanali, S.; Haddad, P. R.; Poole, C. F.; Riekkola, M.-L., Eds. Elsevier: 2017; pp 191-203.

275. Zielińska, A.; Nowak, I., Chapter 10 - Solid lipid nanoparticles and nanostructured lipid carriers as novel carriers for cosmetic ingredients. In *Nanobiomaterials in Galenic Formulations and Cosmetics*, Grumezescu, A. M., Ed. William Andrew Publishing: 2016; pp 231-255.

276. Stark, N. M.; Yelle, D. J.; Agarwal, U. P., 4 - Techniques for Characterizing Lignin. In *Lignin in Polymer Composites*, Faruk, O.; Sain, M., Eds. William Andrew Publishing: 2016; pp 49-66.

277. Jin, W.; Xu, W.; Liang, H.; Li, Y.; Liu, S.; Li, B., 1 - Nanoemulsions for food: properties, production, characterization, and applications. In *Emulsions*, Grumezescu, A. M., Ed. Academic Press: 2016; pp 1-36.

278. Meller, A.; Bar-Ziv, R.; Tlusty, T.; Moses, E.; Stavans, J.; Safran, S. A., Localized Dynamic Light Scattering: A New Approach to Dynamic Measurements in Optical Microscopy. *Biophysical Journal* **1998,** *74* (3), 1541-1548.

279. Stetefeld, J.; McKenna, S. A.; Patel, T. R., Dynamic light scattering: a practical guide and applications in biomedical sciences. *Biophys Rev* **2016,** *8* (4), 409-427.

280. Alawam, K., Chapter Nine - Application of Proteomics in Diagnosis of ADHD, Schizophrenia, Major Depression, and Suicidal Behavior. In *Advances in Protein Chemistry and Structural Biology*, Donev, R., Ed. Academic Press: 2014; Vol. 95, pp 283-315.

281. Gaffney, J. S.; Marley, N. A.; Jones, D. E., Fourier Transform Infrared (FTIR) Spectroscopy. In *Characterization of Materials*, 2012; pp 1-33.

282. Robinson, J. W.; Frame, E. M. S., *Undergraduate Instrumental Analysis*. CRC Press: 2004.

283. Oberlerchner, J. T.; Rosenau, T.; Potthast, A., Overview of Methods for the Direct Molar Mass Determination of Cellulose. *Molecules* **2015,** *20* (6), 10313-10341.

284. Glish, G. L.; Vachet, R. W., The basics of mass spectrometry in the twenty-first century. *Nature Reviews Drug Discovery* **2003,** *2* (2), 140-150.

285. El-Aneed, A.; Cohen, A.; Banoub, J., Mass Spectrometry, Review of the Basics: Electrospray, MALDI, and Commonly Used Mass Analyzers. *Applied Spectroscopy Reviews* **2009,** *44*, 210-230.

286. Nasrollahzadeh, M.; Atarod, M.; Sajjadi, M.; Sajadi, S. M.; Issaabadi, Z., Chapter 6 - Plant-Mediated Green Synthesis of Nanostructures: Mechanisms, Characterization, and Applications. In *Interface Science and Technology*, Nasrollahzadeh, M.; Sajadi, S. M.; Sajjadi, M.; Issaabadi, Z.; Atarod, M., Eds. Elsevier: 2019; Vol. 28, pp 199-322.

287. Adan, A.; Alizada, G.; Kiraz, Y.; Baran, Y.; Nalbant, A., Flow cytometry: basic principles and applications. *Critical Reviews in Biotechnology* **2017,** *37* (2), 163-176.

288. Macey, M. G., Principles of Flow Cytometry. In *Flow Cytometry: Principles and Applications*, Macey, M. G., Ed. Humana Press: Totowa, NJ, 2007; pp 1-15.

289. Vembadi, A.; Menachery, A.; Qasaimeh, M. A., Cell Cytometry: Review and Perspective on Biotechnological Advances. *Frontiers in Bioengineering and Biotechnology* **2019,** *7* (147).

290. Coling, D.; Kachar, B., Principles and Application of Fluorescence Microscopy. *Current Protocols in Molecular Biology* **1998,** *44* (1), 14.10.1-14.10.11.

291. Hillman, E. M. C.; Amoozegar, C. B.; Wang, T.; McCaslin, A. F. H.; Bouchard, M. B.; Mansfield, J.; Levenson, R. M., In vivo optical imaging and dynamic contrast methods for biomedical research. *Philos Trans A Math Phys Eng Sci* **2011,** *369* (1955), 4620-4643.

292. Hickson, J., In vivo optical imaging: Preclinical applications and considerations. *Urologic Oncology: Seminars and Original Investigations* **2009,** *27* (3), 295-297.

293. Shaner, N. C.; Campbell, R. E.; Steinbach, P. A.; Giepmans, B. N. G.; Palmer, A. E.; Tsien, R. Y., Improved monomeric red, orange and yellow fluorescent proteins derived from Discosoma sp. red fluorescent protein. *Nature Biotechnology* **2004,** *22* (12), 1567-1572.

294. Shaner, N. C.; Steinbach, P. A.; Tsien, R. Y., A guide to choosing fluorescent proteins. *Nature Methods* **2005,** *2* (12), 905-909.

295. Landsman, M. L.; Kwant, G.; Mook, G. A.; Zijlstra, W. G., Light-absorbing properties, stability, and spectral stabilization of indocyanine green. *Journal of applied physiology* **1976,** *40* (4), 575-83.

296. Bloch, S.; Lesage, F.; McIntosh, L.; Gandjbakhche, A.; Liang, K.; Achilefu, S., Whole-body fluorescence lifetime imaging of a tumor-targeted

near-infrared molecular probe in mice. *Journal of biomedical optics* **2005,** *10* (5), 054003.

297. Altınoğlu, E. I.; Russin, T. J.; Kaiser, J. M.; Barth, B. M.; Eklund, P. C.; Kester, M.; Adair, J. H., Near-Infrared Emitting Fluorophore-Doped Calcium Phosphate Nanoparticles for In Vivo Imaging of Human Breast Cancer. *ACS Nano* **2008,** *2* (10), 2075-2084.

298. Rao, J.; Dragulescu-Andrasi, A.; Yao, H., Fluorescence imaging in vivo: recent advances. *Current opinion in biotechnology* **2007,** *18* (1), 17-25.

299. Kitture, R.; Ghosh, S., Chapter 10 - Hybrid Nanostructures for In Vivo Imaging. In *Hybrid Nanostructures for Cancer Theranostics*, Ashok Bohara, R.; Thorat, N., Eds. Elsevier: 2019; pp 173-208.

300. Alauddin, M. M., Positron emission tomography (PET) imaging with (18)F-based radiotracers. *Am J Nucl Med Mol Imaging* **2012,** *2* (1), 55-76.

301. Phelps, M. E.; Hoffman, E. J.; Mullani, N. A.; Ter-Pogossian, M. M., Application of annihilation coincidence detection to transaxial reconstruction tomography. *Journal of nuclear medicine : official publication, Society of Nuclear Medicine* **1975,** *16* (3), 210-24.

302. Vaquero, J. J.; Kinahan, P., Positron Emission Tomography: Current Challenges and Opportunities for Technological Advances in Clinical and Preclinical Imaging Systems. *Annu Rev Biomed Eng* **2015,** *17*, 385-414.

303. Wei, X.; Li, F.; Zhao, G.; Chhonker, Y. S.; Averill, C.; Galdamez, J.; Purdue, P. E.; Wang, X.; Fehringer, E. V.; Garvin, K. L.; Goldring, S. R.; Alnouti, Y.; Wang, D., Pharmacokinetic and Biodistribution Studies of HPMA Copolymer Conjugates in an Aseptic Implant Loosening Mouse Model. *Molecular pharmaceutics* **2017,** *14* (5), 1418-1428.

304. Fletcher, N. L.; Houston, Z. H.; Simpson, J. D.; Veedu, R. N.; Thurecht, K. J., Designed multifunctional polymeric nanomedicines: long-term biodistribution and tumour accumulation of aptamer-targeted nanomaterials. *Chemical Communications* **2018,** *54* (82), 11538-11541.

305. Chakravarty, R.; Hong, H.; Cai, W., Positron emission tomography image-guided drug delivery: current status and future perspectives. *Molecular pharmaceutics* **2014,** *11* (11), 3777-3797.

306. Cormode, D. P.; Naha, P. C.; Fayad, Z. A., Nanoparticle contrast agents for computed tomography: a focus on micelles. *Contrast Media Mol Imaging* **2014,** *9* (1), 37-52.

307. Bhang, H.-e.; Tsuchiya, N.; Sysa-Shah, P.; Winkelmann, C. T.; Gabrielson, K., Chapter 9 - In Vivo Small Animal Imaging: A Comparison with Gross and Histopathologic Observations in Animal Models. In *Haschek and Rousseaux's Handbook of Toxicologic Pathology (Third Edition)*, Haschek, W. M.; Rousseaux, C. G.; Wallig, M. A., Eds. Academic Press: Boston, 2013; pp 287-315.

308. Bailey, D. L.; Townsend, D. W.; Valk, P. E.; Maisey, M. N., *Positron Emission Tomography: Basic Sciences*. Springer London: 2006.

309. Drifka, C. R.; Eliceiri, K. W.; Weber, S. M.; Kao, W. J., A bioengineered heterotypic stroma-cancer microenvironment model to study pancreatic ductal adenocarcinoma. *Lab Chip* **2013,** *13* (19), 3965-75.

310. von Ahrens, D.; Bhagat, T. D.; Nagrath, D.; Maitra, A.; Verma, A., The role of stromal cancer-associated fibroblasts in pancreatic cancer. *Journal of hematology & oncology* **2017,** *10* (1), 76-76.

311. Xie, D.; Xie, K., Pancreatic cancer stromal biology and therapy. *Genes & diseases* **2015,** *2* (2), 133-143.

312. Korc, M., Pancreatic cancer-associated stroma production. *American journal of surgery* **2007,** *194* (4 Suppl), S84-6.

313. Apte, M. V.; Pirola, R. C.; Wilson, J. S., Pancreatic stellate cells: a starring role in normal and diseased pancreas. *Front Physiol* **2012,** *3*, 344.

314. Feig, C.; Gopinathan, A.; Neesse, A.; Chan, D. S.; Cook, N.; Tuveson, D. A., The pancreas cancer microenvironment. *Clin Cancer Res* **2012,** *18* (16), 4266-76.

315. Erkan, M.; Hausmann, S.; Michalski, C. W.; Fingerle, A. A.; Dobritz, M.; Kleeff, J.; Friess, H., The role of stroma in pancreatic cancer: diagnostic and therapeutic implications. *Nat Rev Gastroenterol Hepatol* **2012,** *9* (8), 454-67.

316. Armstrong, T.; Packham, G.; Murphy, L. B.; Bateman, A. C.; Conti, J. A.; Fine, D. R.; Johnson, C. D.; Benyon, R. C.; Iredale, J. P., Type I collagen promotes the malignant phenotype of pancreatic ductal adenocarcinoma. *Clin Cancer Res* **2004,** *10* (21), 7427-37.

317. Shields, M. A.; Dangi-Garimella, S.; Redig, A. J.; Munshi, H. G., Biochemical role of the collagen-rich tumour microenvironment in pancreatic cancer progression. *Biochem J* **2012,** *441* (2), 541-52.

318. Lee, J. H.; Kim, S. K.; Khawar, I. A.; Jeong, S. Y.; Chung, S.; Kuh, H. J., Microfluidic co-culture of pancreatic tumor spheroids with stellate cells as a novel 3D model for investigation of stroma-mediated cell motility and drug resistance. *J Exp Clin Cancer Res* **2018,** *37* (1), 4.

319. Kordes, C.; Sawitza, I.; Götze, S.; Herebian, D.; Häussinger, D., Stellate cells are mesenchymal stem cells. *Eur J Med Res* **2014,** *19* (Suppl 1), S6-S6.

320. Ivanov, D. P.; Grabowska, A. M.; Garnett, M. C., High-Throughput Spheroid Screens Using Volume, Resazurin Reduction, and Acid Phosphatase Activity. In *Cell Viability Assays: Methods and Protocols*, Gilbert, D. F.; Friedrich, O., Eds. Springer New York: New York, NY, 2017; pp 43-59.

321. Yen, J. C.; Chang, F. J.; Chang, S., A new criterion for automatic multilevel thresholding. *IEEE transactions on image processing : a publication of the IEEE Signal Processing Society* **1995,** *4* (3), 370-8.

322. Spears, C. P., Volume doubling measurement of spherical and ellipsoidal tumors. *Medical and pediatric oncology* **1984,** *12* (3), 212-7.

323. Furuyama, A.; Mochitate, K., Assembly of the exogenous extracellular matrix during basement membrane formation by alveolar epithelial cells in vitro. *Journal of cell science* **2000,** *113 (Pt 5)*, 859-68.

324. Ivanov, D. P.; Grabowska, A. M., Spheroid arrays for high-throughput single-cell analysis of spatial patterns and biomarker expression in 3D. *Sci Rep* **2017,** *7*, 41160-41160.

325. Maliszewska-Olejniczak, K.; Brodaczewska, K. K.; Bielecka, Z. F.; Solarek, W.; Kornakiewicz, A.; Szczylik, C.; Porta, C.; Czarnecka, A. M., Development of extracellular matrix supported 3D culture of renal cancer cells and renal cancer stem cells. *Cytotechnology* **2019,** *71* (1), 149-163.

326. Wen, Z.; Liao, Q.; Hu, Y.; You, L.; Zhou, L.; Zhao, Y., A spheroid-based 3-D culture model for pancreatic cancer drug testing, using the acid phosphatase assay. *Brazilian journal of medical and biological research = Revista brasileira de pesquisas medicas e biologicas* **2013,** *46* (7), 634-42.

327. Bulin, A.-L.; Broekgaarden, M.; Simeone, D.; Hasan, T., Low dose photodynamic therapy harmonizes with radiation therapy to induce beneficial effects on pancreatic heterocellular spheroids. *Oncotarget* **2019,** *10* (27), 2625-2643.

328. Mori, H.; Ninomiya, K.; Kino-oka, M.; Shofuda, T.; Islam, M. O.; Yamasaki, M.; Okano, H.; Taya, M.; Kanemura, Y., Effect of neurosphere size on the growth rate of human neural stem/progenitor cells. *Journal of neuroscience research* **2006,** *84* (8), 1682-91.

329. Däster, S.; Amatruda, N.; Calabrese, D.; Ivanek, R.; Turrini, E.; Droeser, R. A.; Zajac, P.; Fimognari, C.; Spagnoli, G. C.; Iezzi, G.; Mele, V.; Muraro, M. G., Induction of hypoxia and necrosis in multicellular tumor spheroids is associated with resistance to chemotherapy treatment. *Oncotarget* **2016,** *8* (1), 1725-1736.

330. Hirschhaeuser, F.; Menne, H.; Dittfeld, C.; West, J.; Mueller-Klieser, W.; Kunz-Schughart, L. A., Multicellular tumor spheroids: an underestimated tool is catching up again. *J Biotechnol* **2010,** *148* (1), 3-15.

331. Gould, M. K.; Vu, X. L.; Seebeck, T.; de Koning, H. P., Propidium iodide-based methods for monitoring drug action in the kinetoplastidae: Comparison with the Alamar Blue assay. *Analytical Biochemistry* **2008,** *382* (2), 87-93.

332. Ferlini, C.; Di Cesare, S.; Rainaldi, G.; Malorni, W.; Samoggia, P.; Biselli, R.; Fattorossi, A., Flow cytometric analysis of the early phases of

apoptosis by cellular and nuclear techniques. *Cytometry* **1996,** *24* (2), 106-15.

333. Miura, Y.; Klettner, A.; Nölle, B.; Hasselbach, H.; Roider, J., *Change of Morphological and Functional Characteristics of Retinal Pigment Epithelium Cells during Cultivation of Retinal Pigment Epithelium-Choroid Perfusion Tissue Culture*. 2009; Vol. 43, p 122-33.

334. Palma, P. F. R.; Baggio, G. L.; Spada, C.; Silva, R. d.; Ferreira, S. I. A. C. P.; Treitinger, A., Evaluation of annexin V and Calcein-AM as markers of mononuclear cell apoptosis during human immunodeficiency virus infection. *Brazilian Journal of Infectious Diseases* **2008,** *12*, 108-114.

335. Neri, S.; Mariani, E.; Meneghetti, A.; Cattini, L.; Facchini, A., Calcein-Acetyoxymethyl Cytotoxicity Assay: Standardization of a Method Allowing Additional Analyses on Recovered Effector Cells and Supernatants. *Clinical and Diagnostic Laboratory Immunology* **2001,** *8* (6), 1131-1135.

336. Mehta, G.; Hsiao, A. Y.; Ingram, M.; Luker, G. D.; Takayama, S., Opportunities and challenges for use of tumor spheroids as models to test drug delivery and efficacy. *Journal of controlled release : official journal of the Controlled Release Society* **2012,** *164* (2), 192-204.

337. Zanoni, M.; Piccinini, F.; Arienti, C.; Zamagni, A.; Santi, S.; Polico, R.; Bevilacqua, A.; Tesei, A., 3D tumor spheroid models for in vitro therapeutic screening: a systematic approach to enhance the biological relevance of data obtained. *Sci Rep* **2016,** *6*, 19103.

338. Luo, D.; Hu, S.; Tang, C.; Liu, G., Mesenchymal stem cells promote cell invasion and migration and autophagy-induced epithelial-mesenchymal transition in A549 lung adenocarcinoma cells. *Cell Biochem Funct* **2018,** *36* (2), 88-94.

339. McAndrews, K. M.; McGrail, D. J.; Ravikumar, N.; Dawson, M. R., Mesenchymal Stem Cells Induce Directional Migration of Invasive Breast Cancer Cells through TGF-β. *Sci Rep* **2015,** *5*, 16941.

340. De Boeck, A.; Pauwels, P.; Hensen, K.; Rummens, J.-L.; Westbroek, W.; Hendrix, A.; Maynard, D.; Denys, H.; Lambein, K.; Braems, G.; Gespach, C.; Bracke, M.; Wever, O. D., Bone marrow-derived mesenchymal stem cells promote colorectal cancer progression through paracrine neuregulin 1/HER3 signalling. *Gut* **2013,** *62* (4), 550-560.

341. Saito, K.; Sakaguchi, M.; Maruyama, S.; Iioka, H.; Putranto, E. W.; Sumardika, I. W.; Tomonobu, N.; Kawasaki, T.; Homma, K.; Kondo, E., Stromal mesenchymal stem cells facilitate pancreatic cancer progression by regulating specific secretory molecules through mutual cellular interaction. *J Cancer* **2018,** *9* (16), 2916-2929.

342. Francini, N.; Purdie, L.; Alexander, C.; Mantovani, G.; Spain, S. G., Multifunctional Poly[N-(2-hydroxypropyl)methacrylamide] Copolymers via

Postpolymerization Modification and Sequential Thiol–Ene Chemistry. *Macromolecules* **2015,** *48* (9), 2857-2863.

343. Ebbesen, M. F.; Schaffert, D. H.; Crowley, M. L.; Oupický, D.; Howard, K. A., Synthesis of click-reactive HPMA copolymers using RAFT polymerization for drug delivery applications. *Journal of Polymer Science Part A: Polymer Chemistry* **2013,** *51* (23), 5091-5099.

344. Song, J.; Malathong, V.; Bertozzi, C. R., Mineralization of Synthetic Polymer Scaffolds: A Bottom-Up Approach for the Development of Artificial Bone. *Journal of the American Chemical Society* **2005,** *127* (10), 3366-3372.

345. Arno, M. C.; Inam, M.; Coe, Z.; Cambridge, G.; Macdougall, L. J.; Keogh, R.; Dove, A. P.; O'Reilly, R. K., Precision Epitaxy for Aqueous 1D and 2D Poly(ε-caprolactone) Assemblies. *Journal of the American Chemical Society* **2017,** *139* (46), 16980-16985.

346. Schmidt, B. V. K. J.; Hetzer, M.; Ritter, H.; Barner-Kowollik, C., UV Light and Temperature Responsive Supramolecular ABA Triblock Copolymers via Reversible Cyclodextrin Complexation. *Macromolecules* **2013,** *46* (3), 1054-1065.

347. Pardo, R.; Lo Ré, A.; Archange, C.; Ropolo, A.; Papademetrio, D. L.; Gonzalez, C. D.; Alvarez, E. M.; Iovanna, J. L.; Vaccaro, M. I., Gemcitabine Induces the VMP1 -Mediated Autophagy Pathway to Promote Apoptotic Death in Human Pancreatic Cancer Cells. *Pancreatology* **2010,** *10* (1), 19-26.

348. Thurecht, K. J.; Blakey, I.; Peng, H.; Squires, O.; Hsu, S.; Alexander, C.; Whittaker, A. K., Functional hyperbranched polymers: toward targeted in vivo 19F magnetic resonance imaging using designed macromolecules. *J Am Chem Soc* **2010,** *132* (15), 5336-7.

349. Pearce, A. K.; Rolfe, B. E.; Russell, P. J.; Tse, B. W. C.; Whittaker, A. K.; Fuchs, A. V.; Thurecht, K. J., Development of a polymer theranostic for prostate cancer. *Polymer Chemistry* **2014,** *5* (24), 6932-6942.

350. Zhao, J.; Lu, H.; Wong, S.; Lu, M.; Xiao, P.; Stenzel, M. H., Influence of nanoparticle shapes on cellular uptake of paclitaxel loaded nanoparticles in 2D and 3D cancer models. *Polymer Chemistry* **2017,** *8* (21), 3317-3326.

351. Wang, J.; Mao, W.; Lock, L. L.; Tang, J.; Sui, M.; Sun, W.; Cui, H.; Xu, D.; Shen, Y., The Role of Micelle Size in Tumor Accumulation, Penetration, and Treatment. *ACS Nano* **2015,** *9* (7), 7195-7206.

352. Salmaso, S.; Caliceti, P., Stealth Properties to Improve Therapeutic Efficacy of Drug Nanocarriers. *Journal of Drug Delivery* **2013,** *2013*, 19.

353. Salmaso, S.; Caliceti, P., Stealth properties to improve therapeutic efficacy of drug nanocarriers. *J Drug Deliv* **2013,** *2013*, 374252-374252.

354. Feng, Q.; Liu, Y.; Huang, J.; Chen, K.; Huang, J.; Xiao, K., Uptake, distribution, clearance, and toxicity of iron oxide nanoparticles with different sizes and coatings. *Sci Rep* **2018,** *8* (1), 2082.

355. Zhang, J.; Liu, D.; Zhang, M.; Sun, Y.; Zhang, X.; Guan, G.; Zhao, X.; Qiao, M.; Chen, D.; Hu, H., The cellular uptake mechanism, intracellular transportation, and exocytosis of polyamidoamine dendrimers in multidrug-resistant breast cancer cells. *International journal of nanomedicine* **2016,** *11*, 3677-3690.

356. Liu, P.; Sun, Y.; Wang, Q.; Sun, Y.; Li, H.; Duan, Y., Intracellular trafficking and cellular uptake mechanism of mPEG-PLGA-PLL and mPEG-PLGA-PLL-Gal nanoparticles for targeted delivery to hepatomas. *Biomaterials* **2014,** *35* (2), 760-70.

357. Foroozandeh, P.; Aziz, A. A., Insight into Cellular Uptake and Intracellular Trafficking of Nanoparticles. *Nanoscale Res Lett* **2018,** *13* (1), 339.

358. Xiang, S.; Tong, H.; Shi, Q.; Fernandes, J. C.; Jin, T.; Dai, K.; Zhang, X., Uptake mechanisms of non-viral gene delivery. *J Control Release* **2012,** *158* (3), 371-8.

359. Zhang, Y.; Hoppe, A. D.; Swanson, J. A., Coordination of Fc receptor signaling regulates cellular commitment to phagocytosis. *Proceedings of the National Academy of Sciences* **2010,** *107* (45), 19332-19337.

360. Gustafson, H. H.; Holt-Casper, D.; Grainger, D. W.; Ghandehari, H., Nanoparticle Uptake: The Phagocyte Problem. *Nano Today* **2015,** *10* (4), 487-510.

361. Panariti, A.; Miserocchi, G.; Rivolta, I., The effect of nanoparticle uptake on cellular behavior: disrupting or enabling functions? *Nanotechnol Sci Appl* **2012,** *5*, 87-100.

362. Bishop, N. E., An Update on Non-clathrin-coated Endocytosis. *Rev Med Virol* **1997,** *7* (4), 199-209.

363. Sandvig, K.; Torgersen, M. L.; Raa, H. A.; van Deurs, B., Clathrin-independent endocytosis: from nonexisting to an extreme degree of complexity. *Histochemistry and Cell Biology* **2008,** *129* (3), 267-276.

364. Lu, F.; Wu, S. H.; Hung, Y.; Mou, C. Y., Size effect on cell uptake in well-suspended, uniform mesoporous silica nanoparticles. *Small* **2009,** *5* (12), 1408-13.

365. Choi, H. S.; Liu, W.; Misra, P.; Tanaka, E.; Zimmer, J. P.; Itty Ipe, B.; Bawendi, M. G.; Frangioni, J. V., Renal clearance of quantum dots. *Nature biotechnology* **2007,** *25* (10), 1165-1170.

366. Longmire, M.; Choyke, P. L.; Kobayashi, H., Clearance properties of nano-sized particles and molecules as imaging agents: considerations and caveats. *Nanomedicine (London, England)* **2008,** *3* (5), 703-717.

367. Duncan, R.; Vicent, M. J., Do HPMA copolymer conjugates have a future as clinically useful nanomedicines? A critical overview of current status and future opportunities. *Adv Drug Deliv Rev* **2010,** *62* (2), 272-82.

368. van de Watering, F. C. J.; Rijpkema, M.; Perk, L.; Brinkmann, U.; Oyen, W. J. G.; Boerman, O. C., Zirconium-89 Labeled Antibodies: A New Tool for Molecular Imaging in Cancer Patients. *BioMed Research International* **2014,** *2014*, 13.

369. Deri, M. A.; Zeglis, B. M.; Francesconi, L. C.; Lewis, J. S., PET imaging with (8)(9)Zr: from radiochemistry to the clinic. *Nucl Med Biol* **2013,** *40* (1), 3-14.

370. Yang, Q.; Li, L.; Zhu, X.; Sun, W.; Zhou, Z.; Huang, Y., The impact of the HPMA polymer structure on the targeting performance of the conjugated hydrophobic ligand. *RSC Advances* **2015,** *5* (19), 14858-14870.

371. Markovsky, E.; Baabur-Cohen, H.; Eldar-Boock, A.; Omer, L.; Tiram, G.; Ferber, S.; Ofek, P.; Polyak, D.; Scomparin, A.; Satchi-Fainaro, R., Administration, distribution, metabolism and elimination of polymer therapeutics. *J Control Release* **2012,** *161* (2), 446-60.

372. Choudhury, P. K.; Bagchi, D.; Sangeeth, C. S. S.; Menon, R., Modified conformation and physical properties in conducting polymers due to varying conjugation and solvent interactions. *Journal of Materials Chemistry* **2011,** *21* (5), 1607-1614.

373. Koziolová, E.; Goel, S.; Chytil, P.; Janoušková, O.; Barnhart, T. E.; Cai, W.; Etrych, T., A tumor-targeted polymer theranostics platform for positron emission tomography and fluorescence imaging. *Nanoscale* **2017,** *9* (30), 10906-10918.

374. Jordheim, L. P.; Durantel, D.; Zoulim, F.; Dumontet, C., Advances in the development of nucleoside and nucleotide analogues for cancer and viral diseases. *Nature Reviews Drug Discovery* **2013,** *12*, 447.

375. Estrella, M. C. A. U. J. E. R., Optimal treatment for metastatic bladder cancer. *Optimal treatment for metastatic bladder cancer* **2014,** *10* (6), 347-356-347-356.

376. Fowler, W. C., Jr.; Van Le, L., Gemcitabine as a single-agent treatment for ovarian cancer. *Gynecol Oncol* **2003,** *90* (2 Pt 2), S21-3.

377. Manegold, C., Gemcitabine (Gemzar) in non-small cell lung cancer. *Expert Rev Anticancer Ther* **2004,** *4* (3), 345-60.

378. Heinemann, V., Gemcitabine in metastatic breast cancer. *Expert Rev Anticancer Ther* **2005,** *5* (3), 429-43.

379. Dubey, R. D.; Saneja, A.; Gupta, P. K.; Gupta, P. N., Recent advances in drug delivery strategies for improved therapeutic efficacy of gemcitabine. *European Journal of Pharmaceutical Sciences* **2016,** *93*, 147-162.

380. Hui, Y. F.; Reitz, J., Gemcitabine: A cytidine analogue active against solid tumors. *American Journal of Health-System Pharmacy* **1997,** *54* (2), 162-170.

381. Dasanu, C. A., Gemcitabine: vascular toxicity and prothrombotic potential. *Expert Opinion on Drug Safety* **2008,** *7* (6), 703-716.

382. Bender, D. M.; Bao, J.; Dantzig, A. H.; Diseroad, W. D.; Law, K. L.; Magnus, N. A.; Peterson, J. A.; Perkins, E. J.; Pu, Y. J.; Reutzel-Edens, S. M.; Remick, D. M.; Starling, J. J.; Stephenson, G. A.; Vaid, R. K.; Zhang, D.; McCarthy, J. R., Synthesis, Crystallization, and Biological Evaluation of an Orally Active Prodrug of Gemcitabine. *Journal of Medicinal Chemistry* **2009,** *52* (22), 6958-6961.

383. Vandana, M.; Sahoo, S. K., Long circulation and cytotoxicity of PEGylated gemcitabine and its potential for the treatment of pancreatic cancer. *Biomaterials* **2010,** *31* (35), 9340-9356.

384. Yang, J.; Luo, K.; Pan, H.; Kopečková, P.; Kopeček, J., Synthesis of biodegradable multiblock copolymers by click coupling of RAFT-generated heterotelechelic polyHPMA conjugates. *Reactive and Functional Polymers* **2011,** *71* (3), 294-302.

385. Khare, V.; Kour, S.; Alam, N.; Dubey, R. D.; Saneja, A.; Koul, M.; Gupta, A. P.; Singh, D.; Singh, S. K.; Saxena, A. K.; Gupta, P. N., Synthesis, characterization and mechanistic-insight into the anti-proliferative potential of PLGA-gemcitabine conjugate. *International Journal of Pharmaceutics* **2014,** *470* (1), 51-62.

386. Xie, D.; Xie, K., Pancreatic cancer stromal biology and therapy. *Genes & Diseases* **2015,** *2* (2), 133-143.

387. Korc, M., Pancreatic cancer associated stroma production. *American journal of surgery* **2007,** *194* (4 Supplement 1), s84-s86.

388. Felix, K.; Gaida, M. M., Neutrophil-Derived Proteases in the Microenvironment of Pancreatic Cancer -Active Players in Tumor Progression. *Int J Biol Sci* **2016,** *12* (3), 302-313.

389. Banik, B. L.; Brown, J. L., Chapter 23 - Polymeric Biomaterials in Nanomedicine. In *Natural and Synthetic Biomedical Polymers*, Kumbar, S. G.; Laurencin, C. T.; Deng, M., Eds. Elsevier: Oxford, 2014; pp 387-395.

390. Cook, A. B.; Barbey, R.; Burns, J. A.; Perrier, S., Hyperbranched Polymers with High Degrees of Branching and Low Dispersity Values: Pushing the Limits of Thiol–Yne Chemistry. *Macromolecules* **2016,** *49* (4), 1296-1304.

391. Pan, H.; Marsh, J. N.; Christenson, E. T.; Soman, N. R.; Ivashyna, O.; Lanza, G. M.; Schlesinger, P. H.; Wickline, S. A., Chapter two - Postformulation Peptide Drug Loading of Nanostructures. In *Methods in Enzymology*, Düzgüneş, N., Ed. Academic Press: 2012; Vol. 508, pp 17-39.

392. Perrault, S. D.; Walkey, C.; Jennings, T.; Fischer, H. C.; Chan, W. C. W., Mediating Tumor Targeting Efficiency of Nanoparticles Through Design. *Nano Letters* **2009,** *9* (5), 1909-1915.

393. Acharya, S.; Sahoo, S. K., PLGA nanoparticles containing various anticancer agents and tumour delivery by EPR effect. *Adv Drug Deliv Rev* **2011,** *63* (3), 170-83.

394. Khadka, P.; Ro, J.; Kim, H.; Kim, I.; Kim, J. T.; Kim, H.; Cho, J. M.; Yun, G.; Lee, J., Pharmaceutical particle technologies: An approach to improve drug solubility, dissolution and bioavailability. *Asian Journal of Pharmaceutical Sciences* **2014,** *9* (6), 304-316.

395. Graeser, K. A.; Patterson, J. E.; Zeitler, J. A.; Rades, T., The role of configurational entropy in amorphous systems. *Pharmaceutics* **2010,** *2* (2), 224-244.

396. Amrutkar, M.; Gladhaug, I. P., Pancreatic Cancer Chemoresistance to Gemcitabine. *Cancers* **2017,** *9* (11).

397. Gore, J.; Korc, M., Pancreatic Cancer Stroma: Friend or Foe? *Cancer Cell* **2014,** *25* (6), 711-712.

398. Longati, P.; Jia, X.; Eimer, J.; Wagman, A.; Witt, M. R.; Rehnmark, S.; Verbeke, C.; Toftgard, R.; Lohr, M.; Heuchel, R. L., 3D pancreatic carcinoma spheroids induce a matrix-rich, chemoresistant phenotype offering a better model for drug testing. *BMC Cancer* **2013,** *13*, 95.

399. Kyle, A. H.; Huxham, L. A.; Yeoman, D. M.; Minchinton, A. I., Limited tissue penetration of taxanes: a mechanism for resistance in solid tumors. *Clin Cancer Res* **2007,** *13* (9), 2804-10.

400. Oshikata, A.; Matsushita, T.; Ueoka, R., Enhancement of drug efflux activity via MDR1 protein by spheroid culture of human hepatic cancer cells. *J Biosci Bioeng* **2011,** *111* (5), 590-3.

401. Godugu, C.; Patel, A. R.; Desai, U.; Andey, T.; Sams, A.; Singh, M., AlgiMatrix based 3D cell culture system as an in-vitro tumor model for anticancer studies. *PLoS One* **2013,** *8* (1), e53708.

402. Lu, H.; Utama, R. H.; Kitiyotsawat, U.; Babiuch, K.; Jiang, Y.; Stenzel, M. H., Enhanced transcellular penetration and drug delivery by crosslinked polymeric micelles into pancreatic multicellular tumor spheroids. *Biomater Sci* **2015,** *3* (7), 1085-95.

403. Lazzari, G.; Couvreur, P.; Mura, S., Multicellular tumor spheroids: a relevant 3D model for the in vitro preclinical investigation of polymer nanomedicines. *Polymer Chemistry* **2017,** *8* (34), 4947-4969.

404. Duncan, R., Polymer therapeutics at a crossroads? Finding the path for improved translation in the twenty-first century. *Journal of Drug Targeting* **2017,** *25* (9-10), 759-780.

405. Manji, G. A.; Olive, K. P.; Saenger, Y. M.; Oberstein, P., Current and Emerging Therapies in Metastatic Pancreatic Cancer. *Clinical Cancer Research* **2017,** *23* (7), 1670-1678.

406. Miles, D.; von Minckwitz, G.; Seidman, A. D., Combination versus sequential single-agent therapy in metastatic breast cancer. *Oncologist* **2002,** *7 Suppl 6*, 13-9.

407. Sandler, A.; Ettinger, D. S., Gemcitabine: single-agent and combination therapy in non-small cell lung cancer. *Oncologist* **1999,** *4* (3), 241-51.

408. Leary, M.; Heerboth, S.; Lapinska, K.; Sarkar, S., Sensitization of Drug Resistant Cancer Cells: A Matter of Combination Therapy. *Cancers* **2018,** *10* (12), 483.

409. Pommier, Y.; Leo, E.; Zhang, H.; Marchand, C., DNA Topoisomerases and Their Poisoning by Anticancer and Antibacterial Drugs. *Chemistry & Biology* **2010,** *17* (5), 421-433.

410. Pérez-Manga, G.; Lluch, A.; Alba, E.; Moreno-Nogueira, J. A.; Palomero, M.; García-Conde, J.; Khayat, D.; Rivelles, N., Gemcitabine in Combination With Doxorubicin in Advanced Breast Cancer: Final Results of a Phase II Pharmacokinetic Trial. *Journal of Clinical Oncology* **2000,** *18* (13), 2545-2552.

411. Lombardi, G.; Zustovich, F.; Farinati, F.; Cillo, U.; Vitale, A.; Zanus, G.; Donach, M.; Farina, M.; Zovato, S.; Pastorelli, D., Pegylated liposomal doxorubicin and gemcitabine in patients with advanced hepatocellular carcinoma. *Cancer* **2011,** *117* (1), 125-133.

412. Lammers, T.; Subr, V.; Ulbrich, K.; Peschke, P.; Huber, P. E.; Hennink, W. E.; Storm, G., Simultaneous delivery of doxorubicin and gemcitabine to tumors in vivo using prototypic polymeric drug carriers. *Biomaterials* **2009,** *30* (20), 3466-3475.

413. Liu, D.; Chen, Y.; Feng, X.; Deng, M.; Xie, G.; Wang, J.; Zhang, L.; Liu, Q.; Yuan, P., Micellar nanoparticles loaded with gemcitabine and doxorubicin showed synergistic effect. *Colloids and Surfaces B: Biointerfaces* **2014,** *113*, 158-168.

414. Riber, C. F.; Smith, A. A.; Zelikin, A. N., Self-Immolative Linkers Literally Bridge Disulfide Chemistry and the Realm of Thiol-Free Drugs. *Adv Healthc Mater* **2015,** *4* (12), 1887-90.

415. Riber, C. F.; Smith, A. A. A.; Zelikin, A. N., Self-Immolative Linkers Literally Bridge Disulfide Chemistry and the Realm of Thiol-Free Drugs. *Advanced Healthcare Materials* **2015,** *4* (12), 1887-1890.

416. Sengee, M.; Eksteen, J. J.; Nergård, S. L.; Vasskog, T.; Sydnes, L. K., Preparation and Assessment of Self-Immolative Linkers for Therapeutic Bioconjugates with Amino- and Hydroxyl-Containing Cargoes. *Bioconjugate Chemistry* **2019,** *30* (5), 1489-1499.

417. Chou, T.; Martin, N., CompuSyn for drug combinations: PC software and user's guide: a computer program for quantitation of synergism and antagonism in drug combinations, and the determination of IC50 and ED50 and LD50 values. *ComboSyn, Paramus, NJ* **2005**.

418. Chou, T. C., Theoretical basis, experimental design, and computerized simulation of synergism and antagonism in drug combination studies. *Pharmacol Rev* **2006,** *58* (3), 621-81.

419. Yang, S.; Zhu, F.; Wang, Q.; Liang, F.; Qu, X.; Gan, Z.; Yang, Z., Combinatorial targeting polymeric micelles for anti-tumor drug delivery. *Journal of Materials Chemistry B* **2015,** *3* (19), 4043-4051.

420. Lv, S.; Tang, Z.; Li, M.; Lin, J.; Song, W.; Liu, H.; Huang, Y.; Zhang, Y.; Chen, X., Co-delivery of doxorubicin and paclitaxel by PEG-polypeptide nanovehicle for the treatment of non-small cell lung cancer. *Biomaterials* **2014,** *35* (23), 6118-29.

421. Gustafson, D. L.; Merz, A. L.; Long, M. E., Pharmacokinetics of combined doxorubicin and paclitaxel in mice. *Cancer Lett* **2005,** *220* (2), 161-9.

422. Vicent, M. J.; Greco, F.; Nicholson, R. I.; Paul, A.; Griffiths, P. C.; Duncan, R., Polymer Therapeutics Designed for a Combination Therapy of Hormone-Dependent Cancer. *Angewandte Chemie International Edition* **2005,** *44* (26), 4061-4066.

423. Speelmans, G.; Staffhorst, R. W.; de Kruijff, B.; de Wolf, F. A., Transport studies of doxorubicin in model membranes indicate a difference in passive diffusion across and binding at the outer and inner leaflets of the plasma membrane. *Biochemistry* **1994,** *33* (46), 13761-8.

424. Faraji, A.; Dehghan, H. R.; Mobaraki, M.; Zare, M.; Houshmand, M., Association of ABCB1 and SLC22A16 Gene Polymorphisms with Incidence of Doxorubicin-Induced Febrile Neutropenia: A Survey of Iranian Breast Cancer Patients. *PLOS ONE* **2016,** *11*.

425. Barros, A. S.; Costa, E. C.; Nunes, A. S.; de Melo-Diogo, D.; Correia, I. J., Comparative study of the therapeutic effect of Doxorubicin and Resveratrol combination on 2D and 3D (spheroids) cell culture models. *International Journal of Pharmaceutics* **2018,** *551* (1), 76-83.

426. Hollamby, M. J., Practical applications of small-angle neutron scattering. *Physical Chemistry Chemical Physics* **2013,** *15* (26), 10566-10579.

427. Yeung, C. K.; Himmelfarb, J., Kidneys on Chips. *Emerging Technology for Preclinical Drug Development* **2019,** *14* (1), 144-146.

428. Danaei, M.; Dehghankhold, M.; Ataei, S.; Hasanzadeh Davarani, F.; Javanmard, R.; Dokhani, A.; Khorasani, S.; Mozafari, M. R., Impact of Particle Size and Polydispersity Index on the Clinical Applications of Lipidic Nanocarrier Systems. *Pharmaceutics* **2018,** *10* (2).

429. Zhang, H.; Lyden, D., Asymmetric-flow field-flow fractionation technology for exomere and small extracellular vesicle separation and characterization. *Nature Protocols* **2019,** *14* (4), 1027-1053.

430. Welker, R. W., Chapter 4 - Size Analysis and Identification of Particles. In *Developments in Surface Contamination and Cleaning*, Kohli, R.; Mittal, K. L., Eds. William Andrew Publishing: Oxford, 2012; pp 179-213.

Chapter 9 Appendix

Additional images from PET-CT studies can be found on the attached USB flash Drive.